

# A Cognitive Approach to Improve the Quality of Service in NB-IoT

Madiraju.Sirisha, PhD Scholar, Dept. Of ECE Jawaharlal Nehru Technological University, Ananthapuramu,  
madiraju.sirisha@gmail.com

Dr. P.Abdul Khayum, Professor, Dept. Of ECE, G.Pulla Reddy Engineering College, Kurnool, A.P., India, PIN: 518007,  
abd khayum@rediffmail.com

Joseph Rajiv Kantheti, Assistant Professor of ECE, Nalla Malla Reddy Engineering College, Hyderabad,  
josephrajivk@gmail.com

## Article Info

Volume 82

Page Number: 8741 - 8746

Publication Issue:

January-February 2020

## Article History

Article Received: 5 April 2019

Revised: 18 Jun 2019

Accepted: 24 October 2019

Publication: 08 February 2020

## Abstract:

Narrow Band Internet of Things (NB-IoT), a 3GPP Release-13 proposed technology is well known for its low power consumption and wide area coverage. These are the most urging requirements of current scenarios of industrial, research and also social. To enhance the coverage of NB-IoT, redundant data is transmitted. This redundant data transmission improves the area coverage in NB-IoT when compared with Long Term Evolution (LTE). But a large number of repetitions of the data leads to a reduction in the throughput and a raise in the delay. The battery lifetime of the IoT devices gets reduced and the cost of maintenance increases. In this paper, an efficient routing (Q-AODV routing algorithm) using Reinforcement algorithm is suggested to avoid repetition of data for an extent. A Q-learning algorithm is used for decision making in an Ad hoc On demand Distant Vector (AODV) routing algorithm. This improves the throughput and decreases the delay. Simulation of a network with Q-AODV routing algorithm is performed and compared with the traditional AODV routing algorithm.

## I. INTRODUCTION

Narrowband in NB-IoT refers to its bandwidth of 200 kHz. To meet the global requirements like quality, speed, coverage and low power consumption, a narrow band Internet of Things (NB-IoT) standard was introduced by 3GPP release 13. The major benefits of NB-IoT are its wider coverage and low power consumption. Because of the low power consumption the battery life of the device increases. The coverage area is increased by transmitting of data repeatedly. But this reduces the throughput of the network and also increases the end to end delay. There will be reduction in Quality of Service (QoS). Several efforts are made by many researchers to increase the quality of service in NB-IoT.

NarrowBand IoT is similar to the mobile communication where communication is done between two things or devices. Backbone of any network is its routing. Proactive and Reactive types

of routing algorithms provide routing protocols. In proactive algorithms bandwidth requirement and power consumption are high when compared to reactive routing algorithms. Due the advantage of having low bandwidth requirement and low power consumption, reactive routing algorithms are on demand. Adhoc On Demand Vector Routing (AODV) is a reactive routing algorithm. In this a modified version of AODV, Q-AODV is implemented to increase the Quality of Service in a NB-IoT network. Q-learning a reinforcement algorithm is used with AODV to make it intelligent routing algorithm.

## II. BACKGROUND

In this section AODV and Q-learning algorithms are discussed. Their characteristics and the methodology are analysed. In the next section i.e., in section III motivation towards this approach is given, in section IV proposed algorithm is discussed,

in section V results and in section VI conclusion is given.

(a) AODV (Adhoc On Demand Distance Vector):

In this AODV distance vector routing protocol route to the destination is determined only on demand [11]. To perform routing forwarding tables are used at each node. A route request packet (RREQ) is broadcasted by the node that wants to send a packet. This packet is sent to the neighbour nodes. There after the neighbour node broadcast this packet to other neighbor nodes. This process continues until the packet reaches the destination. A reverse path is established while forwarding the request and the destination node replies back by sending RREP through this path. If there is any route breakage then it is informed with an error, RERR (route error). Fig. I shows a network that uses AODV routing algorithm[6].

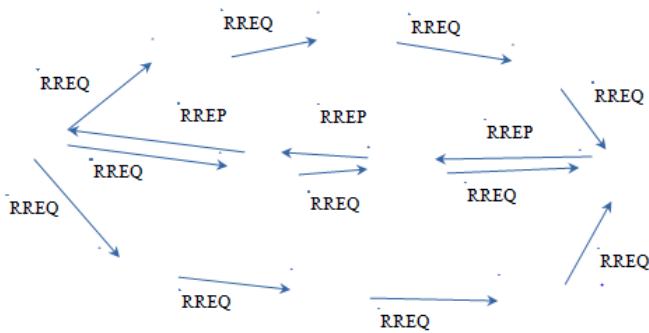


Fig I. Example network using AODV routing protocol

(b) Q-Learning:

Q-Learning is one of the method of reinforcement learning which is a classification of machine learning. Q stands for quality here. It is an off policy algorithm that decides the next state whrn the current state is known and gets rewarded for the next state. It checks for the next state which has a maximum reward and proceeds with that next state. A Q-table [q (state, action)] is created with states, actions and the rewards [8]. This Q-table is updated until an end of the episode is reached. This table is used by the

agent to predict which action to be taken for the current state to get better rewards.

Reaction of an agent with the environment is done in 2 ways, exploiting and exploring. In exploiting, the agent takes the maximum value of reward and does that action. Exploring is where the agent takes the action randomly and decides the next state. Exploring is the best way of taking an action. As the action is chosen randomly, there is a chance of exploring the new states[5].

A q-table is updated at each and every action until the end of an episode is reached. For a network, packet reaching the destination is an end of episode. The agent learns only till the end of episode and gets the optimised values for the q denoted as q\*. After reaching the end of episode it stops learning.

The following code shows the creation of the Q-table.

```
import numpy as np
# Initializing q-table
Q = np.zeros((Size_state, Size_action))
```

Q-learning is the best algorithm in the situations where decision making is crucial at each and every step for a long run goal. Q-learning algorithm implementation in a network improves the throghput of the network as the action of maximum rewards is selected for the next state from the current state.

III. RELATED WORK

NB-IoT is similar to Mobile Adhoc Networks or simple MANET which is basically network of networks[11]. Many routing protocols are proposed to manage these MANETs. There are proactive and reactive protocols which are used to route the data from source to destination. AODV is one such type of protocol. To improve the performance of a network some intelligent component has to be included. AI (Artificial Intelligence) is one which

makes the protocol better. So, a modified AODV with AI gives better performance results.

Ali Nauman et. al. specifies a key solution for NB-IoT UE. It is specified that to increase the performance two hops system is proposed instead of direct transmission [2]. Optimization of Expected packet Delivery Ratio (EDR) and End to End Delay is achieved by opportunistic approach. But this gives an additional delay due to lack of intelligent systems. This lead to design an intelligent system called as deterministic D2D (2D2D) relay selection strategy for NB-IoT UE s (User Equipments).

Coverage in NB-IoT can be enhanced by machine learning algorithms. A dynamic spectrum access is proposed to reduce the repeated transmission of data which in turn increases the coverage and reduces the energy consumption. [1]

Md Khalid Hossain Jewel et. al. Proposes a technique to reduce complexity. To reduce the complexity of Linear Minimum Mean Square Error (LMMSE) which is used to reduce the channel condition, [3] Singular Value Decomposition (SVD) and splitting the channel auto correlation matrices is performed.

Q-learning is one of the reinforcement learning technique. It is used for solving shortest path (STP) problem. The average sum of the rewards is anyway moderate. To address the problem of low average sum, a Multi-Q-Table is proposed [8]. In this method a Q-Table is built at every sub-goal. It helps the agent to know that sub-reward is collected. The proposed modifies algorithm with Multi-Q-Tables collect all rewards and avoids pit in reaching the goal with shortest path.[8]

To improve the Quality of Service (QoS) in NB-IoT, in this paper, a modified AODV routing protocol is used. Q-learning technique is introduced in AODV to make it more efficient. This algorithm improves the throughput of the network and reduces the delay.

Section IV gives the complete knowledge of the proposed algorithm.

#### IV. PROPOSED METHODOLOGY

The proposed methodology is a combination of both the features of AODV routing algorithm and Q-learning algorithm. AODV is used for best routing of the packets from source to destination. Q-learning is a Reinforcement algorithm of machine learning. This is used to make a decision of the next state with the details of the current state. Thus this Q-learning helps AODV for the selection of the best route with smallest distance and with less time.

In AODV protocol the Route discovery overhead is obtained with the two major parameters Route Request (RREQ) overhead and Route Reply (RREP) is mathematically modelled as [4]

$$R_{RREQ} = \sum_{n=1}^H (4)3^{(n-1)} \sum_{i=2}^4 \left[ (n-i-1) - \sum_{j=1}^{H-1} N_j \right] pCi \quad (1)$$

Here, H is number hops expected to reach destination

n is the number value of the tier

N<sub>j</sub> is the number of neighbours expected at j<sup>th</sup> hop

Route Reply overhead is given by

$$R_{RREP} = H + (H/2)(n-h-2)p \quad (2)$$

Route discovery overhead is the combination of route request and route reply and it is given by

$$R_{discovery} = R_{RREQ} + R_{RREP} \quad (3)$$

By substituting Eq.(1) and Eq.(2) in Eq.(3)

$$R_{discovery} = \sum_{n=1}^H (4)3^{(n-1)} \sum_{i=2}^4 \left[ (n-i-1) - \sum_{j=1}^{H-1} N_j \right] pCi + H + (H/2)(n-h-2)p$$

The value of H changes with the implementation of Q-learning protocol. With Q-learning protocol the number of hops expected changes to HQ. So, using Q-AODV protocol the throughput increases and the end to end delay decreases. Then the  $R_{\text{discovery}}$  equation changes to

$$R_{\text{discovery}} = \sum_{n=1}^{HQ} (4)3^{(n-1)} \sum_{i=2}^4 \left[ (n-i-1) - \sum_{j=1}^{HQ-1} N_j \right] p C_i + HQ + (HQ/2)(n-hq-2)p$$

where HQ is the optimal action value function given by

$HQ = \max(q\Pi(s,a))$ ,  $q\Pi(s,a)$  is the Bellman equation of the state value function and is given by

$$q\Pi(s,a) = q \pi(s, a) = R_{s+a}^a + \gamma \sum_{s'} P^a v(s')$$

$v(s')$  is the state value function that gives the long term value of state  $s$  following  $\pi$  policy.

By using optimum value function in the decision making of AODV routing algorithm, the quality of

service of the network gets improved. Implementing Q-learning in AODV routing algorithm, makes that routing algorithm cognitive.

## V. RESULT AND DISCUSSION

The parameters and its values of the simulated network are given in the Table I. A network of 25 nodes with 10 sinks is used. The data rate is 2kbps, transmitted with 75dBm power. The propagation loss model used is FRIIS propagation loss model. The nodes are moving with random mobility model at a constant speed propagation. The positions of nodes are defined by a random rectangular position allocator. The area of simulation is 300m x 1500m. Nodes are moving at a speed of 0-20ms. The packets sent for second are four packets. Each packet consists of 64 bytes of data.

Traditional AODV and Q-AODV routing protocols are simulated using network simulator with all the specifications given in the Table I.

Table I. List of parameters used in the simulated network and its values

S.No.	Name of the parameter used in the simulated network	Value
1.	Number of nodes	25
2.	Number of sinks	10
3.	Rate	2.048 kbps
4.	Transmitted Power	75dBm
5.	Propagation loss model	Fri is propagation loss model
6.	Propagation delay model	Constant speed propagation delay model
7.	Node speed	0-20ms
8.	Mobility model	Random way Mobility Model
9.	Protocols	AODV, Q-AODV
10.	Wifi Manager	Constant Rate Wifi Manager
11.	Mac model	802.11b(11 Mbps)
12.	Position allocator	Random Rectangle Position Allocator
13.	Area of simulation	300m x 1500m
14.	Packet size	4 packets per second

Fig 2. gives the comparison of end to end delay between traditional AODV and Q-AODV routing protocols. It is observed that delay is reduced when AODV is compared with Q-AODV routing algorithm.

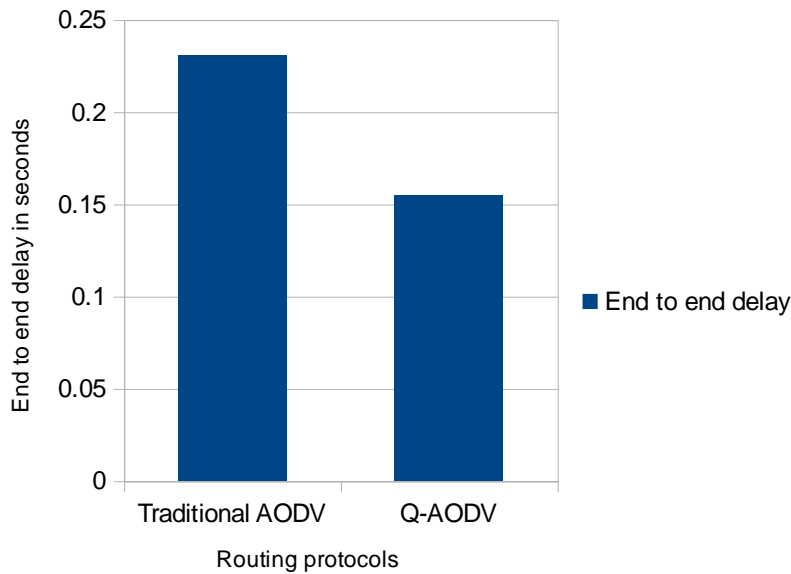


Fig 2. Comparison of End to End delay between traditional AODV and Q-AODV routing protocols

In the Fig. 3 it is very clear that the throughput of the NB-IoT is more with Q-AODV routing rather than traditional AODV routing.

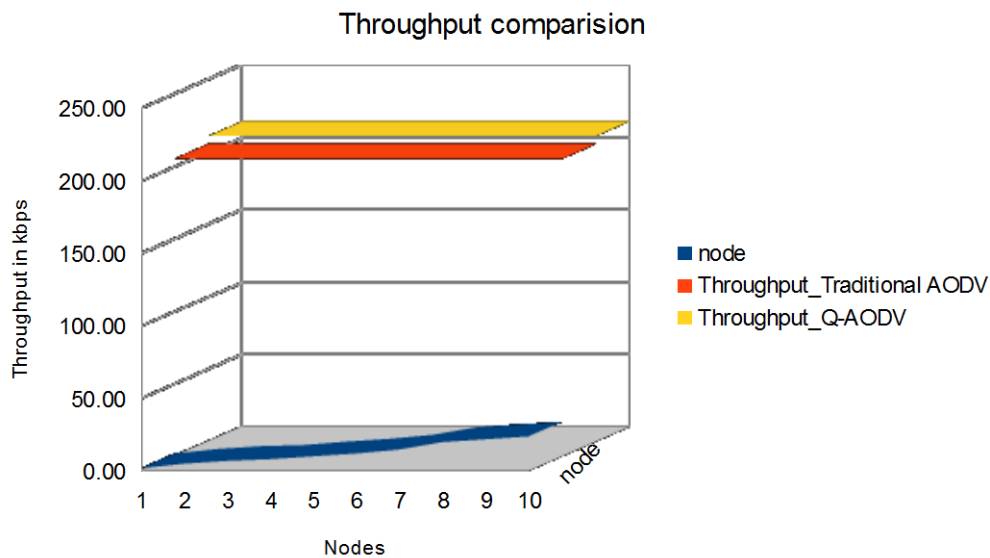


Fig 3. Comparison of throughput between traditional AODV and Q-AODV routing protocols

## VI. CONCLUSION

In this paper an intelligent/ cognitive approach is chosen to improve the Quality of Service. Q-

learning algorithm made AODV more intellectual. Thus, with this proposed new cognitive approach algorithm increases the throughput and reduces the end to end delay.

## VII. FUTURE WORK

Instead of using regular NS-3, a NS3-gym-master is suggested to use for the simulation. It will suit well to the Machine Learning algorithms more. Since, here a Q-learning, reinforcement learning along with AODV is used, NS3-gym-master gives good results.

## VIII. REFERENCES:

1. M. Chafii, F. Bader and J. Palicot, "Enhancing coverage in narrow band-IoT using machine learning," *2018 IEEE Wireless Communications and Networking Conference (WCNC)*, Barcelona, 2018, pp.1-6. doi: 10.1109/WCNC.2018.8377263.
2. A.Nauman, M. A. Jamshed, Y. Ahmad, R. Ali, Y. B. Zikria and S. Won Kim, "An Intelligent Deterministic D2D Communication in Narrow-band Internet of Things," *2019 15th International Wireless Communications & Mobile Computing Conference (IWCMC)*, Tangier, Morocco, 2019, pp. 2111-2115. doi: 10.1109/IWCMC.2019.8766786.
3. M. K. Hossain Jewel, R. Sale Zakariyya, O. J. Famoriji, M. S. Ali and F. Lin, "A Low Complexity Channel Estimation Technique for NB-IoT Downlink System," *2019 IEEE MTT-S International Wireless Symposium (IWS)*, Guangzhou, China, 2019, pp. 1-3. doi: 10.1109/IEEE-IWS.2019.8803938.
4. A. Srivastava, D. Kumar and S. C. Gupta, "Geographic and Reactive Routing Protocols for MANET," *2013 European Modelling Symposium*, Manchester, 2013, pp.590-594. doi: 10.1109/EMS.2013.98.
5. A. Tripathi, A. T S and R. M. R. Guddeti, "A Reinforcement Learning and Recurrent Neural Network Based Dynamic User Modeling System," *2018 IEEE 18th International Conference on Advanced Learning Technologies (ICALT)*, Mumbai, 2018, pp. 411-415. doi: 10.1109/ICALT.2018.00103.
6. A. Singh, T. Singh, M. Mittal and K. Kumar, "Performance improvement in AODV routing protocol with artificial intelligence," *2016 3rd International Conference on Computing for Sustainable Global Development (INDIACom)*, New Delhi, 2016, pp. 45-49.
7. X. Chen, Z. Li, Y. Chen and X. Wang, "Performance Analysis and Uplink Scheduling for QoS-Aware NB-IoT Networks in Mobile Computing," in *IEEE Access*, vol. 7, pp. 44404-44415, 2019. doi: 10.1109/ACCESS.2019.2908985.
8. N. Kantasewi, S. Marukatat, S. Thainimit and O. Manabu, "Multi Q-Table Q-Learning," *2019 10th International Conference of Information and Communication Technology for Embedded Systems (IC-ICTES)*, Bangkok, Thailand, 2019, pp.1-7. doi: 10.1109/ICTEmSys.2019.8695963.
9. W. Su and K. Feng, "QoS-Guaranteed Power-Saving Configuration Prediction Scheme for 5G IoT," *GLOBECOM 2017 - 2017 IEEE Global Communications Conference*, Singapore, 2017, pp. 1-6. doi: 10.1109/GLOCOM.2017.8254684
10. S. Popli, R. K. Jha and S. Jain, "A Survey on Energy Efficient Narrowband Internet of Things (NB-IoT): Architecture, Application and Challenges," in *IEEE Access*, vol. 7, pp. 16739-16776, 2019. doi: 10.1109/ACCESS.2018.2881533
11. J. Xu, J. Yao, L. Wang, Z. Ming, K. Wu and L. Chen, "Narrowband Internet of Things: Evolutions, Technologies, and Open Issues," in *IEEE Internet of Things Journal*, vol. 5, no. 3, pp. 1449-1462, June 2018. doi: 10.1109/JIOT.2017.2783374

# A Novel Hash based Encryption technique on Video steganography integrity verification against attacks

V.Annapurna, S.Nagaraja Rao, M.N.Giri Prasad

*Abstract--- Steganography is an essential task to construct a secure communication among various authorized entities. Video Steganography is one of the essential source of transmitting secret data using data hiding techniques in videos. Securing the embedded data along with video data is an essential task in data hiding techniques. However, this sensitive information is vulnerable to third party attacks such as video content change, copyright change, key change etc. A large number of cryptographic algorithms have been proposed in the literature for integrating the sensitive data into the data hiding techniques. But, as the size of the sensitive data increases these models require high computational memory and time. Also, these cryptographic models are not applicable to large video data for integrity computation and encryption. In order to overcome these issues, a novel integrity verification technique is proposed to find the change bits in the video with high sensitive rate. Also, proposed model use integrity based encryption technique to hide the sensitive information securely in the video. Proposed model use motion vectors to find the integrity of the video for data hiding against the third party attacks. Motion vectors are extracted using the kalman filter in the source video for integrity computation. Proposed integrity computation model use polynomial structures to increase the complexity or sensitive of the hash during the data hiding process. Experimental results proved that the proposed integrity verification based video steganography approach is more sensitive and efficient than the traditional cryptographic approaches in terms of bit rate, runtime and memory are concerned.,*

**Keywords-Video Steganography, Integrity Verification, Kalman filter, Motion Vectors**

## 1. INTRODUCTION

The process of information hiding uses the digital signals in order to embed essential information. Different digital media carriers (audio, video, images, etc.) are used for the processing of information hiding. Steganography can be defined as the process of hiding secret data within a cover media. The cover media can be text, or, audio, or, image, or video. Presently, the video steganographic approaches have become more popular in case of various video sharing and social networking applications just like livestreaming. All of these algorithms are categorized into two types, those are:- watermarking and steganography. Watermarking technique is useful to embed copyright information into the carriers. It explains the rights of the content owner. Also, it provides protection to the content to be copied or modified. Information leakage is usually traced back by using various

authentication schemes. On the other hand, steganography can be defined as a special kind of information hiding in which important information are embedded within the carriers to ensure secure communication. Video information hiding is very much essential now-a-days. The above technique is beneficial for the illegal transmission and distribution of videos.

The process of video steganography is of two types, :-

1. In this kind of video steganography, information is embedded prior to the encoding process. Video is considered as a sequence of motion pictures. It can hide important information inside the video frame pixel depending upon their intensity. This approach is considered as the simplest one. The only limitation of this technique is that, the video information is usually lost after compression encoding.

2. In the second type of video steganography, information embedding occurs at the time of encoding.

Sensitive information are embedded during the coding process of image or video. By integrating various characteristics of coding constraints and detecting the exact information embedding positions, we can modify several intermediate outcomes in order to obtain information embedding. In the above kind of information hiding process, video is transmitted after successful completion of compression coding. Therefore, this kind of embedding approach can be implemented in wide range of applications.

Video data redundancy is eliminated after completion of compression coding. Hence, large amount of data can't be embedded within a particular compressed video stream. Some approaches those can be included within this category are:- DCT transform, entropy coding, kalman motion estimation, and so on. Most of the traditional models use intra prediction during the process of information hiding. All of these approaches changes the intra encoding prediction mode in order to hide information efficiently. These secret information can be embedded inside frame. Hence, the overall embedding capacity of this approach is restricted. DCT transform technique uses large non-zero coefficients in order to hide information. As there are only few numbers of such coefficients, the embedding capacities of these methods are also restricted.

On the other hand, the entropy coding approaches changes the code elements according to the CAVLC and CABAC. It may result with huge distortion and sometimes decoding terminations. Motion estimation approach is

**Revised Manuscript Received on March 10,2019.**

V.Annapurna, Research scholar, JNTUA, Ananthapuram, AP, India  
Dr.S.Nagaraja Rao, Professor, Dept of ECE, G.Pullareddy  
Engineering College, Kurnool, AP, India

Dr.M.N.Giri Prasad, Professor & Director of Admissions, JNTUA  
Ananthapuram, AP, India

implemented to hide information through the modification of motion vector. The distortion of motion estimation is also encoded as well as transferred. The traditional motion vector technique involves hiding of sensitive information through modification of motion estimation. The basic concept behind these approaches is that, the amplitude of modified motion vector must fulfill several constraints.

Some of the traditional hiding approaches perform modification of search range of motion during the process of video encoding. Most of these approaches follow two operations on videos. At first the total numbers of search points are split into two sets. One set can represent the information by 0s and other set by 1s. The hidden information can be searched with 1/4 pixel accuracy. In the second case, a distortion function through exploiting the spatial-temporal correlation in order to decrease the embedding impact on motion vectors.

### Motion Video Steganography:

The main objective of steganalysis is to detect whether there exist any secret message in a hidden format within digital media just like image, video and audio. Almost all steganalysis approaches gives emphasis on image steganography, but since today there is no significant amount of research works in the area of the steganalysis for digital video. With the advancement of video recording devices and video applications, digital video is considered as the most convenient information carrier.

As the volume of a video is comparatively large than that of other digital media, hence the spaces for information hiding inside a video is sufficient. Generally, digital video or compressed digital video consists of different components. These components play significant role in the development process of various steganographic algorithms. Motion vector is considered as the most important and basic component of compressed videos. Presently, numbers of steganography tools or methods is increasing rapidly. With increase of steganographic methods, the challenges of video steganalysis are also increasing day by day.

In between various steganography, the motion vector based technique in H.264/AVC is selected mostly frequently for the process of steganalysis due to two important reasons, those are:-

Improved security and better embedding capacity

Presently, H.264/AVC is considered as the most commonly used video encoding standard. Hence, in most of the real world applications, the motion vector based techniques can be implemented efficiently and effectively.

In case of motion vector based techniques, motion vectors are changed. Additionally, the relevant prediction errors are adjusted at the same time. There exist numbers of different motion vector based techniques. Several traditional approaches use certain previously defined selection rules in order to choose candidate motion vectors. These rules play significant roles during the whole process of embedding. In another type of motion vector based method, selection of motion vector is done by some threshold value. These motion vector components are changed with greater magnitude in order to carry out the process of embedding smoothly. There exists a different type of motion vector based technique in which message is hidden with the help of

phase angle among two different components. Apart from this, the selection rules may lead to various risks. Hence, the process of steganography includes different adaptive techniques in order to enhance the overall security to a great extent.

The traditional adaptive method is modified and extended in order to give rise a new threshold selection. In order to identify various motion vector based steganography techniques, different feature based steganalytic techniques are introduced presently. All of the above mentioned steganography techniques can be broadly classified into three types, those are described below.

The first type of steganalytic approaches use feature based concept case of neighbouring motion vector difference. In other words it can be stated that, each individual feature is extracted from statistical characteristics of neighbouring motion vector difference. In some other steganalytic techniques a combined distribution of neighbouring motion vector difference among a particular macroblock and other two macroblocks are considered. In case of H.264/AVC video coding standard, if two neighbouring macroblocks shows different partition, in that case it is very complicated to evaluate the neighbouring motion vector difference.

The second group of steganalytic approaches usually implements the statistics of the Sum of Absolute Difference. The Sum of Absolute Difference plays vital role throughout the designing process of features. This method considers that, the regional optimality of Sum of Absolute Difference can be modified if and only if, the appropriate motion vector is modified. Another research Idea includes the concept of subjective probability of optimal matching through the implementation of the regional optimal Sum of Absolute Difference. The basic concept of AoSO and SPOM are almost same. In case of large quantization parameter, the stability of the regional optimality of Sum of Absolute Difference gradually decreases because of quantization distortion. Therefore in the above mentioned case, the identification performance also decreases.

The third group of steganalytic approaches which implement calibration functions in order to improve the features. This traditional calibration function is again compressed. After that, the motion vector features are generated from the difference of motion vectors and sum of absolute differences. The above phenomena takes place just before the calibration process. Furthermore, the coding parameters in case of both the compression process is required to be equivalent. However, the identification performance can degrade gradually. The above proposed approach is based upon the basic concept of the correlation in between different neighbouring motion vectors. In the presented case, the locations in existence of neighbouring motion vectors are not at all considered.

All of the above mentioned approaches have certain limitations. Additionally it can be mentioned here that, motion vector based steganography is capable of modifying motion vectors and the corresponding pixels at the same time.

### Video Steganography Techniques and Its Issues:

Steganography is also known as "covered writing". In other words, steganography can be defined as a special way of hiding information in order to avoid identification of hidden messages. Cover object is actually a particular file that has the responsibility to hide sensitive information. Secret message is actually the sensitive data is embedded inside the cover object. Through the integration of cover object and updated sensitive data, stego object is generated. The Secret sensitive message is encrypted prior to the process of embedding.

A specific encryption key is required during the process of encryption. That particular key is known as stego key. On the other hand, steganalysis can be defined as various attacks those try to break the steganographic methods.

Almost all steganographic approaches suffer from different types of challenges. There are four major challenges or issues which are mostly found in all of the traditional steganographic approaches. Those four issues are:-

1. Robustness,
2. Tamper proof,
3. Hiding efficient and
4. Perceptual transparency.

All of these four are inversely proportional with each other. Hence, it will cause sequential data hiding problem. Robustness can be defined as the amount of changes the stego object can manage causing any serious damage. Tamper resistance is a special type of property that increases the difficulty level for an attacker in order to modify the sensitive secret information. The above mentioned secret information is already embedded inside the cover object. Boat hiding capacity and perceptual transparency are interlinked with each other. In case of a large hiding capacity, a very small cover object is required in order to hide the secret message. Very large hiding capacity may give rise to distortions. The attacker always tries to identify the distortion, because in this way he can identify the presence of hidden message. In the above mentioned scenario, the secret communication is visible and the process of steganography is considered as inefficient. Therefore, perceptual transparency is considered as the most important characteristic of steganography.

The visible distortions can easily reveal secret communication. Several steganographic approaches implements a model which assists during the evaluation of relevance of every individual pixel along with the undetectable distortion level. All of these above mentioned approaches are also called as visual masking approaches. They include both physiological & psychological mechanisms of the human visual system in order to carry out the masking phenomena. An advanced visual masking approach for images and videos is applied in various applications. This approach generates a relevance map of the image/frame. The frame size is restricted to 8x8 pixel blocks. This approach involves three important components, those are:-

1. JND model
2. Visual attention model and
3. Weighing model.

Any kind of digital file can be used as covers. The major concerns of all steganographic approaches are to increase the hiding ability and to reduce the embedding distortion. In this case, file formats having large redundancy are considered. The redundant bits if any objects can be replaced easily without any major effect. According to the kind of cover object used, steganography can be classified into six numbers of sub-categories, those are described below:-

1. Text Steganography:- Text steganography is considered as the most common and traditional way of steganography. Some advanced methodologies are included in order to enhance the level of security, those methodologies are:- line shifting, word shifting and feature-based encoding. Now-a-days, text steganography is no more used and it has become outdated. One of the major limitations of text steganography is, the text files always contain restricted amount of redundant data. Therefore, it will decrease the hiding capacity of the secret message. Apart from these, the text files can be modified with an ease and it may cause huge loss of sensitive information.

2. Audio Steganography:- Audio steganography is second commonly used steganography. Here, hiding of secret message occurs in case of one dimensional signal. The whole concept of audio steganography is based upon the masking concept. A poorly audible audio become almost inaudible with presence of another loud audio signal. Among various different types of audio encoding approaches, low bit encoding, phase encoding and spread spectrum are three most common audio encoding approaches.

3. Image Steganography:- The process of image steganography uses images as cover object. In other words, images are considered as the most efficient way to hide secret messages. Images include large amount of redundant data. A digital image can be defined as collection of numbers which are used to represent various light intensities at different places. These numbers are used to build a special grid and that grid is also known as pixel. There are large numbers of digital image file formats. Three most commonly used digital image file formats are:- JPEG, BMP and GIF. Many steganographic approaches are developed by considering all of these image file formats.

4. Video Steganography:- Some researchers consider video steganography as a perfect extension of image steganography. A video stream is a collection of numbers of images. These images are consecutive and located after equal time intervals. There are certain cases where these video streams are associated with audio streams. Hence, some image steganography approaches can also be implemented here. There are huge amount of research works have been performed on video steganography since decades. Some researchers extended their previously developed image steganography technique to video steganography. Video is considered as the most appropriate kind of file that can be used as cover. The reason behind this growing popularity is because a single video can transmit a large amount of secret data with it.

5. Protocol Steganography:- This is a special kind of steganography, where secret data are usually hidden inside network packets. There exist covert channels among various layers of OSI model. In all those places, steganography can be implemented.

Additionally, the storage capacity is comparatively huge as compared to all other media.

Besides the above mentioned categories, there are several other categories of video steganography, those are described below:-

1. Substitution-based Approaches:- In case of substitution-based approaches, all redundant data can be just replaced by secret data. This approach is the simplest one and it also has very high embedding ability as compared to other steganographic approaches. The most commonly used substitution based approaches are:- least significant bit method, bit plane complexity segmentation, tri-way pixel value differencing, and so on. Least significant bit method is considered as the most popular and easy to implement steganographic approach. Again, it is capable to hide huge amount of secret data.

2. Transform domain Approach:- The main problem with substitution-based approaches is the vulnerability to cover changes. Hence, the embedded secret information can be accessed and destroyed within no time. Transform domain approaches are considered as relatively complex approaches. These approaches usually improve the robustness and the perceptual transparency. Following are the phases of a traditional transform domain approach:-

Phase-1: Initially, the cover is transformed to the frequency domain.

Phase-2: After that, the secret message is embedded within certain or all transformed coefficients.

Phase-3: The altered coefficients are again converted to its original form.

Discrete Fourier Transform (DFT), Discrete Cosine Transform (DCT) and Discrete Wavelet Transform (DWT) are some most commonly implemented transform domain approaches. DFT approaches are not much efficient in case of steganography because of huge round off errors.

3. Adaptive steganographic approaches:- Various newly developed embedding methods are included under this category of steganographic approaches. These are also known as masking or statistics-aware embedding. The adaptive approach basically depends upon the statistical behaviors of the cover prior to the secret data modifications. This approach generally assists to detect the best places in order to hide data. Those places are called as regions-of-interest ROI. An adaptive capacity function is used here that decides the amounts of secret data to be embedded. The well-known least significant bits approach has an adaptive version of it.

4. Format-based approaches:- There are different video formats those can be used as cover objects. In this type of steganographic approaches, emphasis is given on video formats. H.264/AVC is considered as the most recent compression standard for video. This approach can achieve very high compression efficiency. This is more suitable for network transmission.

Cover production approaches:- Every individual conventional embedding approach depends upon a particular

cover object. An advanced steganographic approach is implemented in order to hide secret data efficiently. On the other hand, cover production approaches generates an object and use it as a cover inside some secret communication. The above concept is considered beneficial for dynamic cover video production. This approach includes the application of secret key and secret message in order to produce the appropriate cover video. A function  $X(A,D)$  is used during the production process. Here,  $A$  is denoted as the total numbers of samples needed to hide the message and  $D$  is the required secret message bits which must be hidden. The above mentioned approach uses database of images in order to gather necessary images for the process of video creation. This approach is more sustainable for steganalysis, because the original images are actually hidden from the attacker. There exists a single limitation of the above approach that is, when the chosen images are not related to each other, in that case the attacker may doubt

## 2. RELATED WORK

*K. Rajalakshmi et.al*, developed a new and advanced robust secure video steganography with the use of reversible path-wise code-based embedding [1]. At the time of data hiding and transmission, there exist loop holes where the secret data can get leaked to the attacker. Again, there exist numbers of different issues in the field of video steganography. A large video is decomposed into numbers of frames and after that the processing of data gets started. Through implementation of an efficient embedding algorithm, the sensitive confidential data gets embedded inside the cover video. The secret information can be either very large or small in size. Both the encryption and decryption algorithms are implemented in order to get highest level of security in case of data hiding. During the process of data transmission, the decryption process is associated with several issues.

The restoration of compression technique includes several video frames as input and it implements the discrete cosine transform or discrete wavelet transform method. All the information related to pixels are distorted because of frame cover conversion and encoding. Therefore, the overall encryption efficiency is influenced by lossy pixel information. Therefore, a new correlation filtering technique is integrated with blind pixel algorithm in order to hide secret data. In this case, the quality of the secret information is maintained properly. The pixel grouping mechanism is carried out through the replacement of relevant and recurrent pixels. The above mentioned process has significant role throughout encryption process just to decrease lossy pixel information.

This filtering approach is considered as an efficient pre-processing approach just to eliminate noise from the cover and secret video. Fast Fourier Transform implemented in this paper. The pixel optimisation process is carried out by considering various boundary coefficients. Both of the above mentioned phases try to decrease lossy pixel information. According to the least significant bit method,



pixel value of secret message is usually inserted within the pixel value of cover. The limitation of traditional least significant bit algorithm is resolved in this case by considering a group of random pixel among cover and secret data. Additionally, the patch wise code formation technique is implemented in the video encoding process just to result improved level of security.

*S. Balu, et.al*, introduced a secure and effective data transmission approach with using the process of video steganography in case of medical imaging system [2]. Usually steganography method is implemented in order to enhance the security level of data transmission. In case of medical data, medical data are transmitted from one hospital to other hospitals. Therefore, video steganography in case of medical imaging system enhances the security level significantly. The process of steganography emphasizes on information confidentiality, integrity and authenticity. Steganography approach in case of medical imaging system primarily emphasize on all areas except doctor diagnosis. According to the human vision region of interest, both foreground and background object are identified within a video.

After that, an advanced face identification approach is implemented in order to identify moving object. The secret information is usually hidden within the background object. Secret information is never hidden in the face area of foreground object.

*M. Fan, et.al*, implemented a cross correlation feature mining for steganalysis of hash-based LSB video steganography [3]. The popularity of video steganography has increased because of its huge capacity as compared to other traditional steganographic approaches that uses image or audio for its cover. According to this technique, 8 bits of secret message are decomposed into 3, 3, 2 smaller segments. These decomposed messages are embedded into the RGB pixel values. Apart from this, the hash function has the responsibility to identify the embedding locations.

*D. Griberman and P. Rusakov* performed detailed comparative study of various video steganographic approaches in order to embed watermark [4]. In this paper, a detailed survey is carried out on different video steganography embedding techniques and summarized a group of constraints for the process of video steganography.

Apart from the above, robustness property is also analysed and verified against different attacks. The major objective of the proposed technique is to reduce the noise created by the steganographic process.

*P. Kumar and K. Singh* introduced an enhanced data hiding technique with the help of skin-tone identification method [5]. Providing security to the embedded data and reducing the distortions in case of videos is still very complicated task. In this paper, an advanced steganographic technique is introduced in order to reduce the probability of identification of the embedded image data in case of cover objects. Here, human skin locations are assume as regions of interest in order to embed the secret information. It enhances the adaptability of the above presented approach in case of different kinds of image data. Certain consecutive pixels are implemented in order to embed secret data inside the cover object. The third discrete wavelet transform technique is applied here. The approximation coefficient is used in order

to carry out the process of embedding after the implementation of third discrete wavelet transform method.

It improves the robustness of every individual video frame and also improves the quality of the video. The frame matrix is again considered for skin map retrieval in order to generate color based pixel selection. In the above presented technique, 8 pixel retrieval is considered for the red and blue channels.

*S. Manisha et.al*, proposed an advanced two-level data hiding technique in case of video steganography [6]. Sensitive data are interchanged most often in case of both wired and wireless modes of communication. Hence, these secret data are very much vulnerable to unauthorized access. Cryptography is considered as the most appropriate way to resolve the above mentioned problem. After decryption of the secret message, it gets revealed to everyone. In this work, an efficient and effective data hiding and retrieval methodology is introduced. Here, audio video interleave videos are considered and secret messages are embedded inside a bitmap image file. Initially, the secret message was decomposed into smaller bytes and these smaller bytes are hidden inside certain frames of a video. Inserting these secret data inside a video frame increases the overall level of security. The presented research work enforces two highly secure levels of encryption techniques. Both quality and size of the secret message is not at all changed before and after the encryption process. Every individual secret image is capable of embedding certain multimedia data and these data can be again retrieved and recognized. This approach is considered as more secure because it involves two step encryption process and it only includes two bit positions in case of a single video frame. The secret image is located in four separated quadrants. Therefore, both the size and quality of image remains unaffected. The original video size must be compatible with the size of the carried video. Hence, the overall quality of secret data is improved.

*J. Mansouri et.al*, developed an adaptive technique for compressed video steganography [7]. This model uses both temporal and spatial characteristics of video signals. An effective approach for video steganography is implemented in case of covert communication. All secret data are inserted inside a compressed video stream adaptively with the help of temporal and spatial characteristics of the video signal. The process of embedding is carried out by considering human visual system behaviours.

*R. J. Mstafa et.al*, performed a detail survey on both compressed and original video steganography approaches [8]. This paper includes both study and analysis of various video steganographic approaches. The performance evaluation of each and every method is also analysed. In this survey paper, both compressed and original video steganography are considered. In case of compressed video steganography approaches, the video steganography approaches are classified depending upon the video compression phases just like appropriate locations for data embedding. Apart from this, intra frame prediction, inter frame prediction, motion vectors, transformed and quantized

coefficients, and entropy coding are several other categories of video steganography. On the contrary, original video steganographic approaches are decomposed into two broad categories, those are:- spatial domains and transform domains.

H. Noda *et.al*, developed a new video steganography scheme that depends upon the bit plane decomposition of wavelet transform video [9]. This paper introduces a new steganography approach that can efficiently handle lossy compressed video. It is the most convenient and traditional way to transmit huge quantities of secret data. The above presented approach completely depends upon wavelet compression for video data and bit-plane complexity segmentation (BPCS) steganography. Motion-JPEG2000, wavelet coefficients are usually quantized into a bit-plane structure. Hence, this kind of steganography is most efficient for wavelet domain.

Z. Qu, *et.al*, proposed a quantum video steganography protocol in case of large payload based MCQI videos [10]. Quantum video is considered as an important multimedia which is usually found in case of quantum networks. A secure and effective quantum video steganography protocol having huge payload usually depends on the videos strip encoding strategy. This encoding strategy is known as multichannel quantum images encoding strategy.

This new protocol is responsible for embedding secret data randomly. Both the original quantum video and the quantum carrier video show distinct characteristics of video frames. At the time of covert communication, secret information is embedded inside the quantum video. Again, the receiver can retrieve secret information from the video without retaining the carrier video. On the other hand, the original quantum video is restored perfectly.

Y. Ren, *et.al*, proposed a new method of video steganalysis that depends upon subtractive probability of optimal matching feature [11]. In this piece of research work, they have proposed a motion vector-based steganalytic technique. The above presented technique depends upon the optimal matching characteristic in case of a compressed video. By analysing the outcomes we can mention here that, every individual feature is stable and sensitive in nature. Hence, the cover and motion vector based video can be distinguished easily. There are total three numbers of advantages of the above-mentioned feature.

1. According to the standard constraints of motion vector production, feature can be implemented in case of large numbers of video compression standards. The optimal matching motion vector is chosen in order to decrease the overall temporal redundancy.

2. Every individual feature is independent in nature. It is not at all related to the correlation of consecutive motion vectors. In case of relatively large temporal activities, the feature shows better classification capability than that of other traditional approaches.

M. M. Sadek, *et.al*, performed a comparative survey on various video steganographic approaches [13]. Steganography can be defined as a security mechanism usually used for the process of data hiding. There are numerous numbers of covers which are used during the process of steganography.

[13-16] proposed a novel encryption models on compressive image datasets and high dimensional image databases using the chaotic function. These models are efficient on standard image databases with fast encryption time. These models require high decryption time on high dimensional images. Also these models require high computational memory on video frames.

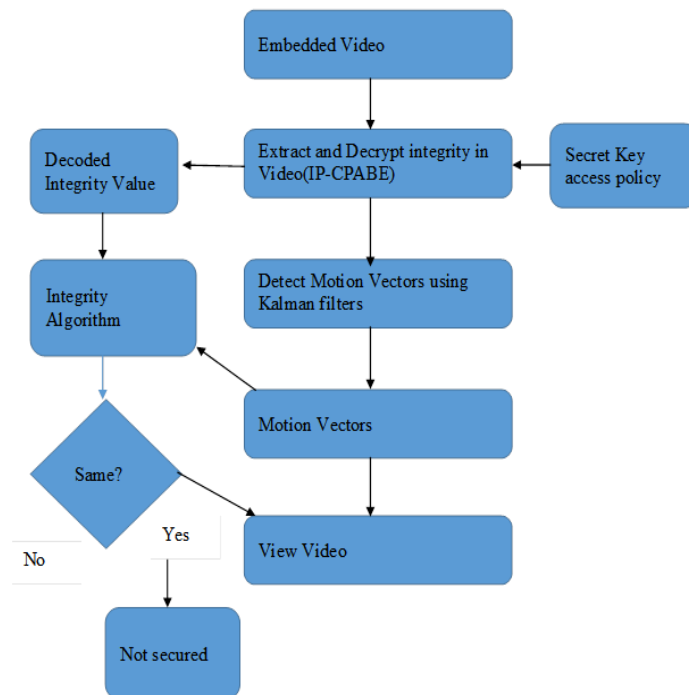
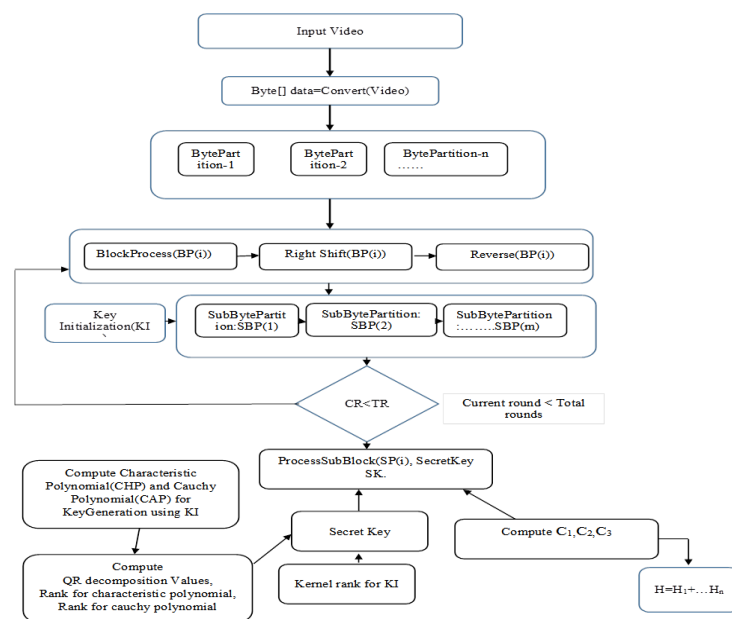
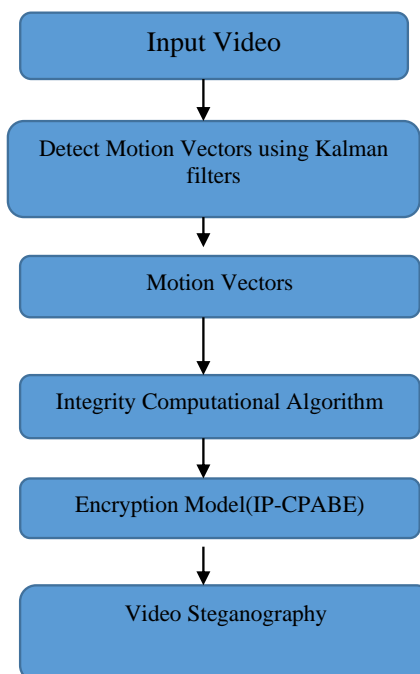


Figure 2: Video Steganography Integrity Verification process



3. Proposed Model: Secured Integrity Verification based Video Steganography Verification Model





In the proposed model, a novel polynomial based integrity verification algorithm is proposed to improve the security issues in the traditional video steganography. The overall approach is described in the fig 1. As shown in the fig 1, initially the video input is used to track the motion vectors in each frame. Here, traditional kalman filter algorithm is used to track the motion vectors in each frame of the video. All the motion vectors in the each frame are integrated to find the hash integrity computation. In the proposed model, a novel polynomial based integrity computation technique is proposed to find the unique signature of the input video motion vectors. In the proposed model, integrity based ciphertext policy attribute based encryption technique is used to embed the encrypted integrity data into the video.

In the figure 2, integrity embedded video steganography file is taken as input for video integrity verification process. Encryption algorithm is used to decrypt the encoded hash integrity value for video integrity checking. Decrypted integrity value is tested against the computed integrity value of the steganography video. If the integrity values of the decrypted one and the computed one are same then there is no modification in the source video.

**Computing characteristic and Cauchy polynomials using the initial key matrix.**

Compute Cauchy Polynomial to initial key as CAP  
 $KI=[k_1, k_2, \dots, k_n]=V$

$$m_1=k_1; n_1= \frac{m_1}{\|m_1\|}$$

$$m_2=k_2-(k_2.n_1)n_1; n_2= \frac{m_2}{\|m_2\|}$$

$$m_r=k_{r+1}-(k_{r+1}.n_1)n_1-\dots-(k_{r+1}.n_r)n_r; n_r= \frac{m_r}{\|m_r\|}$$

Using QR decomposition formula we have

Where  $Q=[n_1, n_2, \dots, n_r]$  and  $R = \begin{pmatrix} k_1.n_1 & \dots & k_1.n_r \\ \vdots & \ddots & \vdots \\ 0 & \dots & k_r.n_r \end{pmatrix}$

Rank  $r1=Rank(QR)$ ;

Compute Characteristic Polynomial to initial key as CHP  
 Find eigen vector  $EV[]=Eigen(CHP)$ ;  
 Rank  $r2=Rank(CHP)$ ;  
 Kernel Rank  $r3= Rank(Q*Q)$ ;  
 secret key  $SK[]=\{EV[0],EV[1],Max\{r1,r2\},r3\}$ ;

**Algorithm Steps:Computing the Hash Function**

- Step 1:** Input Video motions vectors and Hash size.
- Step 2:** Message  $M=Motionvectors$ ;
- Step 3:** Initializing the key as KI.
- Step 4:** Divide the message M into S/8 blocks.  
 if  $(M>S/8)$   
 Partition the block into S/32 subblocks of 4 bytes each(P)  
 Right shift P, Reverse P  
 For each byte in P[i]  
 Compute C1,C2,C3  
 $T1=IK\%(\sum V).PolyTransform(T1)$   
 $T1=m.T1(m=1,2, \dots, \dots)$   
 $T2= PolyTransform(T1) \% (3^{\sqrt{\sum IK}}$   
 $C1=(T1\%256)$   
 $C2=T2$   
 $C3=M$   
 $H1=1+C_1+C_2+C_3$
- Step 5:**  $H=H1+H2-----Hn$

**Encryption Algorithm:**

Cipher text attribute based encryption is the traditional encryption model which is used to encrypt the data with the attributes list and policies. In the proposed model, attributes and policies are initialized with the computed integrity value of the motion vectors. Proposed encryption algorithm is executed in four phases.i.e setup phase, encryption phase, key generation phase for secret key and finally decryption phase. Here, group elements are taken from cyclic group elements with bilinear property.

**Input :**Integrity Value as input message.

**Phase 1: Setup():** In this phase, public key and master key are generated using the bilinear pairing and cyclic group elements.

$$PublicKey = \{g_p, g \in G \wedge H; e(g, g^\alpha)\}$$

$$Masterkey = \{g_\alpha, \beta \in G \wedge H\}$$

**Phase 2:Encryption():** In this phase, integrity value of the video and public key are used to encrypt the message

$$C = \{m \in G_T, s \in Z_r, PolynomialAccessTree(Policy P, s, K), Ciphertext C=\{P, m, g_\alpha^s, h^s\}\}$$

**Phase 3:KeyGeneration():** In this phase, secret key is generated using the public key and master key.

$$SK = \{r \in Z_p, g_r PK.g_p^r, MK(g_\alpha).MK(g_r), D^{MK(\beta)}\}$$

$$\forall A_i(D_{j \in g_r.r_j}, D'_j \in PK.g_p.r_j)$$

**Phase 4: Decryption():** In this phase, data is decrypted using the cipher text , secret key and public key.

$$D = \{C=\{P, m, g_\alpha^s, h^s\}, e(C, Sk, D)\}$$



In the improved approach, the motion vector prediction error is considered as the basic concept behind the selection of motion vector carriers. Secret information are inserted through replacement of least significant bit of motion vector. According to another research idea, the insertion of secret information is carried out through the adjustment of parity of the horizontal component and the vertical component. In case of some other types of motion vector based techniques, embedding process is carried out through replacement of least significant bits of the horizontal and vertical components of each and every motion vectors. Secret bits should be added in place of those replaced bits.

### 3. PERFORMANCE ANALYSIS & RESULTS

#### Statistical Integrity Randomness:

Shannon proposed two measures namely confusion and diffusion as essential features for strong integrity verification process. For an efficient diffusion property, there should be 50 percent bit change in the hash value. Let the initial message and its bit values are taken as original data. The changed bits of the computed hash value are

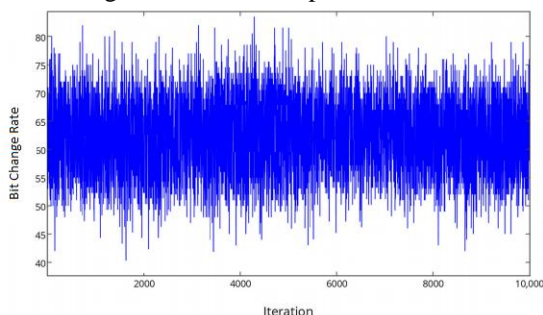


Figure 4: Bitchange rate of the integrity verification algorithm

marked as  $B(i)$ . The computational measures used to compute the confusion and diffusion are given below.

Changed Minimum bit rate :  $B(\min)=\min(\{B(1),B(2),\dots,B(k)\})$ ;

Changed Maximum bit rate :  $B(\max)=\max(\{B(1),B(2),\dots,B(k)\})$ ;

$$\text{Mean changed in bit rate } \bar{B} = \sum_{i=1}^n B(i) / N$$

$$\text{Standard variance in bit rate} = \left\{ \sum_{i=1}^n (B(i) - \bar{B})^2 / N \right\}^{1/2}$$

Table 1. Comparison of integration based Cipher text policy attribute based Encryption and Decryption models with the existing approaches.(Hash bit size=2048)

Algorithm	Avg EncryptionTime(secs)	Avg DecryptionTime(secs)
Proposed	10.53	12.19
Ref.[13]	12.53	14.64
Ref.[14]	12.94	17.35
Ref.[15]	13.83	19.45
Ref.[16]	13.92	19.93

Table 1 describes the comparison of proposed model to the existing models in terms of encryption time and decryption time.

Table 1, describes the encryption and decryption time of the proposed model to the existing models on video steganography video files. As the size of the video increases, proposed model require less computational encryption and decryption time compared to the existing models.

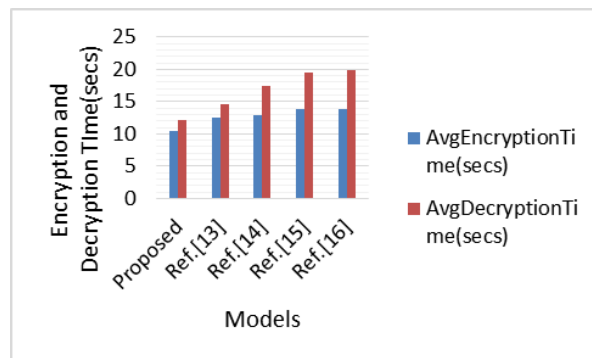


Figure 5: Comparison of the proposed model to the existing models in terms of encryption and decryption time.

Figure 5, describes the encryption and decryption time of the proposed model to the existing models on video steganography video files. As the size of the video increases, proposed model require less computational encryption and decryption time compared to the existing models.

Table 2: Mean changed bit rate of the proposed integrity algorithm to the existing algorithms

Algorithm	AvgHashBitrate
MD5	118
SHA512	124
Mixed Chaotic[17]	127
Proposed Hash	135

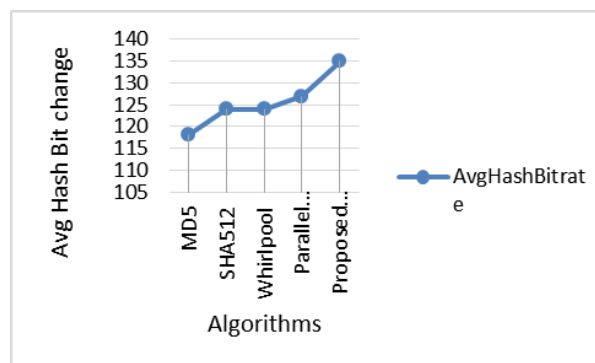


Figure 6: Avg bit change rate of the proposed integrity value to the existing algorithms

Table 2 and figure 6 describe the comparison of proposed hash algorithm to the traditional algorithms on the average bit rate change for sensitive analysis on the motion vectors of the video steganography files. From the results, it is



observed that the proposed model hash high sensitivity compared to the existing algorithms on video files.

#### 4. CONCLUSION

Steganography can be integrated with cryptography or error correction scheme in order to enhance the efficiency and security. Before embedding of secret message, that message will get encrypted. A large number of cryptographic algorithms have been proposed in the literature for integrating the sensitive data into the data hiding techniques. But, as the size of the sensitive data increases these models require high computational memory and time. Also, these cryptographic models are not applicable to large video data for integrity computation and encryption. In order to overcome these issues, a novel integrity verification technique is proposed to find the change bits in the video with high sensitive rate. Also, proposed model use integrity based encryption technique to hide the sensitive information securely in the video. Proposed model use motion vectors to find the integrity of the video for data hiding against the third party attacks. Motion vectors are extracted using the kalman filter in the source video for integrity computation. The results of the evaluation phase demonstrate that, with increase in embedding capability rate, the detectable distortion on label reduces gradually. This technique is very much efficient in order to detect the exact frame containing secret message. The process of embedding must be carried out separately in order to minimize possibilities of identification with the help of statistical approaches. Proposed integrity computation model use polynomial structures to increase the complexity or sensitive of the hash during the data hiding process. Experimental results proved that the proposed integrity verification based video steganography approach is more sensitive and efficient than the traditional cryptographic approaches in terms of bit rate , runtime and memory are concerned.

#### REFERENCES

1. K. Rajalakshmi and K. Mahesh, "Robust secure video steganography using reversible patch-wise code-based embedding" Springer Science Multimed Tools Appl,2018.
2. S. Balu, C. Nelson Kennedy Babu and K. Amudha, "Secure and efficient data transmission by video steganography in medical imaging system" Springer Cluster Computing,pp 2639-2643,2018.
3. M. Fan, P. Liu, H. Wang and X. Sun, "Cross correlation feature mining for steganalysis of hash based least significant bit substitution video steganography", "SPRINGER Telecommunication systems", 2016.
4. D. Griberman and P. Rusakov, "Comparison of Video Steganography Methods for Watermark Embedding", "Applied Computer Systems",pp. 53-61.
5. P. Kumar and K. Singh, "An improved data-hiding approach using skin-tone detection for video steganography s", "Elsevier Multimedia tools application", 2018.
6. S. Manisha and T. Sree Sharmila, "A two-level secure data hiding algorithm for video Steganography" Springer Multidim Syst Sign Process,2018.
7. J. Mansouri and M. Khadem", "An Adaptive Scheme for Compressed Video Steganography Using Temporal and Spatial Features of the Video Signal"

8. R. J. Mstafa and K. M. Elleithy, "Compressed and raw video steganography techniques: a comprehensive survey and analysis", "Elsevier multimedia tools and applications", 2016.
9. H. Noda T. Furuta, M. Niimi and E. Kawaguchi, "Video steganography based on bit-plane decomposition of wavelet transformed video.SPIE-Multimedia contents Vol-5306,pp. 345-353.
10. Z. Qu, S. Chen and S. Ji, "A Novel Quantum Video Steganography Protocol with Large Payload Based on MCCQI Quantum Video", "International Journal of theory physics.
11. Y. Ren, L. Zhai, T. Zhu and L. Wang, "Video Steganalysis Based on Subtractive Probability of Optimal Matching Feature", pp. 83-90.
12. M. M. Sadek, A. S. Khalifa and G. M. Mostafa, "Video steganography: a comprehensive review", "Elsevier Multimedia tools applications".
13. Ahmad J, Hwang S O. A secure image encryption scheme based on chaotic maps and affine transformation [J]. Elsevier Multimedia Tools and Applications, 2015, 75(21):13951-13976
14. Xie Eric Y, Li C Q, Yu S M, Lu J H. On the cryptanalysis of Fridrich's chaotic image encryption scheme [J]. Elsevier Signal Processing, 2017, 132: 150-154
15. Yi S, Zhou Y C. Binary-block embedding for reversible data hiding in encrypted images . ElsevierSignal Processing, 2017, 133:40-51.
16. Xiuli Cha, An image encryption algorithm based on chaotic system and compressive sensing, Elsevier Signal Processing, Vol-143:1-50,2018.
17. Wang, X., Zhu, X., Wu, X. and Zhang, Y. (2018). Image encryption algorithm based on multiple mixed hash functions and cyclic shift. ELSEVIER Optics and Lasers in Engineering, Vol-107, pp.370-379.2017.

# A Novel HMM Based Integrated Technique for Recognizing Clothes Patterns and Colors

K. Kavitha & Dr. P. Abdul Khayum

<sup>1</sup>PG Student, Department of ECE, G. Pullareddy Engineering College (Autonomous), Kurnool, Andhrapradesh, India

<sup>2</sup>Professor, M. Tech., (Ph. D), Department of ECE, G. Pullareddy Engineering College (Autonomous), Kurnool, Andhrapradesh, India

[kavitha.k0212@gamil.com](mailto:kavitha.k0212@gamil.com)<sup>1</sup> & [abd khayum@rediffmail.com](mailto:abd khayum@rediffmail.com)<sup>2</sup>

## Abstract

*There is need to develop such system which will give automatically the pattern of cloth and the color of the cloth, which is selected for recognition. The image acquired by the camera and is further processed for recognizing color and pattern. First we have to get the features of image that we selected for recognition and after that apply the Support vector Machine algorithm for further processing. In this implementation we used total three descriptors. To extract the statistical features we used Random signature descriptor in which there is use of DWT (Discrete Wavelet Transform) for calculating the global features of the cloths we selected. The obtained global features are then combined with local features which are calculated by the scale invariant feature transform to recognize the complex pattern of cloths. After getting the features we used SVM (support vector machine) to classify the images or pattern. In this we used CCNY dataset for recognizing cloth pattern. With the help of this method the physically impaired person can easily recognize the pattern of cloths as well as color of cloth. The MATLAB execution results show the performance of the system developed. Random Signature is used to capture the global directionality features statistical descriptor (STA) to extract the global statistical features on wavelet sub-bands and Scale Invariant Feature Transform (SIFT) to represent the local structural features. The combination of multiple feature channels provides complementary information to improve recognition accuracy. The collection of dataset on clothing*

*pattern recognition including four-pattern categories of plaid, striped, pattern less, and irregular, the method also provides new functions to improve the life quality for blind and visually impaired people. The obtained results are improved to great extent with the help of HMM (Hidden Markov Models).*

**Keywords-** SVM algorithm, CCNY dataset, Radon signature descriptor, SIFT (scale invariance feature transform).

## I. INTRODUCTION

Based on statistics from the World Health Organization (WHO), there are quite 161 million visually impaired people round the world, and thirty seven million of them are blind [1]. therefore in keeping with the World Health Organization (WHO), low vision is outlined as acuity of 20/200 or less within the higher eye with best correction potential (WHO. 2004). At an equivalent time, or so 100% of the male population in Europe suffers from some kind of vision deficiency (blindness), the foremost usual case being Associate in Nursing inability to tell apart between sure (e.g. red/green, blue/yellow). In extreme things, solely reminder gray scale can be distinguishable. Color plays a very important role within the daily life of a unremarkably keen-sighted person. Unremarkably keen-sighted folks use because the basis of variety of everyday tasks, as an example of matching socks, selecting between totally different garments.

Selecting garments with appropriate colors and patterns may be a difficult task for blind or visually impaired folks. They manage this task with the assistance from members of the family, victimization plastic Braille labels or differing types of sewing pattern tags on the garments, or by sporting garments with a homogenous color or with none patterns. There are several challenges in developing a system that helps the visually-impaired folks with the task of determinant consumer goods colors and patterns. Firstly, folks understand a pattern category or color to be a similar despite even terribly massive changes within the spectral composition of sunshine mirrored from the item. Conversely, objects that replicate identical spectra square measure typically according as being of various color, reckoning on lighting conditions and adaptation state. Thus, object colors determined from a camera image might not

perpetually correspond utterly to those according by a person's observer.

Secondly, shadows and wrinkles could also be confused as a part of the feel patterns or mental imagery of the vesture and therefore cause errors. Thirdly, the photographs of garments are often imaged from discretionary viewing directions. Strategies of matching patterns need the input try of pictures should be pattern rotation-invariant. Lastly, several garments have styles with advanced patterns and multiple colours that increase problem of identifications. A system that overcomes these problems, might offer blind folks larger independence as they might be ready to do bound tasks that they're presently unable to perform unaided.

## II. LITERATURE SURVEY

There are different techniques developed to know the pattern as well as color. There are separate development for pattern recognition and separate development of color recognition. Compared to proposed work these methods are having less accuracy as well as time required is more. Assistive systems of different kinds are being developed for the visually impaired people to improve the life quality and safety of such people including indoor navigation and way finding, display reading, banknote recognition, rehabilitation, and many more. In [2] developed a system for blind people to select clothes based on cloth pattern and colors in a cloth shop independently. This is a camera based system that can recognize clothing patterns into four categories (plaid, stripped, pattern-less, and irregular) and identify 11 colors: red, orange, yellow, green, cyan, blue, purple, pink, black, grey and white.

In [3] proposed a system to automatically recognize banknote of any currency to assist visually impaired people. This is also a camera based computer vision technology. This system has features like high accuracy, robustness, high efficiency, ease of use. This system is robust to conditions like occlusion, rotation, scaling, cluttered background, illumination change, wrinkled bills, and also eliminating false recognition and can guide the user to properly and correctly focus at the bill to be recognized using Speed Up Robust Features (SURF). In [4] developed a vision substitution system for travel aid for blind. Out of the three main categories of navigation systems (Electronic Travel Aids, Electronic Orientation systems, Position Locator Aids), they focus on Electronic Travel Aids. In all these works, the needs of blind people are considered. But, the main area where a color blind person faces a problem other than the traffic signals is in a cloth shop for selecting clothes of desired colors and patterns without the help of another

person. The proposed assistive system here depicts the same.

## III. TRAINING AND TESTING IMAGES

The general categories of the cloths are studied as,

- A. Irregular
- B. Pattern less
- C. Plaid
- D. Stripe

These all the patterns are used to train the system, which are given below,



Fig. 1 Dataset used for training images

We used training and testing dataset as CCYN dataset. Each one pattern has its own directionality, intensity and lighting variation. If the test image of stripe pattern the image patches are horizontal direction and but in the training set the image patches are in vertical direction. This can be matched by rotation, illumination changes. Both global and local features are combined in this project. This adjustment can be done only by extracting the global features like energy, entropy, variance, uniformity.

Once the superlative function has been estimated according to the particular image, every pixel in the image is mapped in the same way, independent of the value of surrounding pixels in the image. These techniques are simple and fast, but they can cause a loss of contrast. Examples of common global tone mapping methods are contrast reduction. Local features are the points, small patches and lines. This two features combined together to get the position of each image pixels. These pixels can be in the matrix form. So they

combined together using the classifier. In this project the classifier used is SVM (Support vector Machine).

#### IV. PROPOSED WORK

Clothing colour identification relies on the normalized colour bar chart of every covering image within the HSI colour house. The key plan is to quantize colour house supported the relationships between hue, saturation, and intensity. The proposed work is given for automatic recognition of cloths pattern and color of cloths. The proposed system is capable of real time recognizing the patterns and colors. Choosing the appropriate pattern and color of the clothes is important to assist the blind people to make decisions.

Below block diagram will give us the proposed work in detail. There are two important steps first we have to train the system and further we can check the testing. This system can handle clothes with complex patterns and recognize clothing patterns of four categories they are plaid, striped, pattern less, and irregular. This system is also able to identify 11 colors are red, orange, yellow, green, cyan, blue, purple, pink, black, grey, and white.

In the case of multiple colors in the colors, the first several dominant colors are spoken to users. In order to handle the large intraclass variations the combination of global and local image features significantly outperforms the state-of-the-art texture analysis methods for clothing pattern recognition. Extracting the feature is the important method of classifying the patterns. Each image has its own characteristics.

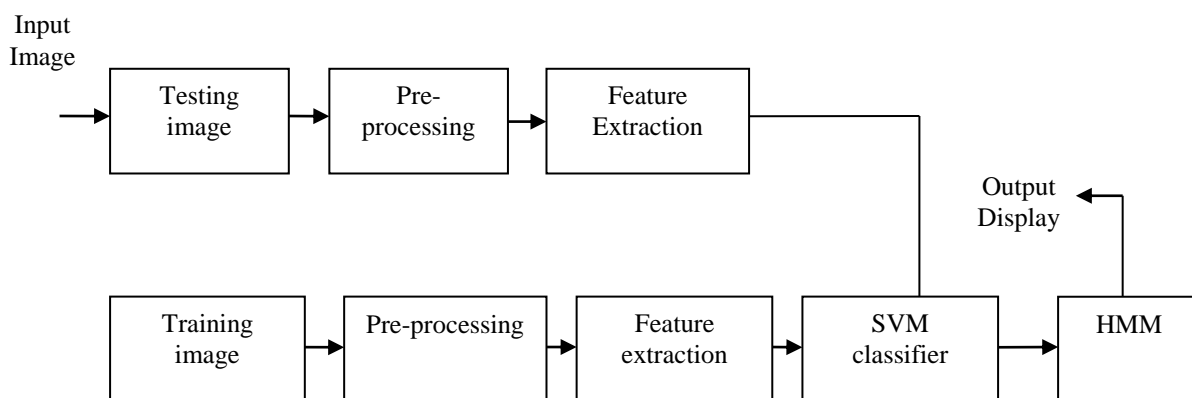


Fig.2. Block Diagram of Proposed Work

The clothing patterns of plaid and striped are both anisotropic. In distinction, the wear patterns within the classes of pattern less and Irregular Square measure isotropic. To form use of this distinction of directivity, we have a tendency to propose a completely unique descriptor, i.e., the Radon Signature, to characterize the directivity feature of wear patterns. Radon Signature (Radon Sig) relies on the atomic number 86remodelthat is usually wont to discover the principle orientation of a picture. The proposed work is having important steps, they are preprocessing and feature extraction they are required to implement a system to recognize the different patterns. For that the training algorithm called support vector machine are used. Following figure 2 will give us block diagram of proposed work,

To analysis this characteristics the features are used. These features can be extracted using the following algorithms.

- A. Statistical (STA) feature extraction
- B. Scale Invariance feature transform (SIFT)
- C. Recurrence Quantification Analysis (RQA)

All these three feature extraction techniques are integrated to get the better results. Statistical feature extraction is done using the wavelet transform. The STA is used to decompose the image pixel into low pixels. STA have 4 features like variance, energy, uniformity and entropy. Using these features the images can be classified. SIFT is the local feature extraction. To perform easier recognition, it is important that the global and local features extracted from the training image be identified even under changes in image scale, noise and illumination, as the name mentioned it is invariant to the scale. The

feature extracted is points, patches in the image. Recurrence Quantification Analysis (RQA) is also a local feature extractor. Mainly it is used to increase accuracy in the SVM classifier. The final feature combined in this way has a low dimension but more discerning power. It represents the accuracy of prediction output based on a particular feature. The Support Vector Machines (SVM) is used as the classifier in clothes pattern recognition system. SVM finds a maximum margin hyper-plane in the feature space.

A. Support Vector Machine Algorithm (Svm)

SVM algorithms are used in classification. This classification can be viewed as the task of separating classes in the feature space. This classification can be used in many applications like bioinformatics, text and image recognition. This can be the fast algorithm for identifying the Support Vectors of a given set of points.

B. Classification using Support Vector Machines (SVM) has gained conspicuity in the field of machine learning and pattern classification. Classification is achieved by realizing a linear or non-linear separation surface in the input space. In Support Vector classification, the separating function can be expressed as a linear combination of kernels associated with the Support Vectors as

$$f(x) = \sum_{x_i \in S} \alpha_j y_j K(x_j, x) + b$$

Where  $x_i$  denotes the training patterns,  $y_i \in \{+1, -1\}$  denotes the corresponding class labels and  $S$  denotes the set of Support Vectors.

C. STEPS INVOLVED IN SVM ALGORITHM

Given the two classes  $X_1$  and  $X_2$ , let us assume  $X_1$  are the positive class and  $X_2$  are the negative class.

Step 1: Find the support vector class, to get the optimum boundary. Let us assume 3 input support vector set.

$$s_1 = \begin{bmatrix} X_{1_i} \\ X_{2_j} \end{bmatrix}, s_2 = \begin{bmatrix} X_{1_i} \\ X_{2_j} \end{bmatrix}, s_3 = \begin{bmatrix} X_{1_i} \\ X_{2_j} \end{bmatrix}$$

Step 2: Compute this support vector set with the bias 1:

$$\overline{s_1} = \begin{bmatrix} X_{1_i} \\ X_{2_j} \\ 1 \end{bmatrix}, \overline{s_2} = \begin{bmatrix} X_{1_i} \\ X_{2_j} \\ 1 \end{bmatrix}, \overline{s_3} = \begin{bmatrix} X_{1_i} \\ X_{2_j} \\ 1 \end{bmatrix}$$

Step 3: Finding the 3 parameters  $\alpha_1, \alpha_2, \alpha_3$

$$\begin{aligned} \alpha_1 \overline{s_1} \cdot \overline{s_1} + \alpha_2 \overline{s_2} \cdot \overline{s_1} + \alpha_3 \overline{s_3} \cdot \overline{s_1} &= -1 \\ \alpha_1 \overline{s_1} \cdot \overline{s_2} + \alpha_2 \overline{s_2} \cdot \overline{s_2} + \alpha_3 \overline{s_3} \cdot \overline{s_2} &= -1 \\ \alpha_1 \overline{s_1} \cdot \overline{s_3} + \alpha_2 \overline{s_2} \cdot \overline{s_3} + \alpha_3 \overline{s_3} \cdot \overline{s_3} &= -1 \end{aligned}$$

Step 4: The hyper plane that discriminates the position class from the negative class is given by:

$$\sum \alpha_i s_i$$

Step 5: The separating hyper plane equation formula is

$$y = wx + b$$

Step 6: Plot the line according to the value. If the value is greater than the augmented value it belongs to the class positive and if it is lesser than the augmented value it belongs to the class negative.

V. EXECUTION RESULTS

A. Proposed Work

a) Training

First we have to train the system by same procedure as mentioned in proposed work.

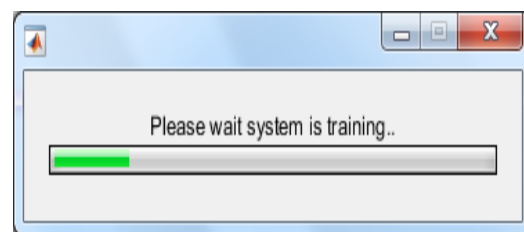


Fig.3 system is processing for training

b) Testing

Select the image for testing from dataset. There are different images with different pattern and color. Select one of the image from given dataset.

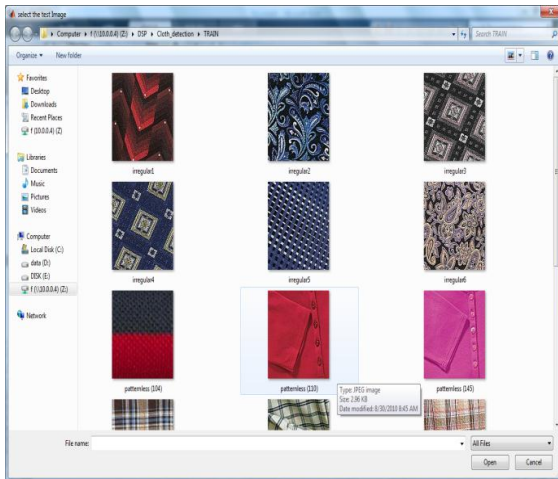


Fig. 4 select the image from available dataset

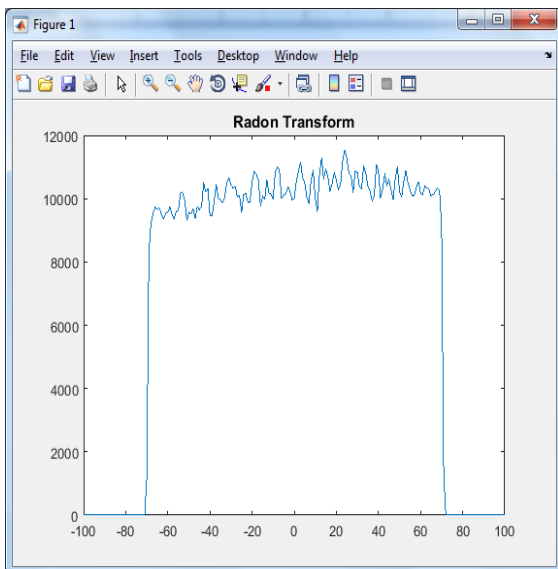


Fig. 5 Radon transform for the proposed work

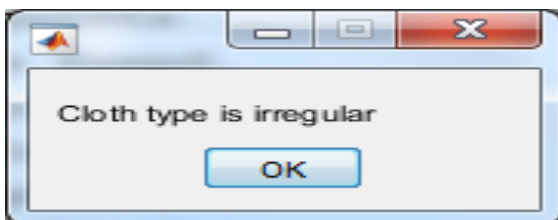


Fig.6 Detected pattern of the cloth.

ans =

The colors is blue with 72.7551 Percent

ans =

The colors is Cyan with 12.7194 Percent

ans =

The colors is Green with 2.1378 Percent

Fig. 7 The color of selected cloth for proposed output

### B. Results for HMM as extension

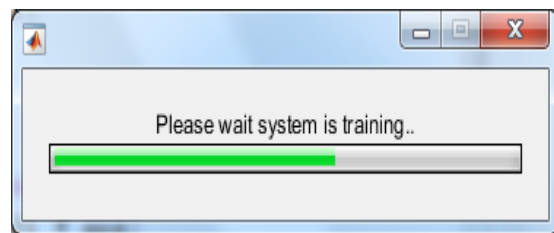


Fig.8 system is processing for training using HMM

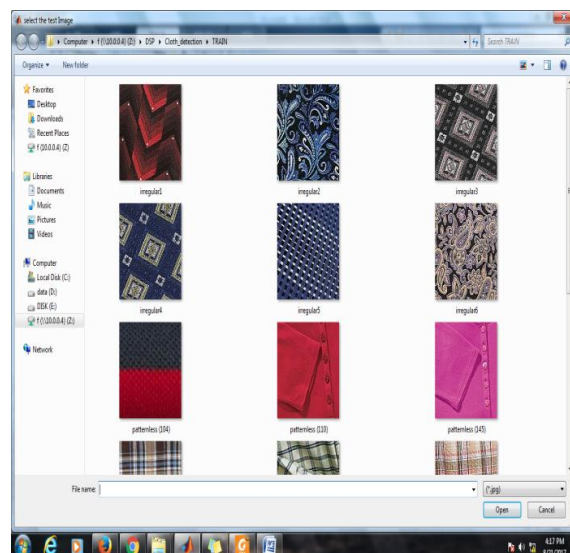


Fig. 9 select the image from available dataset for HMM method

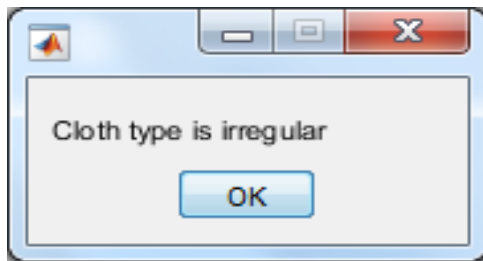


Fig. 10 Detected pattern of the cloth using extension method

```
ans =
The colors is Pink with 99.8112 Percent

ans =
The colors is purple with 0.086735 Percent

ans =
The colors is red with 0.056122 Percent
```

Fig.11 The color of selected cloth for extension output

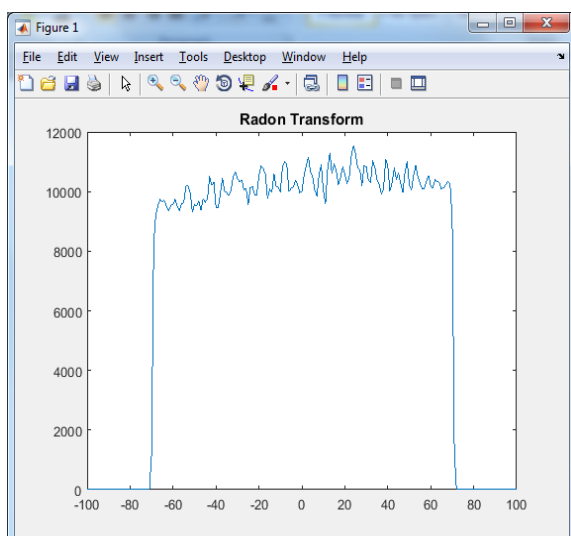


Fig.12 Radon transform for the extension work

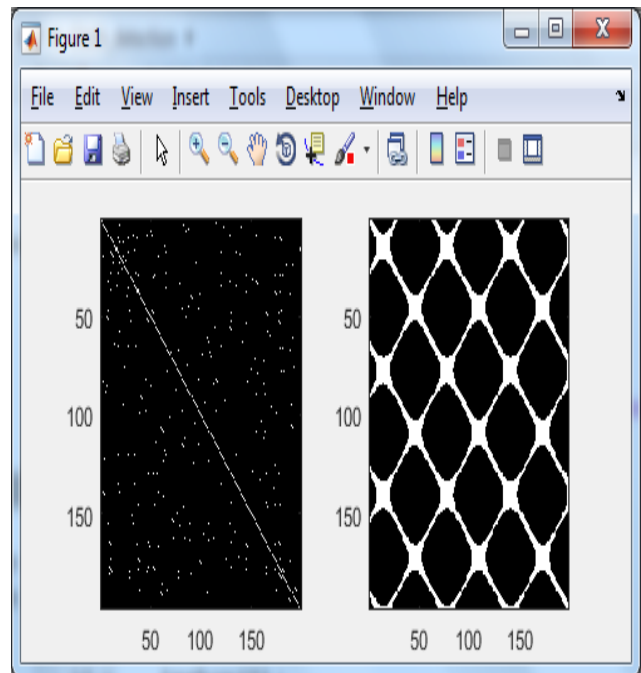


Fig.13 Local feature for irregular image (RQA)

Table I. Recurrence Quantification Analysis of Recurrence Plots

	<i>Proposed work</i>	<i>Extension work</i>
<i>Recurrence rate</i>	0.0097	0.1747
<i>Determinism</i>	0.3526	0.9595
<i>Entropy</i>	0.4260	1.7556
<i>Averaged diagonal line length L</i>	2.2333	6.7125

Recurrence rate RR, The percentage of recurrence points in an RP Corresponds to the correlation sum.

Determinism DET, The percentage of recurrence points which form diagonal lines.

Entropy ENTR, The Shannon entropy of the probability distribution of the diagonal line lengths  $p(l)$ .

Averaged diagonal line length L, The average length of the diagonal lines.

## VI.CONCLUSION

We analyzed the proposed system by MATLAB execution results. Finally it will give the results which are extremely efficient than existing techniques used. Assistive devices are a key aspect in wearable systems for biomedical applications, as they represent potential aids for people with physical and sensory disabilities that might lead to improvements in the quality of life. Globally, an estimated 40 to 45 million people are totally blind, 135 million have low vision and 314 million have some kind of visual impairment. In most industrialized countries, approximately 0.4% of the population is blind while in developing countries it rises to 1%. It is estimated by the World Health Organization (WHO) that 87% of the world's blind live in developing countries. Here, a system is proposed to recognize clothing patterns and colors to help visually impaired people in their daily life. Random Signature is used to capture the global directionality features statistical descriptor (STA) to extract the global statistical features on wavelet sub-bands and Scale Invariant Feature Transform (SIFT) to represent the local structural features. The combination of multiple feature channels provides complementary information to improve recognition accuracy. The collection of dataset on clothing pattern recognition including four-pattern categories of plaid, striped, pattern less, and irregular, the method also provides new functions to improve the life quality for blind and visually impaired people. The obtained results are improved to great extent with the help of HMM (Hidden Markov Models).

## VII.FUTURE SCOPE

Future scope of the proposed work will focus on handling large occlusions by using more discriminative features like door knobs and other hardware, Detecting and recognizing more types of indoor objects and icons on signage, in addition to text for indoor way finding aid, to assist blind people travel independently.

## REFERENCES

- [1] Jarbas Joaci de Mesquita Sa, Andre Ricardo Backes, Paulo Cesar Cortez (2013) "Texture analysis and classification using shortest paths in graphs", Elsevier, pattern recognition, 1314–1319.
- [2] Xiaodong Yang, YingLi Tian (2013) "Texture representations using subspace

embeddings", Elsevier, pattern recognition, 1130-1137.

- [3] Christopher sentelle, Georgios anagnostopoulos, Michael georgiopoulos (2011) "Efficient revised simplex method for SVM training", IEEE transactions on neural networks, 22(10), 1650-1661.

- [4] Yuntao Qian, Minchao Ye, Jun Zhou (2012) "Hyper-spectral Image Classification Based on Structured Sparse Logistic Regression and Three-dimensional Wavelet Texture Features", IEEE transactions on geo-science and remote sensing, 51(4), 2276-2291.

- [5] Sandro cumani, Pietro Laface (2012) "Analysis of large-scale SVM training algorithms for language and speaker recognition", IEEE transactions on audio, speech, and language processing, 20(5), 1585- 1596.

- [6] ShiftXingming Zheng, Ningzhong Liu, (2012), "Colour Recognition of Clothes Based on KMeans and Mean", IEEE transaction on pattern recognition, 49-53.

- [7] Alberto Jard'on Huete, Juan G. Victores, Santiago Mart'inez, Antonio Gim'enez, and Carlos Balaguer, (2012), "Personal Autonomy Rehabilitation in Home Environments by a Portable Assistive Robot", IEEE transactions on systems, man, and cybernetics, 42(4), 561-569.

- [8] Faiz M. Hasanuzzaman, Xiaodong Yang, and YingLi Tian (2012) "Robust and Effective Component Based Banknote Recognition for the Blind", IEEE transaction on system, man and cybernetics, 1024- 1033.

- [9] Chucai Yi, YingLi Tian, Aries Arditi (2011) "Portable Camera-based Assistive Text and Product Label Reading from Hand-held Objects for Blind Persons", IEEE Transactions on Mechatronics, 1-10.

- [10] Yuan and YingLi Tian, (2010), "Rotation and illumination invariant Texture Analysis", IEEE transaction on Image and Signal Processing, 2643-2653

# A Novel Method for Dental Radiographs Contrast Enhancement for Efficient Diagnosis of Dental Diseases

A. Ramana Kumari, S. Nagaraja Rao, P. Ramana Reddy

**Abstract:** Contrast Enhancement for Low resolution image is an active area of research to attain an effective diagnosis results in the medical field through Digital Medical Images. To do this, a novel contrast enhancement method is proposed in this paper based on the spatial correlation characteristics of image pixels. Considering the spatial correlation as main factor, the proposed method focused to improve the contrast of center pixels based on its neighborhood pixels. Extensive simulations are conducted over the proposed method through several dental radiograph images and the obtained results are analyzed both qualitatively and quantitatively. The Quantitative analysis is done through a metric, called contrast root mean square deviation and the obtained values are compared with conventional contrast enhancement techniques, Histogram related methods and Contrast stretching methods.

**Keywords:** Dental Radiograph, Contrast Enhancement, Histogram, Correlation, CMRSD.

## I. INTRODUCTION

In recent years, there has been an increased effort in the development of an automatic computerized system for clinical research and applications in dentistry. Dental image analysis plays an important role in the treatment, clinical diagnosis and surgery of several dental related diseases. The dental radiograph images (DRI) can be used to discover concealed structures of dental images dental, benign masses or malignant cavities and bone losses. During the treatment or diagnosis processes such as diagnosis of caries, root canal operation, orthodontic patient's treatment planning, dental radiograph analysis is necessary. Basically the dental X-ray radiograph images are classified into 2 classes, i.e. the extra-oral ones and the intra-oral ones [1]. The intra-oral dental X-ray images includes the "bite wing X-ray images, occlusal X-ray images, and the periapical X-ray images". The "bite wing X-ray images" are used to represent the particulars about the lower and upper jaw in the mouth. The "occlusal X-ray images" are used to monitor the placement and development of the overall teeth arch in either lower or upper jaw. Further the "periapical X-ray images" are used to track the entire tooth. Instead, the extra-oral images helps in the finding of dental related problems in the skull and jaw, for example, the panoramic X-ray images and cephalometric projections.

Dental image diagnosis defines the elucidation of patient's dental, bony, and soft tissues arrangements and

also offer the entire images in the analysis of planning a treatment for orthodontic problems. But, in clinical assessment, tracking of anatomical (functional) structures of dental images is accomplished during the treatment preparation. This process consumes more and more time and also the process is subjective in nature. To overcome this problem, an automatic detection of dental landmarks like caries, occlusions, cavities and bone structures for diagnosis of orthodontic treatment is an optimal solution. But the detection of dental landmarks with high success rate and precision is a challenging issue. Several research contribution have been accomplished in this decade to build an automatic analytical system for dental image clinical purposes, like image segmentation [2, 3], anatomical landmark identification [4, 5], treatment and diagnosis [6, 7, 8].

In general an automatic image segmentation system accomplishes in two phases, preprocessing and detection. In the preprocessing phase, the input images are processed for feature level adjustments followed by features extraction. In the next phase, the extracted features are processed for detection through supervised learning techniques. Since the features of dental radiographs are more important, extraction of significant features is a challenging task and the proper features are only extracted when the input image quality is high and effective. Considering the quality of dental image as main objective, this paper proposed a new dental image contrast enhancement technique to make the dental image brighter such that the soft tissues and bones are more clearly visible. Further the proposed contrast enhancement technique also boosts the quality of low-contrast image to high contrast image. The simulations conducted over different low-contrast dental images shows the effectiveness of proposed mechanism.

Remaining paper is ordered as: section II discusses the particulars of literature survey. The details of proposed contrast enhancement method are described in section III. Experimental analysis details are enumerated and the conclusions are enumerated in section V.

## II. LITERATURE SURVEY

Since the intra-oral DRIs are low resolution (LR) images due to the low dose usage (LDU). The process of LDU is

Revised Manuscript Received on December 22, 2018.

A. Ramana Kumari, Research scholar, ECE, JNTU Ananthapur, Ap, India,

Dr. S. Nagaraja Rao, Professor, dept of ECE, G. Pulla Reddy Engineering college (autonomous), Kurnool, AP, INDIA,

Dr. P. Ramana Reddy, Professor, dept of ECE, JNTU ANANTHAPUR, India



dependent on the health condition of patient [9, 10]. Hence the image enhancement techniques can be useful to the DRIs to increase the quality. Generally the image quality enhancement is accomplished through the manipulation of its contrast such that the tissues and bones in the dental image are clearly visible.

The most popular contrast enhancement (CE) techniques such as “Histogram Equalization (HE) [14], Adaptive Histogram Equalization (AHE) [15], and contrast limited adaptive histogram equalization (CLAHE) [16]” are being extensively used in the medical field to increase the contrast of LR images. HE results in the CE image with over brightness and also introduces noise and harshness in resultant image. Furthermore, the CLAHE tends to introduce some instantaneous changes at the borders of images through their grey pixel intensities. Since the architectures of DIRs are somewhat typical in nature, the quality improvement approach should be specific in nature. A study about the outcome of the novel HE on the quality of image in digital “periapical X-ray images” was carried out by M. Mehdizadeh and S.Dolatyar [11].

In [12], a new CE method is proposed to improve the quality in LDU X-ray images through wavelet features. By considering the corrections in the contrast, a new contrast enhancement is proposed in [13] through histogram registration (HR). This HR remodels the histograms of the 2 DRIs in such a manner that they are complemented with respect to their deviation in the contrast levels.

Further, in [17], a new method was proposed to increase the contrast of DRIs through a new method called “sharp contrast-limited adaptive histogram equalization (SCLAHE)”. Totally 10 intra-oral images periapical dental x-ray images are processed for evaluation. With an aim of improving the contrast of LR DRIs, [18] proposed a contrast stretching (CS) technique and also analyzed the evaluation of the variable CS technique. With an extension to the method developed in [17], an integrated method is proposed in [19] by combining three different CE techniques namely, “sharp adaptive histogram equalization (SAHE), sharp median adaptive histogram equalization (SMAHE) and SCLAHE”.

### III. PROPOSED METHOD

In this section, the complete details of proposed approach are outlined briefly. The proposed considers the spatial correlations between the GLs for contrast enhancement whereas the conventional approach didn't considered these spatial dependencies by which the GLs in the contrast enhanced image don't have any relationship with neighboring pixels which makes the entire process more complex and not clear. The complete details or proposed approach is outlined as follows;

For example, lets assumes an input image ‘*I*’ with height *H* and width *W* and having the gray-levels (GL) range of [*I<sub>d</sub>*, *I<sub>u</sub>*] and the enhanced image ‘*O*’ of range [*O<sub>d</sub>*, *O<sub>u</sub>*], having the visual perception quality better than the input image ‘*I*’. Mathematically these input and output images are represented as,

$$\begin{aligned} I &= \{I(m, n) | 0 \leq m \leq M - 1, 0 \leq n \leq N - 1\} \\ O &= \{O(m, n) | 0 \leq m \leq M - 1, 0 \leq n \leq N - 1\} \end{aligned} \quad (1)$$

Here the range of input and output images such as  $I(m, n) \in [I_d, I_u]$  and  $O(m, n) \in [O_d, O_u]$  varies from 0 to

255 for an 8-bit image. This range is ideal, i.e., 0-255 only if the enhancement process utilizes the entire dynamic gray-level range. In such case, the lower limit  $O_d = 0$  and the upper limit  $O_u = 255$ .

#### A. Spatial Entropy based Contrast Enhancement (SECE) [20]

Let the input image *I* has *K* discrete gray levels and the obtained gray levels after sorting them is  $\{I_1, I_2, \dots, I_K\}$ . Initially, the *I*s decomposed into various grids, distributed spatially. The 2D spatial histogram (SH) of a gray-level *I<sub>k</sub>* on the spatial grid of *I* is calculated as,

$$h_k = \{h_k(h, w) | 1 \leq h \leq H, 1 \leq w \leq W\} \quad (2)$$

Where  $h_k(h, w)$  defines the number of gray-level occurrences of *I<sub>k</sub>* in the spatial grid present in the region of size,  $\left[ \left( (h-1) * \frac{M}{H}, h * \frac{M}{H} \right) \times \left( (w-1) * \frac{N}{W}, w * \frac{N}{W} \right) \right]$ . The total grids number on the 2D SH is *H*\**W* which was estimated vigorously through the aspect ratio,  $r = \frac{M}{N} = \frac{H}{W}$ .

$$W = \left\lfloor \left( \frac{K}{r} \right)^{1/2} \right\rfloor \text{ and } H = \left\lfloor (Kr)^{1/2} \right\rfloor \quad (3)$$

Where the function  $\lfloor \cdot \rfloor$  makes the value round off to its nearest neighbor value.

In the every grid, the distribution of a gray-level *I<sub>k</sub>* can be measured through the spatial entropy and the spatial entropy *S<sub>k</sub>* for a gray-level *I<sub>k</sub>* is obtained according to

$$S_k = - \sum_{h=1}^H \sum_{w=1}^W h_k(h, w) \log_2 h_k(h, w) \quad (4)$$

Further, the obtained spatial distribution has to evaluate with respect to the distributions of the other GLs to know the importance and it is measured through a discrete function *f<sub>k</sub>* as,

$$f_k = S_k / \sum_{l=1, l \neq k}^K S_l \quad (5)$$

Further the obtained discrete function *f<sub>k</sub>* is normalized as,

$$\hat{f}_k = f_k / \sum_{l=1}^K f_l \quad (6)$$

And based on the obtained normalized discrete function  $\hat{f}_k$ , a CDF *F<sub>k</sub>*, of a gray-level *I<sub>k</sub>* is defined as,

$$F_k = \sum_{l=1}^k \hat{f}_l \quad (7)$$

Finally the Contrast Enhanced Gray-level of an output image *O* is attained based on the following mapping criterion

$$O_k = \lfloor F_k(O_u - O_d) + O_d \rfloor \quad (8)$$

The final output *O* denotes the contrast enhanced image. Further the performance of this mechanism is measured through the performance metrics like expected measure of enhancement by gradient (EMEG) and gradient magnitude similarity deviation (GMSD).

#### B. Spatial Correlation based Contrast Enhancement (SCCE)

Though the conventional approach achieved an increased contrast in the output image, this method didn't considered the mutual; correlations between the gray levels, hence, generally, the output contrast enhanced GLs are simply a linear mappings of input GLs, i.e., a particular gray-level in the output image is just linearly related to the input GL and don't have any spatial relationship with the other GLs. In order to address this issue, this work proposes a new contrast enhancement mechanism by considering the spatial relations between the GLs. To obtain a normalized 2D SH, the 2D histogram values are further normalized as



$$h_k(h, w) = h_k(h, w)/HW \quad (9)$$

Such that

$$\sum_{k=1}^K \sum_{h=1}^H \sum_{w=1}^W h_k(h, w) = 1 \quad (10)$$

Here the spatial entropy is measured by evaluating the joint 2D spatial histograms for a given two GLs  $I_k$  and  $I_l$  on the spatial grid found on the area of  $\left[ \left( h * \frac{M}{H}, (h+1) * \frac{M}{H} \right) \times (w * NW, (w+1) * NW) \right]$ , as

$$h_{k,l}(h, w) = \min(h_k(h, w), h_l(h, w)) \quad (11)$$

The above expression gives a new evaluation procedure to measure the spatial relationships between two GLs  $I_k$  and  $I_l$ . Further to obtain the spatial dependencies of GLs and the respective spread over the image spatial domain, a new metric called Spatial Correlation (SC) is derived here and formulated as,

$$SC_{k,l} = \sum_{h=0}^{H-1} \sum_{w=0}^{W-1} h_{k,l}(h, w) \left( \frac{h_{k,l}(h, w)}{h_k(h, w)h_l(h, w)} \right) \quad (12)$$

Where  $SC_{k,l}$  is the spatial correlation between two GLs  $I_k$  and  $I_l$ . The above expression gives a spatial relationship between the GLs  $I_k$  and  $I_l$ . The SC is high when the GLs  $I_k$  and  $I_l$  happen jointly over the nearest spatial areas and the spread over the image spatial domain. Hence, this approach can distribute the GLs in a wide fashion with higher discriminations between the GLs  $O_k$  and  $O_l$  such that the obtained contrast should be high.

After measuring the spatial correlations for every GL in accordance to all other GLs, one rank is assigned to that relation based on the closeness and finally the output gray-level  $O_k$  is obtained through the following mapping function,

$$O_k = \lfloor O_{k-1} + \Delta_{k-1,k}(O_u - O_d) \rfloor \quad (13)$$

Where

$$\Delta_{k-1,k} = \frac{r(k-1) + r(k)}{2} \quad (14)$$

The term  $\Delta_{k-1,k}(O_u - O_d)$  in Eq. (13) is the semantic gap between the output GLs  $O_{k-1}$  and  $O_k$ . This semantic gap is discovered with respect to the mutual contribution of successive GLs that are defined based on their average rankings. The proposed mapping function always ensures that the obtained contrast enhanced GLs range is definitely in between the allowed dynamic range only. Thus the proposed approach efficiently exploits the allowable dynamic range and produces an effective contrast enhanced image.

#### IV. SIMULATION RESULTS

This section describes the details of simulation experiments conducted over the proposed approach through different dental X-ray images. The proposed approach was assessed both quantitatively and qualitatively. Qualitative assessment is mostly apprehensive with visual perception of the contrast enhanced image. But, this is a non-trivial procedure which indirectly be contingent to the human observation. Particularly, in the case of small differences in the contrast. Therefore, the quantitative assessment is performed additionally based on the objective evaluations on the contrast enhanced images.

##### A. Qualitative Assessment

In the case of qualitative assessment, the performance of proposed mechanism is observed by human observer. To

show the performance enhancement with respect to the qualitative assessment, several images are processed through the developed mechanism and the obtained results are depicted in this section. Moreover to compare the proposed method with conventional approaches, the test imagery was also processed through conventional approaches for contrast enhancement. The conventional approaches considered here for comparison are namely, CLAHE [16], Histogram Registration (HR) [13], and Contrast Stretching (CS) [18]. The obtained contrast adjusted images of different dental x-ray images are shown below.

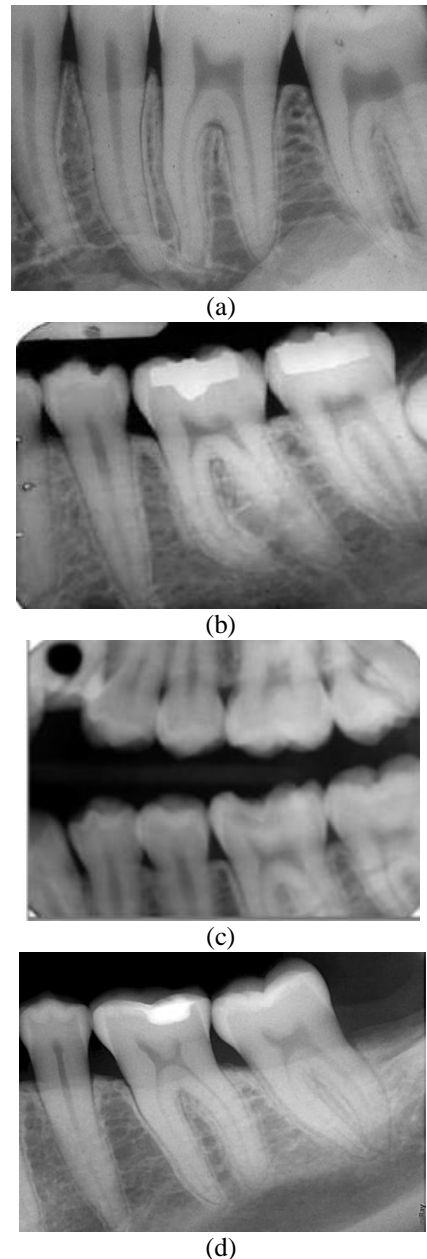
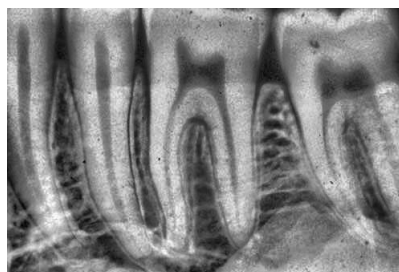
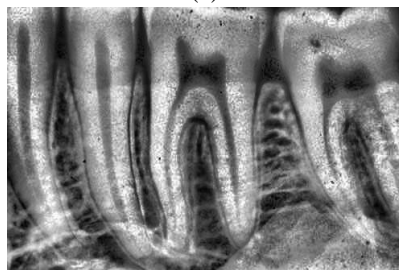


Figure.1 Test Images of dental radiographs



(a)



(b)



(c)

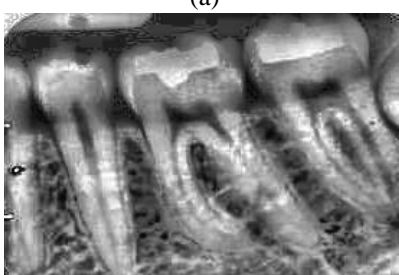


(d)

Figure.2 Obtained results for test image (figure.1a) through, (a) CLAHE, (b) Histogram Registration, (c) Contrast Stretching and (d) Proposed Approach



(a)



(b)

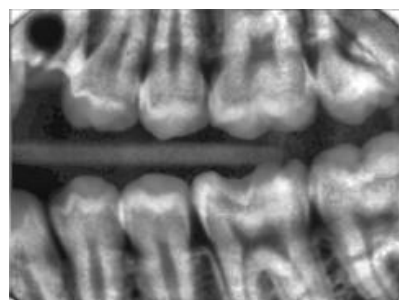


(c)

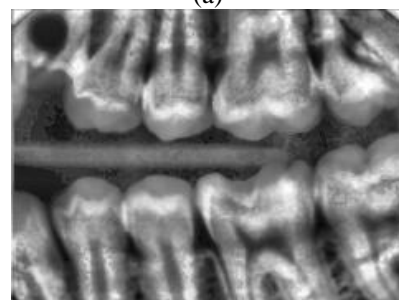


(d)

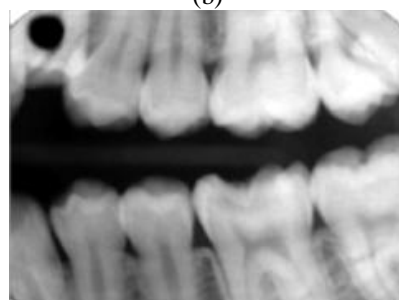
Figure.3 Obtained results for test image (figure.1b) through, (a) CLAHE, (b) Histogram Registration, (c) Contrast Stretching and (d) Proposed Approach



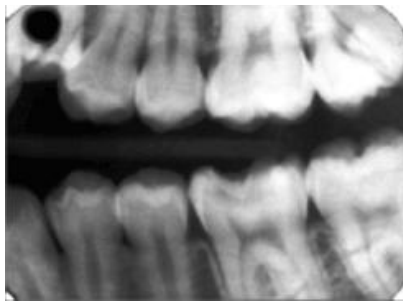
(a)



(b)



(c)



(d)

Figure.4 Obtained results for test image (figure.1c) through, (a) CLAHE, (b) Histogram Registration, (c) Contrast Stretching and (d) Proposed Approach



(a)



(b)



(c)



(d)

Figure.5 Obtained results for test image (figure.1d) through, (a) CLAHE, (b) Histogram Registration, (c) Contrast Stretching and (d) Proposed Approach

B. Quantitative Assessment

The performance metric used here is “contrast root mean square difference (CRMSD)”. CRMSD is an adaption of the

conventional “root mean square deviation (RMSD)”, generally used to evaluate the performance with respect to the deviation between two pixels [28]. In this case, the pixel values form two images considered, one is original image and another is contrast enhanced image. For a given image of width N and height M, the CRMSD is defined as;

$$CRMSD = \sqrt{\frac{\sum_{m=0}^M \sum_{n=0}^N (E(m,n) - O(m,n))^2}{M \cdot N}} \quad (15)$$

Where  $O(m,n)$  and  $E(m,n)$  are the contrast of single pixels with coordinates  $(m,n)$  from the original and enhanced images respectively. The particular quantities can be obtained through the following equation.

$$O(m,n) = \frac{lv(m,n)}{lm(m,n)} \quad (16)$$

For each pixel  $(m,n)$ , of image  $I(m,n)$ , the quantities can be evaluated according to the following equations.

$$lm(m,n) = \frac{1}{(2m+1)^2} \sum_{k=-m}^m \sum_{l=-m}^m I(m+k, n+l) \quad (17)$$

$$lv(m,n) = \frac{1}{(2m+1)^2} \sum_{k=-m}^m \sum_{l=-m}^m (I(m+k, n+l) - lm(m,n))^2 \quad (18)$$

Where  $I(m+k, n+l)$  is the pixel intensity in the coordinates  $(m+k, n+l)$  and  $(2m+1)^2$  is a constant which determines the square block size through the pixels. In the present scenario, it is considered as  $3 \times 3$ . The obtained CRMSD details for all the above test imagery is represented in the following table.1.

Table.1 Obtained CRMSD for Test Imagery

	Image 1	Image 2	Image 3	Image 4
Original	0.997	0.820	0.686	0.882
CLAHE [16]	0.954	0.768	0.633	0.812
Histogram Registration [13]	0.887	0.722	0.587	0.770
Contrast Stretching [18]	0.852	0.709	0.559	0.754
Proposed	<b>0.811</b>	<b>0.681</b>	<b>0.517</b>	<b>0.719</b>

As described in the table.1, the obtained CRMSD values are more far from the original CRMSD values for every test image. Further it can also be observed that the proposed approach has attained a much improvement in the contrast of test imagery when compared the conventional approaches. From the above both qualitative and quantitative assessments, it is proved that the proposed contrast enhancement mechanism can improve the contrast of any type of image.

V. CONCLUSIONS

A new quality improvement mechanism is proposed in this



paper to enhance the quality of low contrast dental radiographs such that they can be processed for efficient dental diseases diagnosis. Since the approximation of proper grey levels is most important for an automatic diagnosis system accomplishing through digital image processing techniques, this paper tried to improve the contrast levels of a low contrast dental radiographs such that making the image more informative and effective. The proposed method considered the spatial correlations between the pixels of image for contrast enhancement of neighboring pixels. The obtained simulation results proved the performance effectiveness of proposed method through both quantitative and qualitative assessments.

### REFERENCES

1. Kumar, 2011. Extraoralperiapical radiography: an alternative approach to intraoral periapical radiography. *Imag. Sci. Dent.* 41, 161–165.
2. Lai, Y.H., Lin, P.L., 2008. Effective segmentation for dental x-ray images using texture-based fuzzy inference system. *Adv. Concepts Intell. Vis. Syst. Lect. Notes Comput. Sci.* 5259, 936–947.
3. Rad, A.E., 2013. Digital dental X-ray image segmentation and feature extraction. *TELKOMNIKA* 11, 3109–3114.
4. Nikneshan, S., 2015. The effect of emboss enhancement on reliability of landmark identification in digital lateral cephalometric images. *Iran. J. Radiol.* 12, e19302.
5. Zhou, J. Abdel-Mottaleb, M., 2005. A content-based system for human identification based on bitewing dental X-ray images. *Pattern Recognit.* 38, 2132–2142.
6. Lpez-Lpez, J., 2012. Computer-aided system for morphometric mandibular index computation (using dental panoramic radiographs). *Med. Oral Patol. Oral* 17, e624–e632.
7. Nakamoto, T., 2008. A computer-aided diagnosis system to screen for osteoporosis using dental panoramic radiographs. *Dentomaxillofacial Radiol.* 37, 274–281.
8. Wriedt, S., 2012. Impacted upper canines: examination and treatment proposal based on 3d versus 2d diagnosis. *J. Orofac. Orthop.* 73, 28–40.
9. M. Sakata and K. Ogawapp, "Noise Reduction and contrastenhancement for small-dose X-ray images in wavelet domain," presented at the Nuclear Science Symposium Conference record(NSS/MIC), 2009.
10. R. Aufrichtig and P. Xue, "Dose efficiency and low-contrastdetectability of an amorphous silicon x-ray detector for digitalradiography," *Phys. Med. Biol.*, vol. 45, pp. 2653–2669, 2000.
11. M. Mehdizadeh and S.Dolatyar, "Study of Effect of AdaptiveHistogram Equalization on Image Quality in Digital Preapical Image inPre Apex Area", research *Journal of Biological Science*, pp: 922 – 924, vol: 4, issue: 8, 2009.
12. M. Sakata and K. Ogawapp, "Noise Reduction and contrastenhancement for small-dose X-ray images in wavelet domain," presented at the Nuclear Science Symposium Conference record(NSS/MIC), 2009.
13. TL Economopoulos, PA Asvestas, GK Matsopoulos, K Gro'ndahl and H-G Gro'ndahl, "A contrast correction method for dental images based on histogram registration", Technical Report, *Dentomaxillofacial Radiology* (2010) 39, 300–313.
14. M. H. A. Hijazi, F. Coenen, and Y. Zheng, "Retinal image classification using a histogram based approach," in *Proc. of Int. Joint Conf. on Neural Networks*, pp. 1–7, Barcelona (2010).
15. Wang, Q., & Ward, R. K. (2007). Fast image/video contrast enhancement based on weighted thresholded histogram equalization. *IEEE transactions on Consumer Electronics*, 53(2), 757-764.
16. A. W. Setiawan, T. R. Mengko, O. S. Santoso, and A. B. Suksmono, "Color retinal image enhancement using CLAHE," in *Proceedings of the International Conference on ICT for Smart Society (ICISS '13)*, pp. 1–3, Jakarta, Indonesia, June 2013.
17. SitiArpahBt Ahmad, "The effect of sharp contrast-limited adaptive histogram equalization (SCLAHE) on Intra-oral dental radiograph images", *IEEE EMBS Conference on Biomedical Engineering and Sciences (IECBES)*, 2010.
18. Haris B Widodo, AriefSoelaiman, Yogi Ramadhani and RetnoSupriyanti, "Calculating Contrast Stretching Variables in Order to Improve Dental Radiology Image Quality", *IOP Conference Series: Materials Science and Engineering*, Volume 105, 2016.
19. SitiArpah Ahmad, MohdNasirTaib, Noor ElaizaA.Khalid, Rohana Ahmad, HaslinaTaib, " A comparison of image enhancement techniques for dental x-ray image interpretation", *GCSE 2011: 28-30 December 2011*, Dubai, UAE.
20. TurgayCelik, "Spatial Entropy-Based Global and Local Image Contrast Enhancement", *IEEE Transactions On Image Processing*, Vol. 23, No. 12, December 2014.

# Blood Vessel Leakage Detection in Diabetic and Malarial Retinopathy by Using Saliency and Leakage Detection

B.MALLIKA (M.tech scholar)<sup>1</sup>

Dr. S.NAGARAJARAO, M.TECH, PH.D (Professor of ECE)<sup>2</sup>

Department of Electronics & Communication Engineering<sup>1,2</sup>

G. PULLAREDDY Engineering College (Autonomous), Kurnool, Andhra Pradesh-518007,India<sup>1,2</sup>

[mallikamalli901@gmail.com](mailto:mallikamalli901@gmail.com)<sup>1</sup>, [suryakari2k9@gmail.com](mailto:suryakari2k9@gmail.com)<sup>2</sup>

## ABSTRACT

Nowadays we can see so many retina diseases, the symptoms of the disease is leakage in the retinal angiography. The major retina diseases are diabetic maculopathy and paediatric malarial retinopathy. In this paper we are proposing a saliency based method to detect the leakage of fluorescein angiography. First step is dividing the image into parts by using the super pixels. The second step is estimation of saliency map. For every level of super pixel we proposed intensity and compactness saliency cues. After this by using the averaging operator all the saliency maps are combined. By using the pixel-wise multiplication operator the two saliency maps are combined. The leakage regions in the retina are detected by using thresholding, after this graph-cut segmentation is applied. The experimental result shows that comparing the latest methods the saliency maps given the best results.

Index Terms— Leakage, diabetic, malarial, retinopathy, fluorescein angiogram, saliency, segmentation.

## I. INTRODUCTION

Fluorescein angiography (FA) is a valuable imaging modality that offers a map of retinal vascular structure and function by means of highlighting blockage of, and leakage from, retinal vessels [1]. Although FA is invasive and high-priced, and exposes patients with rare but doubtlessly critical side consequences, it's far vital in differential analysis of retinal diseases such as diabetic retinopathy (DR), age-associated macular degeneration (AMD), malarial retinopathy (MR), and so forth [2]–[4]. Incarnated as beneficial signal of high depth, retinal leakage in angiography is currently a key function for

clinicians to decide the activities and improvement of lesions within the retina. Fig. 1 suggests the arrival of leakages in MR and DR respectively. MR is assumed to be critical for the differential prognosis of cerebral malaria, while DR is a leading cause of vision loss within the running age population. Identification of sites and assessment of the volume of leakage permit choice making for remedy and monitoring of ailment activities. More specially, the detection of retinal lesions in wellknown is vital for automated diagnosis of retinal ailment while the leakage detection is essential for therapy planning and remedy outcome monitoring. Current practical procedures for quantitative analysis of FA capabilities require large manual delineation by way of experienced graders. In eye and vision technological know-how studies the requirement for such intervention generally introduces human errors, and slows down the process, which makes it impractical to process the sizeable quantity of statistics accumulated at some point of recurring clinics. There is an growing call for for the automated detection of the leakage in FA.

In this paper we gift a brand new, unsupervised approach to stumble on and quantify leakage in FA images with the subsequent contributions. First, we advocate a novel green way to enhance leakage regions by using the usage of the concept of saliency [5].

Saliency indicates the relative importance of visible features, and is intently associated with the characteristics of human notion and processing of visual stimuli [5]–[7]. Saliency emerges from such traits in functions of the image as visible uniqueness, unpredictability, or rarity, and is regularly attributed to variations in specific picture attributes together

with color, gradient, edges, and boundaries [7]–[9]. Such attributes also are characteristics of retinal leakage in FA snap shots.

For example, leakage of fluorescent dye causes a huge increase in brightness in leaking areas while in comparison to surrounding non-leaking areas. For this utility, leaking areas may be defined as the ones of excessive saliency. In consequence, we are prompted to first of all identify the leaking regions in FA photographs through a saliency detection approach, after which estimate their regions from the received saliency map. Second, we've got proposed a new manner to generate multi-scale saliency maps with integration of the depth and compactness cues of high-quality pixels for this unique utility.

More particularly, traditional saliency extraction methods generally compute the saliency of an picture in a pixel-by way of-pixel manner, and ignore the neighborhood and side facts of the gadgets of hobby. Inspired through the reality that human vision is commonly greater worried with gadgets than with man or woman pixels and the gadgets of hobby might also vary in size, in this paper we firstly advise to use patches) at exclusive degrees to represent the given snap shots, and the effective simple linear iterative clustering (SLIC) technique [10] is hired for this assignment.

The reminder of this paper is based as follows. Section II in brief evaluations the related paintings on leakage detection and saliency detection. Section III details the proposed technique. Section IV describes the datasets and metrics for the evaluation of the proposed method. In Section V we first defined our experiments on distinctive datasets in contrast to those previous proposed methods and document the experimental effects. Section VI experimentally investigates the choice of saliency cues and the setting of a few hyper parameters used within the proposed method. Section VII concludes the paper.

## II. LITERATURE SURVEY

[1] **T. Y. P. Chui et al:** Recent advances to the adaptive optics scanning mild ophthalmoscope (AOSLO) have enabled finer in vivo evaluation of the human retinal microvasculature. AOSLO confocal reflectance imaging has been coupled with

oral fluorescein angiography (FA), permitting simultaneous acquisition of structural and perfusion pix. AOSLO offset pinhole (OP) imaging blended with movement evaluation submit-processing techniques, are capable of create a comparable set of structural and perfusion pix without using exogenous assessment agent. In this examine, we compare the similarities and variations of the structural and perfusion snap shots acquired via both approach, in healthful control topics and in sufferers with retinal vasculopathy along with hypertensive retinopathy, diabetic retinopathy, and retinal vein occlusion. Our outcomes display that AOSLO OP movement comparison provides perfusion maps corresponding to the ones acquired with AOSLO FA, even as AOSLO OP reflectance photos offer additional data which includes vessel wall best structure no longer as simply seen in AOSLO confocal reflectance snap shots. AOSLO OP gives a non-invasive opportunity to AOSLO FA without the need for any exogenous contrast agent.

[2] **N. Patton et al.:** The retinal and cerebral micro vasculatures percentage many morphological and physiological homes. Assessment of the cerebral microvasculature requires pretty specialized and expensive strategies. The capacity for the usage of non-invasive scientific evaluation of the retinal microvasculature as a marker of the kingdom of the cerebrovasculature gives clean benefits, attributable to the convenience with which the retinal vasculature can be immediately visualized in vivo and photographed due to its crucial -dimensional nature. The use of retinal virtual picture evaluation is turning into more and more common, and offers new strategies to analyze special components of retinal vascular topography, which include retinal vascular widths, geometrical attributes at vessel bifurcations and vessel monitoring. Being predominantly automatic and objective, these strategies provide an thrilling possibility to study the capability to become aware of retinal micro vascular abnormalities as markers of cerebrovascular pathology. In this assessment, we describe the anatomical and physiological homology between the retinal and cerebral micro vasculatures. We overview the proof that retinal micro vascular modifications occur in cerebrovascular sickness and assessment modern retinal image evaluation equipment which could

allow us to use one-of-a-kind components of the retinal microvasculature as capacity markers for the state of the cerebral microvasculature.

[3] **M. J. Potchen et al:** There had been few neuro-imaging studies of pediatric cerebral malaria (CM), a commonplace, regularly deadly tropical scenario. We undertook a capacity study of pediatric CM to higher signify the MRI abilities of this syndrome, evaluating findings in children assembly a stringent definition of CM to the ones in a manage organization who have been infected with malaria but who were in all likelihood to have a non-malarial cause of coma. Go to: Materials and Methods Consecutive kids admitted with traditionally described CM (parasitemia, coma and no different coma etiology glaring) had been eligible for this observe. The presence or absence of malaria retinopathy become decided. MRI findings in sufferers with retinopathy-high-quality (ret+) CM (cases) were in comparison to those with retinopathy-negative (ret-) CM (controls). Two radiologists blinded to retinopathy popularity mutually evolved a scoring procedure for picture interpretation and provided independent opinions. MRI findings had been in contrast among patients with and without retinopathy, to assess the specificity of modifications for patients with very strictly defined CM

### III. PROPOSED METHOD

The entire framework for detecting leakages in FA pix is summarized in Algorithm 1. It includes predominant steps: saliency detection and leakage detection. In the following subsections, each step can be particular.

#### A. Saliency Detection

‘Salient’ regions are those areas of a clinical photo that include meaningful information for diagnostic purposes. Typically, the intensities and/or shapes of those regions are extensively different from their surroundings or buddies [6], [23]–[26]. As shown in Fig. 1, the leaking regions in an FA picture are conspicuous items, and may easily be outstanding visually by using their intensity or shape. The depth based technique seems to be a natural desire for computational leakage area detection [11]. However, massive vessels and the optic disc may additionally be falsely detected as salient regions for comparable

motives in this application. Consequently, the vessel extraction and optic disc detection are critical on this framework: surely protecting them will help to enhance the accuracy of leakage detection. In this paper, for convenience we outline all the aforementioned regions that is probably assigned a excessive saliency value as the areas of interest (ROIs). After the complete process, the fake ones which include massive vessels and the optic disc can be removed even as only the leakage regions might be retained. In the following subsections, the super-pixel primarily based saliency detection approach might be certain.

#### 1) Super-pixel Segmentation:

A place-primarily based technique is properly set up in saliency measurement: as an example, Cheng et al. [8] have used a histogram-based contrast technique: the saliency price of each pixel relative to the others in the whole image is envisioned and then smoothed inside the color space, and similarly improved through partitioning the given image into regions and assigning saliency values to such regions via considering each their worldwide evaluation rating and neighborhood spatial coherence. This is a two-step technique and step one may also assign unique saliency values to similar colorings because of colour quantization. In our technique, amazing-pixels are hired to keep away from discontinuities at the bin edges of the histogram.

A cutting-edge awesome-pixel algorithm, called Simple Linear Iterative Clustering (SLIC) [10], is hired on this work to generate a desired wide variety n of everyday, compact brilliant-pixels to replace the inflexible shape of the pixel grid, at a low computation price, in which the default cost of 10 for the compactness time period is adopted. The SLIC is a k-approach clustering method, and is able to assign every pixel to a incredible-pixel in line with its depth and spatial location. The SLIC is capable of grouping meaningful entities right into a first-rate-pixel with the aid of assembling spatially neighboring pixels with comparable residences. It no longer most effective gives exceptional segmentation consequences, however additionally generates a suitable quantity of segments for leakage image

evaluation. Similar research the usage of unique technique has also been reviewed [27].

In this work, a multi-stage notable-pixel technique is proposed. The enter picture is segmented into L (L = 3) levels of high-quality-pixels independently, and the corresponding wide variety n of excellent-pixels is about to be 333, 666, and one thousand at every ranges, respectively. Fine tuning of the values for those parameters: L and n might be mentioned later in Section VI.

**2) Intensity-Based Saliency Detection:**

Let  $P_i \in I$  be a viable nearby representation as a notable-pixel  $i$  ( $i = 1, 2, \dots, n$ ), and let  $I$  indicate the input image. The splendid-pixels can be visible as samples of a multivariate possibility density characteristic (PDF) of the imaged items. A kernel density estimator (KDE) is selected, as, being non-parametric, it's going to permit the estimation of any PDF. The chance of a patch  $P_i$  may now be described as:

$$p(P_i) = \frac{1}{nh} \sum_{j=1}^n K\left(\frac{d(P_i, P_j)}{h}\right) \tag{1}$$

Where  $d$  is a distance function with the intention to be discussed later,  $K$  is a kernel, and  $h$  is a smoothing parameter. The KDE method has the potential to common out the contribution of every pattern  $P_i$  by means of spreading it over a sure location [28], that's described through  $K$ . The multivariate distribution can have a better probability if an exquisite-pixel is in dense and comparable regions. From our revel in, the most typically used and appropriate kernel is the Gaussian function with 0 mean and well known deviation  $\sigma$ . In this example, the probability of a exceptional-pixel  $p(P_i)$  can be defined as:

$$p(P_i) = \frac{1}{n\sigma} \sum_{j=1}^n \exp\left(-\frac{d^2(P_i, P_j)}{2\sigma^2}\right) \tag{2}$$

The estimated possibilities  $p(P_i)$  may be normalized to end up a real PDF  $H(P_i)$  by using putting a proper consistent.  $\sigma = 0.2$  is chosen to alternative for  $h$ . The relative distance  $d$  is utilized in case the distribution of the exquisite-pixels is not uniform, and the space metric mainly makes a speciality of the relationships

among comparable outstanding-pixels. The relative common distinction of a couple of top notch-pixels  $P_i, P_j \in W$  in depth is described as

$$d(P_i, P_j) = \frac{|a(P_i) - a(P_j)|}{ave_{p_k \in W} (|a(P_i) - a(P_j)|)} \tag{3}$$

Wherein  $W = P_1, P_2, \dots, P_n$  and  $[ave]_{(p \in W)}$  (average distinction between the common depth  $a(P_i)$  of pixels interior  $P_i$  and people  $a(P_k)$  of other super-pixels  $P_k$  in  $W$ . Compared to absolutely the difference, the relative difference is extra constant for two units of pixels with similar neighboring relationships but unique resolutions and scales [29].

After determining the possibilities of the exquisite-pixels, the dissimilarity degree  $dis_I(P_i, P_j)$  among  $P_i$  and  $P_j$  is described as:

$$dis_I(P_i, P_j) = \frac{(H(P_i) - H(P_j))^2}{H(P_i) + H(P_j)} \tag{4}$$

The large the relative difference of a superb-pixel from every other, the much less the similar they're, and the extra dissimilar it's far.

The distinctness value of every exceptional-pixel can be predicted the use of the dissimilarity measurement above. Super-pixel  $P_i$  is considered salient whilst it's miles exceptionally distinct to different extraordinary-pixels. The saliency fee of  $P_i$  is described as:

$$S_i(P_i) = 1 - \exp\left(-\frac{1}{n-1} \sum_{j=1, j \neq i}^n dis_I(P_i, P_j)\right) \tag{5}$$

However, with a view to lessen computational complexity, we notice that it is unnecessary to assess the individuality of a high-quality-pixel by using computing its dissimilarity to all the others. For example, if the most comparable high-quality-pixels  $P_j$  are notably special from super-pixel  $P_i$ , then it follows logically that all the opposite fantastic-pixels are also quite one of a kind from amazing-pixel  $P_i$ . Therefore, for superb-pixel  $P_i$ , most effective the  $M$  maximum comparable terrific-pixels  $Q_m$   $M=1$  ( $M =$

10 in this paper) want to be located and processed. Hence, the saliency value of superb-pixel  $P_i$  can be rewritten as:

$$S_I(P_i) = 1 - \exp\left(-\frac{1}{M} \sum_{m=1}^M \text{dis}_I(P_i, Q_m)\right) \quad (6)$$

The final depth-primarily based saliency is received by means of fusing the saliency maps  $S_I$  ( $P_i$ ) of various excellent-pixels  $P_i$  at extraordinary tiers  $I$ . More especially, all of the pixels  $u$  within a superpixel will have the equal value at every level (the identical for fusing the compactness based saliency maps over all the ranges). The fusion is achieved pixel through  $\in$   $P_i$ ).

### 3) Compactness-Based Saliency Detection:

Intuitively, the leakage area in an FA photo will gift different intensity data when compared with the others. However, it's far found in practice that the usage of the intensity feature by myself to stumble on salient areas is not usually successful. For instance, the purple rectangle vicinity of the top row of Fig. 2 (c) shows that non-vessel areas within the middle of the photo with excessive brightness due to choppy illumination have also been detected as quite salient, while a human observer perceives best The leakage regions and vessels as greater salient. Therefore, this section proposes some other feature - compactness. Normally, human observers pay more interest to a extra compact object than to a greater diffuse object. The measure of compactness of an object may consequently be of use as a complementary feature to intensity for saliency measurement, with the purpose of lowering the variety of falsely-detected salient areas. For brilliant-pixel  $P_i$ , its compactness  $c(P_i)$  is described as

$$c(P_i) = \exp\left(-\alpha \frac{\sigma_{x,i} + \sigma_{y,i}}{\sqrt{X^2 + Y^2}}\right) \quad (7)$$

Wherein  $\sigma_{x,i}$  and  $\sigma_{y,i}$  are the same old deviations of the  $x$  and  $y$  coordinates of the pixels in the superpixel  $P_i$ , and  $\alpha$  is a consistent factor this is empirically set to  $X$  and  $Y$  are the width and peak of the enter photo. By incorporating the compactness function with the depth characteristic of a given image, the degree

$\text{dis}_C(P_i, P_j)$  of dissimilarity in compactness among  $P_i$  and  $P_j$  is defined as:

$$\begin{aligned} \text{dis}_C(P_i, P_j) &= |a(P_i) - a(P_j)| \\ &\times \left(1 + \frac{c(P_i) - c(P_j)}{2}\right) \\ &\times \exp\left(-\frac{\beta d(P_i, P_j)}{\sqrt{X^2 + Y^2}}\right) \end{aligned} \quad (8)$$

Where time period difference of the common depth ( $a$ ) characteristic of super-pixels  $P_i$  and  $P_j$ .  $D(P_i, P_j)$  is the relative common difference among super-pixels  $P_i$  and  $P_j$ , as proposed in Eq. (3). The steady component  $\beta$  is empirically set to three hundred. The large the dis-similarity  $\text{dis}_C(P_i, P_j)$ , the higher the opportunity that human interest might be paid from super pixel  $P_j$  to  $P_i$ . Hence, the following policies in TABLE I can be used to help in estimating the saliency cost  $S_C(P_i)$  of super-pixel  $P_i$ .

Similar to Eq. (6), the compactness-based totally saliency cost  $S_C(P_i)$  of  $P_i$  is described as

$$S_C(P_i) = 1 - \exp\left(-\frac{1}{M} \sum_{m=1}^M \text{dis}_C(P_i, R_m)\right) \quad (9)$$

Where  $R_m$  ( $m = 1, 2, \dots, M$ ) is the  $M$  most comparable superpixels to  $P_i$  in the sense of compactness. Again, we calculate the very last compactness-primarily based saliency primarily based at the imply value of the saliency maps  $S_C(P_i)$  of various super-pixels  $P_i$  at one-of-a-kind tiers  $I$ , and the fusion is executed pixel by means of pixel as nicely  $u \in P_i$ )

### 4) Saliency Map Fusion:

Two bottom-up tactics in our proposed super-pixel based saliency detection approach have been defined so far. It is possibly that each of them has its personal drawbacks if used by myself in real applications. Therefore, an overall saliency map through fusing the saliency maps based totally on depth and compactness is anticipated to offer better overall performance. Linear summation [5] or pixel-clever multiplication (additionally referred to as the matrix Hadamard product) [30] are generally used

techniques to fuse the Saliency maps. In this work, the depth and compactness saliency maps are fused with the useful resource of using the pixel-clever multiplication method if you want to force first-class the areas with higher values in each intensity and compactness channels to be assigned better values inside the final saliency map  $S$ . By integrating the two saliency measures, the belongings of human vision through which attention declines as the brink of the region of hobby is approached may be mimicked. That is, the final saliency map highlights salient object regions of hobby and suppresses historical past regions, as illustrated in Fig. 2 (d).

### B. Graph Cut for Leakage Detection

The proposed super-pixel primarily based saliency detection method has effectively stronger the comparison between vessels/ leakages and history. Some example results are shown in Fig. Three (b). The appearances of these leakages are highlighted, at the same time as the history regions are suppressed, while in comparison to the unique photos. Once the saliency map is computed and normalized to  $[0, 1]$ , a threshold cost  $T = \text{zero}$ . Sixty five is carried out to the saliency map to gain the ROIs. The thresholding method itself cannot assure the bounds of the segmented structures are clean and often generates isolated fragments. In light of this inadequacy, greater state-of-the-art segmentation techniques [31]–[36] may be needed for better effects. On the opposite hand, the computational cost is likewise an crucial component for a segmentation tool to be taken into account for potential actual applications. For those two motives, we endorse right here a graph cut primarily based segmentation approach [33], [34] on the obtained ROIs to become aware of the leakage. This method imposes the constraint that the neighboring pixels generally tend to belong to the same elegance and therefore penalizes the remote pixels in one of a kind instructions.

Let  $N$  be a set of edges  $(u, v)$  wherein a pixel  $u$  is attached to its 8 nearest neighbors  $v$ , and  $M$  denote the set of pixels inside the given photograph  $I$ , the discrete power function is described as:  $E(x) = \sum_{u \in M} E_u(x_u) + \sum_{(u,v) \in N} E_{uv}(x_u, x_v)$  (10)

Where  $x = \{x_1, \dots, x_N\}$  is the binary labeling where the  $x_u$  is either 0 or 1 depending on whether the pixel  $u$  belongs to the background or foreground. The first term here approximates the region terms while the second term approximates the regularization term. The unary term  $E_u$  is defined as:

$$E_u^0(x_u) = \lambda_1(I_u - c_1)^2, E_u^1(x_u) = \lambda_2(I_u - c_2)^2 \quad (11)$$

Where  $E_u^0, E_u^1$  Denote the weights between the node  $u$  and the 2 terminals,  $\lambda_1$  and  $\lambda_2$  are the non-bad location weighting parameters,  $I_u$  is the depth of the pixel  $u$ , and  $c_1$  and  $c_2$  indicate the common intensities of the historical past and foreground respectively. The binary time period  $E_{uv}$  is described as:

$$E_{uv}(x_u, x_v) = \begin{cases} \mu\omega_{uv}, & \text{if } x_u \neq x_v \\ 0, & \text{otherwise} \end{cases} \quad (12)$$

Where  $\omega_{uv}$  denotes the weight between neighboring pixels  $u$  and  $v$ , as suggested in [37]:

$$\omega_{uv} = \frac{\delta^2 \cdot \Delta\phi_{uv}}{2 \cdot |e_{uv}|} \quad (13)$$

Where  $\delta$  is the cell-size is the Euclidean period of the edge  $e_{uv}$ , and  $\phi_{uv}$  is the distinction between the angular orientations  $\phi_u$  and  $\phi_v$  of the pixels  $u$  and  $v$  and is constrained to the c program language period  $[0, \pi]$ . In this paintings, we set  $\lambda_1 = \lambda_2 = \lambda = \text{zero}$ . Five (see Section VI for the parameter tuning), and  $\mu$  is empirically set as 0.2. C. Final Refinement After the graph cut segmentation, a few vessels, the optic disc and some small items can also nonetheless stay as they may additionally had been superior during the saliency detection steps. It is important to take away them so that you can enhance the leakage detection overall performance. To this end, the following steps are carried out: (i) the countless perimeter active contour with hybrid vicinity (IPACHR) technique [38] is used to segment retinal vessels for its suitable overall performance. In short, this technique makes use of a countless perimeter active contour version for its effectiveness in detecting items (e.g. Vessels) with abnormal and oscillatory obstacles.

Moreover, this method considers hybrid region records (nearby phase based vesselness map and

intensity) in a photo on the way to attain similarly improved overall performance as compared to the same old limitless perimeter lively contour model [38]. For extra details, we refer readers to the authentic paper [38]. (ii) Any small and/or remote objects are eliminated via the use of a disk-fashioned establishing operation with a radius of 2 pixels. (iii) In maximum instances, the optic disc stays as leakage regions after the graph reduce primarily based segmentation and have to be removed. It has been nicely found that the wide variety of vessels surrounding the optic disc is a lot large than that near massive focal leaking websites [11], [39]. Thus, any region with some of surrounding vessels more than a threshold of 5 will be assumed to be the optic disc, and will be eliminated. In our experiments this technique is determined to be green and powerful. However, other sophisticated strategies may go equally nicely.

#### IV. RESULTS

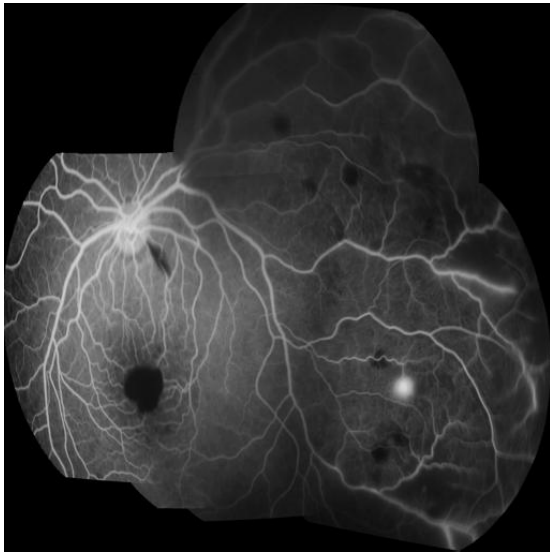


Fig.1 input image

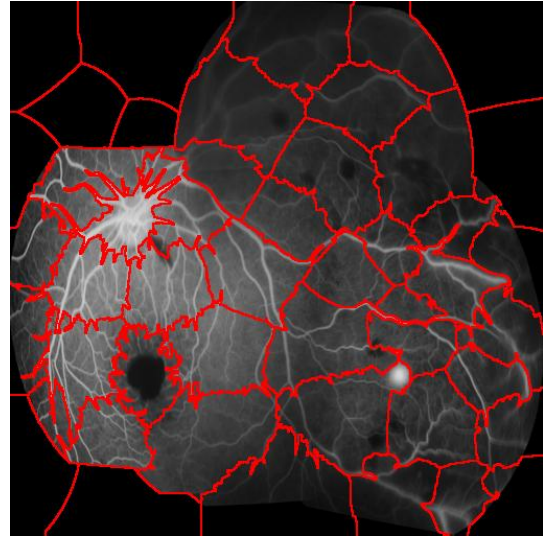


Fig.2 super pixels image

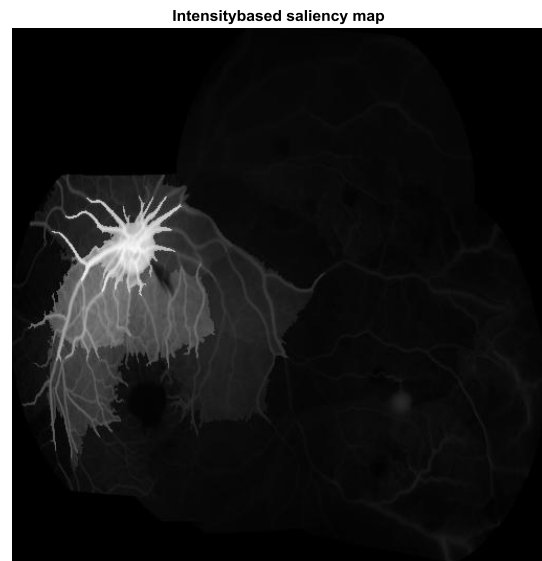


Fig.3 intensity based saliency map

Compactness saliency map

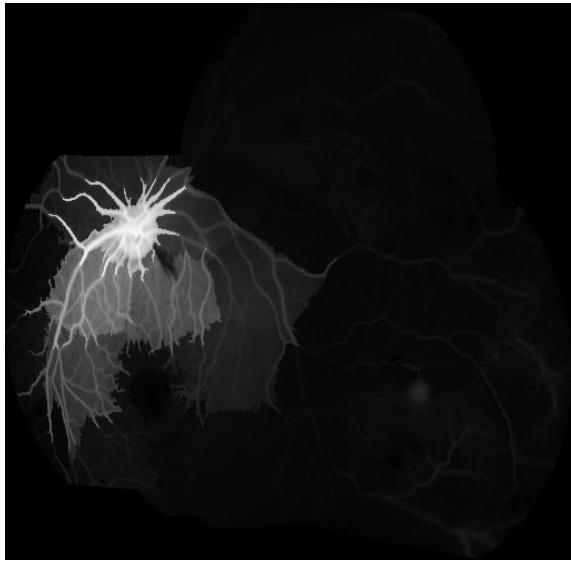


Fig.4 compactness saliency map

outPutof Graph Cut



Fig.6 output of graph cut method

Fusion saliency map



Fig.5 fusion saliency map

Final segmented output

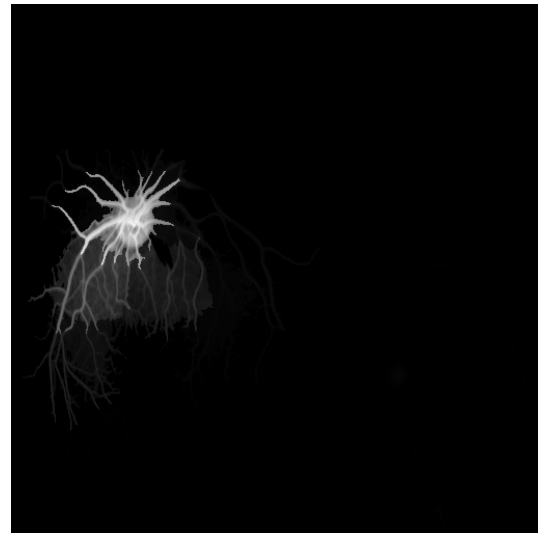


Fig.7 final segmented output

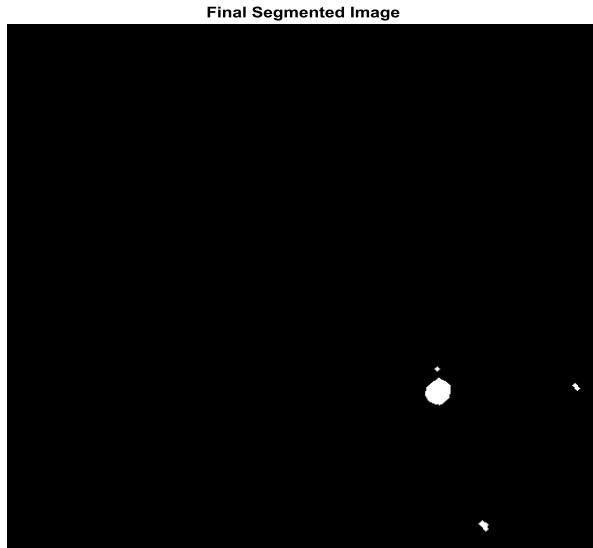


Fig.8 Final Segmented Image

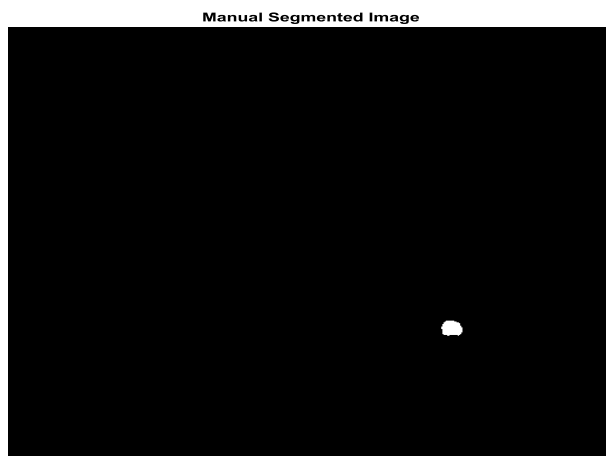


Fig.9 Manual Segmented Image

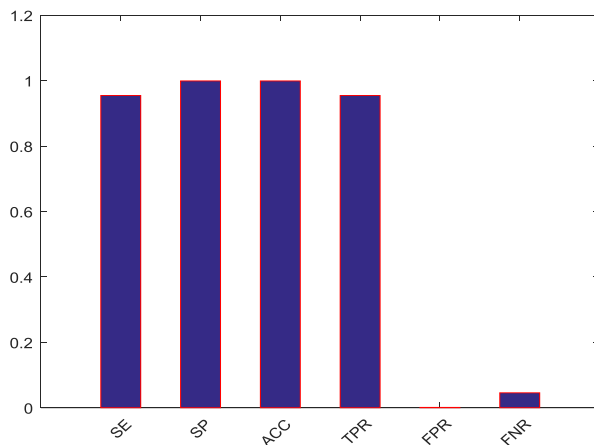


Fig.10 Bar Graphs of SE, SP, ACC, TPR, FPR, FNR.

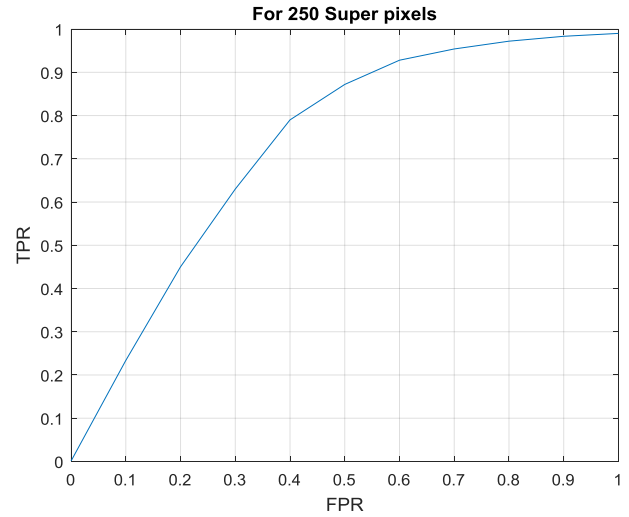


Fig.11 False Positive Rate vs. True Positive Rate

### V. CONCLUSION

In this paper we proposed two-level saliency detection method for the detection of retina leakages in the retina. The saliency maps are intensity and compactness features by using the super pixels. The super pixel saliency values are finding out by using these two methods. The intensity cue will check the contrast in between the super-pixels and the compactness will check how sparsely the salient pixels distributed in a super pixel. By using the pixel-wise multiplication operator the different level saliency map at same cue are combined. Based on the MR and DR Datasets the experimental results are performed. Comparing to the conventional methods the saliency maps are giving the best results because here we are finding the leaking regions and also we are able to find the size of that regions.

### REFERENCES

[1] G. Richard, G. Soubrane, and L. Yanuzzi, Fluorescein and Icg Angiography: Textbook and Atlas, 2nd ed. New York: Thieme, 1998.

[2] T. Y. P. Chui et al., “Comparison of adaptive optics scanning mild ophthalmoscopic fluorescein angiography and offset pinhole imaging,” Biomed. Opt. Exp., vol. Five, no. Four, pp. 1173–1189, 2014.

[3] N. Patton et al., “Retinal vascular photograph assessment as a capacity screening tool for

cerebrovascular sickness: A rationale primarily based mostly on homology among cerebral and retinal microvasculatures,” *J. Anatomy*, vol. 206, no. Four, pp. 319–348, 2005.

[4] M. J. Potchen et al., “Acute mind MRI findings in 100 and twenty Malawian youngsters with cerebral malaria: New insights into an historical sickness,” *Am. J. Neuroradiol.*, vol. 33, no. Nine, pp. 1740–1746, 2012.

[5] L. Itti, C. Koch, and E. Niebur, “A version of saliency-based totally visible interest for rapid scene evaluation,” *IEEE Trans. Pattern Anal. Mach. Intell.*, vol. 20, no. 11, pp. 1254–1259, Nov. 1998.

[6] R. Achanta, S. Hemami, F. Estrada, and S. Susstrunk, “Frequencytuned salient location detection,” in *Proc. IEEE CVPR*, Jun. 2009, pp. 1597–1604.

[7] C. Koch and C. Ullman, “Shifts in selective visual attention: Towards the underlying neural circuitry,” *Human Neurbiol.*, vol. 4, no. Four, pp. 219–227, 1985.

[8] M.-M. Cheng, G.-X. Zhang, N. J. Mitra, X. Huang, and S.-M. Hu, “Global comparison based salient area detection,” in *Proc. IEEE CVPR*, Jun. 2011, pp. 409–416.

[9] X. Chen, H. Zhao, P. Liu, B. Zhou, and W. Ren, “Automatic salient object detection through most entropy estimation,” *Opt. Lett.*, vol. 38, no. 10, pp. 1727–1729, 2013.

[10] R. Achanta et al., “SLIC superpixels in evaluation to fashionable day superpixel techniques,” *IEEE Trans. Pattern Anal. Mach. Intell.*, vol. 34, no. Eleven, pp. 2274–2282, Nov. 2012.

# Brain Tumor Edge Detection Based on GWT & DWT Fusioning

C.Padma<sup>1</sup> Dr.S.Nagaraja Rao<sup>2</sup>

<sup>1</sup>P.G. Scholar <sup>2</sup>M.Tech., Ph.D, MISTE, MISOI, Professor

<sup>1,2</sup>Department of Electronics & Communication Engineering

<sup>1,2</sup>G.Pulla Reddy Engineering College (Autonomous), Kurnool, A.P., India

*Abstract*— Brain tumor Edge detection plays a vital role in medical image processing. Edge of the image is one of the most significant features which is mainly used for image analyzing process. An edge is in general a border which separates the adjacent zones of image having distinct brightness. The development of an edge detector is often based on a specific characteristic of the image. An important property of the edge detection method is its ability to extract the accurate edge line with good orientation, and much literature on edge detection has been published in the past three decades. It is encountered in the areas of feature selection and feature extraction in Computer Vision. An edge detector accepts a digital image as input and produces an edge map as output. The edge maps of some detectors include explicit information about the position and strength of the edges and their orientation. An efficient algorithm for extracting the edge features of images using Gabor Wavelet and fusion technique is proposed in this work. Gabor wavelets can effectively abstract local and discrimination features. In textural analysis and image segmentation, GW features have achieved outstanding results, while in machine vision, they found to be effective in object detection, recognition and tracking. The most useful application of the Gabor Wavelets is for edge detection. Gabor wavelet along with DWT and fusion based approach is highly effective at detecting both the brain tumor location and orientation of edges. The results proved that the performance of proposed method is superior to conventional Gabor Wavelet and other edge detection algorithms. The performance of the proposed method is proved with the help of Entropy, PSNR & spectral analysis is also computed for proposed method edge detected output image, gabor wavelet edge detected output image, original input MRI brain image.

**Key words:** Digital Image Processing, Edge detection, GWT, DWT, Fusion

## I. INTRODUCTION

Bjoern H. Menze, et.al [1] proposed Multimodal Brain Tumor Image Segmentation Benchmark (BRATS) organized in conjunction with the MICCAI 2012 and 2013 conferences. They found that different algorithms worked best for different sub-regions (reaching performance comparable to human inter-rater variability), but that no single algorithm ranked in the top for all sub-regions simultaneously. Fusing several all good algorithms using a hierarchical majority vote yielded segmentations that consistently got ranked above all individual algorithms, indicating remaining opportunities for further methodological improvements. The BRATS image data available and found through an online evaluation system as an ongoing benchmarking resource. Evaluating the accuracy of automated routines in longitudinal settings including both pre- and postoperative images are important directions for

future work along with further algorithmic developments. Finally they concluded, by using BRATS they generated the largest public dataset available for this task and they evaluated a large number of state-of-the-art brain tumor segmentation methods

### A. Brain Tumor

Brain tumors are created by abnormal and uncontrolled cell division in brain itself. Identification of tumor involves tests like CT and MRI. MRI plays an efficient role in identifying location, size and type of brain tumor. This makes this technique a very special one for the brain tumor detection. A brain tumor is known an uncontrolled growth of solid mass formed by the undesired cells either normally found in the different part of the brain such as glial cells, neurons, lymphatic tissue, blood vessels, pituitary and pineal gland, skull, or spread cancers mainly located in other organs. Brain tumors are divided based on the type of tissue involved in the brain, the positioning of the tumor in the brain, whether it is benign tumor or malignant tumor and other different considerations. Brain tumors are occurred at the solid portion that permeate the surrounding tissues or distort the surrounding structures. There are different types of brain tumors

- 1) Pre-Malignant Tumor
- 2) Malignant Tumor

### B. Problem Statement

Edge detection is used to characterize the intensity changes in the image in terms of the physical processes that have originated them. An intermediate target of edge detection is the detection and characterization of significant intensity changes. This work discusses this part of the edge detection problem. To characterize the types of intensity changes derivatives of different types, and possibly different scales, are needed. Basically Edge detection consists of two steps, a filtering step and a differentiation step. Gradient based edge detectors have no smoothing filter, and they are only based on a discrete differential operator. The main drawbacks of zero crossing based operators are responding to some of the existing edges and very sensitive to noise. The problem with canny operator is that these two thresholds are not easily determined and low threshold produces false edges, but a high threshold misses important edges.

### C. Scope of Work

In this work, an image is decomposed into sub bands using discrete wavelet transform. Thereafter we are applying Gabor wavelet transform is applied LL (Approximate band) of DWT decomposed image. Then we are fusing this Gabor wavelet transformed image with HH (Diagonal Band) of DWT decomposed image. The results of proposed method are better than that of the Gabor wavelet transform method. From proposed method the exact size and shape of tumor

can be identified efficiently. Spectral analysis is computed for proposed method output.

## II. PROPOSED METHOD

### A. Edge Detection

An edge is in general a border which separates the adjacent zones of image having distinct brightness. The development of an edge detector is often based on a specific characteristic of the image. One of the property of the edge detection method is its ability to extract accurate edge lines with good orientation. An edge detector accepts a digital image as input and produces an edge map as output. The edge maps of some detectors include explicit information about the position and strength of the edges and their orientation. we are using gradient based image edge detection in our proposed method.

### B. Wavelet Approach

Wavelet transforms are classified into discrete wavelet transforms (DWTs) and continuous wavelet transforms (CWTs). The Discrete Wavelet Transform (DWT) has been a successful technique used in edge detection. The 2-D discrete wavelet transform decomposes the image into sub-images, 3 details and 1 approximation. The approximation looks just like the original; only on 1/4 the scale. The 2-D DWT is an application of the 1-D DWT in both the horizontal and the vertical directions. DWT separates image into low pass filter and high pass filter and again low & high pass filter divides into a lower resolution approximation image (LL) as well as horizontal (HL), vertical (LH) and diagonal (HH) detail components. DWT is used for edge detection.

### C. Edge Detection Using Conventional Gabor Wavelet

Gabor wavelets can effectively abstract local and discrimination features. In textural analysis and image segmentation, GW features have achieved outstanding results, while in machine vision, they found to be effective in object detection, recognition and tracking. The most useful application of the Gabor Wavelets is for edge detection. For given an input image  $I(x, y)$ , the Gabor Wavelet features are extracted by convolving  $I(x, y)$  with  $G(x, y)$  as in equation

$$\Phi(x, y) = G(x, y) \otimes I(x, y) \quad (1)$$

Where  $\otimes$  denotes the 2-D convolution operation. The Gabor wavelets (GWs) respond strongly to edge if the edge direction is perpendicular to the wave vector  $(\omega \cos \theta, \omega \sin \theta)$ . When hitting an edge, the real and imaginary parts of  $\Phi(x, y)$  oscillate with the characteristic frequency instead of providing a smooth peak.

### D. Discrete Wavelet Transform

DWT can be implemented by filtering operations with well-defined filter coefficients. In order to compute forward DWT, the input signal (x) is filtered separately by a low-pass filter (h~) and a high pass filter (g~). The two output streams are sub-sampled again by simply dropping the alternate output samples in each stream to produce the low-pass (yL) and high-pass (yH) sub band outputs as shown in Fig2. The original signal can be reconstructed by a synthesis filter bank (h, g) starting from yL and yH. The two filters (h~, g~) constitutes the analysis filter bank.. Given a discrete

signal  $x(n)$ , the output signals  $yL(n)$  and  $yH(n)$  can be computed as

$$y_L(n) = \sum_{i=0}^{\tau L-1} h(i) * x(2n - i),$$

$$y_H(n) = \sum_{i=0}^{\tau H-1} g(i) * x(2n - i) \quad (2)$$

Where  $\tau L$  and  $\tau H$  are the lengths of the low-pass (h~) and high-pass (g~) filters respectively. For inverse transform, both  $yL$  and  $yH$  are first up-sampled by inserting zeros in between two samples and then filtered by low-pass (h) and high-pass (g) filters respectively. Then they are added to obtain the signal (x').

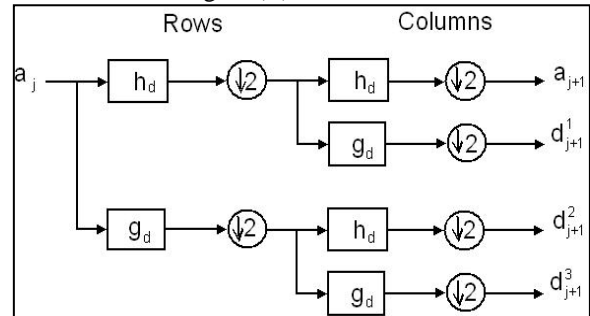


Fig. 1: One-level 2D DWT decomposition scheme

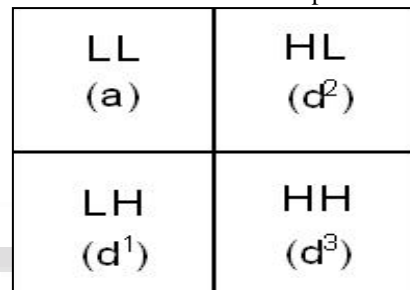


Fig. 2: 2D DWT coefficients' image

For multi-resolution wavelet decomposition, the low-pass sub band (yL) is further decomposed in a similar fashion in order to get the second-level of decomposition, and the process is repeated. The inverse process follows similar multi-level synthesis filtering to reconstruct the signal. Image signals are two-dimensional signals. In order to increase the quality of the low resolution image, preserving the edges is essential. Therefore, DWT and SWT have been employed in order to preserve the high frequency components of the image. In this correspondence, one level DWT is used to decompose an input image into different sub band images.

### E. Image Fusion

The term Fusion means in general an approach to extraction of information acquired in several domains. Most recently, with the evolution of wavelet based multi resolution analysis concepts, the multi-scale wavelet decomposition has begun to take the place of pyramid decomposition for image fusion. Actually, the wavelet transform can be considered one special type of pyramid decompositions. It retains most of the advantages for image fusion but has much more complete theoretical support. The real Discrete Wavelet Transform (DWT) has the property of good compression of signal energy. Perfect reconstruction is possible using short support filters. The unique feature of DWT is the absence of redundancy and very low computation. Therefore, DWT has been used extensively for Multi Resolution Analysis (MRA) based image fusion

### F. Proposed Block Diagram

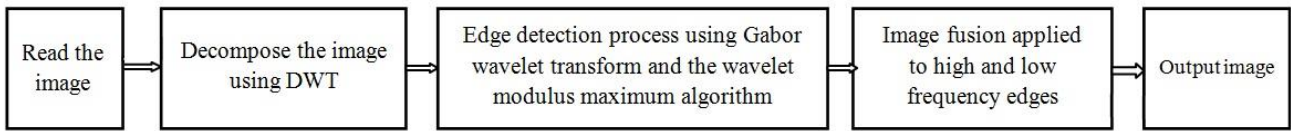


Fig. 3: Proposed block diagram

### G. Algorithm

- 1) Take any color or gray scale image as input image
- 2) If it is color image convert into gray scale image
- 3) Now apply Discrete Wavelet Transform to the input image
- 4) The resultant image will be decomposed into 4 sub bands
- 5) Apply Gabor wavelet to the LL band
- 6) Now fuse resultant image with HH band
- 7) Tumor size and shape can be identified efficiently, Tumor part can be detected.

### H. Spectral Analysis

Fourier Transform is used to decompose an image into its sine and cosine components. The output of the transformation represents the image in the Fourier or frequency domain, while the input image is the spatial domain equivalent. In a wide range of applications Fourier transform is used, such as image analysis, image filtering, image reconstruction and image compression. As we are using only digital images, we will restrict this discussion to the Discrete Fourier Transform (DFT).

The DFT contains only a set of samples which is large enough to fully describe the spatial domain image. The number of frequencies corresponds to the number of pixels in the spatial domain image, i.e. the image in the spatial and Fourier domain is of the same size.

For a square image of size  $N \times M$ , the two-dimensional DFT is given by:

$$F(k,l) = \sum_{i=0}^{n-1} \sum_{j=0}^{m-1} f(i,j) e^{-i2\pi(\frac{ki}{n} + \frac{lj}{m})} \quad (3)$$

where  $f(a,b)$  is represented the image in the spatial domain and the exponential term is the basis function corresponding to each point  $F(k,l)$  in the Fourier space. The equation can specifies as the value of each point  $F(k,l)$  is obtained by multiplying the spatial image with the corresponding base function and summing the result. The basic functions are cosine and sin waves with increasing frequencies, DC-component of the image represents  $F(0,0)$  the which corresponds to the average brightness and  $F(N-1,M-1)$  represents the highest frequency.

In a similar way, the Fourier image can be re-transformed to the spatial domain. The inverse Fourier transform is given by:

$$f(a,b) = \frac{1}{N^2} \sum_{k=0}^{N-1} \sum_{l=0}^{M-1} F(k,l) e^{i2\pi(\frac{ka}{n} + \frac{lb}{m})} \quad (4)$$

Note the  $\frac{1}{N^2}$  normalization term in the inverse transformation. This normalization is sometimes applied to the forward transform instead of the inverse transform, but it should not be used for both.

To obtain the result for the above equations, a for each image point double sum has to be calculated. However, because the Fourier Transform is separable, it can be written as

$$F(k,l) = \frac{1}{N} \sum_{a=0}^{N-1} P(k,b) e^{-i2\pi ib/N} \quad (5)$$

Where

$$P(k,b) = \frac{1}{N} \sum_{a=0}^{N-1} f(a,b) e^{-i2\pi ka/N} \quad (6)$$

Even with these computational savings, the ordinary one-dimensional DFT has  $N^2$  complexity. The Fast Fourier Transform (FFT) reduced to  $N \log_2 N$  to compute the one-dimensional DFTs. This is a significant improvement, in particular for large images. There are various forms of the. The mathematical details are well described in the literature. The Fourier Transform produces a complex number valued output image which can be displayed with two images, either with the real and imaginary part or with magnitude and phase.

### I. Advantages

- 1) Gabor filter for edge detection is based on frequency and orientation representations. .
- 2) 2D Gabor filter is a Gaussian kernel function modulated by a sinusoidal plane wave.
- 3) They can be designed for a number of dilations and rotations.
- 4) In general, the expansion is not applied for Gabor wavelets.
- 5) It is well suited for a specific spatial location in distinctive between the objects of an image.
- 6) The main important activations can be extracted from the Gabor space in order to create a sparse object representation.
- 7) Gabor wavelets are used for “feature extractions.

### J. Applications

- 1) Satellite image analysis
- 2) Smoothing and image de-noising
- 3) Fingerprint verification
- 4) Biology for cell membrane recognition, to distinguish the normal from the pathological membranes
- 5) DNA analysis, protein analysis
- 6) Industrial supervision of gear-wheel
- 7) Computer graphics and multi-fractal analysis

## III. RESULTS

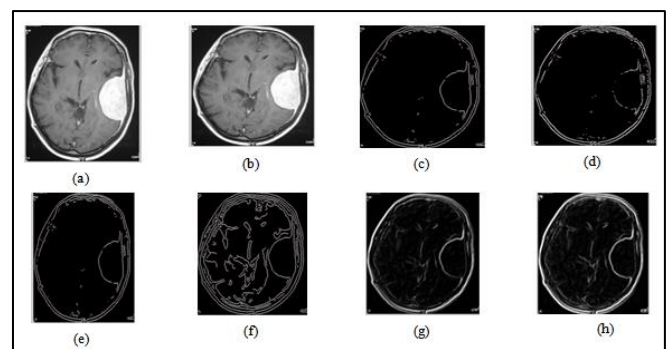


Fig.No.4: (a) Original image, (b) Grayscale image, (c) Prewitt image, (d) Robert image, (e) Sobel image, (f) canny image, (g) Gabor image, (h) Proposed method image

A. Performance Measures

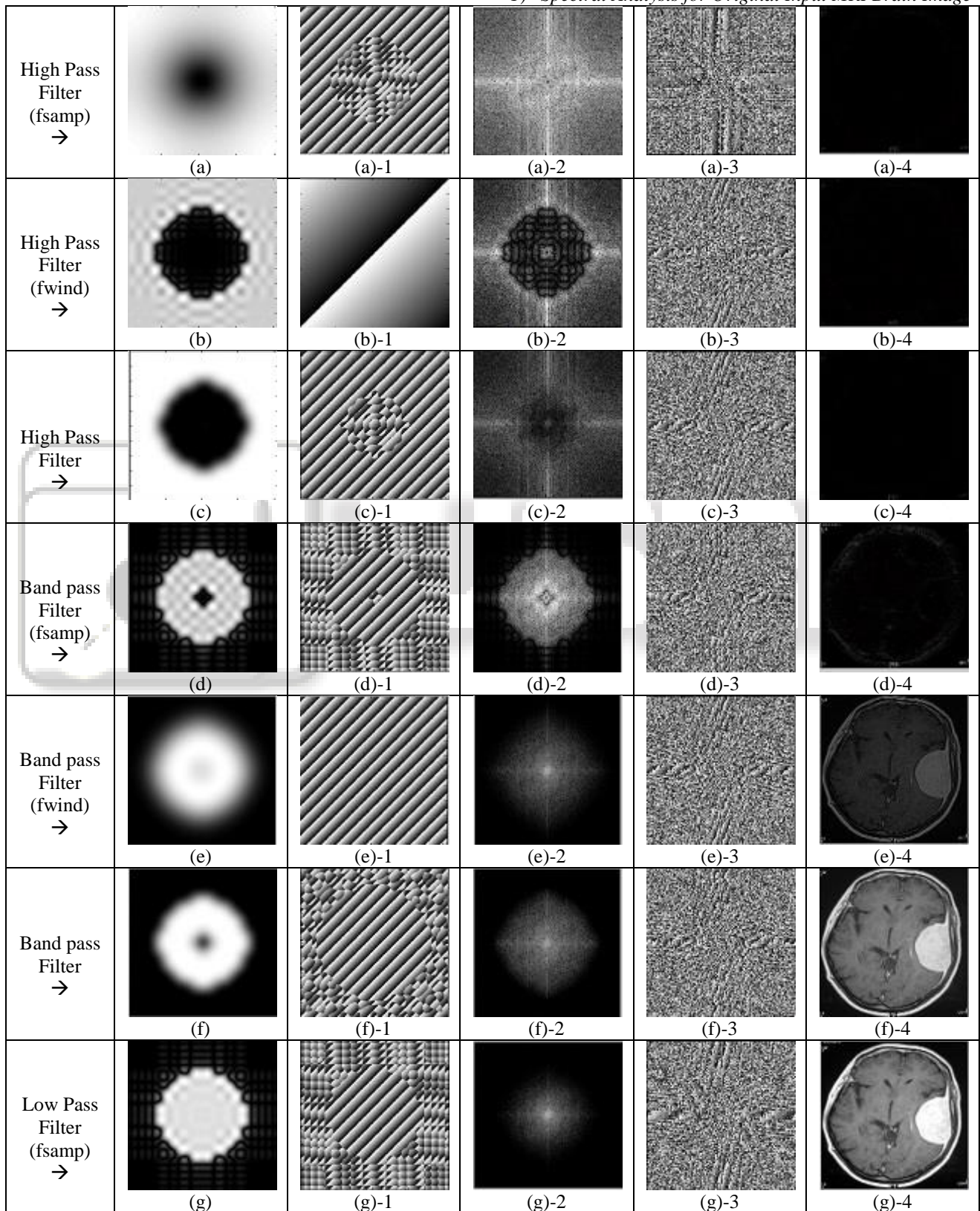
ALGORITHM	ENTROPY OF BRAIN IMAGE
CANNY	1.7328
PREWITT	1.6706
ROBERT	1.6810
SOBEL	1.6704

GABOR WAVELET	3.0979
PROPOSED METHOD	3.5766

Table 1: Entropy of brain image  
PSNR PERFORMANCE=22.07 DB

B. Results of Spectral Analysis:-

1) Spectral Analysis for Original Input MRI Brain Image



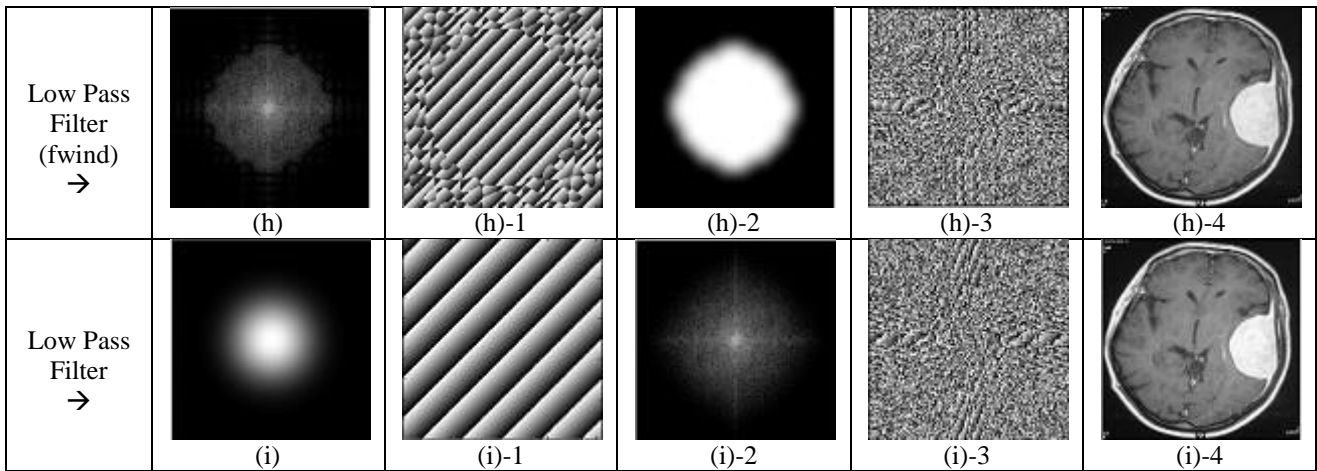
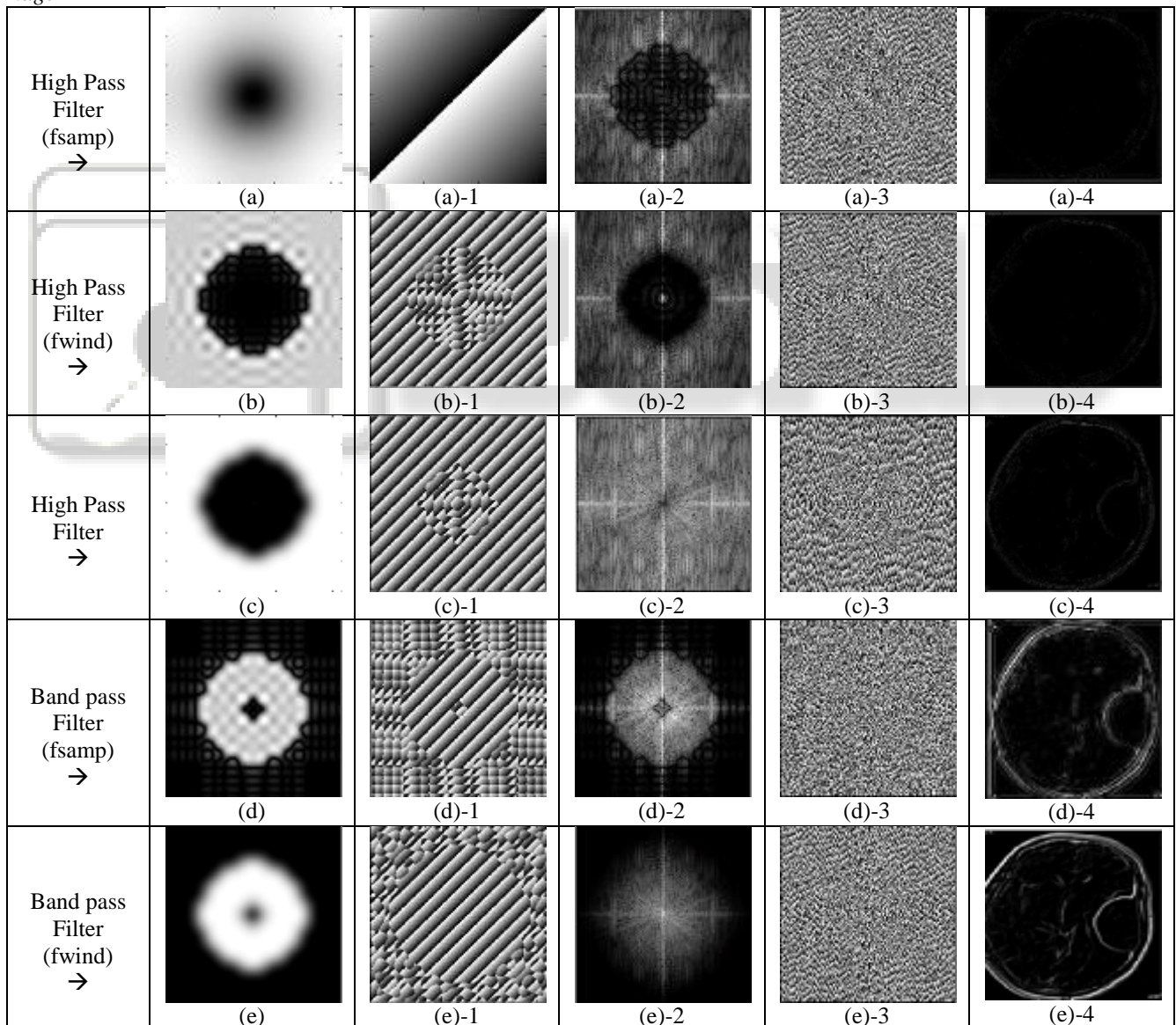


Fig. 5: (a),(b),(c),(d),(e),(f),(g),(h) and (i) :-Magnitude Images, (a)-1,(b)-1,(c)-1,(d)-1,(e)-1,(f) 1,(g)-1,(h)-1 and (i)-1 :-Phase Images, (a)-2,(b)-2,(c)-2,(d)-2,(e)-2,(f)-2,(g)-2,(h)-2 and (i)-2 : Log Magnitude Images, (a)-3,(b)-3,(c)-3,(d)-3,(e)-3,(f)-3,(g)-3,(h)-3 and (i)-3 :-Phase Images, (a)-4,(b)-4,(c)-4,(d)-4,(e)-4,(f)-4,(g)-4,(h)-4 and (i)-4 :-Inverse FFT Images

2) Spectral Analysis for Gabor wavelet Edge Detected Image



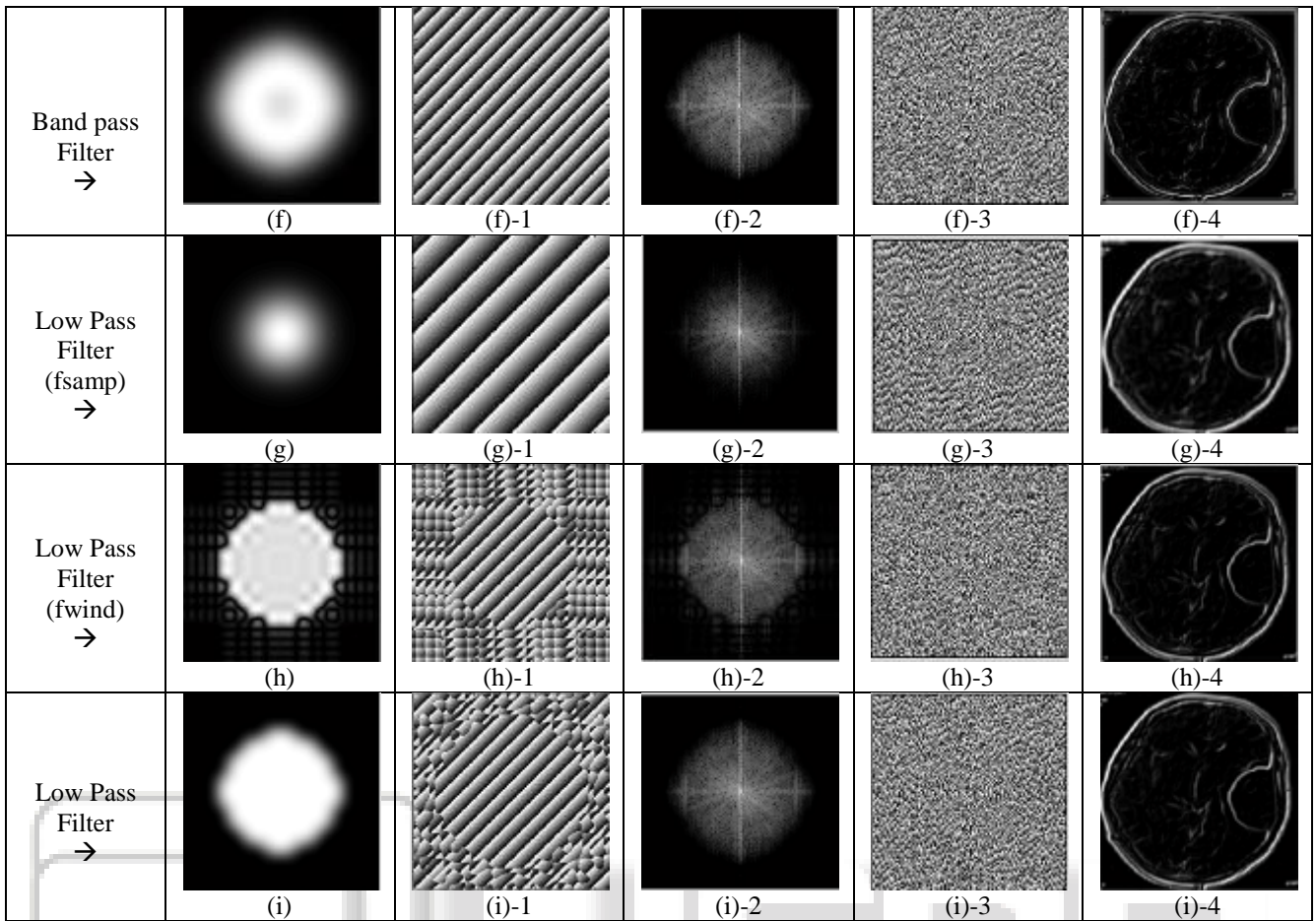
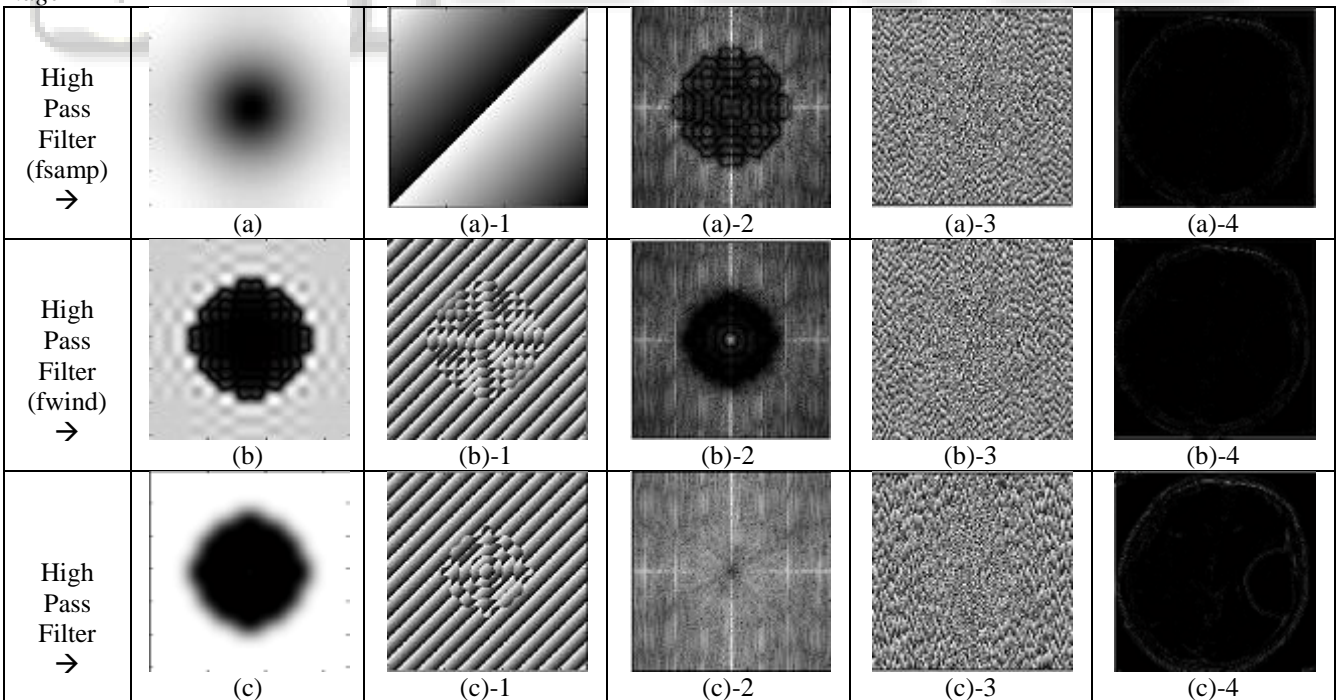


Fig. 6: (a),(b),(c),(d),(e),(f),(g),(h) and (i) :-Magnitude Images, (a)-1,(b)-1,(c)-1,(d)-1,(e)-1,(f)-1,(g)-1,(h)-1 and (i)-1 :-Phase Images, (a)-2,(b)-2,(c)-2,(d)-2,(e)-2,(f)-2,(g)-2,(h)-2 and (i)-2 :-Log Magnitude Images, (a)-3,(b)-3,(c)-3,(d)-3,(e)-3,(f)-3,(g)-3,(h)-3 and (i)-3 :-Phase Images, (a)-4,(b)-4,(c)-4,(d)-4,(e)-4,(f)-4,(g)-4,(h)-4 and (i)-4 :-Inverse FFT Images

3) Spectral Analysis for Proposed Method Edge Detected Image



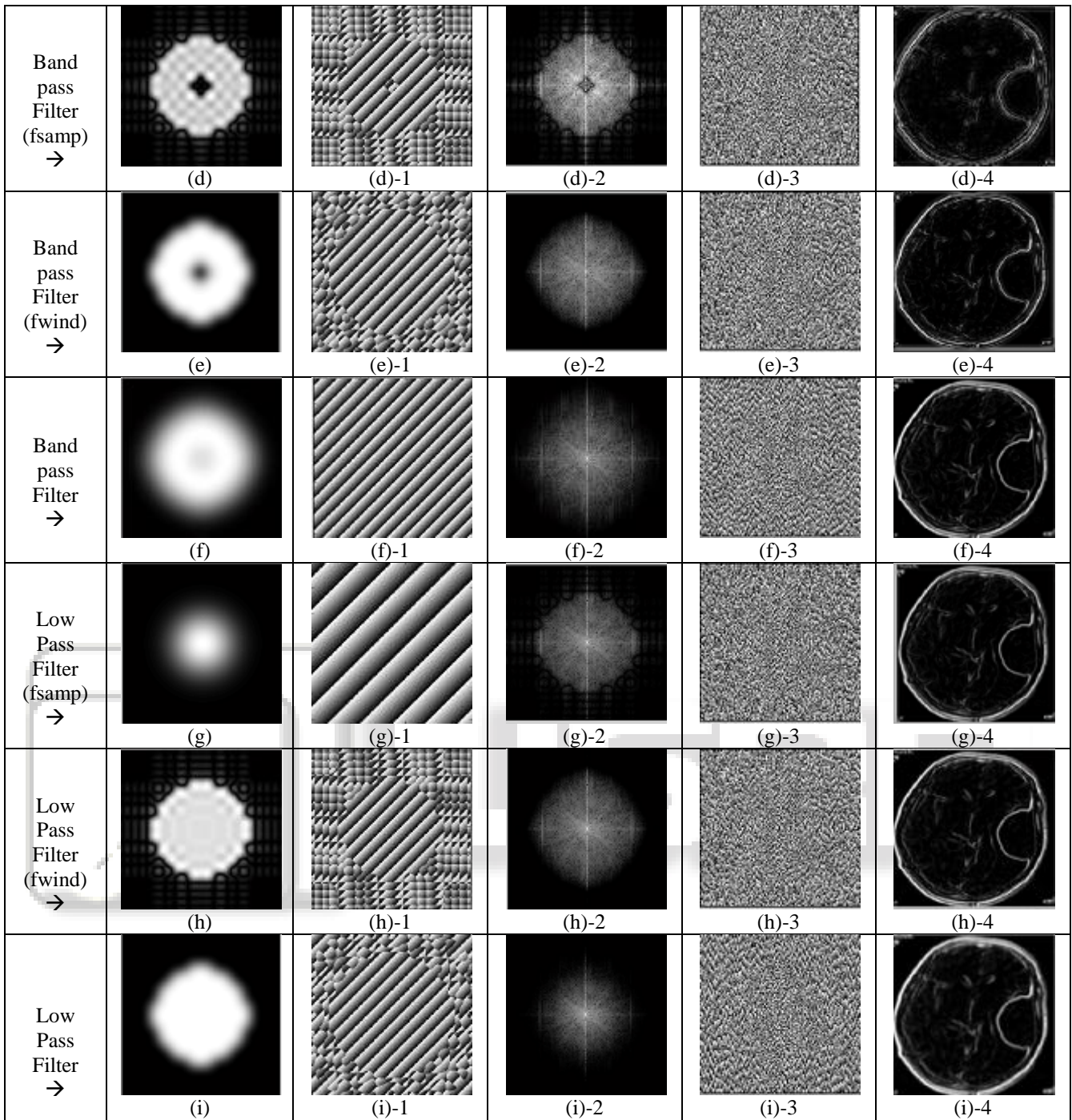
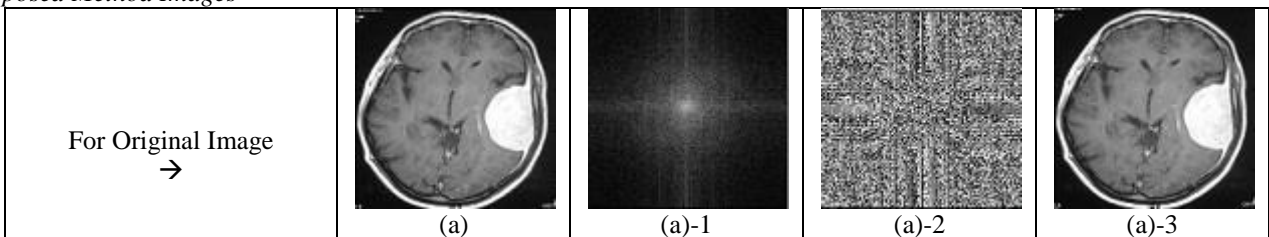


Fig. 7: (a),(b),(c),(d),(e),(f),(g),(h) and (i) :-Magnitude Images, (a)-1,(b)-1,(c)-1,(d)-1,(e)-1,(f)-1,(g)-1,(h)-1 and (i)-1 :-Phase Images, (a)-2,(b)-2,(c)-2,(d)-2,(e)-2,(f)-2,(g)-2,(h)-2 and (i)-2 :-Log Magnitude Images, (a)-3,(b)-3,(c)-3,(d)-3,(e)-3,(f)-3,(g)-3,(h)-3 and (i)-3 :-Phase Images, (a)-4,(b)-4,(c)-4,(d)-4,(e)-4,(f)-4,(g)-4,(h)-4 and (i)-4 :-Inverse FFT Images

4) Final Spectral Analysis for Original, Gabor and Proposed Method Images



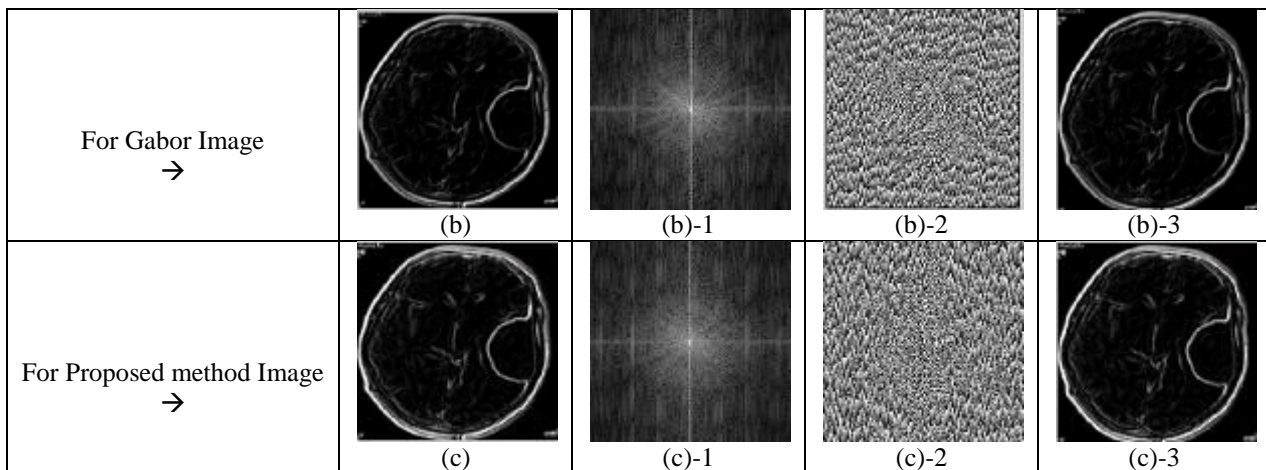


Fig. 8: (a), (b), (c): Input Images, (a)-1, (b)-1, (c)-1: Log Magnitude Images, (a)-2, (b)-2, (c)-2: Phase Images, (a)-3, (b)-3, (c)-3: Spectral Image for Input Images

Low pass filter: Let the low frequencies pass and eliminates high frequencies. Frequency analysis is applied on image, Image is the combination of group of pixels for each and every pixel frequency analysis is applied and it is sampled then displays output with magnitude and phase generates image with overall shading. The function of gain of filter at every frequency is called the amplitude response (or magnitude response). Low pass filter is used to find imaging details. Low pass filter with windowing function is also calculated and it is shown in fig.(h),(h)-1,(h)-2,(h)-3,(h)-4,(h)-5. Low pass filtered image and its spectrum is calculated. In all these we computed magnitude, phase, inverse FFT. Magnitude is used to find intensity. Phase is used for occurrence of integrity and to reconstruct the detected part of tumor.

High pass filter: Let the high frequencies pass and eliminates low frequencies, Frequency analysis is applied on image, Image is the combination of group of pixels for each and every pixel frequency analysis is applied and it is sampled then displays output with magnitude and phase. High pass filter it acts like edge enhancer. High pass filter is used especially to find edges. High pass filter with windowing function is also calculated and it is shown in fig (b),(b)-1,(b)-2,(b)-3,(b)-4,(b)-5. High pass filtered image and its spectrum is calculated.

Band pass filter: This filter allows to cut low and high frequencies of signal. An ideal band pass filter would have a completely flat pass band (e.g. with no gain/attenuation throughout) and would completely attenuate all frequencies outside the pass band. Frequency analysis is applied on image, Image is the combination of group of pixels for each and every pixel frequency analysis is applied and it is sampled then displays output with magnitude and phase. Band Pass filter is used especially to select band of frequencies. Band pass filter with windowing function is also calculated and it is shown in fig (e),(e)-1,(e)-2,(e)-3,(e)-4. Band pass filtered image and its spectrum is calculated.

#### IV. CONCLUSION

Many algorithms and techniques are available in recent days to detect edges of an image. All techniques and algorithms have it's own advantage and disadvantage. In our work edge detection methods are classified into five categories such as gradient based edge detection, zero crossing based edge

detection, Gaussian based edge detection, Laplacian of Gaussian (LoG) based edge detection and transform based edge detection. Some of the conventional edge detection approaches such as sobel, canny, prewitt, Robert and LoG have been implemented and results for various types of images are shown. Similarly wavelet transform based edge detection approaches namely Gabor wavelet and simplified Gabor techniques are implemented for various types of images and those images are given. The experimental results shows that canny provides better result than other classical approaches and Gabor wavelet provides better result than other transform based approach. Spectral analysis is also computed.

#### REFERENCES

- [1] Bjoern H. Menze e.tal," The Multimodal Brain Tumor Image Segmentation Benchmark (BRATS)", IEEE TRANSACTIONS ON MEDICAL IMAGING, Vol. 34, No. 10, October 2015
- [2] Madhumanveenaskar, "an automated system for brain tumor detection & segmentation", Journal of engineering research and studies, Vol.no.6, Issue No.1, January-March 2015.
- [3] Poojabang, e.tal, "Novel approach for detection of brain tumor using segmentation techniques" IJCSET, Vol No.7 March 2016.
- [4] Vitin Y. Borole, e.tal, "image processing techniques for brain tumor detection" IJETTCS, Vol No.4, Issue 5(2), September-October 2015.
- [5] Roshan G. Selkar, e.tal, " brain tumor detection and segmentation by using thresholding and watershed algorithm" IJAICT Volume 1, Issue 3, July 2014.
- [6] C. Senthil Singh e.tal, " Brain tumor mri image segmentation and detection in image processing", eISSN: 2319-1163 | pISSN: 2321-7308.
- [7] Nagalkar v. j e.tal, " Brain tumor detection using digital image processing based on soft computing", Journal of Signal and Image Processing ISSN: 0976-8882 & E-ISSN: 0976-8890, Volume 3, Issue 3, 2012, pp.-102-105.
- [8] Rajeshwari G Tayade e.tal, " A Review on Various Techniques of Brain Tumor Detection", International Journal of Computer Science Trends and Technology (IJCS T) – Volume 4 Issue 2, Mar - Apr 2016.

- [9] Amarjot Singh e.tal," Malignant Brain Tumor Detection", International Journal of Computer Theory and Engineering, Vol. 4, No. 6, December 2012.
- [10] Dr. KuldipPahwa e.tal," Brain tumor detection, segmentation using watershed segmentation and morphological operation", International Journal of Advanced Research in Electronics and Communication Engineering (IJARECE) Volume4, Issue 6, June 2015.
- [11] Swati Ghare e.tal," Detection of Possibility of Brain Tumor Using Image Segmentation", International Journal of Innovative Research in Computer and Communication Engineering, Vol. 3, Issue 4, April 2015.
- [12] ManaliPatil e.tal," Brain Tumor Identification Using K-Means Clustering", International Journal of Engineering Trends and Technology, Volume4, Issue3- 2013.
- [13] KimmiVerma e.tal," Image processing techniques for the enhancement of brain tumor patterns", International Journal of Advanced Research in Electrical, Electronics and Instrumentation Engineering Vol. 2, Issue 4, April 2013.
- [14] Esmail Hassan e.tal," Detecting brain tumour from mriimage using matlabguiprogramme", International Journal of Computer Science & Engineering Survey (IJCSES) Vol.6, No.6, December 2015.
- [15] Vrishali A. Walanj e.tal," Detection Of Brain Tumor Using Mri Image", International Journal of Engineering Research in Electronic and Communication Engineering (IJERECE) Vol 2, Issue 11, November 2015.
- [16] S.Meera e.tal," A Survey on Detecting Brain Tumorinmri Images Using Image Processing Techniques", International Journal of Innovative Research in Computer and Communication Engineering (An ISO 3297: 2007 Certified Organization) Vol. 3, Issue 1, January 2015.
- [17] AndacHamamci e.tal "Tumor-Cut: Segmentation of Brain Tumors on Contrast Enhanced MR Images for Radiosurgery Applications," IEEE Transactions on medical imaging, 2012.
- [18] AmruthaRavi e.tal," A Review on Brain Tumor Detection Using Image Segmentation", International Journal of Emerging Technology and Advanced Engineering, Volume 5, Issue 6, June 2015.
- [19] Logeswari e.tal, "An Enhanced Implementation of Brain Tumor Detection Using Segmentation Based onSoft Computing", IEEE International Conference on Signal Acquisition and Processing, pp. 243-247, 2010.
- [20] Priyanka e.tal, "An improvement in brain tumor detection using segmentation and bounding BOX", IJCSMC, Vol. 2, pp.239 – 246, 2013.
- [21] Shivani P. Deshmukh e.tal," Detection and segmentation of brain tumor from mri images", [IJESAT] [International Journal of Engineering Science & Advanced Technology] Volume-4, Issue-5, 426-430.
- [22] S. Murugavalli e.tal "A high speed parallel fuzzy c-mean algorithm for brain tumour segmentation", BIME Journal", Vol. no: 06, Issue (1), Dec., 2006.
- [23] [23] Mohamed LamineToure e.tal, "Advanced Algorithm for Brain Segmentation using Fuzzy to Localize Cancer and Epilepsy Region", International Conference on Electronics and Information Engineering (ICEIE 2010), Vol. no 2.
- [24] Dr.G.Padmavathi e.tal, "Non linear Image segmentation using fuzzy c means clustering method with thresholding for underwater images", IJCSI International Journal of Computer Science Issues, Vol. 7, Issue 3, No 9, May 2010.
- [25] T.Logeswari e.tal," An improved implementation of brain tumor detection using segmentation based on soft computing" Journal of Cancer Research and Experimental Oncology Vol. 2(1) pp. 006-014, March, 2010.
- [26] WankaiDeng e.tal"MRI brain tumor segmentation based on improved fuzzy c-means" Method. Laboratory of Education Ministry for Image Processing and Intelligence Control Institute for Pattern Recognition and Artificial Intelligence SPIE Vol. 7497, 74972N, 2009.
- [27] S. Dickson e.tal , "Using neural networks to automatically detect brain tumours in MR images", International Journal of Neural Systems, 4(1):91-99, 1997.
- [28] A. Kharrat, e.tal "Detection of brain tumor in medical images," in Proc. of International Conference on Signals, Circuits and Systems, Medenine, 2009, pp. 1-6.

# Classification and Detection of Plant Diseases using higher order Dynamic Conditional Random Fields Through Spatial and Multitemporal images

A. Gayathri, Dr. P. Abdul Khayum

A. Gayathri, M.Tech (CSP) student, Department of ECE, G.P.R.E.C, Kurnool, Andhra Pradesh, India.(Email: gayathriavvari24@gmail.com)

Dr. P. Abdul Khayum, M.Tech, Ph.D., Professor, Department of ECE, G.P.R.E.C, Kurnool, Andhra Pradesh, India.(Email: abdkhayum@rediffmail.com)

## Article Info

Volume 81

Page Number: 6336 - 6341

Publication Issue:

November-December 2019

## Article History

Article Received: 5 March 2019

Revised: 18 May 2019

Accepted: 24 September 2019

Publication: 28 December 2019

## Abstract:

Agricultural areas should be continuously monitored, because they undergo random changes throughout the year. The problem arises when different crops show similar phenology and backscatter. This occurs when crops are classified based on single date remote detecting pictures. We should consider multitemporal images of crops. In this paper for classification of crops, we design an ensemble classifier which combines both spatial and temporal images of crops. To detect the affected areas of crops we implement first order and higher order dynamic conditional random fields (HDCRF). In order to enhance the diseased area of crop, we use k-means segmentation. All the training datasets are stored in multisvm (support vector machine). By the obtained results from this paper, we consider HDCRF as the best technique when compared with MRF (Markov Random Field) and CRF (Conditional Random Field) techniques.

**Keywords:** phenology, backscatter, multitemporal, ensemble classifier, MRF, CRF, HDCRF, k-means segmentation.

## I. INTRODUCTION

Demand for food production has been raised enormously because of the increase in population. Farmers and strategy producers should have an idea that, how much amount of food production is required. But the major problem is the detection of affected crops by the farmers. It becomes difficult for farmers in order to classify the healthy and diseased crops, so we prefer remote detecting by radar to capture the images of the entire crop [1].

TerraSAR-X microwave images are used to detect the dynamic changes and phenology, which refers to stages that crops go through from seeding to harvesting [2]. Different crops may show similar phenology, but they can be discriminated on their backscatter values. Some crops will exhibit different backscatter values for same type of crops. These changes can be found out by using radar detectors, which take into account different properties of crops like spatial and temporal images, backscatter values for each crop etc., so it is not sufficient to consider only single date remote detecting pictures, we must consider multitemporal images of crops. All these images are stored in an ensemble classifier. The ensemble classification technique is only used to classify the crops, but it does not detect the diseased crops. This paper fills this gap by detecting the affected crops by using higher order dynamic conditional random fields. By using HDCRF method, we can classify the crops as well as identify the affected crops in the field.

## II. EXISTING MECHANISMS

### Markov Random Field (MRF)

In the earlier works, they have proposed MRF[3] technique for incorporating spatial data in image classification. Later, this method was extended for ordering of the multitemporal pictures based on the Bayesian theory network. Based on the conditional probability dependencies of the dynamic data, MRF was considered as the useful method for classifying the temporal images rather than spatial images. The figure depicts the MRF concept.

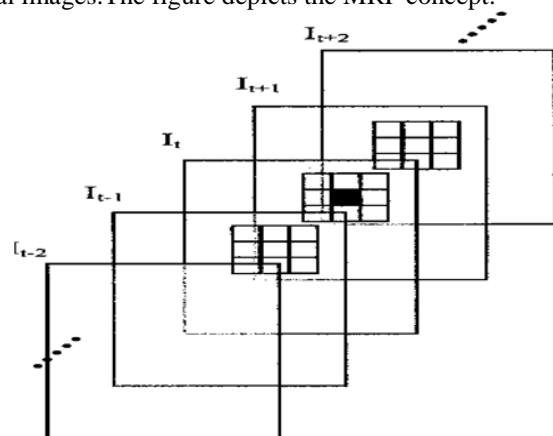


Fig 1 MRF based temporal dependencies of each plant in strawberry crop.

It gives the result of an individual crop at a time i.e., it calculates the cumulative distribution function (CDF) of a particular crop and is stored in group transitional matrix. MRF[4] was extended to provide multitemporal images of crops and has ignored spatial information. By skipping the spatial data, it is difficult to know the phenology of crops and also to identify the damaged areas of leaves. Another problem with this technique was, it does not support multiple fields means the entire crop area cannot be shown. It gives only the individual images of crops and which consumes more time while grouping the crops. So, for calculating spatial pixels, CRFs are proposed.

#### *Conditional Random Fields (CRF)*

CRFs [5] are proposed for spatial information of crops. Initially it was used for 1-D ordering and later expanded to 2-D image class [6]. This method calculates the probability distribution function (PDF) of the adjacent pixels in the given specimen. So it gives the overall layout of crop field as shown in the below figure.



**Fig 2 Original image of entire plantation of strawberries considered as an input image.**

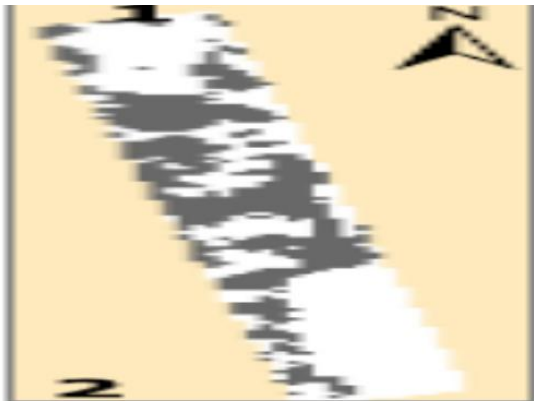


**Fig 3 Outline map depicting the above image.**

In fig 3 the black colour portion depicts the planted crops area, and the white colour portion shows the emptied area. By using this method, we cannot able to find the diseased plants, so we use Higher order Dynamic Conditional Random Fields. All these datasets are stored in local group transitional grid. Global class modulation matrix contains expert based phenological knowledge of diverse crops. While analyzing the spacial and dynamic pixels of a plant, they are compared with the patterns accumulated in global group grid. If the respective subsets of particular picture don't match with the data kept in predefined database, some

error has been occurred during the processing of spatial and random nodes. Therefore categorizing resemblance of crops is decreased and we cannot determine the affected leaves in plants[7]. In this paper, we develop a multi-dynamic spacial and temporal dependence model for grouping of crops and also discover the altered leaves present in plants.

#### *Contribution*

The main contributions that are considered for designing this model are

A functional interaction model is designed, where the spacial coordinates and temporal datasets specified by the user are compared with the information present in the database.

The remaining part of this paper is sorted out as follows. Section III introduces the proposed work. Section IV displays the results of the above technique. Conclusions for this work are manifested in section V.

### **III. PROPOSED WORK**

A plant or leaf structure, which is piled up in input data points is selected by the client, for the purpose of crop association as well as to examine, whether that given plant is healthy or altered one.

#### *Contrast Enhanced image*

The intensity levels of a picture are ameliorated by making the difference in lightness. The purpose of executing the degree of diverse improvement in image is to batten the darker regions, so that we can easily form sets of crops and to expose, whether the leaves of plants are attacked.

#### *Segmentation of Picture*

For viewing the leaf outlines and the malfunctioned area, we prefer to divide the given object. The method used for this process is K-means clumping. By using this procedure, we can extract the features from the region of interest.

#### *K-Means Clustering Algorithm*

1. Consider K number of lumps, which contains a set of input data points
2.  $(X_1, X_2, \dots, X_n)$ .
3. The algorithm starts by placing K clusters at random locations in high dimensional vector space.
4. The below steps are computed iteratively.
5. For each input event  $(X_i)$ , we find the nearest clump center by calculating Euclidean distance between every node and to all cluster centers.
6. That particular data element is assigned to the lump having minimum distance.
7. For each one of the input points, the above process is repeated.
8. The mean is reckoned for all repositioned context, and then divided by the total elements present in linear space.
9. After calculating the average, the clump centers are changed.
10. The above steps are performed recursively, until further division of data sets is not possible.

#### *Segmentation Process*

In this work, a consumer determined graph is taken from the predefined arguments, which is considered as the original object that is to be segmented. Here we assume three clusters.

- In first lump, the leaf epochs of the user referred file is measured by the Euclidean span formula. To obtain more precise outer layers of leaves, we calculate the mean of all the displaced pixels. The expression is formulated as

$$P_{ij} = \frac{\sqrt{\sum_{i=1}^s |g_i(x) - g_j(x)|^2}}{s} \quad (1)$$

- In second cluster, if the given image contains any disordered leaves, then that part is exaggerated, or else there will be no issues with the healthy plants.

- In third clump, the background region of the assumed object is captured.

In this way, the algorithm is applied for dividing the image into clusters.

#### Extraction of Features from ROIsegmented Object

As our aim is to identify the affected crops, we consider the abnormal regions of leaves as our Region of Interest. The following features are processed from the selected cluster.

#### Affected space

The impacted leaves of assumed clump image can be calculated by using below formula.

Affected part of leaf = (Disease Attacked area) / (Total leaf region).

The below properties are computed from ROI clump.

#### Homogeneity

This template describes the closeness of distribution, among adjacent pels that are accumulated in the dim level grid. The equation is

$$\text{Homogeneity} = \sum_i \sum_j \frac{S[i,j]}{1+|i-j|} \quad (2)$$

#### Energy

It is defined as the sum of squares of all spacial pixels, which are stored in co-occurrence grid. If the given subset has greater homogeneity, then energy is also high. The formula is given as

$$\text{Energy} = \sum_i \sum_j S_{ij}^2 \quad (3)$$

#### Contrast

It gives the deviation in intensity levels of a pel with its neighboring piscels over the total picture. Difference in brightness values should be low, so that image can be viewed appropriately. The expression is

$$\text{Contrast} = \sum_i \sum_j (i-j)^2 S[i,j] \quad (4)$$

#### Inverse Distinct Moment (IDM)

It tells the homogeneity in the adjacent pels of the local gray array, which covers only a particular region of a file. It is represented by the following form

$$\text{IDM} = \frac{\sum_i \sum_j S_{ij}}{1+(i-j)^2} \quad (5)$$

#### Entropy

It calculates the loss of data, during processing of the spatial range. This is specified as

$$\text{Entropy} = -\sum_i \sum_j S_{ij} \log S_{ij} \quad (6)$$

#### Correlation

It describes the similarity between one pel to its side piscels over the entire portray.

$$\text{Correlation} = \frac{\sum_i \sum_j (i,j) S(i,j) - \mu_x \mu_y}{\sigma_x \sigma_y} \quad (7)$$

#### Mean

It calculates the average of all pixels, gathered in the local gray grid. This is evaluated as

$$\text{Mean} = \frac{1}{N} \sum_{i=0}^{N-1} x_i \quad (8)$$

#### Standard Deviation

It measures by how much amount each pel deviates from its center pel in the given image.

$$\sigma^2 = \frac{1}{N-1} \sum_{i=0}^{N-1} (x_i - \mu)^2 \quad (9)$$

#### Skewness

It measures the symmetrical properties over the entire graph, by considering center pictels as reference point.

#### Kurtosis

It measures whether the data values are having high or low amplitudes, which are represented in Gaussian distribution.

From all the above features, the spacial interactions of pixels in the given subset are processed. The temporal relations of piscels are computed by using upcoming method.

#### Dynamic Conditional Random Fields (DCRF)

The goal of DCRF is to classify the given plant, and to specify the disease name if the leaves are imparted. It proposes the temporal function, which gives the graphical model having similar weighing pixels deviations at various timing slots. It defines the program based on the conditional probability dependencies of the multitemporal and spatial nodes. Consider the image (x), where c denotes the set of random variables and K represents the timing levels for the model at  $\Delta t = t \pm 1$ .

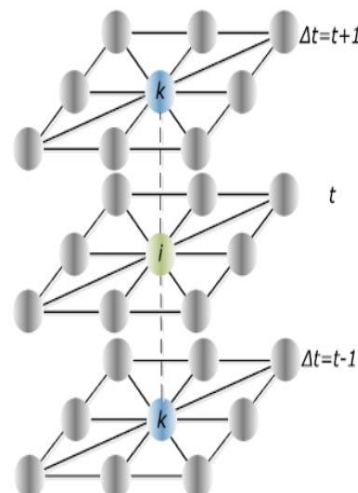


Fig 4: Spacial and temporal node relations at different instants of time.

The first order DCRF function is modeled by the following expression.

$$P(y/x) = \frac{1}{z(x)} \exp\{\sum_{i \in S} A(y_i, x) + \sum_{i \in S} \sum_{j \in N} I(y_i, y_j, x) + \sum_{t \in T} \sum_{i \in S} \sum_{c \in C} DP(y_{i,t,c}, x, \Delta t)\} \quad (10)$$

Where DP represents dynamic potential, used for interpreting the altered plants in run time. By using first order DCRF, we get knowledge about sum of all the stochastic and spacial pixels, which gives the overall field outlay. The main drawback of this method is that, it cannot discriminate the plants with same phenology. So we go for HDCRFs.

*Higher order Dynamic Conditional Random Fields(HDCRF)*

Different crops with similar backscatter can be discriminated by using a transform technique called Discrete Wavelet form. By using this method, the lower and higher levels in the image are differentiated, that gives more exactness for association of plants. All the categorized groups of varying pel differing values are stocked in optimal classifier, where we can assign corresponding gray level weights to various crops based on expert knowledge. Hence by using HDCRFs, condition probability subordinates of random nodes are improved, so that distinguishing of leaf outlines can be easily identified. The expression is:

$$P(y/x) = \frac{1}{z(x)} \exp\{\sum_{i \in S} A(y_i, x)^{\Psi_1} + \sum_{i \in S} \sum_{j \in N} I(y_i, y_j, x)^{\Psi_2} + \sum_{t \in T} \sum_{i \in S} \sum_{k \in K} DP(y_i, y_k, x_{1:T}, t)^{\Psi_3}\} \quad (11)$$

Where  $\Psi_1, \Psi_2, \Psi_3$  are weights corresponding to association, interaction, dynamic potentials respectively. The individual or user defined plants can be determined by using the increasing order of DCRFs. The optimized collection classifier can be designed as depicted in the following diagram. Each plant data is accumulated in an appraised database management system. The model and equation for reckoning is as follows:

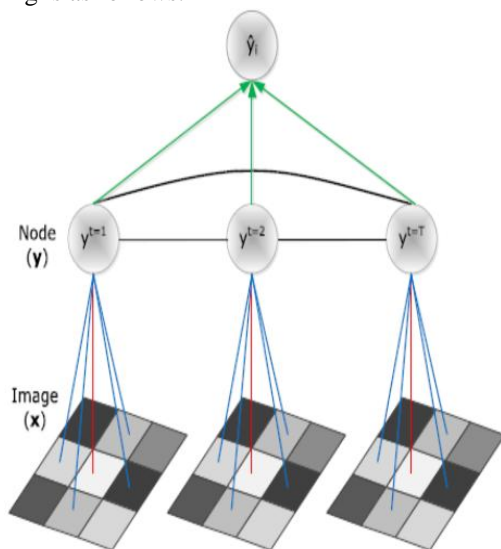


**Fig 5: Estimated ensemble classifier of higher order DCRFs from the arrangement of dynamic nodes.**

As shown in the above figure, the center pel collects the information from neighboring pels, and transmits it to other temporal images for improving accuracy. The below

equation gives the user selected plant picture from the entire field. This overall crop layout was calculated by previous method named CRF.

$$y_i^{\hat{}} = \arg_{S=1}^m \max \{\max_{t=1}^T F[P(y_i|x), t]\} \cdot \text{User accuracy} \quad (12)$$

Where  $F[P(y_r|x), t]$  is the conditional probability, representing to group r, having maximum F-score at time t. Here arg denotes atmost number of levels selected from the entire crop field, max gives the user defined plants. F-score is used for accumulating all the processed images, which is calculated as

$$F\text{-score} = \frac{2(\text{Predefined accuracy} \cdot \text{User accuracy})}{(\text{predefined accuracy} + \text{User accuracy})} \quad (13)$$

In the above function, the entire expert based phenology crop images are grouped in predefined databank and User given input pictures are stored in training dataset for plant recognition purpose. Dot product in the above mentioned equation represents the comparison of point to point summation of the images based on corresponding producer and user accuracies.

If the given source picture matches with any one of the frames that are preserved in the database, then classification of plant along with the disease name can be obtained if that particular plant is abnormal, or else it forms a new template in the databank. All these input files, classes of various crops respective testing matrices and the corresponding resultant output attributes are aggregated in multisvm (support vector machine). The percentage of the affected region is calculated by using the linear kernel function. It computes the iterations until we get the exact value of the influenced part of leaf. So, by using segmentation process, HDCRFs and logical core we are able to classify the plants and recognize the disease name from the extracted features of ROI image. The results are shown in the upcoming section.

**IV. SIMULATED RESULTS**

The input picture is taken from the training dataset, which is shown below



**Fig 6: Healthy leaves plant image**

Using HDCRFs concept, we get to know which plants are healthy and diseased with the help of spatial and temporal images of crops. If the particular crop doesn't match with the normal plant as shown in below figure, then all the parameters are calculated which are defined in the proposed work. Finally the affected area of the leaves is computed.



**Fig 7: Diseased leaf Image**



**Fig 8: Contrast Image**

The above image gives the enhanced contrast form for given query picture which is in the altered way.

The segmented layouts are depicted below in the form of individual clumps.

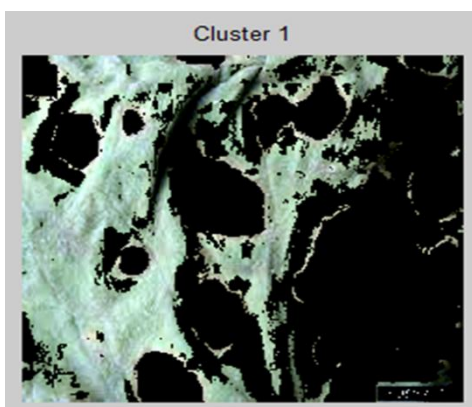


**Fig 9: Outline of the given leaf**

The above lump shows the leaf epochs, which are calculated by using Euclidean distance metric.

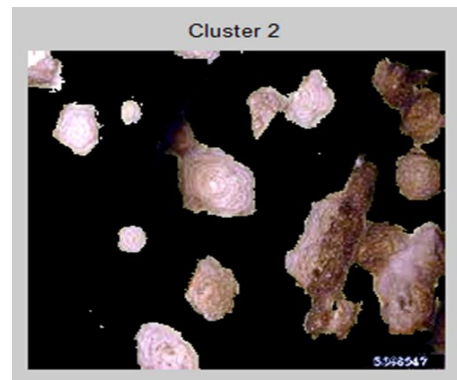


**Fig 10 Affected areas of given image**

The infected areas are highlighted in overhead cluster. It is taken as Region of Interest by the user, to extract the features of input picture.

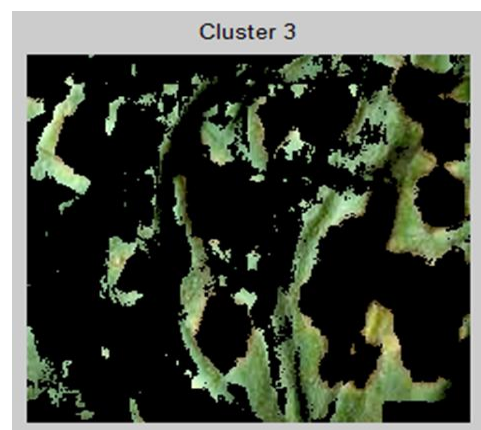


**Fig 11**

In the above layout, we can view the background scene of the given dataset. Here we took cluster 2 as our ROI image and performed the analysis.

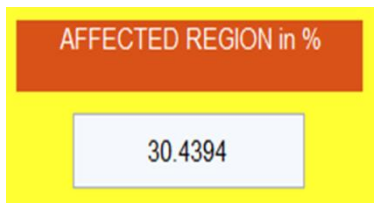
FEATURES	
Mean	71.8145
S.D	90.5264
Entropy	3.89944
RMS	9.44023
Variance	5343.55
Smoothness	1
Kurtosis	1.5368
Skewness	0.583604
IDM	255
Contrast	1.85335
Correlation	0.870152
Energy	0.332283
Homogeneity	0.871057

These are the features that are computed for the selected clump. From the evaluated data, we can find out the disease

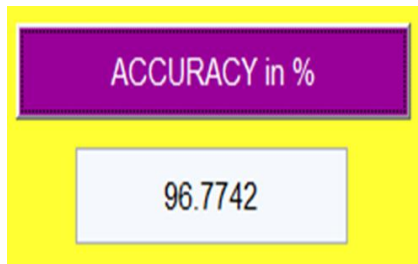
name, along with the affected area of the given diseased leaf which can be shown as



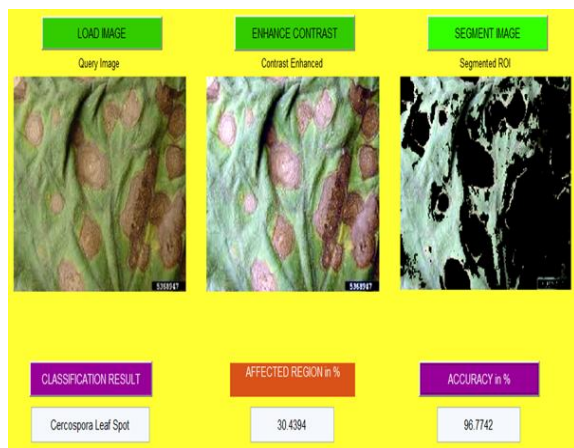
In this way, the given pictures are classified by considering all these aspects. Then we can know the altered part of the segmented area in terms of percentage as displayed beneath.



Linear kernel program is used to determine the accuracy of dysfunction region of the input subset, which can be viewed as



The entire output for the defined input image is displayed as



## V. CONCLUSION

The main goal of this paper is to classify the plants based on their computed parameters and to acknowledge the name of the disease, if it has infected leaves. We also estimated the disordered region accuracy, so that it will be treated properly with the suitable pesticides. Therefore we can differentiate the defected crops from healthy ones in a field, which helps the farmers in the cultivation process.

**TABLE 1**  
Comparison with previous methods in terms of accuracy for the above diseased plant.

Method	Accuracy
Markov Random Field	66.5
Conditional Random Field (CRF)	67.06
Dynamic Conditional Random Fields (DCRF)	75.78
Higher order Dynamic Conditional Random Fields max F1-score (HDCRF)	96.77

The accuracy is calculated from the above mentioned equations 10, 11, 12 for proposed work i.e., HDCRF. Accuracies for other methods are computed already from the existing papers. The accuracy can be improved by using Higher orders of Dynamic Conditional Random Fields.

## REFERENCES

1. A. Kross, D. Lapen, R. Caves, "Early season monitoring of corn and soya beans with TerraSAR-X and RADARSAT-2," Int. J. Appl. Earth Observ, May 2016.
2. S. Siachalou, G. Mallinis,, "A Hidden Markov models approach for crop classification: Linking crop phenology to time series of multi-sensor remote sensing data," 2015.
3. OpenCV. Random Trees, accessed on Nov 20, 2014.
4. R.Sonobe, H. Tani, N.Kobayashi, "Discrimination of crop types with TerraSAR-X derived information.
5. B.K. kenduiywo, Spatial-Temporal Dynamic Conditional Random Fields Crop Type Mapping Using Radar Images, 2016.
6. D. Bargiel, U. Sorgel, "Spatial-temporal conditional random field crop classification from TerraSAR-X images," 2015.
7. T. Hoberg, F. Rottensteiner, C. Heipke, "Conditional Random Fields for Multitemporal and Multiscale classification of optical satellite imagery," Feb 2015.

# Cryptography Based Image Encryption by Secure Reversible Data Hiding Technique

Kammari Kalyani (M. Tech scholar)<sup>1</sup>,

Dr. P. Abdul Khayum, **M. Tech, Ph. D** (Professor of ECE)<sup>2</sup>

Department of Electronics & Communication Engineering<sup>1,2</sup>

G. PULLAREDDY Engineering College (Autonomous), Kurnool, Andhra Pradesh-518007, India<sup>1,2</sup>

[kammarikalyani902@gmail.com](mailto:kammarikalyani902@gmail.com)<sup>1</sup>, [abdkhayum@rediffmail.com](mailto:abdkhayum@rediffmail.com)<sup>2</sup>

## ABSTRACT

*In this paper we are proposing novel reversible image data hiding scheme by using encrypted domain. Embedding of information can be done by using public key modulation process; here there is no need to access the secret encrypted key. Two-class SVM classifier is used at the decoder side to separate the encrypted and non-encrypted images. And we can decode the embedded message and original signal. Compared to the conventional methods the proposed work is going to give the high embedding capacity and the original image and embedded message is going to be reconstructed perfectly. By seeing the experimental results we can conclude that SVM is giving better results.*

**Key Words**— Feature extraction, reversible image data hiding (RIDH), signal processing over encrypted domain, SVM.

## I. INTRODUCTION

### A. Basics of Image Data Hiding

Reversible image information hiding (RIDH) is a distinct category of knowledge hiding procedure, which ensures ideal reconstruction of the duvet snapshot upon the extraction of the embedded message. The reversibility makes such an photograph knowledge hiding strategy exceptionally attractive within the crucial scenarios, e.g., army and remote sensing, scientific picture sharing, regulation forensics, and copyright authentication, the place high fidelity of the reconstructed cover snapshot is required. The vast majority of the existing RIDH algorithms are designed over the plaintext area, namely, the message bits are embedded into the customary unencrypted pix compress targeted snapshot facets, to vacate room for message embedding.

### B. Data Hiding most important terms and Notions

Among the many lossless procedures of information embedding there are two common domains of operation: spatial and frequency. Spatial methods are characterized by using the embedding of messages into the least massive bits (LSBs) of photograph pixels, whilst in frequency ways the message is embedded after a targeted develop into is performed by means of enhancing frequency coefficients of the quilt photograph.

Recently, the study on signal processing over encrypted domain has won increasing awareness, exceptionally pushed with the aid of the desires from cloud computing platforms and more than a few privacy-retaining functions. This has brought about the investigation of embedding extra information within the encrypted pics in a reversible trend. In many useful situations, e.g., at ease far off sensing and cloud computing, the parties who process the photo information are un-trusted. To defend the privacy and safety, all portraits might be encrypted before being forwarded to a un-trusted third party for further processing. For example, in comfy remote sensing, the satellite images, upon being captured by means of on-board cameras, are encrypted, and then sent to the base station(s), as proven in Fig. 1. After receiving the encrypted pix, the bottom station embeds a confidential message, e.g., base station identification, area knowledge, time of arrival, nearby temperature, wind pace, etc, into the encrypted portraits.

## II. LITERATURE SURVEY

### J. Tian, "Reversible knowledge embedding using a difference growth"

In this paper, we've got provided a easy and efficient reversible data-embedding process for digital pictures. We explored the redundancy in the digital content to attain reversibility. Each the payload capability limit and the visible pleasant of embedded portraits are among the many first-rate in the literature.

### Z. Ni, Y. Q. Shi, N. Ansari, and W. Su, Reversible knowledge hiding

A novel reversible data hiding algorithm, which can get well the customary image with none distortion from the marked picture after the hidden information had been extracted, is provided in this paper. This algorithm utilizes the zero or the minimal points of the histogram of an photograph and rather

modifies the pixel grayscale values to embed information into the photograph. It may embed more knowledge than most of the present reversible information hiding algorithms.

## III. PROPOSED METHOD

### A. RIDH Scheme over Encrypted Domain

As a substitute of due to the fact that committed encryption algorithms tailored to the scenario of encrypted-area data hiding, we here stick with the conventional circulate cipher applied in the typical format. That is, the cipher text is generated through bitwise XOR using the plaintext with the important thing circulation. If not in any other case distinctive, the commonly used movement cipher AES in the CTR mode (AES-CTR) is assumed.

Flowchart of the proposed work is given below,

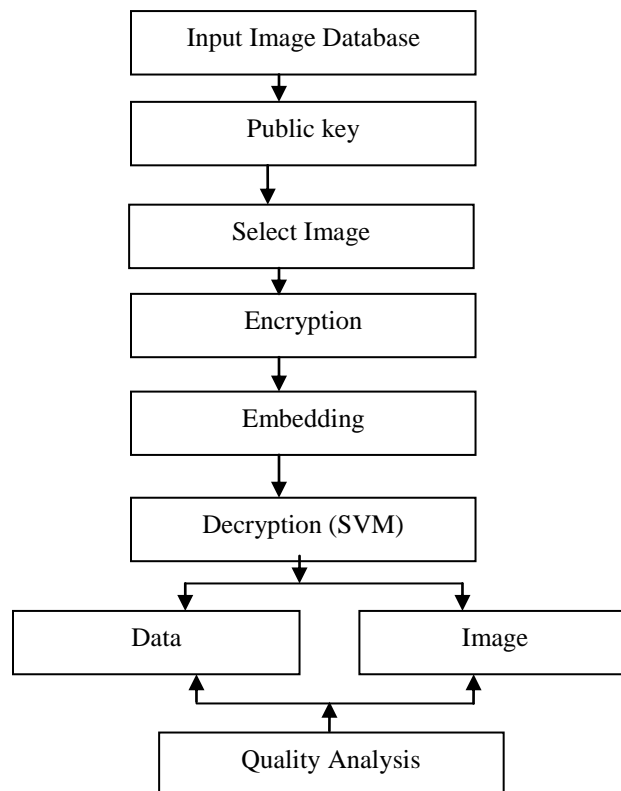


Fig.1 Flow Chart of Proposed System

The ensuing data hiding paradigm over encrypted area would be extra almost valuable since of two explanations.

1) Move cipher used in the average format (e.g., AES-CTR) is still probably the most preferred and secure encryption tools, because of its provable safety and high software/hardware implementation affectivity. It is probably not easy, and even infeasible, to influence consumers to adopt new encryption algorithms that have not been utterly evaluated.

2) massive amounts of information have already been encrypted utilizing move cipher in a general means. When move cipher is employed, the encrypted image is generated by

$$[[f]] = Enc(f, K) = f \oplus K \quad (1)$$

Where  $f$  and  $[[f]]$  denote the long-established and the encrypted pix, respectively. Here,  $K$  denotes the important thing circulate generated utilizing the secret encryption key  $K$ . In this paper, without lack of generality, the entire snap shots are assumed to be 8 bits. During this paper, we use  $[[x]]$  to represent the encrypted variation of  $x$ . Clearly, the common photograph can be got via performing the following decryption function:

$$f = Dec([[f]], K) = [[f]] \oplus K. \quad (2)$$

As mentioned previous, the encrypted photograph  $[[f]]$  now serves as the cover to accommodate message to be hidden. We first divide  $[[f]]$  into a series of non overlapping blocks  $[[f]]^{i's}$  of dimension  $M \times N$ , where  $i$  is the block index. Each block is designed to hold  $n$  bits of message. Letting the quantity of blocks within the image be  $B$ , the embedding ability of our proposed scheme becomes  $n \cdot B$  bits. To permit efficient embedding, we advise to use  $S = 2n$  binary public keys  $Q_0, Q_1, \dots, Q_{S-1}$ , each of which is of size  $L = M \times N \times \text{eight bits}$ . All  $Q_j$ 's, for  $0 \leq j \leq S - 1$ , are made publicly obtainable, which implies that even the attacker knows them. These public keys are preselected prior to the message

embedding, in step with a criterion of maximizing the minimal Hamming distance amongst all keys. The algorithm developed by way of MacDonald can be utilized to this end.

Notice that all of the public keys are constructed into the information hider and the recipient when the whole method is installed, and for this reason, it is not crucial to transmit them during the information embedding stage. Also, for constant  $S$  and  $L$ , Hamming confirmed that an higher bound on the minimum Hamming distance can accept as follows. First, examine two integers  $m_1$  and  $m_2$  by using  $m_1$

$$\sum_{i=0}^{m_1} \binom{L}{i} \leq \frac{2^L}{S} < \sum_{i=0}^{m_1+1} \binom{L}{i} \quad (3)$$

$$\begin{aligned} \sum_{i=0}^{m_2} \binom{L-1}{i} &\leq \frac{2^{L-1}}{S} \\ &< \sum_{i=0}^{m_2+1} \binom{L-1}{i} \end{aligned} \quad (4)$$

Where,  $\binom{L}{i} = (L!/i!(L-i)!)$ .

It can be shown that both  $m_1$  and  $m_2$  are unique. Then, the minimum Hamming distance among all  $Q_j$ 's satisfies

$$d_{min} \leq \max\{2m_1 + 1, 2m_2 + 2\}. \quad (5)$$

The schematic diagram of the proposed message embedding algorithm over encrypted area is shown in Fig. 2. In this paper, we do not remember the case of embedding more than one watermark for one single block, meaning that each and every block is processed once at most. For simplicity, we expect that the quantity of message bits to be embedded is  $n \cdot A$ , where  $A \leq B$  and  $B$  is the quantity of blocks inside the image.

The steps for performing the message embedding are summarized as follows.

Step 1: Initialize block index  $i = 1$ .

Step 2: Extract  $n$  bits of message to be embedded, denoted by  $W_i$ .

Step three: in finding the general public key  $Q_{[W_i]d}$  associated with  $W_i$ , the place the index  $[W_i]d$  is the decimal illustration of  $W_i$ . For example, when  $n =$  three and  $W_i = 010$ , the corresponding public secret is  $Q_2$ .

Step 4: Embed the length- $n$  message bits  $W_i$  into the  $i$ th block by way of

$$[[f]]_i^\omega = [[f]]_i \oplus Q_{[W_i]d} \quad (6)$$

Step 5: Increment  $i = i + 1$  and repeat Steps 2–4 except all the message bits are inserted. The watermark length parameter  $A$  desires to be transmitted on my own with the embedded message bits. There are numerous ways to clear up this drawback.

For instance, the present non separable RIDH schemes upon trivial changes, can still make sure embedding safety even if the data hiding secret is eliminated, if we repair the way in which of partitioning a block into  $S_0$  and  $S_1$  (specifically, do not use knowledge hiding key to randomize the block partitioning), then an attacker nonetheless can't compute the fluctuation operate [18, eq. (10)] so as to decode the embedded message. This is considering the fact that an attacker does no longer access to the secret encryption key  $k$ . In different words, the safety mechanism in the encrypted domain will also be naturally expanded to provide safety for message embedding, putting off the need of introducing one more knowledge hiding key.

Moreover to deciding on this property, we, in section VI, will exploit the message in distinguish capacity to show that the removing of knowledge hiding key will not hurt the embedding protection. Before providing the data extraction and photo decryption methods, let us first investigate the facets that can be used to discriminate encrypted and no encrypted picture blocks. The classifier designed consistent with these aspects might be shown to be primary within the proposed joint information extraction and snapshot decryption method.

### ***B. Feature Resolution for Discriminating Encrypted and Non-encrypted photo Blocks***

To differentiate encrypted and customary unencrypted picture blocks, we here design a feature vector  $\rho = (H, \sigma, V)$ , integrating the traits from multiple views. Right here,  $H$  is a tailor-made entropy indicator,  $\sigma$  is the SD of the block, and  $V$  represents the directional neighborhood complexities in four directions. The formation of the above feature factors will likely be designated as follows. When put next with the fashioned unencrypted block, the pixels in the encrypted block tend to have a much more uniform distribution. This motivates us to introduce the neighborhood entropy into the characteristic vector to capture such individual characteristics.

However, we need to be cautious when calculating the entropy values on the grounds that the number of on hand samples in a block can be rather restricted, leading to estimation bias, especially when the block dimension is small. For instance, within the case that  $M = N =$  eight, we most effective have 64 pixel samples, whilst the range of each and every sample is from 0 to 255. To curb the negative influence of inadequate quantity of samples relative to the large variety of every pattern, we advise to compute the entropy variety established on quantized samples, the place the quantization step dimension is designed based on the block measurement. In particular, we first follow uniform scalar quantization to each and every pixel of the block

$$f^\wedge = \left\lfloor \frac{MN \cdot f}{256} \right\rfloor \quad (7)$$

Where  $f$  and  $f^\wedge$  denote the common and the quantized pixel values, respectively. Undoubtedly,  $f^\wedge$  falls into the range  $[0, MN - 1]$ . The entropy indicator  $H$  founded on quantized samples is then given through

$$H = - \sum_{j=0}^{MN-1} p(j) \log p(j) \quad (8)$$

Where  $p(j)$  is the empirical chance of  $j$  within the quantized block. As a single first-order entropy quantity is probably not adequate to duvet the entire underlying characteristics of a block, we endorse

augmenting the characteristic vector with the aid of introducing a further element, i.e., the SD outlined by using

$$\sigma = \sqrt{\frac{1}{MN} \sum_j (f(j) - \mu)^2} \quad (9)$$

the place  $f(j)$  is the  $j$ th pixel in the block and  $\mu = (1/MN) \sum_j f(j)$  is the pattern imply over the entire samples within the block. Via together with this option detail, we are able to strengthen the classification performance as the data depressiveness and denseness will also be better mirrored.

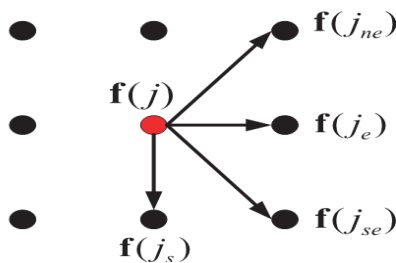


Fig.2 Illustration of the neighbors of  $f(j)$ .

In addition to the above feature components, we also include directional complexity indicators that encode the local geometric information. To this end, we define a four-tuple vector  $V = (v_1, v_2, v_3, v_4)$ , where

$$\begin{aligned} v_1 &= \sum_j |f(j) - f(j_{ne})| \\ v_2 &= \sum_j |f(j) - f(j_e)| \\ v_3 &= \sum_j |f(j) - f(j_{se})| \\ v_4 &= \sum_j |f(j) - f(j_s)| \end{aligned} \quad (10)$$

where  $f(j_{ne})$ ,  $f(j_e)$ ,  $f(j_{se})$ , and  $f(j_s)$  represent the neighbors in the  $45^\circ$  (northeast),  $0^\circ$  (east),  $-45^\circ$  (southeast), and  $-90^\circ$  (south) directions, relative to  $f(j)$ , as shown in Fig. 2. Upon the determination of the

feature vector  $\rho$ , we train a two-class SVM classifier with RBF (Gaussian) kernel [29] taking the for

$$\begin{aligned} Ker(X_i, X_j) &= e^{-\gamma \|X_i - X_j\|} \end{aligned} \quad (11)$$

The zero-class and 1-class correspond to the unencrypted and encrypted photo blocks, respectively. Here, the learning image set contains one hundred images of dimension  $512 \times 512$ , with a broad form of traits including average scenes, artificial snap shots, synthetic images, and textual images. The offline trained SVM classifier will probably be used to discriminate the encrypted and non-encrypted photograph patches within the method of information extraction and photograph decryption.

C. Joint Data Extraction and Picture Decryption

The decoder within the data core has the decryption key  $k$  and makes an attempt to recover both the embedded message and the long-established photograph at the same time from  $[[f]]^w$ , which is assumed to be flawlessly got without any distortions. Word that this assumption is made in just about the entire existing RIDH methods. As a result of the interchangeable property of XOR operations, the decoder first XORs  $[[f]]^w$  with the encryption key movement  $ok$  and obtains

$$f^\omega = [[f]]^\omega \oplus K. \quad (12)$$

The resulting  $f^\omega$  is then partitioned into a series of non overlapping blocks  $f_i^{w's}$  of size  $M \times N$ , similar to the operation conducted at the embedding stage. From (6), we have

$$\begin{aligned} f_i^\omega &= \\ f_i \oplus Q_{[w]_d} \end{aligned} \quad (13)$$

The joint knowledge extraction and photo decryption now turns into a blind sign separation trouble as both  $W_i$  and  $f_i$  are unknowns. Our approach of fixing this main issue is founded on the following statement:  $f_i$ , because the common photo block, in all probability displays detailed picture structure, conveying semantic information. Be aware that  $Q_{[w]_d}$  ought to

in shape probably the most elements in  $Q = Q_0, Q_1, \dots, Q_{S-1}$ . Then, if we XOR  $f_i^w$  with all  $Q_j$ 's, one of the results must be  $f_i$ , which might reveal structural know-how. As will grow to be clear shortly, the other outcome corresponds to randomized blocks, which will also be individual from the customary structured  $f_i$ . Extra particularly, we first create  $S$  decoding candidates with the aid of XOR ing  $f_i^w$  with all of the  $S$  viable public keys

$$f_i^{(0)} = f_i^w \oplus Q_0 = f_i \oplus Q_{[W_i]d} \oplus Q_0$$

$$f_i^{(1)} = f_i^w \oplus Q_1 = f_i \oplus Q_{[W_i]d} \oplus Q_1$$

$$f_i^{(S-1)} = f_i^w \oplus Q_{S-1} = f_i \oplus Q_{[W_i]d} \oplus Q_{S-1} \quad (14)$$

As mentioned earlier, one of the above  $S$  candidates must be  $f_i$ , while the others can be written in the form

$$f_i^{(t)} = f_i \oplus Q_{[W_i]d} \oplus Q_t \quad (15)$$

the place,  $t = [W_i]d$ . The outcome  $f_i^{(t)} = \text{Enc}(f_i, Q_{[W_i]d} \oplus Q_t)$  corresponds to an encrypted variant of  $f_i$  with

equivalent key circulation being  $Q_{[W_i]d} \oplus Q_t$ . Be aware that the entire public keys  $Q_j$ 's, for  $0 \leq j \leq S - 1$ , are designed to have maximized minimum Hamming distance, and the higher bound is given in (5). For this reason,  $f_i^{(t)}$  tends to lose the picture structural information, making it appear random. To identify which candidate corresponds to  $f_i$ , we follow the designed two-classification SVM classifier to these  $S$  candidates. Let  $r = (r_0, r_1, \dots, r_{S-1})$  be the vector recording the classification outcome, the place  $r_j = 0$  and  $r_j = 1$  correspond to the original (structured) and randomized blocks, respectively. If there exists a particular  $j$  such that  $r_j = 0$ , then we decode the embedded message bits as

$$W_i = [j]_2 \quad (16)$$

where  $[j]_2$  denotes the length- $n$  binary representation of  $j$  and  $n = \log_2 S$ . For example, if  $n = 3$  and  $j = 7$ , then  $[j]_2 = 111$ . Upon determining  $W_i$ , the original image block can be easily recovered by

$$f_i = f_i^w \oplus Q_{[W_i]d} \quad (17)$$

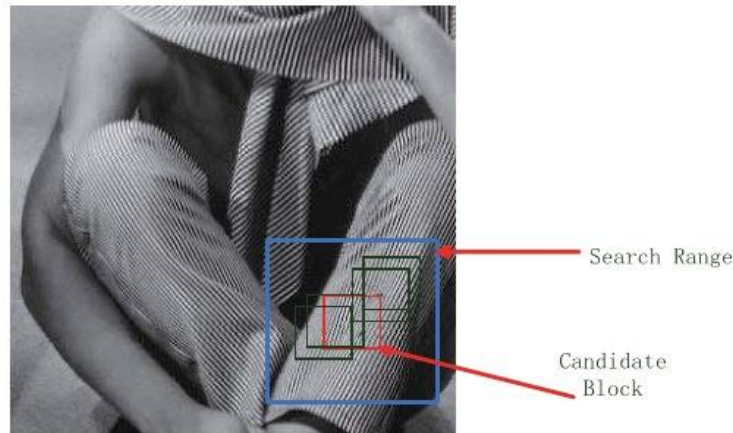


Fig.3 Illustration of the error correction mechanism based on image self similarity.

Nonetheless, we do notice a few circumstances the place there exist a couple of  $j$ 's or no  $j$  such that  $r_j = 0$ . When any of these two instances happens, it indicates that some decoding errors show up.

To formally analyze these error and later propose an mighty error correction mechanism, we define two types of classification mistakes.

- 1) Type I Error:  $f_i^{(j)} = f_i$ , while  $r_j = 1$ .
- 2) Type II Error:  $f_i^{(j)} = f_i$ , while  $r_j = 0$ .

Form I error almost always happens when the normal block  $f_i$  is very elaborate, e.g., from incredibly textured regions, behaving similarly as an encrypted block. Variety II error regularly arises when the block size is rather small, making an encrypted block mistakenly be categorized as an long-established unencrypted one. As validated experimentally from 200 scan photos of size  $512 \times 512$ , for a designated block, we anticipate that at most one form of error will occur. Beneath this assumption, both sort I and kind II mistakes can be conveniently detected.

Even for those incredibly textured pictures, it's discovered that similar blocks would be determined in a nonlocal window [30], as additionally shown in Fig. Four. In step with this phenomenon, the proposed error correction method is headquartered on the next key commentary: if a block is appropriately decoded, then with very high probability, there are some equivalent patches around it. This sort of property of nonlocal photograph similarity motivates us to rank the entire abilities candidate blocks in step with the minimal distance with the patches in a nonlocal search window. To this finish, we first outline a to-be-corrected set  $C$  via

$$C = \begin{cases} \{f_i^{(j)} | 0 \leq j \leq s - 1\} & \text{Type I error detected} \\ \{f_i^{(j)} | r_j = 0\} & \text{Type II error detected} \end{cases} \quad (19)$$

Variety I error detected type II error detected. (19) For any candidate block  $f_i^{(j)}$  in  $C$ , we calculate its 2 distances from all of the different blocks in a search variety  $D \setminus \{f_i^{(j)}\}$ , the place  $D$  shares the equal center as  $f_i^{(j)}$  and its dimension is experimentally decided as  $5M \times 5N$ . We then can compute the minimal patch distance inside the hunt window

$$d_i^{(j)} = \min_{D \in D \setminus f_i^{(j)}} \|f_i^{(j)} - D\|^2 \quad (20)$$

The place  $D$  is an arbitrary block of measurement  $M \times N$  inside  $D \setminus f_i^{(j)}$ . Here, we hire the straightforward MSE criterion when ranking the candidate blocks. Through including the feel course and scale into the above minimization framework, we could extra strengthen the error correcting performance, however

we find that the further attain is as a substitute restricted and the incurred complexity is giant. The candidate  $f_i^{(j)}$  that gives the smallest  $d_i^{(j)}$  is then selected because the decoded block.

Assume that the encryption is performed without destroying the constitution of JPEG bit flow. For instance, the encryption scheme proposed in can be utilized to this finish. We can XOR the encrypted parts with some of the designed  $S$  binary public keys, in step with the message bits to be embedded. On the extraction stage, we try all of the  $S$  potentialities and establish the one that generates structured snapshot patches in the pixel area. The embedded message can then be extracted based on the index of the identified public key.

**Protection analysis**

According to the context of the assault, the attacker could have access to special amounts of expertise. Naturally, the attacker as a minimum can entry to watermarked sign, specifically,  $[[f]]^w$ . In some events, the embedded message or the quilt sign will also be on hand to the attacker [31]. Accordingly, the security degree of the encrypted-area RIDH scheme should be assessed for distinctive contexts. Just like the drawback of evaluating the protection for encryption primitives, Cayre defined three forms of attacks.

- 1) The watermarked most effective attack (WOA), in which the attacker simplest has entry to watermarked portraits.
- 2) The recognized message attack, where the attacker has entry to a couple of pairs of previously watermarked pix and the related messages. Without doubt, the presently transmitted message bits aren't known to the attacker.
- 3) The recognized normal assault, where the attacker has access to a couple of pairs of earlier watermarked pics and the corresponding quilt photo. Surely, the current quilt photo will not be identified to the attacker. As defined in [31], the needs of the final two assaults are more often than not to recover the data hiding key, as a way to extract the long run embedded messages or hack distinctive portions of content material watermarked with the same key.

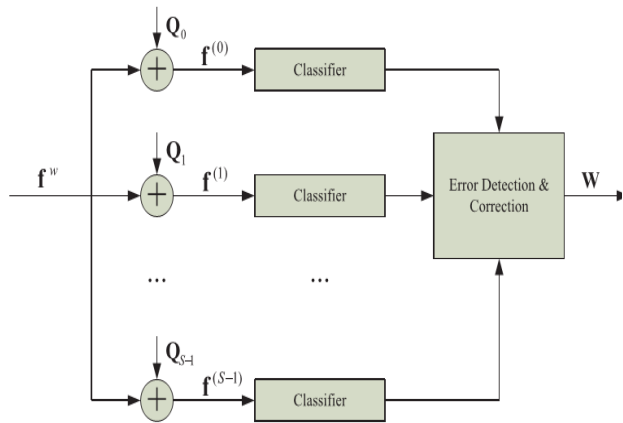


Fig.4 Schematic of the data extraction.

In our proposed RIDH scheme, the information hiding key has been eliminated, and for that reason, these two attack units usually are not relevant. Underneath the WOA, the one assault sort relevant to our scheme, the attacker attempts to extract the embedded message and/or get well the customary photograph from the watermarked and encrypted photo  $[[f]]^w$ . Before evaluating the security beneath WOA, allow us to first give the definition of message indistinguishability, which must preserve for any comfy encryption system. Definition of Message Indistinguishability—Concrete variant [32]:

We say that an encryption scheme (Enc, Dec) is (c, ) message indistinguishable if for every two messages G and G', and for each Boolean perform T of complexity no bigger than c, now we have

$$|P[T(Enc(K, G)) = 1] - P[T(Enc(K, G')) = 1]| \leq \epsilon \quad (21)$$

The place, the chance is taken over the randomness of Enc() and the alternative of k . The message indistinguishability implies that the attacker can do no higher than easy random guessing if he simplest observes the cipher textual content. This property is regarded as a general requirement for any cozy encryption scheme. We then have the following theorem involving the safety of our RIDH algorithm.

Theorem 1: Assuming that the encryption scheme (Enc, Dec) is secure in terms of message indistinguishability, then our RIDH process is relaxed

under WOA assault. Sketch of the Proof: once you have the watermarked and encrypted snapshot  $[[f]]^w$ , we can nonetheless partition it into non overlapping blocks of measurement  $M \times N$ . For every block, we can generate S decoding candidates in a similar fashion as (14)

$$f_i^{(0)} = [[f]]_i^w \oplus Q_0 = [[f]]_i^w \oplus Q_0 \oplus K_i = Enc(f_i^w \oplus Q_0 \oplus K_i)$$

$$f_i^{(1)} = [[f]]_i^w \oplus Q_1 = [[f]]_i^w \oplus Q_1 \oplus K_i = Enc(f_i^w \oplus Q_1 \oplus K_i)$$

$$f_i^{(S-1)} = [[f]]_i^w \oplus Q_{S-1} = [[f]]_i^w \oplus Q_{S-1} \oplus K_i = Enc(f_i^w \oplus Q_{S-1} \oplus K_i) \quad (22)$$

Where,  $K_i$  denotes the sub key flow for the  $i^{th}$  block. With any discovered  $f_i^{(j)}$ , it is computationally infeasible to figure out, with likelihood drastically higher than  $1/S$ , which one among  $f_i^w \oplus Q_0, f_i^w \oplus Q_1, \dots, f_i^w \oplus Q_{S-1}$  is the message encrypted by  $K_i$ , due to the property of message indistinguishability described in (21). For this reason, the attacker making an attempt to extract the embedded message bits from  $[[f]]^w$  should be equipped to do no higher than random guessing. This proves the protection of our proposed encrypted-domain RIDH technique against WOA attack.

#### IV. RESULTS

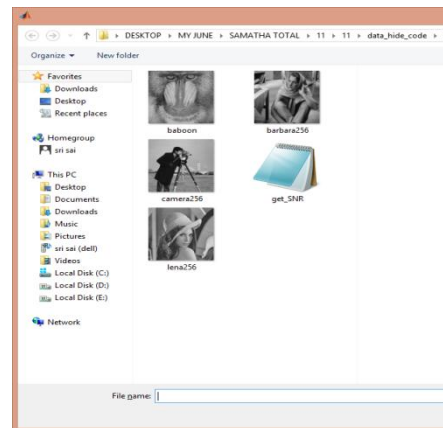


Fig.4.1 select an input image

There is a chance to select image for user from given image data base so for selected image will calculate the parameters

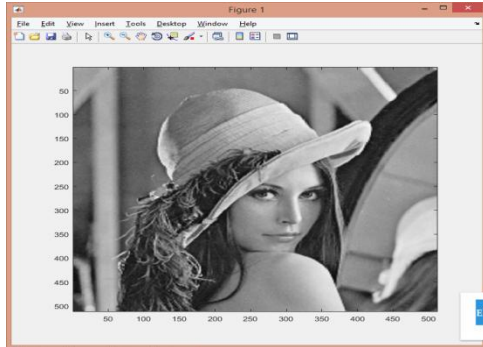


fig.4. 2 Input image selected by the user

lena.bmp image is selected for proposed implementation.and all the parameters are calculated for these leno.bmp

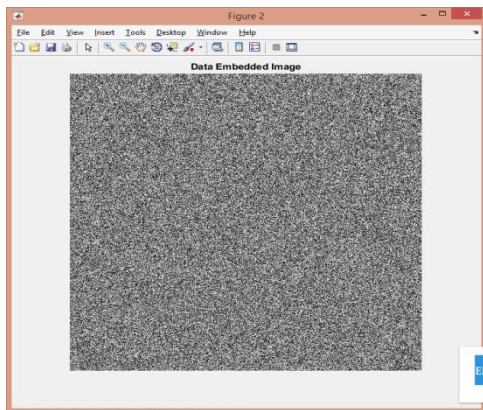


Fig.4.3 Data embedded image after encryption.

First we will apply public key cryptography and after that we will embed the data.

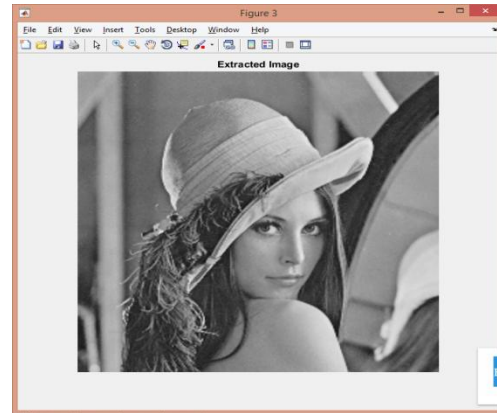


Fig.4.4 Extracted image

Finally with the help of SVM classifier we extracted data as well as image.

PERFORMANCE PARAMETRS FOR DIFFERENT IMAGES(PROPOSED[SVM])

Images	PSNR	ERR OR	ACCURACY	CAPACITY
Lena.bmp	27.29	0	100	16384
Baboon.bmp	27.47	0	100	16384
Cameraman .bmp	27.45	0	100	16384
Barbara.bmp	26.84	0	100	16384

Elapsed time is 27.3284 seconds.

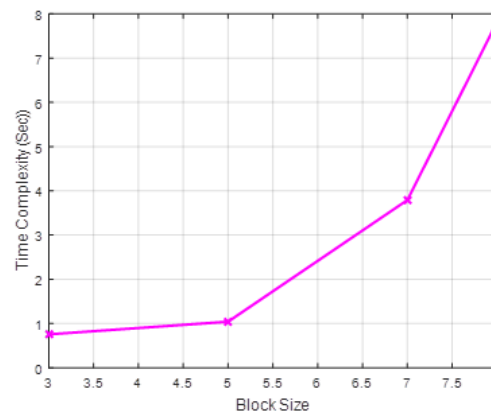
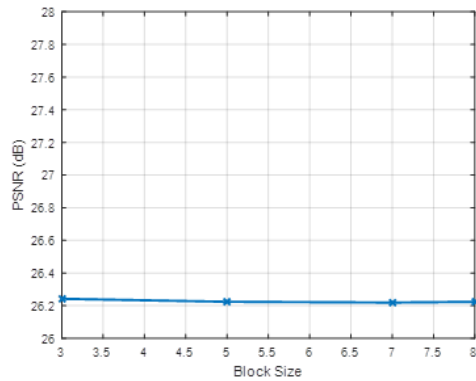
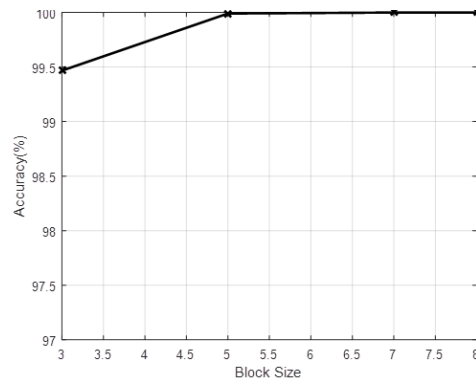


Fig.4 Block size vs. time complexity



**Fig.4 Block size vs. PSNR**



**Fig.4 Block size vs. accuracy**

## CONCLUSION

In this paper for the encryption process we are using RIDH method and the modulation can be done by public key. So no need to use any secret encrypt key and we can embed the information by using the XOR operations. in the side of decryption we are using Two-class SVM classifier to divide the encrypted and decrypted image. The proposed

experimental results giving better results compared to the previous methods. The SVM classifier is giving high efficiency.

## REFERENCES

- [1] M. U. Celik, G. Sharma, A. M. Tekalp, and E. Saber, "Lossless generalized-LSB data embedding," *IEEE Trans. Image Process.*, vol. 14, no. 2, pp. 253–266, Feb. 2005. [2] M. U. Celik, G. Sharma, and A. M. Tekalp, "Lossless watermarking for image authentication: A new framework and an implementation," *IEEE Trans. Image Process.*, vol. 15, no. 4, pp. 1042–1049, Apr. 2006.
- [3] Z. Ni, Y.-Q. Shi, N. Ansari, and W. Su, "Reversible data hiding," *IEEE Trans. Circuits Syst. Video Technol.*, vol. 16, no. 3, pp. 354–362, Mar. 2006.
- [4] X. Li, W. Zhang, X. Gui, and B. Yang, "A novel reversible data hiding scheme based on two-dimensional difference-histogram modification," *IEEE Trans. Inf. Forensics Security*, vol. 8, no. 7, pp. 1091–1100, Jul. 2013.
- [5] C. Qin, C.-C.Chang, Y.-H.Huang, and L.-T. Liao, "An inpaintingassisted reversible steganographic scheme using a histogram shifting mechanism," *IEEE Trans. Circuits Syst. Video Technol.*, vol. 23, no. 7, pp. 1109–1118, Jul. 2013.
- [6] W.-L. Tai, C.-M.Yeh, and C.-C. Chang, "Reversible data hiding based on histogram modification of pixel differences," *IEEE Trans. Circuits Syst. Video Technol.*, vol. 19, no. 6, pp. 906–910, Jun. 2009.
- [7] J. Tian, "Reversible data embedding using a difference expansion," *IEEE Trans. Circuits Syst. Video Technol.*, vol. 13, no. 8, pp. 890–896, Aug. 2003.
- [8] Y. Hu, H.-K. Lee, and J. Li, "DE-based reversible data hiding with improved overflow location map," *IEEE Trans. Circuits Syst. Video Technol.*, vol. 19, no. 2, pp. 250–260, Feb. 2009.

## Discrete Wavelet Transmission and Modified PSO with ACO Based Feed Forward Neural Network Model for Brain Tumour Detection

Machiraju Jayalakshmi<sup>1,\*</sup> and S. Nagaraja Rao<sup>2</sup>

**Abstract:** In recent years, the development in the field of computer-aided diagnosis (CAD) has increased rapidly. Many traditional machine learning algorithms have been proposed for identifying the pathological brain using magnetic resonance images. The existing algorithms have drawbacks with respect to their accuracy, efficiency, and limited learning processes. To address these issues, we propose a pathological brain tumour detection method that utilizes the Weiner filter to improve the image contrast, 2D- discrete wavelet transformation (2D-DWT) to extract the features, probabilistic principal component analysis (PPCA) and linear discriminant analysis (LDA) to normalize and reduce the features, and a feed-forward neural network (FNN) and modified particle swarm optimization (MPSO) with ant colony optimization (ACO) to improve the accuracy, stability, and overcome fitting issues in the classification of brain magnetic resonance images. The proposed method achieves better results than other existing algorithms.

**Keywords:** Discrete wavelet transformation, ant colony optimization, feed-forward neural network, linear discriminant analysis.

### 1 Introduction

Brain tumours are life-threatening growths faced by people of different age groups around the world. The pathological brain detection system (PBDS) was developed to check the human brain for the effects of tumours [Mohsin, Sheikh and Abbas (2009); Sanchez, Garcia, Angulo et al. (2010)] and has proven to be highly effective in directing health care practitioners to make correct decisions. Magnetic resonance imaging (MRI) is the advanced imaging technology used in the PBDS to analyse the human brain. In addition to this, MRI is radiation-free and non-invasive compared to CT scans and X-rays. Compared with other techniques, MRI produces clearer images of the brain tissue [Li, Chao and Zhang (2019)]. The aforementioned properties have made the MRI a popular tool for brain diagnosis. However, analysing the large volumes of brain images manually is a tedious task. Hence,

---

<sup>1</sup> Department of Electrical & Computer Engineering, JNTUA Anantapuramu, Andhra Pradesh, India.

<sup>2</sup> Department of ECE, G. Pulla Reddy Engineering College (Autonomous), Kurnool, Andhra Pradesh, India.

\* Corresponding Author: Machiraju Jayalakshmi. Email: jayaraju15phd@gmail.com.

Received: 25 May 2020; Accepted: 13 July 2020.

# Effect Of K-Fold Cross Validation on Mri Brain Images Using Support Vector Machine Algorithm

M.Jaya Lakshmi, S.Nagaraja Rao

**Abstract**—Recently, exact detection of the cancerous tumor in brain images is a critical task, especially at the early stage of the diseases. Various investigators have used machine-learning methods for the computer-aided diagnosis (CAD) to detect the tumor. In this paper an accurate and an automatic CAD system frame work has been done for verifying, the effect of K-fold cross validation for different values of k. K-means the segmentation technique is in the initial phase of the framework and the image is pre-processed for feature extraction and feature reduction using 2D-DWT and PCA respectively. The reduced features are given to the machine learning algorithm called the kernel support vector machine to classify magnetic resonance images. The K-fold stratified cross validation scheme is utilized to simplify the ability of the suggested strategy. The proposed method uses the different fold cross validation schemes, it is found that the RBF type kernel achieves the maximum classification with  $k=5$  for the given data set. This method of classification of MR brain images, can help radiologists to analyze whether the patient's stage is normal or abnormal.

**Keywords:** Brain tumor, principal component analysis, feature extraction, classification, segmentation, image de-noising, principal component analysis (PCA), two-dimensional discrete wavelet transform (2D- DWT), kernel support vector machine (KSVM).

## I. INTRODUCTION

The growth of unnatural cells which cannot be controlled, within the human body leads to Cancer. A collection or a mass of tissue, with those unnatural cells is known as a brain tumour. While brain tumours are not extremely normal, they are dangerous amongst the most deadly cancers [1], which leads to death.

Depending upon their originating point, brain tumours are classified as “fundamental brain tumours or metastatic brain tumours”. In fundamental type of brain tumours, the starting point of the cells is within the brain tissue itself, whereas in the other type of tumours, cells start destructing various body parts and expand into the “brain”. “Gliomas” are a kind of tumour cells that start growing from “glial cells”, found in the supportive tissue of the brain. The term “glioma” interprets various kinds of “gliomas”, extending to next range like “astrocytoma”. These growth of tumour arises from “star-shaped glial cells called astrocytes” and “Oligodendrocyte-gliomas”, which grow from cells that make the fatty substance which cover and protect nerves. The foremost widely known essential harmful brain tumour is Glioblastoma multiform (GBM), [2]. Different Medical

procedures, “Chemotherapy and Radiotherapy” are utilized for detecting and treating gliomas. [3].

Early stage analysis of gliomas is an important job in enhancing and giving treatment. Restorative Imaging methods, for example, “Positron Emission Tomography (PET), computerised axial Tomography (CT) and Magnetic Resonance Imaging (MRI)” are utilized to give important information like “shape, size, area and digestion of tumours aiding determination”. The standard procedure for tumour detection is MRI, as it is more comfortable and does not affect the human body, since there is no emission of harmful radiations. Various “MRI image series” are created by changing excitation and redundancy time while securing the image. These series deliver many kinds of tissue details, like division of tumours aboard their sub-regions. Four standard MRI modalities are utilized to analyse glioma, are shown in Figure. 1.

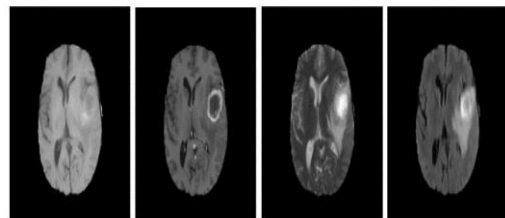


**Figure. 1. Four different standard models of MRI used for glioma diagnosis include T1, T2, T1-Gd and FLAIR.**

When “MRI images” are acquired from various sources, there is variation from one device to another. Around 150 frames of “2D images” are needed to make “3D brain images”. In general, by considering T1, healthy tissues are recognized, even though T2 are used, because they coincide with edema, and which makes the tumour to look bright. In T1-Gd, the border of the tumour is not clearly visible and cannot be recognized by the bright signal, in the dynamic cell area of tumour effected tissue. As “necrotic cells” do not cooperate with the differentiation operator, they are seen by hypo exceptional piece of the tumour core creating it conceivable to effortlessly portion from the dynamic cell space on a similar grouping. In FLAIR, an indication of water atoms are blocked, that helps in recognizing an edema distinct from Cerebrospinal Fluid (CSF) [4].

“Image segmentation” for instance, a pixel based appropriation, texture Distribution, and so on., are the

Revised Manuscript Received on April 05, 2019.

M.Jaya lakshmi, Research scholar, JNTUA., Department of ECE, G.Pullareddy Engineering College, Kurnool, India (jayaraju15kumar@gmail.com)

Dr.S.Nagaraja Rao, Professor, Department of ECE, G.Pullareddy Engineering College, Kurnool, India (deanece@gprec.ac.in)

# EFFECT OF K-FOLD CROSS VALIDATION ON MRI BRAIN IMAGES USING SUPPORT VECTOR MACHINE ALGORITHM

methods which converts an “image” into a limited number of segmented areas, considering a few characteristics which are non-overlapped. Segmentation of restorative images is necessary for some medicinal conclusions like radiation effect treatment, regions of interest (ROI) characterizing the “limit of tumour and intra cerebral brain haemorrhage”, etc. [5, 6]. Many methods depend on “fuzzy logic and Neural Networks (NN)” conveyance and so on... The division of therapeutic images is analysed using restorative analyses methods. Essentially, “image segmentation methods” are been characterized into three major classes: “based on edge, region, texture and pixel” [7].

“K-means clustering” which is a crucial system of “pixel-based techniques”. In which pixels are situated in cluster and they are generally low contrasted and unsupervised. The application of this segmentation method when compared to other alternative techniques, is more practicable [8, 9]. This paper suggests automatic strategy to detect, characteristics of Tumour cells utilizing “Morphological procedure” for smoothening the tumour [10-12].

Wavelet Transform is a prominent tool for extracting the features from Brain Images. This is one of the transformation method which results as a multi-resolution analytic property, which allows to study the images at various “levels of resolution” requiring large data storage and it is expensive form of data processing [13]. To overcome this and to increase the efficiency which is due to its dimensionality, in terms of data storage and cost effectiveness, PCA is used [14] which efficiently reduces the spatiality property of the “data” and therefore the “computational cost” for analysing the new data is reduced [17]. Then, the problem is the classification of the input data. At present, to solve this problem researchers have proposed many classification approaches of two different categories where one is supervised, which has “support vector machine (SVM) [16] and k-nearest neighbours (k-NN)” [18]. Self-organization feature map (SOFM) [15] and fuzzy c-means are classified as unsupervised form [19].

Good results are obtained from all these methods, and the supervised performance is better than unsupervised classifier considering the accuracy parameter. However, the good classifier methods have the classification accuracies less than 95%. In this paper among supervised classification methods, more accurate methods are found like “SVMs” classification method based on machine learning theory [20– 22].

Original “SVMs” are linear classifiers and have advantages like it avoids over fitting by considering less number of training samples, have good accuracy, and direct geometric interpretation, when compared to other like “decision tree, ANN, and Bayesian network” [23]. In this paper, we considered a non-linear SVM classifier, kernel SVMs (KSVMs), which is the extension of linear “SVMs” by applying the “kernel function” to replace the “dot product form in the original SVMs” [24]. The “KSVMs” is used to “fit the maximum-margin hyper-plane” in a transformed feature space. Since, the transformation is “nonlinear and the transformed space is of high dimension”, the classifier a “hyper-plane” in the high dimensional feature space is created which may be nonlinear within “the original input space”.

The remaining part of the paper is arranged in such a way that, Section 2 gives the methodology for this paper. Section 3 introduces the procedure of “K- fold cross validation”. Experiments in Section 4 includes a data set consisting of 160 images. Finally, in Section 5 the paper comes to a conclusion.

## II. METHODOLOGY

There are several pathological brain tumour detection systems (PBDS) which are utilized by many researchers for the classifying MRI brain image to be normal or abnormal. The PBDS consists of segmentation, pre-processing and classification. Among all the various segmentation algorithms, k-means segmentation algorithm which is generally used on “MRI” by several researchers. The segmented output, from which features are extracted by using “feature extraction method”, is done by wavelet transform in this paper. The features which are extracted are then dimensionally reduced using PCA. Then the reduced features are classified using SVM.

Recently, the “brain tumour” is the major cause of death, for different age groups. With the development of PBDS system, it is expected to give more detailed information for the radiologist about the tumour so that accurate decision can be taken for “better healthcare”. Using the imaging modality, the tumours can be identified and further processed for accurate classification of tumours for which we operate the image using different image processing tools. Many researchers have suggested various “pre-processing, segmentation and classification algorithms”. The “pre-processing” is done with a suitable filter, so that edges of the image are not affected and the noise is removed. The generalized block diagram for the detection of tumour, consisting of pre-processing, segmentation and classification is shown in Figure 2. The images which are to be tested undergo processes like “pre-processing, feature extraction, feature reduction, segmentation and classification of images”.

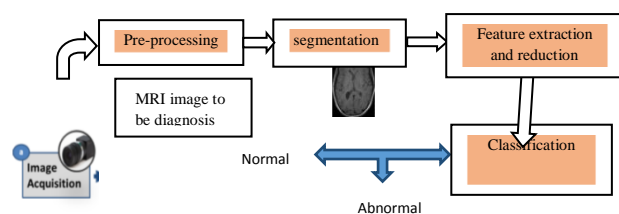


Figure 2. Process for detecting the brain tumour

### 2.1. preprocessing

This pre-processing method includes feature extraction and feature reduction.

#### 2.1.1. Feature Extraction

The Fourier transform (FT) is the most classical procedure for analysing the signal, and converts a time-domain into sinusoidal components of various

“frequencies”, thus, it converts the signal from “time domain to frequency domain”. However, it has a disadvantage, it discards some of the time details of the signal. As an example, “Fourier spectrum” does not give the information about the tumour existence for the physician.

To analyse a small portion of the signal at a given selected “time”, a method known as Gabor modified FT, called as “short-time Fourier transform” (STFT) or windowing is used. This method applies a mask of particular shape to the signal. This compromises the time and frequency information by providing little information about both. However, the window size restricts the data accuracy. “Wavelet transform” (WT) is also known as a “windowing technique” having “variable size”. Thus, it conserves both “frequency and time information of the signal” which is transformed. The signal analysis development of WT is in the Fig. 3.

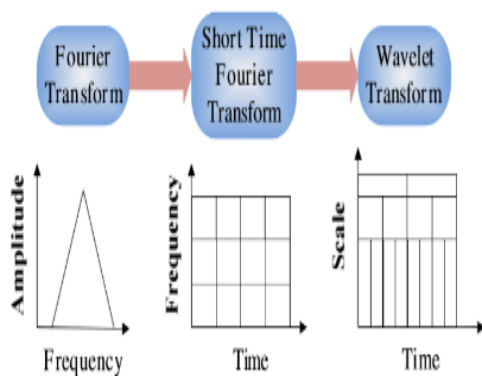


Figure. 3. The development of signal analysis

Additional benefit of “WT” is, rather than the traditional “frequency” parameter. It utilizes “scale”, it does not yield “time-frequency” however, it produces a signal of time-scale view, wherever it gives a different view for a data, which is a powerful and more natural way, when we compare to “frequency” & “scale” parameters, it is found that scale parameter is frequently used in the standard of living. Because large/small scale can be conveniently well understood than “in high/low frequency”.

2.1.1.1. Discrete Wavelet Transform

The “DWT” is good implementation of “Wavelet Transform” using “the scales and positions”. [24]. The fundamentals of “DWT” are discussed. Let square-integrable function  $be x(t)$ , then the “continuous WT” of  $x(t)$  is given, “ $W\psi(t)$ ” is mentioned as

$$W_{\psi(a,b)} = \int_{-\infty}^{\infty} x(t)\psi_{a,b}(t)dt \text{----- (1)}$$

Where,  $\psi_{a,b}(t) = (1/\sqrt{a})\psi\frac{(t-a)}{b}$  ----- (2)

Here, the “wavelet  $\psi_{a,b}(t)$ ” is considered by “translation and dilation of the mother wavelet  $\psi(t)$ ”: “ $a$ ” is the dilation factor and “ $b$ ” the translation parameter, with real positive numbers. There are a number of wavelets which are popular during the wavelet analysis development, out of which the important one is “Harr wavelet”, with lot of applications as it is the simplest one [25-27]. The Equation (1) is made discrete by limiting “ $a$ ” and “ $b$ ” to a discrete lattice for “ $a = 2^j$  and  $a > 0$  to give the DWT”, which can be expressed as.

$$ca_{j,k}(n) = DS[\sum_n x(n)g * j(n - 2^j k)i]$$

$$cd_{j,k}(n) = DS[\sum_n x(n)h * j(n - 2^j k)i] \text{----- (3)}$$

With respect to this, approximation-coefficients and detail components are  $ca_{j,k}$  and  $cd_{j,k}$ , respectively.  $h$  and  $g$  denote the transfer function of high-pass and low-pass filter, respectively.  $k$  and  $j$  determine the wavelet translation and scale factor, “DS” is the mathematical operator which implies the down sampling. The Equation (3) is of wavelet decomposition. In one level decomposition process, the signal  $x(n)$  is decomposed into 2 signals, which are the approximation and detail components. The above decomposition method is typically iterative with successive approximation, so that each signal is made into two components with numerous levels of resolution. The complete method is called “wavelet decomposition tree”, shown in Fig. 4.

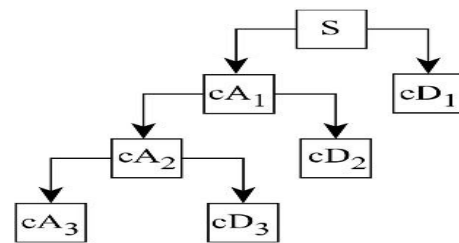


Figure 4. A 3-level decomposition tree of wavelet transforms.

2.1.1.2. 2D DWT

The DWT is applied individually to each dimension. Fig. 5 gives the “schematic diagram of DWT”. It consists of 4 sub-bands which are “LL, LH, HH, and HL images” at every level of decomposition. For further processing the LL is used.

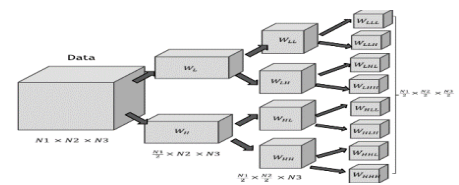


Figure5. The schematic diagram of 2D DWT.

Formation of more sub-signals and detailed information at larger temporal scales are seen sa the level of decomposition is increased. More information would give a better performance of the model, however might reduce the computing efficiency if more input neutrals and the model stability is decreased. However, it is necessary to select a suitable decomposition level for wavelet-neutral modelling. This is the way through which wavelet gives an easy “hierarchical framework” for getting more information. In mentioned algorithm, decomposition at level-3 using “Harr wavelet” was used to get features of image. The step by step process for feature extraction is given in algorithm 1[43].

**Algorithm 1.** Feature extraction.

**Require:**  $N$ : Total number of brain MR images having size  $K \times K$  taken for experiment  
**Ensure:**  $FM[1 : N, 1 : M]$ : Feature matrix,  $M$ : number of features  
 \* Function `waveAppCoeff()` computes the approximation coefficients of level-3 Haar wavelet and  $MRI_n$  is the  $n^{th}$  brain MR image

- 1: Initialize  $i \leftarrow 1, M \leftarrow K/8 \times K/8$  \* Total number of features to be extracted from the brain MR image
- 2: Create an empty matrix  $EM[1 : K/8, 1 : K/8]$  and empty vector  $FV[1, 1 : M]$
- 3: **for**  $n \leftarrow 1$  to  $N$  **do**
- 4:   Get  $MRI_n$
- 5:    $EM_n[1 : K/8, 1 : K/8] \leftarrow \text{waveAppCoeff}(MRI_n)$
- 6:   **while**  $i \leq M$  **do**
- 7:     **for**  $s \leftarrow 1$  to  $(K/8)$  **do**
- 8:      **for**  $t \leftarrow 1$  to  $(K/8)$  **do**
- 9:        $FV_n[1, i] \leftarrow EM_n[s, t]$
- 10:        $i \leftarrow i + 1$
- 11:      **end for**
- 12:     **end for**
- 13:   **end while**
- 14:  $FM[n, 1 : M] \leftarrow FV_n[1, 1 : M]$
- 15: **end for**

In the DWT the border distortion technique, digital filter is usually used. Once the digital filter is applied on to the image, at the edges the filter mask could extend beyond the image, the solution for that is to do the padding process to the pixels outside the images, which is done using a symmetric padding method [28].

2.1.2. Feature Reduction

There will be an increase in the computation period and memory storage, if there are more number of features in the image. Further, the classification, complication increases, which are meant as a curse of dimensionality. So there is a need for the researcher to reduce the features.

The most effective tool: PCA is used to reduce the least square reconstruction error and redundancy in the data set which consists of a more number of dependent variables in turn to reduce the dimensionality, while preserving many of the variations. This process can be done by mapping method where the input data set is mapped to a new set of ordered parameters considering their variance. This type of mapping method has three steps: the components of input vectors are normalized so that they do not correlate with each other. The resulting orthogonal components are arranged in such a way, that the elements with large variation are considered first in the data set and others are eliminated". The input vectors are normalized to possess zero mean and unity variance. Steps involved for implementing PCA is shown in figure 6.

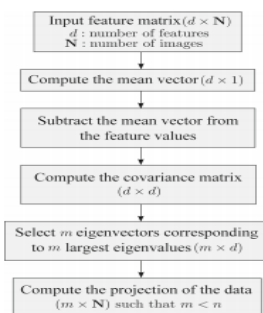


**Figure.6.** steps for PCA implementation.

2.2. K-means based segmentation

This method is broadly used for segmentation in biomedical applications among the different “clustering methods that are based on minimizing a formal objective function”. Modifications are done to the “K-means clustering method” which is unsupervised, statistical, non-deterministic and iterative, which makes the PBDS system faster, and more efficient. A main technique in pixel-based methods is this clustering technique. Compared with all different region or edge, pixel-based methods with clustering methods are simple and with low complexity for computation, the application is more practicable. The flow chart of “K-means based segmentation method” is in figure 7.

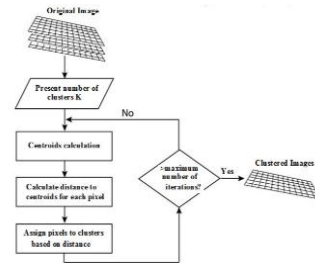


**Figure.7-Working flowchart of K-Means clustering method**

The main objective is to decrease the intensive distance computation, that takes place at iteration of this segmentation algorithm between all cluster centres and each data point. An easy mechanism is used to reduce the intensive distance between these two is, at each iteration, the space between them is computed and recorded in a data structure. Thus, in the successive iterations, “the distance between each data point and its previous nearest cluster is calculated again in an iterative manner”.

2.3. KERNEL SVM

An image of brain has 4 regions, “white matter (WM), background, grey matter (GM), and cerebra spinal fluid (CSF)”. To avoid the wrong classification risk, an input image is to be separated into four categories. In the field of a “machine learning”, the SVM is a landmark. The advantages of SVM contain high accuracy to solve the problem of classification, control to reduce over-fitting, good performance and direct geometric interpretation to classify accurately [29]. There is a rapid growth in advanced SVMs in the area of machine learning, among them KSVMs are popular and effective.

Advantages of KSVMs [30]: they are symmetric, in practice, they work very well and so they have been a success in bioinformatics, language categorization and computer vision which is remarkable; it has very few tuneable parameters, and training which often include optimization which are quadratic [31-36]. Later, solutions are global and distinctive, thus local minima displayed using alternative statistical learning methods which avoid convergence, like NNs. To classify data, SVMs constructs a hyper-plane, so that it does not have any classification



problem to locate the data on different sides of the hyper-plane. The kernel strategy is applied to this method [37, 38], the algorithm is same, except that a nonlinear kernel function is placed at inner product. The kernel is related to the transform function  $\psi(x_i)$  is given by  $k(x_i; x_j) = \psi(x_i)\psi(x_j)$ .

The value “w” is available in the “transformed space”, with w value  $\sum_i a_i y_i k(x_i, x)$ . Classification can be calculated with Dot products “w” by

$$w \cdot \psi(x) = \sum_i a_i y_i k(x_i, x).$$

In another perspective, this method permits to “fit to the greatest-margin on the hyper-plane of a feature space which is transformed”, which is of large dimension and the transformation may be nonlinear and however, the classifier consists of hyper plane within the large-dimensional feature space, in the first input, the space is nonlinear. For every kernel, there would be at a minimum of one change in the parameter to do the kernel more flexible and change the data which is practical.

### III. K- FOLD STRATIFIED CROSS VALIDATION

The given dataset is trained to the classifier, so the classification accuracy is high for this trained dataset when compared to other datasets. To escape from overfitting, we utilize cross validation process in our model. Because of which there will not be any increase the final classification accuracy. However, classification reliability can be improved and can be added to other independent datasets.

There are three validation methods: “K-fold cross validation, Random subsampling validation, and leave-one-out validation”. The properties of the first validation method are simple and easy to apply, and complete data is used for “training and validation” by researchers. To make a K-fold partition of the complete dataset, K times it is to be repeated to use “K-1 folds for training and a rest for validation, and finally average the error rates of K different experiments”. In this method, as K folds are often randomly partitioned, but, some of the folds could have different distributions compared to other folds. Where each fold has almost the same sort of distribution [39].figure 8 give the basics structure of “k-fold cross validation method”.

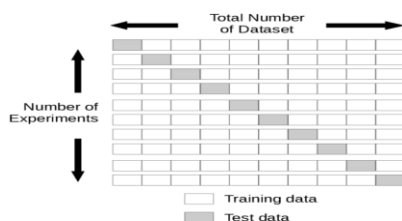


Figure 8. Basic k-folds for cross validation.

The present challenging situation is to take a decision about the number of folds required. If K value is taken too large, then bias will be small of the “true error rate estimator”, but large will be the variance of the estimator and its time-consumption is more. Alternatively, if small the K, there will be a decrease in time computation, variance of the estimator is small, but more will be the estimator bias [40]. During this, we change the “K values from 3 to 10” by

varying with a factor 1, and there after the SVM is trained for every value. As a result, we hereby we take the best value of K, where we are supposed to get the “largest classification accuracy”.

### IV. RESULTS AND DISCUSSIONS

The process is done with T2, as these images possess high contrast and vision is clear when compared to that of T1 and PET modals. 20 images are randomly selected from each type of brain. Since, we have different kinds of MRI images within the dataset collected, one hundred sixty images are considered, out of which 20 are normal and rest of them are abnormal brain images.

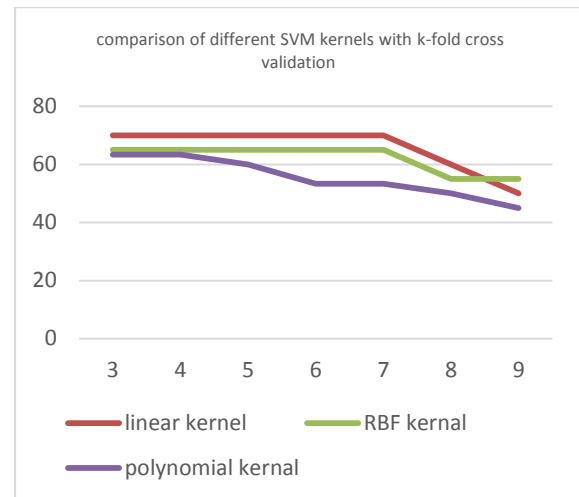


Figure 9. A Comparison of different SVM kernels accuracy on y-axis and different k-fold cross validation on x-axis.

The statistical measures for analyzing are:

*Sensitivity* (true positive fraction), measures the proportion of actual positives that are correctly identified, which is given by the formula,

$$\frac{TP}{TP + FN}$$

*Specificity* (true negative rate fraction), measures the proportion of actual negatives that are correctly identified, which is given by the formula,

$$\frac{TN}{TN + FP}$$

*Accuracy*: The degree to which the result of a measurement, to the correct value or a standard.

$$\frac{TP + TN}{TP + TN + FP + FN}$$

By observing the plot in figure 9, which is the effect of the cross validation on different SVM kernels. We can say that the 5 cross validation of all the SVM kernel behaviour is horizontal and it is utilized as it gives high classification accuracy for the given data set as shown in the figure 10.

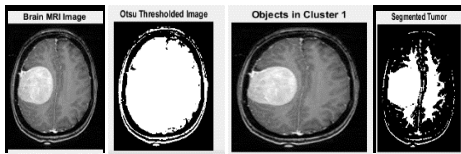


Figure 10. The MRI images with the DWT+PCA+KSVM with 5-cross validation.

### V. CONCLUSIONS

In the article, “DWT with PCA and KSVM technique” for checking the effect of k-fold cross validation for various MRIs of the brain have been used. For which three completely different kernels have been chosen which are LIN, IPOL and GRB. Wherever GRB-KSVM is obtained, classification accuracy of 99.38% on 160 MR images, is more when compared to IPOL and GRB kernels.

The future of this work can be further extended considering these four analyzations: The SVM is the primary method which may be utilized for “MR images” of other kinds. The other one is by using different advanced transformation methods for the execution and consumption time to be reduced, Multi-classification that centers on specific diseases to avoid any mistreatment. Finally by the usage advanced kernels, the classification accuracy can be increased.

The information extracted from the images using DWT is more efficient with less loss. Spatial resolution is the advantage of DWT over DFT, after that, feature reduction is to be done if not, we would like a large search space which can cause significant computation risk that leads to decrease in accuracy of classification [41,42]. There are many good feature extracting methods such as Curvelet, Ridgelet, extreme learning etc. in Future one can specialise the work and the performance of those algorithms considering parameter metrics.

In this proposed DWT+PCA+KSVM Model used to extract brain tumour is with GRB kernel technique is superior to other kernels SVMs. As GRB kernel is an exponential function, because of which it can increase the distance between samples for which HPOL cannot. Therefore, GRB kernel is the better one to apply for other mechanical fields.

### REFERENCES

- 1 De Angelis L M. Brain Tumors. N. Engl. J. Med. 2001; 344:114-23.
- 2 Deimling A. Gliomas. Recent Results in Cancer Research vol 171. Berlin: Springer; 2009.
- 3 Stupp R. Malignant glioma: ESMO clinical recommendations for diagnosis, treatment and follow-up. Ann Oncol 2007; 18(Suppl 2):69-70.
- 4 Drevelgas A and Papanikolou N. Imaging modalities in brain tumors Imaging of Brain Tumors with Histological Correlations. Berlin: Springer; 2011; chapter 2:13-34.
- 5 M. Masroor Ahmed and Dzulkifli Bin Mohamad "Segmentation of Brain MR Images for Tumor Extraction by Combining Kmeans Clustering and Perona Malik Anisotropic Diffusion Model" International Journal of Image Processing, Volume(2)Issue(1),2010.
- 6 Arash Azim Zadeh Irani and Bahari Belaton "A K-means Based Generic Segmentation System" 2009 Sixth International Conference on Computer Graphics, Imaging and Visualization.
- 7 Ming-Ni Wu, Chia-Chen Lin and Chin-Chen Chang "Brain Tumor Detection Using Color-Based K-Means Clustering Segmentation" International Conference on Computer Graphics, 2009.

- 8 S.Sathish Kumar, M.Moorthi, M.Madhu3and Dr.R.Amutha "An Improved method of Segmentation using Fuzzy-Neuro Logic"Second International Conference on Computer Research and development, 2009.
- 9 S.Murugavalliand,V.Rajamani"An improved Implementation of Brain tumor Detection Using Segmentation Based on Neuro Fuzzy Technique", Journal of Computer Science,3,2007october.
- 10 Kharrat, A. Benamrane, N. Ben Messaoud, M. Abid, Computer. & Embedded System Lab.(CES),Nat.Eng.Sch.of Sfax,Tunisia,Nov.2009.
- 11 M. Schmidt, I. Levner, R. Greiner, A. Murtha, and A. Bistriz. "segmenting Brain Tumors using Alignment-Based Features". International Conference on Machine Learning and Applications, Los Angeles,December 2005.
- 12 S.R. Kannan ,Jan. 2005 "Segmentation of MRI using new Unsupervised Fuzzy Cmeansalgorithm,"ICGST-GVIPJournal,Volume5,Issue2.
- 13 Emin Tagluk., et al., "Classification of sleep apnea by using wavelet transform and artificial neural networks, " Expert Systems with Applications, Vol. 37, No. 2, 1600–1607, 2010.
- 14 Zhang, Y., et al., "A new classifier for polarimetric SAR images, " Progress in Electromagnetics Research, Vol. 94, 83– 104, 2009.
- 15 Camacho, J., et al., "Corrigendum to “The best approaches in the on-line monitoring of batch processes based on PCA: Does the modelling structure matter?” [Anal. Chim. Acta Volume 642 (2009) 59-68], " Analytica Chimica Acta, Vol. 658, No. 1, 106–106, 2010.
- 16 Chaplot,S., et al., "Classification of magnetic resonance brain images using wavelets as input to support vector machine and neural network, " Biomedical Signal Processing and Control, Vol. 1, No. 1, 86–92, 2006.
- 17 Cocosco, C. A., et al., "A fully automatic and robust brain MRI tissue classification method, " Medical Image Analysis, Vol. 7, No. 4, 513–527, 2003.
- 18 Zhang, Y. ., et al., "Weights optimization of neural network via improved BCO approach, " Progress In Electromagnetics Research, Vol. 83, 185–198, 2008.
- 19 Yeh, ., et al., "A hierarchical genetic algorithm for segmentation of multi-spectral human-brain MRI, " Expert Systems with Applications, Vol. 34, No. 2, 1285–1295, 2008.
- 20 Patil, N. S., et al., "Regression models using pattern search assisted least square support vector machines, " Chemical Engineering Research and Design, Vol.83, No.8, 1030–1037, 2005.
- 21 Wang, F., et al., "The support vector machine for dielectric target detection through a wall, " Progress In Electromagnetics Research Letters, Vol. 23, 119–128, 2011.
- 22 Xu, Y., et al., "An support vector regression based nonlinear modeling method for Sic mesfet, " Progress In Electromagnetics Research Letters, Vol. 2, 103–114, 2008.
- 23 Li, D., et al., "Classification of foreign fibers in cotton lint using machine vision and multi-class support vector machine, " Computers and Electronics in Agriculture, Vol.4, No.2, 274–279, 2010.
- 24 Gomes, T. A. F., et al., "Combining meta-learning and search techniques to select parameters for support vector machines, " Neuro computing, Vol. 75, No. 1, 3–13, 2012.
- 25 Hable, R., "Asymptotic normality of support vector machine variants and other regularized kernel methods, " Journal of Multivariate Analysis, Vol. 106, 92–117, 2012.
- 26 Howard Lee ., et al., “Image based computer aided diagnosis system for cancer detection”, Expert Systems with Applications 42 (2015) 5356–5365.
- 27 Zhang Y ., et al., “Feature extraction of brain MRI by stationary wavelet transform,” in Proc. Int. Conf. Biomed. Eng. Comput. Sci., Wuhan, China, 2010, pp. 1–4.
- 28 Messina, A., “Refinements of damage detection methods based on wavelet analysis of dynamical shapes,” International Journal of Solids and Structures, Vol. 45, Nos. 14–15, 4068–4097, 2008.
- 29 Martiskainen, P., et al., “Cow behaviour pattern recognition using a three-dimensional accelerometer and support vector machines,” Applied Animal Behaviour Science, Vol. 119, Nos. 1–2, 32–38, 2009.



- 30 Bermejo, S., B. Monegal, and J. Cabestany, "Fish age categorization from otolith images using multi-class support vector machines," *Fisheries Research*, Vol. 84, No. 2, 247–253, 2007.
- 31 Muniz, A. M. S., et al., "Comparison among probabilistic neural network, support vector machine and logistic regression for evaluating the effect of subthalamic stimulation in Parkinson disease on ground reaction force during gait," *Journal of Biomechanics*, Vol. 43, No. 4, 720–726, 2010.
- 32 Bishop, C. M., "Pattern Recognition and Machine Learning" (Information Science and Statistics), Springer-Verlag New York, Inc., 2006.
- 33 Vapnik, V., "The Nature of Statistical Learning Theory," Springer-Verlag New York, Inc., 1995.
- 34 Jeyakumar, V., et al., "Lagrange multiplier characterizations of robust best approximations under constraint data uncertainty," *Journal of Mathematical Analysis and Applications*, Vol. 393, No. 1, 285–297, 2012.
- 35 Cucker, F. and S. Smale, "On the mathematical foundations of learning," *Bulletin of the American Mathematical Society*, Vol. 39, 1–49, 2002.
- 36 Poggio, T. and S. Smale, "The mathematics of learning: Dealing with data," *Notices of the American Mathematical Society (AMS)*, 388 Zhang and Wu Vol. 50, No. 5, 537–544, 2003.
- 37 Acevedo-Rodríguez, J., et al., "Computational load reduction in decision functions using support vector machines," *Signal Processing*, Vol. 89, No. 10, 2066–2071, 2009.
- 38 Deris, A. M., et al., "Overview of support vector machine in modeling machining performances," *Procedia Engineering*, Vol. 24, 308–312, 2011.
- 39 May, R. J., et al., "Data splitting for artificial neural networks using SOM-based stratified sampling," *Neural Networks*, Vol. 23, No. 2, 283–294, 2010.
- 40 Armand, S., et al., "Linking clinical measurements and kinematic gait patterns of toe-walking using fuzzy decision trees," *Gait & Posture*, Vol. 25, No. 3, 475–484, 2007.
- 41 El-Dahshan, et al., "Hybrid intelligent techniques for MRI brain images classification," *Digital Signal Processing*, Vol. 20, No. 2, 433–441, 2010.
- 42 Evans, A. C., et al., "Brain templates and atlases," *NeuroImage*, Vol. 62, No. 2, 911–922, 2012.
- 43 D. R. Nayak, R. Dash, B. Majhi, "Brain MR image classification using two-dimensional discrete wavelet transform and AdaBoost with random forests", *Neurocomputing*, Vol. 177, 188–197, 2016.

## BIBLIOGRAPHY



international level.

Dr. S. Nagaraja Rao, Professor & Dean of ECE dept., G. Pulla Reddy Engg College, Kurnool. Received his Ph.D. degree from JNTUA, Anantapuramu, Andhra Pradesh, in 2011. His area of interest is communication systems, Image & Signal processing. He is a professional member of ISTE and ISOI. He is authorised for more than 50 papers in journals and conferences at



image processing.

M. Jayalakshmi, Research scholar received her M.Tech degree in the year 2010 from SK University, Anantapuram, India. She is currently pursuing Ph.D. degree from JNTUA, Anantapuramu, and Andhra Pradesh. Her current research includes biomedical

# Efficient Image Enhancement Techniques Applied on Medical Imaging-A State- of- The Art Survey

Munipraveena Rela, S. Nagaraja Rao, P. Ramana Reddy

**ABSTRACT---** *Medical image Enhancement is very crucial part to improve quality of medical images and to detect the diseases in the image. In this paper, a few image enhancement techniques used in literature are discussed. We also discussed different image quality parameters used to measure the quality of images. We also compared all the methods discussed in literature.*

**Index Terms—** *Computed tomography images, denoising, image enhancement, and Image fusion.*

## I. INTRODUCTION

Now a days, Medical images are very much essential to obtain information about internal organs. Usually Computed tomography, MRI and PET images are used to analyze internal organs. Most of the medical images are degraded with noise and other artifacts. Medical image enhancement is very important to enhance low contrast images for diagnosis purpose. In this paper, Section 2 gives a literature review. Section 3 describes CT image denoising methods. Section 4 includes the parameters used to measure the image denoising performance.

## II. RELATED WORK

[1] Zohair Al-Ameen, developed a method of enhancement in spatial domain. This technique is applied directly on entire image instead of processing each and every pixel of the image. The following procedure is used to enhance the image: (i) obtain the size of processed image, (ii) calculate the enhancement variable (K) calculated using the following equation:

$$K = \frac{\sum_{i=1}^i \sum_{j=1}^j x(i, j)}{m \times n}$$

Where x is the degraded image of size m X n. Finally, the image is enhanced using value k as shown in the following equation:

$$EI = \frac{[x - \min(x)] \times e^K}{[\max(x) - \min(x)]}$$

In [2] Fathi KALLEL, a technique for low contrast CT image enhancement is proposed. The algorithm is as follows: DWT is applied to the image, then SVD of LL sub

band is obtained, then an adequate correction factor is used to generate an enhanced LL component, then inverse SVD is applied, then LL sub-band image is categorized into two classes as low contrast and moderate contrast classes, then adaptive dynamic gamma correction function and finally inverse DWT is applied

[3] P. Sreeja, used following procedure: The image is filtered using range filter with 7X1 and 1X7 kernel and added filtered images together to get edge of the image. The Gaussian low pass filter and gradient magnitude is used to smoothen the image and to enhance the edges of image respectively. The fusion rule are applied to the input image and to the Gaussian filtered image. To obtain better texture enhancement, fused the original image and Gaussian image. The better edge enhancement is obtained by fusing gradient magnitude image with the original image.

In [4] Manoj Diwakar, recommended a denoising technique which can be used for two identical images with uncorrelated noise. In this denoising method, noise in the first input image is eliminated by applying non-local means (NLM) filter and a wavelet packet thresholding technique is used to eliminate noise in the second image. The output due to NLM filter gives very good noise suppression but the small details of the input image would not be recovered properly. To recover small details of input image, the wavelet packet thresholding technique using correlation is used. This method is outstanding for noise suppression and structure preservation.

In [5] Khakon D, A Denoising scheme using Haar wavelet transform for brain images is proposed. To enhance the brain images, combine two images of brain obtained using two different modalities is image fusion. Modified Haar wavelet transform using lifting and in-place calculation has shown efficient performance relating to denoising parameters.

In [6] Huafeng Li, designed a low-rank sparse component de- composition and dictionary learning method for fusion, denoising, and improving quality of medical images. Specifically, in the dictionary learning model, low-rank and sparse regularization are used to increase the capability of the learned dictionaries. Additionally, in the image decomposition model, the sparse component is designed using a weighted nuclear norm and sparse constraint to eliminate noise and reserve textural details. Lastly, the fused image is obtained by merging the low-rank and sparse components of the source images.

**Revised Manuscript Received on April 05, 2019.**

**Munipraveena Rela**, Research Scholar, Jawaharlal Nehru Technological University Anantapuramu, Anantapuramu. (E-mail: chagpraveena@gmail.com)

**S. Nagaraja Rao**, Professor, Department of ECE, G. Pulla Reddy Engineering College (Autonomous), Kurnool .(E-mail: Suryakari2k9@gmail.com)

**P. Ramana Reddy**, Professor, Department of ECE, JNTUA College of Engineering, Anantapuramu, India. (E-mail: prjntu@gmail.com)



In [7] Jinlan Guan, a medical image enhancement method by using fractional differential and directional derivative is presented. This method is based on the image edge, clarity, texture information and structural features of different pixels, as well as the directional derivative of each pixel in constructing the masks. This method improves both high frequency content and low frequency content of the image. Finally, this method improves the texture information of the image.

[8] Ebenezer Daniel, proposed a dynamic unsharp masking technique using Optimum wavelet based masking (OWBM)

[9] Xuehang Zheng, proposed a PWLS (penalized weighted least squares) using Union of Learned TRAnsforms (PWLS-ULTRA) reconstruction method. The square transforms union is designed from several patches of image taken from CT images. The PWLS-based cost function is improved by interchanging between a clustering step, a sparse coding, and CT image reconstruction step. A Lagrangian technique with ordered-subsets is used to reconstruct the CT image reconstruction so that it decreases the forward and back projections. For both low-dose level and normal-dose level, this technique considerably increases reconstructed image quality when it is compared to PWLS-EP (PWLS with a non-adaptive edge preserving regularizer) reconstruction. This method gives better results in image reconstructions compared to a single learned square transform. Image quality and uniformity image resolution can be improved when PWLS-ULTRA designed using weights based on patches.

### III. CT IMAGE DENOISING METHODS

There are various methods present for image denoising [11,12]. Generally, image denoising can be done in : (i) transform domain methods and (ii) spatial domain methods

#### A. Spatial domain filtering

Spatial filters reduce noise in original noisy image by applying spatial filtering mask directly on all pixels of original input. Spatial filters are: (1) linear spatial filters and (2). non-linear spatial filters.

##### a. Linear and non-linear filters

Linear filters are used to decrease the noise in spatial domain but the details over the images cannot be obtain properly. The Gaussian noise can be reduced by mean filtering but this filter blurs the image if it contains high frequency noise component. Non-linear filters like median filter is used to remove impulse noise. A low pass filter in spatial domain operated on neighborhood of pixels by considering that the noise occupied at the high frequency. Generally, linear filters also introduces blur in the image.

The low contrast CT image quality is not good when compared with high dose CT images. Low contrast images in the CT occur when the photon detectors receive less information. Low contrast images are also used in diagnostic when the quality of these low contrast CT images will be enhanced by using image processing algorithms [10].

##### b. Non-local means (NLM) and Bilateral filters

Non local mean filter replace each and every pixel in input using a weighted average from a specified region of image. Bilateral filter is a non-linear, smoothing, noise-reducing, and edge enhancement filter. Both Non-local means filters and bilateral give good output in relations to noise decrease and enhancing the details of image.

#### B. Transform domain filtering

Wavelets are functions used to decompose image into dissimilar frequency constituents. Wavelet transform is a technique for image processing applications due to its localized in frequency, sub banding, multi-resolution analysis, and time domain.

##### a. Wavelet Transformed based denoising

In DWT, two parameters should be defined. First, a wavelet function is used for decomposition. The decomposition can be done by following wavelet decomposition filter: haar, meyr, dmey, db, sym, coif, bior, rbio, gaus, and etc. Next, decomposition level is chosen for thresholding all sub bands. The procedure for noise removal using wavelet can be expressed as follows:

- low frequency and high frequency coefficients of the image is obtained by using wavelet transform.
- Evaluate noise variance.
- Thresholding is applied on detail parts.
- Denoised image is obtain by applying Inverse wavelet transform.

Wiener filter (Linear filter) in the wavelet domain produce better results when gaussian noise is present in the image. However, this filter did not produce visually accepted result, but the filtering operation effectively decreases the MSE.

The another best method in Wavelet Transform based denoising is the non-linear method using thresholding. In this method, a threshold value is determined. Large wavelet coefficients are not disturbed and small wavelet coefficients in high frequency sub-bands are eliminated by using this value. Thresholding methods are used to eliminate unwanted values, to pre-serve significant coefficient values, and for noise elimination [10].

Histogram methods are used to evaluate distribution of intensity values in the image so that the valleys, peaks, and curves of the histogram can be obtained. Clustering-based methods is applied to clustered the image into different parts. The histogram of background and foreground can be represented as probability distribution function as two Gaussian distributions. Thresholding can be done by an entropy-based method.

##### b. Non-Subsampled Contourlet Transform(NSCT) based enhancement

The NSCT is the enhanced Contourlet transform, which may excellently solve the matter of artefact development within the increased curve image. Moreover, selecting the improvement perform and also the NSCT filter can directly influence the image improvement impact.

In [12], the input image is disintegrate into the NSCT domain with a low frequency, and a different high-frequency sub-bands. Linear transformation is considered for the coefficients of the low frequency sub-band. Adaptive thresholding methodology is employed for removing noise in the high-frequency sub-bands. Then, the inverse of NSCT is used to reconstruct sub-bands of low and high frequency into spatial domains. Finally, the fine details of the reconstructed image are enhanced by unsharp masking.

In [13], the NSCT and the enhancement function with nonlinear characteristic are used to improve the image quality. Initially, a sine gray-scale transform is considered as the factor to improve the image quality and this is a transform function of nonlinear nature. Second, the NSCT is employed to obtain both low frequency component and high frequency component. Then, the enhancement function is employed to the NSCT coefficients. Lastly, the NSCT is inversed to get the improved image.

The Contourlet transform is built by the Laplacian pyramid (LP) filter and directional filter bank (DFB). it has multi-direction, multi-resolution, and locality characteristics. The Contourlet transform is translation-variant due to its filter bank structure. Further, Contourlet transform can induce the artefact within the enhanced image. but the NSCT is built by the non-subsampled pyramid (NSP) and non-subsampled directional filter bank (NSDFB) it has the translational invariance and also good frequency selectivity and regularity.

The diagram of the NSCT is as shown in Fig.1. The decomposition levels are three and also the directional numbers are four, eight, and sixteen respectively.

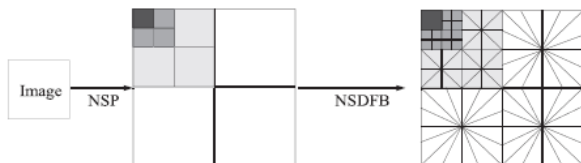


FIG. 1. The NSCT decomposition.

### c. Threshold estimation

Selection of a threshold value for CT image denoising is a very difficult for edge enhancement and noise reduction. If threshold value is small, then noise will not be eliminated completely. If threshold is high value, then image becomes blurry. There are various algorithms used to select appropriate threshold value. There are three methods of threshold estimation are VisuShrink, SureShrink, and BayesShrink. VISUShrink is a non-adaptive global threshold, which has only one threshold value for complete image, this value is obtain from all pixel values in the image. This global threshold is used to all decomposition levels. The input image is over smoothed by using VisuShrink method.

SureShrink thresholding is based on a sub band adaptive threshold. A different threshold is obtained for each sub band using Steins unbiased risk estimator (SURE). BayesShrink utilizes a Bayesian mathematical framework and undertakes generalized Gaussian distribution for the

wavelet coefficients in each detail sub band to obtain the threshold.

## IV. MEASURES OF IMAGE DENOISING PERFORMANCE RESULTS

SSIM is Structural Similarity Index defined as:

$$SSIM(X, R) = \frac{(2\mu_X\mu_R + C_1)(2\sigma_{XR} + C_2)}{(\mu_X^2 + \mu_R^2 + C_1)(\sigma_X^2 + \sigma_R^2 + C_2)}$$

where  $C_1$  and  $C_2$  are predefined constants,  $\mu_X$ ,  $\mu_R$  are the averages of  $X$  and  $R$ ,  $\sigma_X^2$ ,  $\sigma_R^2$  are the variance of  $X$  and variance of  $R$  respectively,  $\sigma_{XR}$  is the covariance between  $X$  and  $R$ . The values of SSIM is varies from  $-1$  to  $1$ . The value  $1$  shows good results.

The Image Quality Index (IQI) is:

$$IQI = \frac{4\sigma_{XR}\bar{X}\bar{R}}{(\sigma_X^2 + \sigma_R^2)((\bar{X})^2 + (\bar{R})^2)}$$

Where

$$\begin{aligned} \bar{X} &= \frac{1}{N} \sum_{i=1}^N X_i, \\ \bar{R} &= \frac{1}{N} \sum_{i=1}^N R_i, \\ \sigma_X^2 &= \frac{1}{N-1} \sum_{i=1}^N (X_i - \bar{X})^2, \\ \sigma_R^2 &= \frac{1}{N-1} \sum_{i=1}^N (R_i - \bar{R})^2 \\ \sigma_{XR} &= \frac{1}{N-1} \sum_{i=1}^N (X_i - \bar{X})(R_i - \bar{R}) \end{aligned}$$

The range of IQI is between  $1$  and  $-1$ . The value  $1$  shows that input image pixel is equal to output image pixel.

The Peak Signal to Noise ratio is:

$$PSNR = 10 \times \log_{10} \left( \frac{255 \times 255}{MSE} \right)$$

Where mean square error, is

$$MSE = \frac{1}{mn} \sum_{i=0}^{m-1} \sum_{j=0}^{n-1} [X(i, j) - R(i, j)]^2$$

Root mean square error can be given as:

$$RMSE = \sqrt{MSE}$$

Absolute Mean Brightness Error (AMBE) is given as

$$AMBE(x, y) = |X_m - Y_m|$$

Where  $X_m$  is input image mean and  $Y_m$  is output image mean. For the brightness preservation, The AMBE value should be very less.

Entropy is used to describe the input image texture.

Entropy Difference (ED) is given as  $ED = SE(X) - SE(R)$ .

Shannon entropy (SE) is given by following equation:

$$SE = -\sum_i X_i \log X_i^2.$$

DIV, difference in variances is given as

$$DIV = 1 - \frac{\sigma_R^2}{\sigma_X^2}.$$



# EFFICIENT IMAGE ENHANCEMENT TECHNIQUES APPLIED ON MEDICAL IMAGING-A STATE- OF- THE ART SURVEY

Where X is input image and R is denoised image  
Table I gives various image enhancement methods, it's methodology, and different parameters.

If the values of RMSE, ED and DIV closer to 0 indicates that the performance algorithm gives better results.

**Table I: image enhancement Techniques, It's Methodology**

S.No	Reference	Methodology	Parameters measured	Remarks
1	[1]	Spatial domain method $K = \frac{\sum_{i=1}^i \sum_{j=1}^j x(i,j)}{m \times n}$ $EI = \frac{[x - \min(x)] \times e^K}{[\max(x) - \min(x)]}$	Universal Image Quality Index (UIQI)	Fast implementation due to normalization technique
2	[2]	Using DWT and SVD	Mean, STD, PSNR, WPSNR, QRCM	Transformation is applied only on low frequency image details.
3	[3]	Fusion rules applied on Gaussian filtered image and gradient image	Entropy, PSNR, SSI M.	low contrast image enhancement.
4	[4]	a non-local means (NLM) filter and correlation-based wavelet packet thresholding	PSNR, IQI, ED	two different detectors are used
5	[5]	Modified Haarwavelet transform and image fusion.	MSE, PSNR (dB), MI, UIQ	image fusion is used
6	[6]	low-rank sparse component decomposition and dictionary learning.	mutual information, Tsallis entropy, nonlinear correlation information entropy	multi-modal medical images can be simultaneous fusion, denoising, and enhancement
7	[7]	fractional differential and directional derivative.	Mean, clarity, entropy.	The best order of the fractional differential is $\alpha=0.8$
8	[8]	A dynamic unsharp masking using optimum wavelet based masking.	Absolute Mean Brightness Error (AMBE)	a dynamic unsharp masking technique
9	[9]	PWLS-ULTRA	RMSE, SSIM	for low-dose CT imaging

## V. CONCLUSION

Computed Tomography images mainly used in medical for diagnostic purpose. The noise present in CT image mainly while acquiring the image and transmitting the image. The level of noise can be decreased and/or eliminated by applying suitable denoising technique. Therefore, appropriate image denoising can be applied to increase the image quality for mainly diagnosis purpose.

This paper discusses CT denoising techniques and various image quality parameters used to check the quality of denoised image such as SSIM, PSNR, MSE, RMSE, ED and DIV.

Only one image denoising method to CT image is not sufficient to obtain all important parameters with regards to noise decrease, edge protection, and strength. The techniques used to obtain CT imaging and CT imaging types are upgrading every day. Therefore, the denoising

techniques used for CT images has to be modified and enhanced.

## REFERENCES

- [1] Zohair Al-Ameen, Ghazali Sulong and Md. Gapar Md. Johar, "Enhancing the Contrast of CT Medical Images by Employing a Novel Image Size Dependent Normalization Technique", International Journal of Bio-Science and Bio-Technology, Vol. 4, No. 3, pp. 63-68, Sep. 2002.
- [2] Fathi KALLEL, Ahmed BEN HAMIDA, "A new adaptive gamma correction based algorithm using DWT-SVD for non-contrast CT image enhancement", IEEE Transactions on NanoBioscience Vol. 16, Issue: 8, pp. 666 - 675, Dec. 2017.
- [3] P. Sreeja, S. Hariharan, "An improved feature based image fusion technique for enhancement of liver lesions" Biocybernetics and Biomedical Engineering Volume 38, Issue 3, pp. 611-623, May 2018.
- [4] Manoj Diwakar, Manoj Kumar, "CT image



- denoising using NLM and correlation-based wavelet packet thresholding”, IET Image Processing, Vol. 12 Iss. 5, pp. 708-715, 2018.
- [5] Das K., Maitra M., Sharma P., Banerjee M. (2019) Early Started Hybrid Denoising Technique for Medical Images. In: Bhattacharyya S., Mukherjee A., Bhaumik H., Das S., Yoshida K. (eds) Recent Trends in Signal and Image Processing. Advances in Intelligent Systems and Computing, vol 727. Springer, Singapore.
- [6] Huafeng Li, Xiaoge He, Dapeng Tao, Yuanyan Tang, Ruxin Wang, “Joint medical image fusion, denoising and enhancement via discriminative low-rank sparse dictionaries learning” Pattern Recognition, vol. 79, pp. 130–146, Feb. 2018.
- [7] Jinlan Guan, Jiequan Ou, Zhihui Lai and Yuting Lai, “Medical Image Enhancement Method Based on the Fractional Order Derivative and the Directional Derivative”, International Journal of Pattern Recognition and Artificial Intelligence, Vol. 32, No. 3, pp. 1857001 (22 pages), 2018.
- [8] Ebenezer Daniel, J. Anitha, “Optimum wavelet based masking for the contrast enhancement of medical images using enhanced cuckoo search algorithm”, Computers in Biology and Medicine, Volume 71, Pages 149-155, April 2016.
- [9] X. Zheng, S. Ravishankar, Y. Long and J. A. Fessler, "PWLS-ULTRA: An Efficient Clustering and Learning-Based Approach for Low-Dose 3D CT Image Reconstruction," in IEEE Transactions on Medical Imaging, vol. 37, no. 6, pp. 1498-1510, June 2018
- [10] Manoj Diwakara, Manoj Kumar, “A review on CT image noise and its denoising”, Biomedical Signal Processing and Control, Volume 42, pp. 73-88, April 2018
- [11] Munipraveena Rela , S. Nagaraja Rao, “Comparative analysis of image enhancement techniques applied to CT liver image” International Journal of Engineering & Technology, 7, pp. 285-289, 2018.
- [12] Lu Liu, Zhenhong Jia, Jie Yang, Nikola Kasabov, “A Medical Image Enhancement Method Using Adaptive Thresholding in NSCT Domain Combined Unsharp Masking”, International Journal of Imaging systems and Technology, Volume 25, Issue 3, Pages 199-205, September 2015
- [13] Changdong Wu, Zhigang Liu, and Hua Jiang, “Choosing the filter for catenary image enhancement method based on the non-subsampled contourlet transform”, Review of Scientific Instruments 88, 054701 (2017); doi: 10.1063/1.4983375

See discussions, stats, and author profiles for this publication at: <https://www.researchgate.net/publication/344122962>

# Extraction and Classification of tumor in CT Liver Image

Article in *Test Engineering and Management* · September 2020

---

CITATION

1

READS

65

3 authors, including:



**Munipraveena Rela**

CMR Institute of Technology

11 PUBLICATIONS 13 CITATIONS

SEE PROFILE

Some of the authors of this publication are also working on these related projects:



EFFICIENT IMAGE ENHANCEMENT TECHNIQUES APPLIED ON MEDICAL IMAGING-A STATE- OF- THE ART SURVEY [View project](#)

# Extraction and Classification of tumor in CT Liver Image

Munipraveena Rela, Research Scholar, Department of ECE, JNTUA, Ananthapuramu, A.P., India, [chagpraveena@gmail.com](mailto:chagpraveena@gmail.com)

S. Nagaraja Rao, Professor, Department of ECE, G. Pulla Reddy Engineering College(Autonomous), Kurnool, A.P., India, [Suryakari2k9@gmail.com](mailto:Suryakari2k9@gmail.com)

P. Ramana Reddy, Professor, Department of ECE, JNTUA, Ananthapuramu, A.P., India, [prjntu@gmail.com](mailto:prjntu@gmail.com)

## Article Info

Volume 82

Page Number: 8747 - 8753

Publication Issue:

January-February 2020

## Article History

Article Received: 5 April 2019

Revised: 18 Jun 2019

Accepted: 24 October 2019

Publication: 03 February 2020

## Abstract:

In this paper, we have extracted liver and tumor region in the CT image. Liver and tumor are extracted by using region growing method, and morphological operations such as filling holes, erosion, dilation and close. Features of tumor such as area and perimeter are calculated using regionprop operation. Using these feature, tumor is classified as benign or malign.

**Keywords:** Liver cancer, CT image, Region growing, morphological operation, area and perimeter, etc.

## I. INTRODUCTION

Liver cancer starts in the cells of liver. Liver is a largest organ that presents in the upper right side of abdomen, above stomach and below diaphragm.

Hepatocellular carcinoma is the primary liver cancer, which starts in hepatocyte liver cell. Other liver cancer which are less common are intrahepatic cholangiocarcinoma and hepatoblastoma.

Compare to the cancer that begins in liver than cancer spread to the liver from other body parts is most common. That is cancer from colon, lung or breast is spread to liver. Such type of cancer is called metastatic cancer. If cancer spreads for colon to liver, then that cancer is called metastatic colon cancer.

Hepatocellular carcinoma starts in the people with cirrhosis caused by hepatitis B or hepatitis C infection(chronic liver diseases). Hepatocellular carcinoma occur in the people who drink alcohol more and who has growth of fat in the liver. Fig.1showa the imageof liver cancer.Fig.2. is CT image of liver cancer.s,

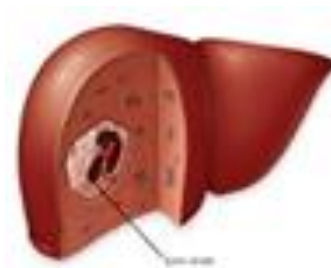


Fig. 1. Liver cancer

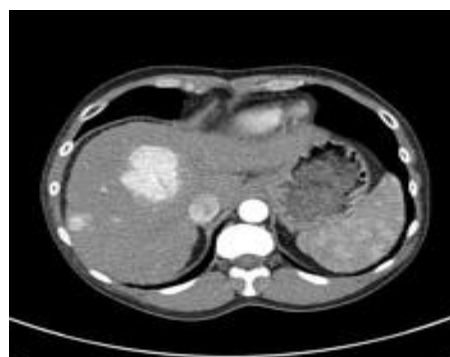


Fig. 2. CT image of liver cancer

## II. PRELIMINARIES

To extract the tumor region in Liver image, The CT Liver image must be enhanced. There are different

medical image enhancement techniques are discussed in [1], [2], [4], [6], [10] and [11]. Medical image enhancement techniques based on fusion are discussed in [3], [9]. Image denoising techniques are discussed in [8]. One of the method for CT liver and tumor segmentation is Region based segmentation. Region based segmentation and its application for CT liver image is discussed in this section.

- *Region-based segmentation*

Region-based image segmentation is done by region growing method. In this method, initial seed points must be selected. Hence it is called a pixel-based image segmentation method. If the neighboring pixels of seed points are satisfied some predefined conditions, then these pixels are added to the region. This type of segmentation is used to partition an image into regions.

*Seed Points:* In region based segmentation, the first method is to select the seed points. Pixels in the region where the image need to be segmented are selected as seed points. Region will be growing from these seed points to adjacent pixels depending on pixel intensity and using 4-connected neighborhood or 8-connected neighborhood condition. If adjacent pixels of seed point are in 4-neighbors or 8-neighbors and have the intensity of seed point then these adjacent pixels will become seed points. This process will be continued till images are segmented into regions.

- *Morphological processing*

Morphological operators are applied on binary image and structuring element which has characteristic of object shape in input image. Usually structuring element is odd sized matrix and its origin is at the center. The structuring element is shifted such that center of structuring element is overlapped with the each and every pixel of the image and the structuring element and image pixels underlying are compared every time.

*Erosion and dilation:*

The erosion will generate new binary image with the center of structuring as 1 if structuring element completely fits in the image pixels underlying the structuring element, otherwise center will be 0. This process is repeated for all the pixels in the input image. Using erosion, small holes and gaps in the region become larger and small details in the image are eliminated.

The erosion is denoted by  $E=A\ominus B$ , where A is a binary image and B is structuring element

The dilation of an image produce new binary image with the center of structuring as 1 if at least one pixel value of structuring element fits in the image pixels underlying the structuring element, otherwise center will be 0. Dilation adds a layer of pixels to inner and outer boundary of region with the shape of structuring element. The holes and gaps in the region will be reduced by dilation.

The *opening* of an image A by a structuring element B is denoted as  $A\circ B$  is obtained by performing erosion first and dilation next. This operation eliminates thin bridges between two regions.

The *closing* of an image A by a structuring element B is denoted as  $A\bullet B$  is obtained by performing dilation first and then erosion.. the gaps in the image are filled by closing operation.

- *bwtraceboundary*

$B = \text{bwtraceboundary}(BW,P,\text{fstep})$  is MATLAB code is used to obtain the trace of the object boundary in binary image specified by BW. P is a two element vector which will specify the point on the boundary of object from where trace should begin. fstep is a string which specify the direction for next object pixel connect to P such as 'S' for south. The following figure shows different possible strings for fstep. B contains rows and columns of all boundary pixels.

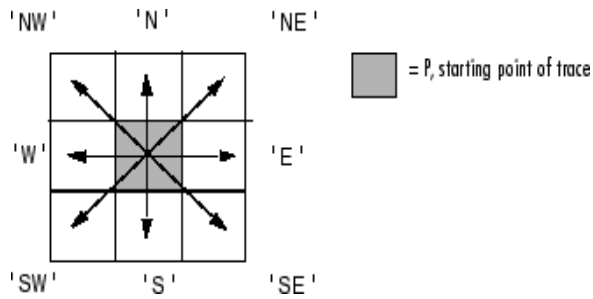


Fig. 3. All possible values for fstep

### Regionprops

regionprops is used to measure different properties of region.

stats = regionprops(B,properties) gives the values for properties specified for objects in the binary image. B is input binary image. The string 'all' or 'basic' can be used in the place of properties. If basic is used, then regionprops gives 'Area', 'centroid' and 'boundingBox' measurements. If all is used, then it gives all properties of object such as 'Area', 'BoundingBox', 'Centroid', 'FilledArea', 'FilledImage', 'Image', 'PixelIdxList', 'PixelList', and 'SubarrayIdx'..

### III. PROPOSED METHOD

The Block diagram in fig 4 explains the proposed method

The algorithm for proposed method is given as:

**1)Preprocessing:** the input CT image must be preprocessed before extracting the liver region. The preprocessing includes removing noise, input image dimensionality change, converting input image from rgb to gray scale image.

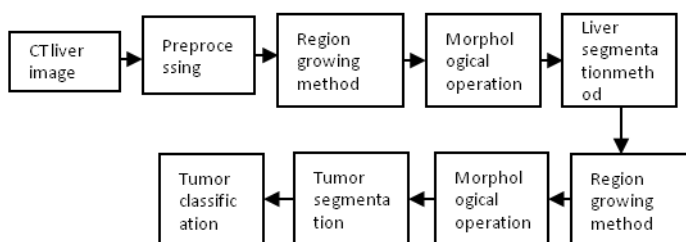


Fig. 4. Block Diagram of Proposed method

**2)region growing algorithm** is applied to segment the liver. To apply region growing algorithm, first seed point must be selected in the image. After observing the input image, seed point is selected in liver region.

### 3)Liver region is extracted

**4)Obtained boundary of liver region** using bwtraceboundary

**5)To detect tumor region,** again region growing algorithm is applied. Here seed point is selected in the tumor region.

### 6)Tumor in the liver region is extracted

**7)Obtained the boundary of tumor** using bwtraceboundary

**8)Region properties of tumor** such as area, perimeter are obtained by regionprops

### IV. EXPERIMENTAL RESULTS

Original CT image is shown in figure 5. Figure 6 is the output after applying Region growing algorithm to figure 5. Morphological operation is applied to fill the gaps in figure 6, the result is as shown in figure 7.

Liver region is segmented, it is as shown in figure 8. Figure 9 shows the trace of boundary of liver region. Figure 10 shows the detection of tumor. Trace of boundary of tumor in CT image is shown in figure 11. Extraction of tumor region is shown in figure 12.

Classification of tumor based on total number of pixels in tumor area is shown in figure 13. Figure 14 to Figure 22 are the outputs obtain for CT image 2. Figure 23 to Figure 30 are the outputs obtain for CT image 3.



Fig. 5. Original CT image1

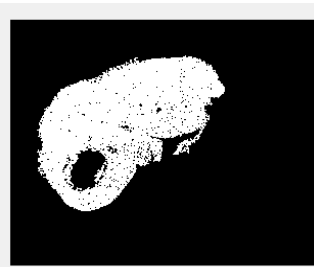


Fig. 6. Region growing output

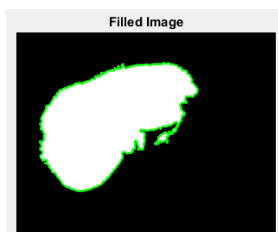


Fig. 7. morphological

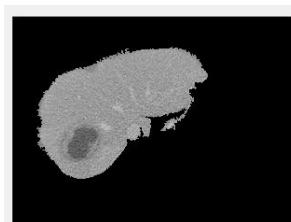


Fig. 8. Liver segmentation operation



Fig. 9. liver boundary

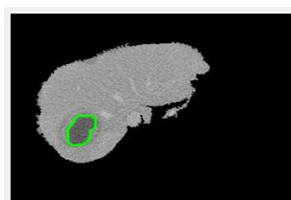


Fig. 10. Tumor detection



Fig. 11. Tumor Boundadary

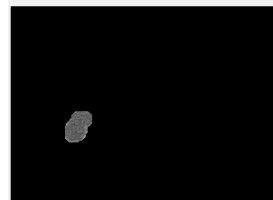


Fig. 12. Tumor Extraction

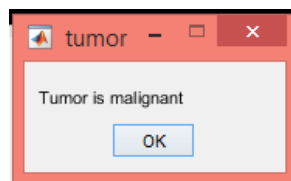


Fig. 13. Tumor Classification



Fig. 14. original CT image2

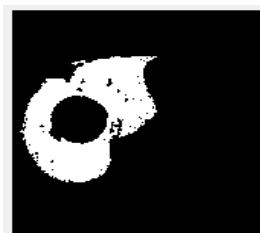


Fig. 15. Region growing output

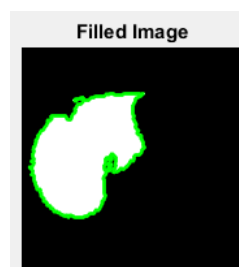


Fig. 16. morphological

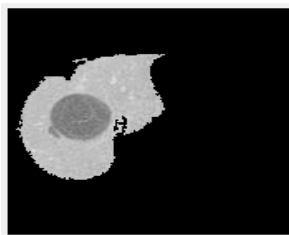


Fig. 17. Liver segmentation operation



Fig. 18. liver boundary



Fig. 19. Tumor detection



Fig. 20. Tumor Boundary

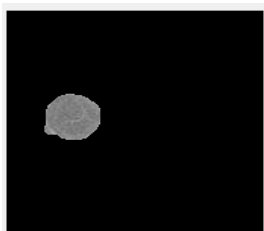


Fig. 21. Tumor Extraction

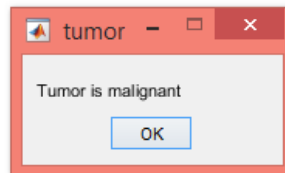


Fig. 22. Tumor Classification



Fig. 23. original CT image3

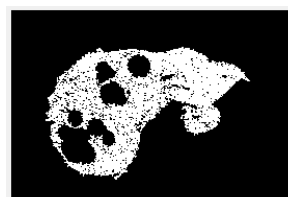


Fig. 24. Region growing output

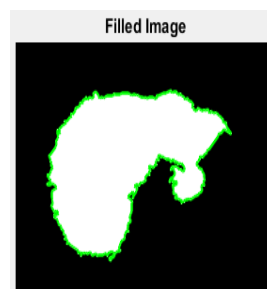


Fig. 25. morphological operation

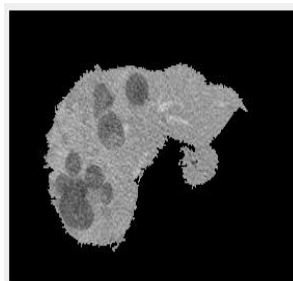


Fig. 26. Liver segmentation

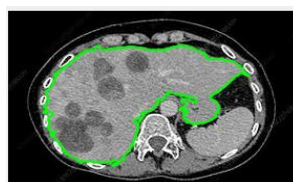


Fig. 27. liver boundary

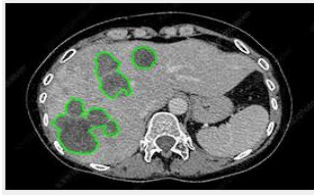


Fig. 28. Tumor detection

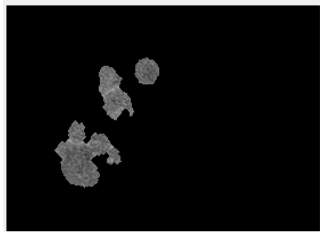


Fig. 29. Tumor extraction

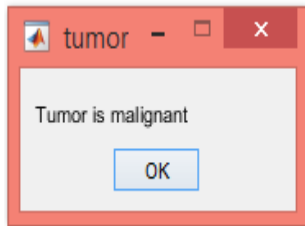


Fig. 30. classification of Tumor

Area and perimeter of tumor region is calculated using regionprop code. Area and perimeter of tumors in CT image1, CT image2 and CT image 3 are shown in Table1.

TABLE I. AREA AND PERIMETER OF TUMOR REGION IN CT IMAGES

Area and Perimeter/CT image	CT image 1	CT image 2	CT image 3
Area & Perimeter of tumor	Area: 850 Perimeter: 107.8520	Area: 1068 Perimeter: 115.3860	Area = 39192 Perimeter = 2.1210e+03

## V. CONCLUSION

Region growing and morphological operations applied on different CT images. Area and perimeters are obtained for tumor regions in the image. Using

area of tumor, tumor is classified as malignant or benign. In this method, seed points must be selected manually in liver region and in tumor region. Further study includes application of machine learning and deep learning methods to segmentation of tumor in the liver region without

## VI. REFERENCES

- [1] Zohair Al-Ameen, Ghazali Sulong and Md. Gapar Md. Johar, "Enhancing the Contrast of CT Medical Images by Employing a Novel Image Size Dependent Normalization Technique", International Journal of Bio-Science and Bio- Technology, Vol. 4, No. 3, pp. 63-68, Sep. 2002.
- [2] Fathi KALLEL, Ahmed BEN HAMIDA, "A new adaptive gamma correction based algorithm using DWT-SVD for non-contrast CT image enhancement", IEEE Transactions on NanoBioscience Vol. 16 , Issue: 8 , pp. 666 - 675, Dec. 2017.
- [3] P. Sreeja, S. Hariharan, "An improved feature based image fusion technique for enhancement of liver lesions" Biocybernetics and Biomedical Engineering Volume 38, Issue 3, pp. 611-623, May 2018.
- [4] RELA, Munipraveena; NAGARAJA RAO, S. Comparative analysis of image enhancement techniques applied to CT liver image. International Journal of Engineering & Technology, [S.l.], v. 7, n. 3.29, p. 285-289, aug. 2018. ISSN 2227-524X. doi:http://dx.doi.org/10.14419/ijet.v7i3.29.1917 6.
- [5] Anil K. Jain. "Fundamentals of Digital Image Processing", Prentice Hall Inc., prentice hall international edition, 1989. https:// www.mathworks .com/ discovery/ digital- image-processing.
- [6] Munipraveena Rela , S. Nagaraja Rao, P. Ramana Reddy, "Efficient Image Enhancement Techniques Applied on Medical Imaging-A State- of- The Art Survey", International Journal of Recent Technology and Engineering

(IJRTE), ISSN: 2277-3878, Volume-7, Issue-6S4, April 2019.

- [7] Jayanthi, M.; Kanmani, B., "Extracting the Liver and Tumour from Abdominal CT Images", IEEE, Fifth International Conference on Signal and Image Processing (ICSIP), 2014 .
- [8] Das K., Maitra M., Sharma P., Banerjee M. (2019) Early Started Hybrid Denoising Technique for Medical Images. In: Bhattacharyya S., Mukherjee A., Bhaumik H., Das S., Yoshida K. (eds) Recent Trends in Signal and Image Processing. Advances in Intelligent Systems and Computing, vol 727. Springer, Singapore.
- [9] Huafeng Li, Xiaoge He, Dapeng Tao, Yuanyan Tang, Ruxin Wang, "Joint medical image fusion, denoising and enhancement via discriminative low-rank sparse dictionaries learning" Pattern Recognition, vol. 79, pp. 130–146, Feb. 2018.
- [10] Jinlan Guan, Jiequan Ou, Zhihui Lai and Yuting Lai, "Medical Image Enhancement Method Based on the Fractional Order Derivative and the Directional Derivative", International Journal of Pattern Recognition and Artificial Intelligence, Vol. 32, No. 3, pp. 1857001 (22 pages), 2018.
- [11] Ebenezer Daniel, J. Anitha, "Optimum wavelet based masking for the contrast enhancement of medical images using enhanced cuckoo search algorithm", Computers in Biology and Medicine, Volume 71, Pages 149-155, April 2016.



# Indoor Tracking by Adding IMU and UWB Using Unscented Kalman Filter

B. Venkata Krishnaveni<sup>1</sup> · K. Suresh Reddy<sup>2</sup> · P. Ramana Reddy<sup>1</sup>

Accepted: 20 October 2021

© The Author(s), under exclusive licence to Springer Science+Business Media, LLC, part of Springer Nature 2021

## Abstract

In recent days Internet of Things (IoT) applications becoming prominent, like smart home, connected health, smart farming, smart retail and smart manufacturing, will lead to a challenging task in providing low cost, high precision localization and tracking in indoor environments. Positioning in indoor is yet an open issue mostly because of not receiving the signals of GPS in the context of indoor. Inertial Measurement Unit can give an exact indoor tracking, however, they regularly experience the cumulated error as the speed and position are gotten by incorporating the increasing acceleration constantly as for time. At the same time Ultra Wideband localization and tracking will be influenced by the real time indoor conditions. It is difficult to utilize an independent localization and tracking system to accomplish high precision in indoor conditions. In this paper, we come up with an incorporated positioning system in indoor by joining IMU and the UWB over the Unscented Kalman Filter (UKF) and the Extended Kalman Filter (EKF) to enhance the precision. All these algorithms are analyzed and assessed dependent on their exhibition.

**Keywords** Extended kalman filter · Indoor positioning · IoT · Ultra wideband · IMU · Unscented kalman filter

## 1 Introduction

High-precision and low-cost localization and navigating systems for indoor portable devices have gotten basic in IoT applications, like smart home and smart manufacturing [1]. As of late, real-time location systems (RTLS) are being utilized for stock

---

✉ B. Venkata Krishnaveni  
Krishnavenibv@gmail.com

K. Suresh Reddy  
sureshkatam@gmail.com

P. Ramana Reddy  
prjntu@gmail.com

<sup>1</sup> Electronics and Communication Engineering Department, Jawaharlal Nehru Technological University Anantapur, Ananthapuramu, Andhra Pradesh 515002, India

<sup>2</sup> Electronics and Communication Engineering Department, G Pulla Reddy Engineering College (Autonomous), Kurnool, Andhra Pradesh 518007, India

administration and security uphold in manufacturing plants and circulation focuses. It is vital in RTLS to appraise the position of moving articles, for example, forklifts and laborers along with the fixed bodies. To evaluate the position of movable items, an exceptionally fast and exact algorithm is needed.

The precise and strong indoor position is a major facilitator in forthcoming Internet applications. Inertial navigation is a technique utilizing the estimation from the IMU, primarily, gyroscopes and accelerometers for positioning and navigation [2]. Utilizing the estimation given by the IMU, the Inertial Navigation System (INS) can enumerate the velocity, position and the direction of the system beginning from some known starting point. In any case, because of their drawn out floats, for example, accelerometer inclination and scale factor mistakes, from the calculated states of navigation (position, velocity, and attitude) will gain with time. For tracking of target in indoor 3D environment, there are many technical issues to reduce because of the indoor environment complexity [3, 4]. The effect of bumps like equipment, furniture, walls, the existence of human etc. causes multi path and fading problems. There are individual technologies which are used in wireless network, for example, Wi-Fi, Bluetooth, ZigBee and UWB. The better appropriate innovation for large precision localization is UWB.

Ultra-Wideband is a radio innovation, which is essentially different in relation to the at present generally utilized conventional radio technologies. It transmits signals over various groups of frequencies (3.1–10.6 GHz) all the while with hundreds MHz of transmission capacity (more prominent than 500 MHz). It is intended for Indoor Positioning Systems (IPSs) to conquer numerous difficulties, for example, signals because of extreme multi path reflect from furniture and wall, Non-Line-of-Sight (NLOS) signal because of blockages, and scattering of signal because of more prominent thickness of obstacles. With the known positions of reference nodes, by estimating the Time-of-Arrival (TOA) from each of the reference node to target, the relating distances can be calculated. By using calculated distances, the location of the target can be estimated utilizing various methods of positioning [5–8]. Since 2010, localization devices based on UWB radio sensor, like Pozyx from KickStarter and DWM1000 from DecaWave [9], have gotten industrially accessible. At present, a few IPSs like the Ubisense System and Zebra System, utilizing UWB radio sensor have been conveyed [10, 11].

In spite of the fact that UWB has been recognized as perfect radio technology in indoor scenario for getting accurate data about the location, still there is a challenge for the IPS based on UWB technology to predict precise location data because of the multi path propagation of the direct LOS signal and propagation of the NLOS signal. To defeat the multi path impacts, a simple method is to eliminate the obstructions that may cause those inferences or to consider the open zone. This choice may not be conceivable in most indoor situations. IMU-based INSs are obtuse toward these interference but the errors resulted from the estimated position will increase over time. So these two technologies, IMU and UWB can be coupled for applications of IPS because these two technologies are corresponding to one another.

In [12], the examination on three-dimensional UWB positioning utilizing distinctive conservative reference node configurations is conducted. Linear least squares with TOA values obtained using threshold based search back algorithm is used for positioning. To defeat the issues with respect to positioning, the development of the structure of two algorithms named Extended Kalman Filter (EKF) and Unscented Kalman Filter (UKF) positioning methods are presented at [13]. But here the authors considered a two-dimensional system only. Demonstration of calculating the TOA values utilizing the

two-way-ranging, positioning using the least squares (LS) and tracking with help of the EKF algorithm presented in [14].

In [15] an altered EKF sequential update, here, the Jacobian matrix and vector of measurement with the pseudo versions, for tracking of the target in indoor following applications to ultra-wideband systems utilizing Time Difference of Arrival (TDOA) estimation is introduced. We will get high exactness with TDOA on account of the enormous transmission capacity of UWB signals, however, its application is compelled by the corresponded measurement noise because of TDOA values. A multi-sensor combination design is presented in [16] for the IPS. At the point where UWB can be accessible and reliable, the IMU error of long term drift is aligned using UWB. Something else, then it shift to IMU from UWB promptly to obtain status of location and tracking. In [17], a combined solution of localization using both UWB, IMU is presented, that results continuous and precise location, particularly on account of NLOS situations. But, in [17], regarding the time synchronization issue, all the UWB modules are associated with a central regulator through the fibre line. This will build the deployment complexity and the expense of the system.

TOA algorithm is used in both [16] and [17] and have not taken the clock drift impact into account. Besides, despite the fact that acceleration noise of IMU is taken in the acceleration measurements, the impact of this on the displacement, velocity because of incorporation is not evaluated in [16, 17].

In [18], a tracking and positioning algorithm coupling IMU, UWB and sensors specific to an area is recommended. This indicated that combination solution will acquire high precise 3D velocity and knowledge of height by utilizing the biomechanical lower body model. Note that large portion of the current indoor navigation and positioning methods depended on lower body frameworks of human that expands expense and deployment difficulty [19].

Hence, to accomplish less price and more precise navigation, positioning of indoor system, this paper centers on coupling of UWB and IMU dependent on Filter calculations. The information received from IMU is utilized to equation of state and information received from UWB is utilized to equation of observation for filter calculations. For improving accuracy of indoor positioning further, the nonlinear kalman filter, namely, UKF algorithm is considered in this paper.

In [2], considered that the target moves in 2D environment and for range measurement Time of Flight (TOF) ranging method is used and Least Square method for calculating the position using TOF values. In this paper 3D environment is considered for comparing performance of algorithms. For Calculating the TOF values time synchronization is needed between the target and reference nodes, which can overcome by using TOA estimation algorithms using the samples of energy signal and for positioning Iterative method is considered. The accuracy of position can be improved by using Iterative method and convergence problem can be overcome.

The main contributions of this paper can be summarized as follows:

Positioning with UWB using the Iterative method compared with linear least squares method using TOA values for two different configurations of reference node placement. An UKF fusion positioning algorithm introduced to decrease the computational complexity and to get better accuracy compared with EKF. From the results of simulation, we can conclude that algorithm based on UWB can obtain high precision of position compared to EKF fusion positioning algorithm in a three-dimensional area. The effect of the number of reference nodes or reference nodes density is also performed for all the algorithms.

In Sect. 2, Indoor positioning System using IMU is explained first and then positioning using UWB, which uses TOA values as range measurements and Iterative Method

for position estimation is explained. In Sect. 3, the calculations dependent on coupling IMU and UWB positioning system is introduced in environment of 3D. In Sect. 4, results of simulation are given and localization accuracy of all algorithms are analyzed and explained. Conclusions are given in Sect. 5.

## 2 Positioning and Tracking System Using the Coupling of IMU and UWB

The proposed positioning and tracking system by coupling sensor based IMU and UWB localizing system in indoor environment of three dimension is given in Fig. 1. Here the three axis( $x$ ,  $y$ , and  $z$ ) accelerometers, one UWB radio sensor (given as Target sensor) are placed on the body of a platform, and four UWB radio sensors (given as reference sensors) are placed inside the building with known locations.

### 2.1 Positioning Algorithm Using IMU

To change the coordinates from one set to another, we need a rotation matrix that reveals to us precisely how one frame is rotated with respect to the other. Rotations are especially precarious mathematical objects and they can be the source of significant bugs if not managed cautiously and determinedly. There is a wide range of approaches to represent rotations [20].

The best method of representing a rotation is utilizing the euler angles. These angles represent an arbitrary rotation as the creation of three separate rotations about different principal axes. Euler angles are attractive in part because they are a parsimonious representation, requiring only three parameters instead of nine for a full rotation matrix, and it is easier to understand than another way of quaternion method and no need to calculate quaternion multiplication [2].

$C_1$ ,  $C_2$ , and  $C_3$  are the Euler angles about  $x$ ,  $y$ , and  $z$  axis respectively, given as shown below.

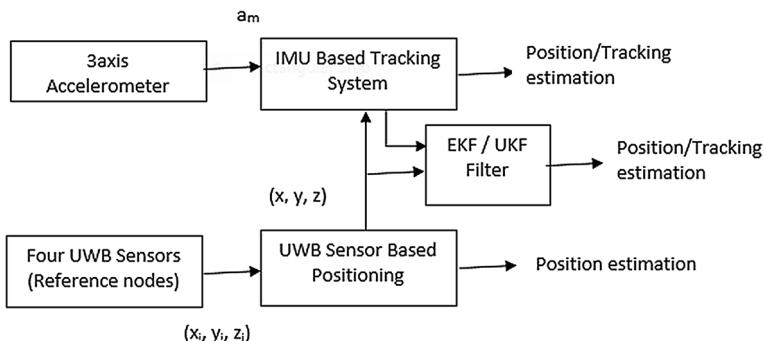


**Fig. 1** Proposed sensor based indoor positioning and tracking system by coupling IMU and UWB

$$C_3 = \begin{bmatrix} \cos\theta_3 & \sin\theta_3 & 0 \\ -\sin\theta_3 & \cos\theta_3 & 0 \\ 0 & 0 & 1 \end{bmatrix}$$

$$C_2 = \begin{bmatrix} \cos\theta_2 & 0 & -\sin\theta_2 \\ 0 & 1 & 0 \\ \sin\theta_2 & 0 & \cos\theta_2 \end{bmatrix}$$

$$C_1 = \begin{bmatrix} 1 & 0 & 0 \\ 0 & \cos\theta_1 & \sin\theta_1 \\ 0 & -\sin\theta_1 & \cos\theta_1 \end{bmatrix}$$

And

$$C = C_3 \times C_2 \times C_1 \tag{1}$$

By considering rotations with infinite, then the functions of trigonometry approximate as  $\sin(\theta) \approx \theta$  and  $\cos(\theta) \approx 1$ . Using these approximations, C can be written in terms of angular velocity as shown in (2).

$$C \approx \begin{bmatrix} 1 & 0 & 0 \\ 0 & 1 & -\theta_1 \\ 0 & \theta_1 & 1 \end{bmatrix} \begin{bmatrix} 1 & 0 & \theta_2 \\ 0 & 1 & 0 \\ -\theta_2 & 0 & 1 \end{bmatrix} \begin{bmatrix} 1 & -\theta_3 & 0 \\ \theta_3 & 1 & 0 \\ 0 & 0 & 1 \end{bmatrix}$$

$$\approx \begin{bmatrix} 1 & -\theta_3 & \theta_2 \\ \theta_3 & 1 & -\theta_1 \\ -\theta_2 & \theta_1 & 1 \end{bmatrix} \tag{2}$$

**a**, the accelerometers of the three axis are used to calculate the acceleration in system A as follows

$$a = [a_x \ a_y \ a_z]^T \tag{3}$$

Then, the acceleration in system B, **a<sup>b</sup>**, can be calculated using the rotation matrix as follows

$$a^b = [a_x^{b1} \ a_y^{b1} \ a_z^{b1}]^T = C \times a \tag{4}$$

If we consider the acceleration gravity **g**, then the acceleration in system B can be calculated by subtracting it from its value as follows

$$a^b = \begin{bmatrix} a_x^b \\ a_y^b \\ a_z^b \end{bmatrix} = \begin{bmatrix} a_x^{b1} \\ a_y^{b1} \\ a_z^{b1} \end{bmatrix} - \begin{bmatrix} 0 \\ 0 \\ g \end{bmatrix} \tag{5}$$

If we consider the sampling interval is short, then constant force is subjected to the carrier with a linear motion of uniform acceleration. Let the position of the system B be **x<sup>b</sup>**, can be calculated as follows

**Fig. 2** Energy samples of the received signal

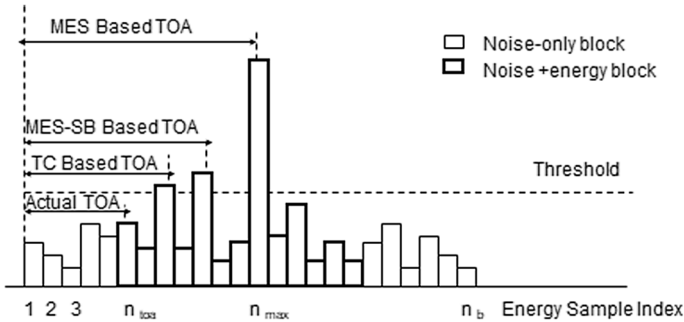
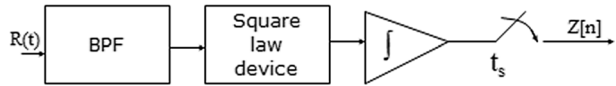


**Fig. 3** TOA estimation algorithms using the samples of energy

$$\begin{bmatrix} x_x^b(t+1) \\ x_y^b(t+1) \\ x_z^b(t+1) \end{bmatrix} = \begin{bmatrix} x_x^b(t) \\ x_y^b(t) \\ x_z^b(t) \end{bmatrix} + \begin{bmatrix} v_x^b \\ v_y^b \\ v_z^b \end{bmatrix} (\Delta t) + \frac{1}{2} \begin{bmatrix} a_x^b \\ a_y^b \\ a_z^b \end{bmatrix} (\Delta t)^2 \tag{6}$$

where  $x^b(t)$ ,  $v(t)$  and  $a^b(t)$  be the position, velocity and the acceleration of the system respectively measured at 't',  $x^b(t+1)$  be the location at '(t+1)' time,  $(\Delta t)$  be the sampling interval.

## 2.2 Position Processing Algorithm Using UWB

UWB positioning of an unknown target node can be made by using fixed known locations of reference nodes. For a 3D environment a minimum of four reference nodes will be enough for positioning. Positioning of the target node can be performed in two steps. First one is measuring the signal parameters either time difference of arrival (TDOA) or time of arrival (TOA) or direction of arrival (DOA) or received signal strength (RSS), of the transmitted signal from reference nodes utilized as range values for target positioning. Second step, using range values, the location of the target can be calculated. The most applicable one for the UWB system is TOA as this takes the advantage of a huge time resolution of UWB signals [21]

### 2.2.1 TOA Estimation Algorithms

Measuring the TOA values is difficult because of the scattering nature of UWB signals. Always the path which arrived first need not be the robust path. Hence, there is requirement of proper range and low complexity methods at attainable rates of sampling. The Fig. 2 represents the technique for measurement of TOA values. Here TOA evaluation is realized utilizing the  $z[n]$  samples, which are appropriated from the square-law mechanism.

The TOA calculation adopting the samples of energy obtained from square law mechanism, shown in Fig. 3. Maximum Energy Selection, where the sample output

having maximum energy is selected as the first path. But in indoors due to multi path it is not necessary that the maximum energy sample is the direct path between the target and reference node. Next one is Threshold Comparison, where the sample first exceeds the threshold can be calculated as TOA value. This method performance is poor at lower SNR's because there may be more threshold crossings due to the noise addition. The next suitable technique is Maximum energy Selection Search Back, where the window of search-back from a maximum energy selection sample given by  $w_{sb}$  assigned using the measurements of the channel. It performs best among the above mentioned techniques. The equation for calculating TOA value using Maximum energy Selection Search Back is given by

$$t_{MES-SB} = [\min \{ \check{Z}[n] > \xi \} - 0.5 + n_{max} - w_{sb} - 1] T_b \quad (7)$$

here

$$\check{Z}[n] = \{ z[n_{max}-w_{sb}] z[n_{max} - w_{sb} + 1] \dots z[n_{max}] \}$$

## 2.2.2 Estimation of Position

Position of the target node can be calculated by using well known triangulation/ trilateration (2D) or multilateration for higher dimensions by two ways. One is equations of type nonlinear obtained using nonlinear relations like maximum likelihood (ML) and nonlinear least squares (NLS) algorithms. Another way is converting these equations into linear like weighted linear least squares (WLLS), linear least squares (LLS) algorithms. But in triangulation/ trilateration the three circles with radius as the measured distance between a reference sensor and the target sensor using TOA values may not converge to a single point there by the performance of the system decreases. If we consider three dimensions where we require four reference nodes, this convergence issue still extends and degrades the performance. So another method called Iterative method with Hessain function is used.

The function for optimization method is

$$f(x) = \sum_{i=1}^N \left[ \left[ (p - p_i)^2 + (q - q_i)^2 + (r - r_i)^2 \right]^{1/2} - c(t_i - t_m) \right]^2 \quad (8)$$

where,  $\mathbf{x} = [p, q, r, t_0]^T$  be the position to calculate,  $t_i, t_m$  be the  $i^{\text{th}}$  reference sensor received time and target sensor transmitted time.

To calculate the location of the target sensor the following iterative equation is used.

$$\mathbf{x}_{k+1} = \mathbf{x}_k - \delta \mathbf{B}_k \mathbf{s}_k \quad (9)$$

where,  $\mathbf{x}_k$  be the location at the  $k^{\text{th}}$  iteration,  $\delta$  be the size of the increment,  $\mathbf{s}_k$  be the objective function

$$\mathbf{s}_k = \Delta f(p, q, r, t_0) = \left[ \frac{\partial f}{\partial p}, \frac{\partial f}{\partial q}, \frac{\partial f}{\partial r}, \frac{\partial f}{\partial t_0} \right]_{p=p_k}^T$$

$B_k$  is the Hessian function increased by utilizing below equation

$$B_{k+1} = B_k + \frac{h_k h_k^T}{h_k^T q_k} - \frac{B_k q_k q_k^T B_k}{q_k^T B_k q_k} \quad (10)$$

here,

$$h_k = x_{k+1} - x_k$$

$$q_k = s_{k+1} - s_k$$

The mean of known reference nodes is taken as the initial estimate and the Identity matrix (I) as the hessian grid beginning.

### 3 Algorithm Based on IMU and UWB

To beat the individual deficiencies of the UWB and IMU, we execute an UKF that couple the two positioning systems so that the UWB sensor based result of position is used to change the IMU mistakes and the IMU sensor based result of position solution is used to distinguish and isolate the adjusted UWB sensor data to build the general precision of positioning performance. Here, we present the coupling algorithm using EKF first, then the coupling algorithm using UKF [2].

#### 3.1 EKF Algorithm

Here we are considering a plane of three -dimensions target moving with uniform acceleration. The vector of state at time  $k$ , is given by

$$x(k) = [x_x(k) \ x_y(k) \ x_z(k) \ v_x(k) \ v_y(k) \ v_z(k) \ a_x(k) \ a_y(k) \ a_z(k)] \quad (11)$$

here,

$x(k)$  be the position,  $v(k)$  be the velocity, and  $a(k)$  be the acceleration.

Let  $(\Delta t)$  be the sample interval and  $(\Delta t)w(k)$  is the process noise of acceleration. Then  $\frac{(\Delta t)^2}{2}w(k)$  represents the process noise of velocity and  $\frac{(\Delta t)^3}{6}w(k)$  represents the process noise of position, because of integrating acceleration two times. The velocity and acceleration values can be obtained from IMU.

The equation of state at time  $(k + 1)$  with uniform acceleration motion is given in (12)

$$x_x(k+1) = x_x(k) + v_x(k)(\Delta t) + a_x(k)\frac{(\Delta t)^2}{2} + \frac{(\Delta t)^3}{6}w_x(k)$$

$$x_y(k+1) = x_y(k) + v_y(k)(\Delta t) + a_y(k)\frac{(\Delta t)^2}{2} + \frac{(\Delta t)^3}{6}w_y(k)$$

$$x_z(k+1) = x_z(k) + v_z(k)(\Delta t) + a_z(k)\frac{(\Delta t)^2}{2} + \frac{(\Delta t)^3}{6}w_z(k)$$

$$\begin{aligned}
 v_x(k+1) &= v_x(k) + a_x(k)(\Delta t) + \frac{(\Delta t)^2}{2} w_x(k) \\
 v_y(k+1) &= v_y(k) + a_y(k)(\Delta t) + \frac{(\Delta t)^2}{2} w_y(k) \\
 v_z(k+1) &= v_z(k) + a_z(k)(\Delta t) + \frac{(\Delta t)^2}{2} w_z(k) \\
 a_x(k+1) &= a_x(k) + (\Delta t)w_x(k) \\
 a_y(k+1) &= a_y(k) + (\Delta t)w_y(k) \\
 a_z(k+1) &= a_z(k) + (\Delta t)w_z(k)
 \end{aligned} \tag{12}$$

The matrix form of the state equation written as

$$\mathbf{x}(k+1) = \mathbf{F}\mathbf{x}(k) + \mathbf{G}\mathbf{w}(k) \tag{13}$$

where  $\mathbf{F}$  represents the transition matrix of state,  $\mathbf{G}$  represents the driving matrix of noise.

The vector of process noise having mean as zero and matrix of covariance  $\mathbf{Q}$  is given by

$$\mathbf{w}(k) = [w_x(k) \ w_y(k) \ w_z(k)]^T$$

And

$$\mathbf{Q} = \text{diag}([\sigma_{ax}^2 \ \sigma_{ay}^2 \ \sigma_{az}^2])$$

$$\mathbf{F} = \begin{bmatrix}
 1 & 0 & 0 & (\Delta t) & 0 & 0 & \frac{(\Delta t)^2}{2} & 0 & 0 \\
 0 & 1 & 0 & 0 & (\Delta t) & 0 & 0 & \frac{(\Delta t)^2}{2} & 0 \\
 0 & 0 & 1 & 0 & 0 & (\Delta t) & 0 & 0 & \frac{(\Delta t)^2}{2} \\
 0 & 0 & 0 & 1 & 0 & 0 & (\Delta t) & 0 & 0 \\
 0 & 0 & 0 & 0 & 1 & 0 & 0 & (\Delta t) & 0 \\
 0 & 0 & 0 & 0 & 0 & 1 & 0 & 0 & (\Delta t) \\
 0 & 0 & 0 & 0 & 0 & 0 & 1 & 0 & 0 \\
 0 & 0 & 0 & 0 & 0 & 0 & 0 & 1 & 0 \\
 0 & 0 & 0 & 0 & 0 & 0 & 0 & 0 & 1
 \end{bmatrix}$$

And

$$G = \begin{bmatrix} \frac{(\Delta t)^3}{6} & 0 & 0 \\ 0 & \frac{(\Delta t)^3}{6} & 0 \\ 0 & 0 & \frac{(\Delta t)^3}{6} \\ \frac{(\Delta t)^2}{2} & 0 & 0 \\ 0 & \frac{(\Delta t)^2}{2} & 0 \\ 0 & 0 & \frac{(\Delta t)^2}{2} \\ (\Delta t) & 0 & 0 \\ 0 & (\Delta t) & 0 \\ 0 & 0 & (\Delta t) \end{bmatrix}$$

Let the observation vector be  $z(k)$ , including the correct distance from reference sensor to target sensor  $d_i(k)$  and the observation noise  $n_i(k)$ .

The equation of observation matrix including the range between the target sensor, four reference sensors and the angle between target sensor to four reference sensors is expressed as

$$z(k) = \begin{bmatrix} d_1(k) + n_1(k) \\ d_2(k) + n_2(k) \\ d_3(k) + n_3(k) \\ d_4(k) + n_4(k) \\ \varphi_1(k) + n_5(k) \\ \varphi_2(k) + n_6(k) \\ \varphi_3(k) + n_7(k) \\ \varphi_4(k) + n_8(k) \end{bmatrix} = H(k)x(k) + n(k) \tag{14}$$

Here at time ‘ $k$ ’,  $H(k)$  denotes the observation matrix.

And  $n(k)$  represents the vector of noise having mean with zero and covariance of the matrix as

$$R = \text{diag} \left( \sigma_{d1}^2, \sigma_{d2}^2, \sigma_{d3}^2, \sigma_{d4}^2, \sigma_{\varphi1}^2, \sigma_{\varphi2}^2, \sigma_{\varphi3}^2, \sigma_{\varphi4}^2 \right)$$

The equations of true distances are given as

$$\begin{bmatrix} d_1(k) \\ d_2(k) \\ d_3(k) \\ d_4(k) \end{bmatrix} = \begin{bmatrix} \sqrt{(x_x(k) - x_1)^2 + (x_y(k) - y_1)^2 + (x_z(k) - z_1)^2} \\ (x_x(k) - x_2)^2 + (x_y(k) - y_2)^2 + (x_z(k) - z_2)^2 \\ (x_x(k) - x_3)^2 + (x_y(k) - y_3)^2 + (x_z(k) - z_3)^2 \\ (x_x(k) - x_4)^2 + (x_y(k) - y_4)^2 + (x_z(k) - z_4)^2 \end{bmatrix} \tag{15}$$

And equations of true angle are given by

$$\vartheta_i(k) = \arccos \left( \frac{x(k) \cdot x_i}{|x(k)||x_i|} \right) \text{ for } i = 1, 2, 3, 4 \tag{16}$$

where.

$(x(k) \cdot x_1) = x_x x_1 + x_y y_1 + x_z z_1$  be the dot product of two vectors namely the position of reference sensor and the position of target sensor for  $i = 1$ .

$$|\mathbf{x}(k)| = \sqrt{x_x^2 + x_y^2 + x_z^2} \quad (17)$$

And,

$$|x_i| = \sqrt{x_i^2 + y_i^2 + z_i^2} \quad \text{for } i = 1, 2, 3, 4 \quad (18)$$

The above nonlinear equations require linearization, so the EKF algorithm is used with Taylor expansion of first order.

$\mathbf{H}(k)$ , the matrix of Jacobian is given as in (19).

Here in EKF we are calculating the matrix of Jacobian, which increases the algorithm's complexity of computation. If the assumption of linearization is not correct, then algorithm of EKF performance will diverge and degrade. Algorithm 1 gives the EKF algorithm process step by step.

$$\mathbf{H}(k) = \begin{bmatrix} \frac{\partial d_1(k)}{\partial x_x(k)} & \frac{\partial d_1(k)}{\partial x_y(k)} & \frac{\partial d_1(k)}{\partial x_z(k)} \\ \frac{\partial d_2(k)}{\partial x_x(k)} & \frac{\partial d_2(k)}{\partial x_y(k)} & \frac{\partial d_2(k)}{\partial x_z(k)} \\ \frac{\partial d_3(k)}{\partial x_x(k)} & \frac{\partial d_3(k)}{\partial x_y(k)} & \frac{\partial d_3(k)}{\partial x_z(k)} \\ \frac{\partial d_4(k)}{\partial x_x(k)} & \frac{\partial d_4(k)}{\partial x_y(k)} & \frac{\partial d_4(k)}{\partial x_z(k)} \\ \frac{\partial \mathcal{O}_1(k)}{\partial x_x(k)} & \frac{\partial \mathcal{O}_1(k)}{\partial x_y(k)} & \frac{\partial \mathcal{O}_1(k)}{\partial x_z(k)} \\ \frac{\partial \mathcal{O}_2(k)}{\partial x_x(k)} & \frac{\partial \mathcal{O}_2(k)}{\partial x_y(k)} & \frac{\partial \mathcal{O}_2(k)}{\partial x_z(k)} \\ \frac{\partial \mathcal{O}_3(k)}{\partial x_x(k)} & \frac{\partial \mathcal{O}_3(k)}{\partial x_y(k)} & \frac{\partial \mathcal{O}_3(k)}{\partial x_z(k)} \\ \frac{\partial \mathcal{O}_4(k)}{\partial x_x(k)} & \frac{\partial \mathcal{O}_4(k)}{\partial x_y(k)} & \frac{\partial \mathcal{O}_4(k)}{\partial x_z(k)} \end{bmatrix} \quad (19)$$

where,

$$\begin{aligned} \frac{\partial d_i(k)}{\partial x_x(k)} &= \frac{x_x(k) - x_i}{\sqrt{(x_x(k) - x_i)^2 + (x_y(k) - y_i)^2 + (x_z(k) - z_i)^2}} \\ \frac{\partial d_i(k)}{\partial x_y(k)} &= \frac{x_y(k) - y_i}{\sqrt{(x_x(k) - x_i)^2 + (x_y(k) - y_i)^2 + (x_z(k) - z_i)^2}} \\ \frac{\partial d_i(k)}{\partial x_z(k)} &= \frac{x_z(k) - z_i}{\sqrt{(x_x(k) - x_i)^2 + (x_y(k) - y_i)^2 + (x_z(k) - z_i)^2}} \end{aligned} \quad (20)$$

---

 Algorithm of Extended Kalman Filter
 

---

- Initialization: Mean  $\mu(0) = E[x(0)]$   
 Covariance  $P(0) = var(x(0))$
- 1: Prediction of state  

$$\bar{x}_k = F \hat{x}_{k-1} + G w_{k-1}$$
  - 2: Prediction of state covariance  

$$\bar{P}_k = F_{k-1} \hat{P}_{k-1} F_{k-1}^T + G_{k-1} Q_{k-1} G_{k-1}^T$$
  - 3: Gain calculation of Kalman filter  

$$K_k = \bar{P}_k H_k^T [H_k \bar{P}_k H_k^T + R_k]^{-1}$$
  - 4: State correction  

$$\hat{x}_k = \bar{x}_k + K_k (Z_k - H_k \bar{x}_k)$$
  - 5: State co-variance correction  

$$\hat{P}_k = (I - K_k H_k) \bar{P}_k$$
- 

### 3.2 Unscented Kalman Filter

For the estimation of parameter EKF is the standard technique, but EKF is having some drawbacks. In EKF, the non-linear equations of the system are converted into linear equations. In this situation, the accuracy of EKF can attain up to first order of Taylor's series and also, it needs to calculate the matrix of Jacobian. Because of the mentioned drawbacks and issues, UKF has been used to present better performance as compared to the EKF algorithm and especially for the non-linear systems. UKF is based on unscented transformation (UT), the approach used to estimate the statistics of the random variable. In UKF, some points are used to catch the actual covariance and mean of the random variables.

Dissimilar to EKF, UKF doesn't have to calculate matrix of Jacobian at every instance and embraces unscented transform to produce reliable measurements which undergo transformation of nonlinear. To random variable with distribution as Gaussian, unscented transform can catch covariance, mean precisely to Taylor series 3<sup>rd</sup> order. So it can successfully conquer the low precision restriction of the EKF algorithm. So the algorithm of UKF is more advantageous and exact when contrasted with the algorithm of EKF.

In the 3D plane expecting that the target sensor is moving with uniform acceleration, the vector of state contains acceleration, velocity and position and the vector of measurement containing distances and angles from reference sensors to target sensors is the equivalent to that in the algorithm EKF.

Here the  $2n + 1$  sigma points can be calculated by using (21), these points are propagated through the nonlinearity and are used to calculate the covariance and mean of the variable after transformation.

$$X = [m..m] + \sqrt{c} \begin{bmatrix} 0 & \sqrt{P} & -\sqrt{P} \end{bmatrix} \quad (21)$$

And calculate the weights using (22).

$$\begin{aligned} \mathbf{W}_m^{(0)} &= \lambda / (n + \lambda) \\ \mathbf{W}_c^{(0)} &= \lambda / (n + \lambda) + (1 - \alpha^2 + \beta) \\ \mathbf{W}_m^{(i)} &= \lambda / 2(n + \lambda) \\ \mathbf{W}_c^{(i)} &= \lambda / 2(n + \lambda) \end{aligned} \quad (22)$$

$i = 1, \dots, 2n$ .

here  $\lambda$  is to decrease the prediction error, given by

$$\lambda = \alpha^2(n + k) - n$$

$\alpha$ ,  $\beta$  and  $k$  are positive values. where  $\mathbf{W}_m^{(i)}$  is the sigma points mean weight and  $\mathbf{W}_c^{(i)}$  is the sigma points covariance weight,  $i$  in the above weights is the sample point index.

Generally,  $\alpha$  is normally taken as a small positive value to maintain the sigma points mean nearer to  $x$ ,  $\beta$  is a positive coefficient to integrate the  $x$  prior distribution, and  $\kappa$  is taken as zero to make the matrix  $P(n + \lambda)$  as a non-negative-definite matrix. The algorithm begins considering the initial mean as  $m_0$  and co-variance as  $\mathbf{P}_0$ .

The algorithm of Unscented Kalman Filter algorithm is given below.

---

Algorithm 2 Unscented Kalman Filter Algorithm

---

**Initialization:**

$$m_0 = E[x_0]$$

$$P_0 = E[(x_0 - m_0)(x_0 - m_0)^T]$$

**Step 1:** Calculate the predicted mean of state  $m_k^-$  and covariance  $P_k^-$  from transformed sigma points

$$X_{k-1} = [m_{k-1} \quad \cdot \quad \cdot \quad m_{k-1}] + \sqrt{c} [0 \quad \sqrt{P_{k-1}^-} \quad -\sqrt{P_{k-1}^-}]$$

$$X_k = f_{ij}(X_{k-1}, k-1)$$

$$m_k^- = \sum_k W_m X_k$$

$$P_k^- = \sum_k W_k [X_k] [X_k]^T + Q_{k-1}$$

Here vector  $w_m$  and weighted matrix  $W$  are given as

$$w_m = [W_m^0 \quad \cdot \quad \cdot \quad W_m^{2n}]^T$$

$$W = (I - [w_m \quad \cdot \quad \cdot \quad w_m]) \times \text{diag}[W_m^0 \quad \cdot \quad \cdot \quad W_m^{2n}]$$

$$\times (I - [w_m \quad \cdot \quad \cdot \quad w_m])^T$$

**Step 2:** Calculate the measurement predicted covariance  $S_k$  and mean  $\mu_k$ , the measurement and state cross covariance  $C_k$  as

$$X_k^* = [m_k^- \quad \cdot \quad \cdot \quad m_k^-] + \sqrt{c} [0 \quad \sqrt{P_k^-} \quad -\sqrt{P_k^-}]$$

$$Y_k^* = h_d(X_k^*, k)$$

$$\mu_k = Y_k^* w_m$$

$$S_k = Y_k^* W [Y_k^*]^T + R_k$$

$$C_k = X_k^* W [Y_k^*]^T$$

**Step 3:** Calculate the gain of the filter  $K_k$  and mean  $m_k$  and co-variance  $P_k$  of the state

$$K_k = C_k S_k^{-1}$$

$$m_k = m_k^- + K_k (y_k - \mu_k)$$

$$P_k = P_k^- - K_k S_k K_k^T$$


---

## 4 Results and Discussion

A number of Monte Carlo simulations were performed to estimate the performance of algorithms, in terms of precision for both the localization and tracking methods. We are considering two scenarios for placement of reference nodes. First one, at the top four corners of the building and second one Cuboid-Shape Configuration as shown below. For the given two scenarios the reference nodes are fixed accordingly and the unknown target position is randomly selected. The estimated position of the target using Iterative method (IM) is compared with the traditional linear least squares (LLS) method of UWB for two scenarios in Figs. 4 and 5

The estimated target position for each run result is obtained and averaged over 1000 runs are presented. The result shows that the Iterative method gives better accuracy compared to the linear least squares method.

The variance of time of arrival error,  $\sigma_{TOA,i}^2$ , is assigned proportional to the distance between reference node  $i=1,2,3,4$  and the target node,  $d_i^2$  with  $SNR = d_i^2 / \sigma_{TOA,i}^2$ .

Here the mean square position error MSPE of the linear least squares (LLS) method and iterative method (IM) for SNR belongs to  $[-10, 60]$  dB are compared. The MSPE is given

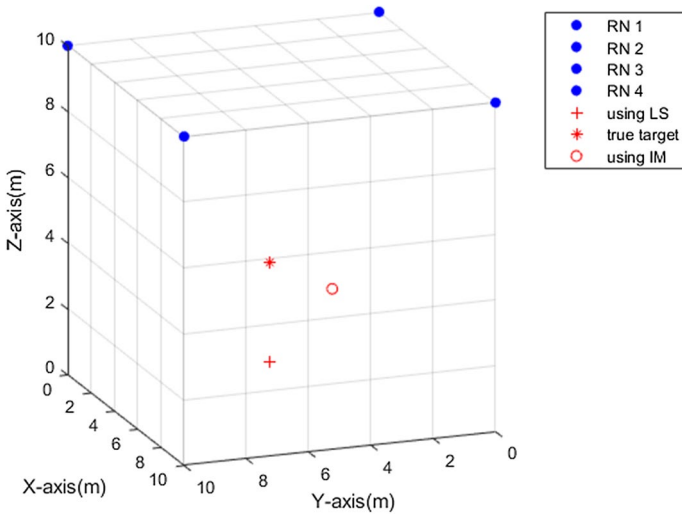


Fig. 4 Comparison of linear least squares and Iterative method for scenario 1

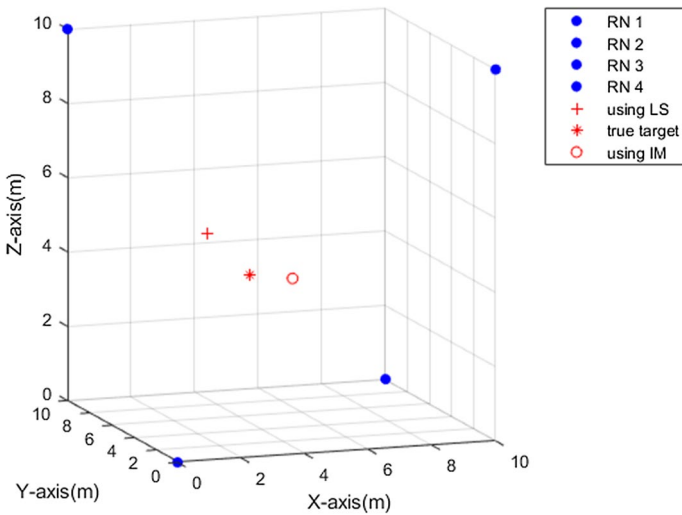
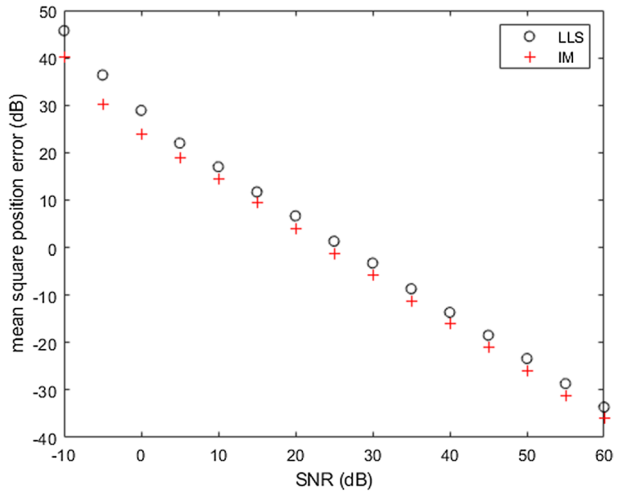


Fig. 5 Comparison of linear least squares and Iterative method for scenario 2

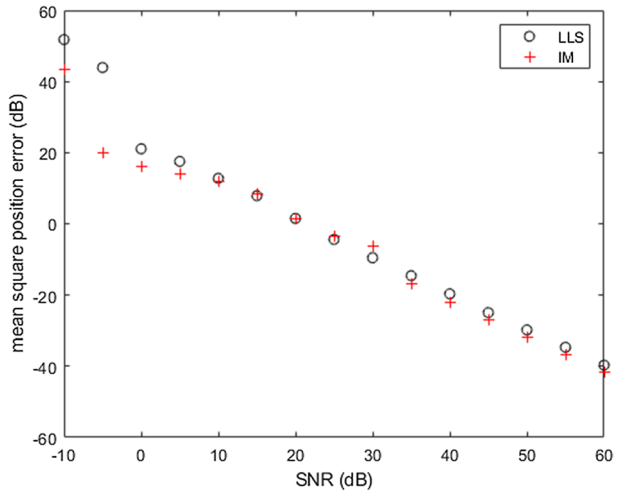
by  $MSPE = E\{(\hat{x} - x)^2 + (\hat{y} - y)^2 + (\hat{z} - z)^2\}$ . As expected, the iterative method is preferable to the LLS method and the MSPE is less for both scenarios as given in Figs. 6 and 7 for two scenarios respectively.

The comparison of two scenarios is given in Fig. 8. And among the scenarios, the second with Cuboid-Shape Configuration gives better performance compared to the first scenario with reference nodes at the top four corners of the building. The MSPE of iterative method, with reference nodes fixed as second scenario is smaller by around 1 dB at  $SNR \in [-10, 60]$  dB compared to the first scenario. For the second scenario, the reference nodes occupy four corners including top and bottom of the area of localization. Hence,

**Fig. 6** Comparison of mean square position error for linear least squares and iterative method for scenario 1



**Fig. 7** Comparison of mean square position error for linear least squares and iterative method for scenario 2



almost the total area of localization is covered. In the case of the scenario1 reference sensors at top of the positioning area covered less area compared to previous one. So geometry of the reference nodes plays an important role in calculating positioning. The Cumulative distribution function of location errors for both scenarios are given in Fig. 9. It can be observed that scenario 2 is the best precise technique with an error under 2 m in 90% of situations, for scenario 1 a similar exactness is accomplished in just between 60 and 70% of situations.

A simulation to evaluate the performance of indoor tracking with UWB positioning and IMU tracking is compared with EKF and is compared with the true (ground truth) trajectory in Fig. 10. EKF gives better performance compared to UWB with IMU. In this simulation, for the first time the estimated state vector is taken as  $X_{est}$  is Zero matrix, in which  $X_{true} = X_{est}$ . The parameters of UKF are taken as  $\alpha = 0.001$ ,  $k = 0$ , and  $\beta = 2$ . The state vector size is  $n = \text{length}(X_{est})$ . Where the process noise vector is taken as Gaussian white sequences noise with zero mean and covariance  $R = I \sigma^2$ , where,  $\sigma = 0.01$ . The covariance

**Fig. 8** Comparison of mean square position error scenario 1 and scenario 2

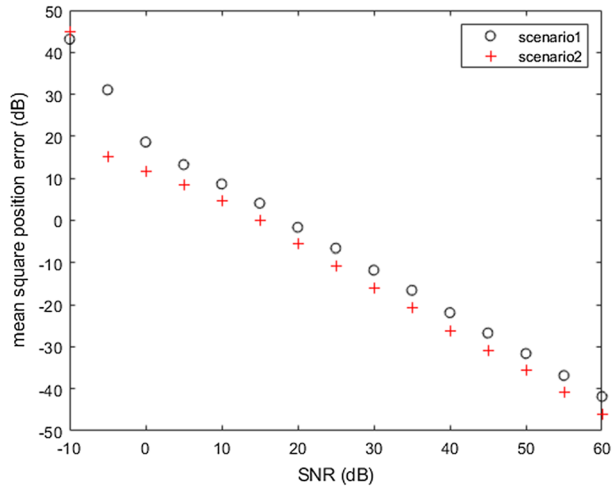
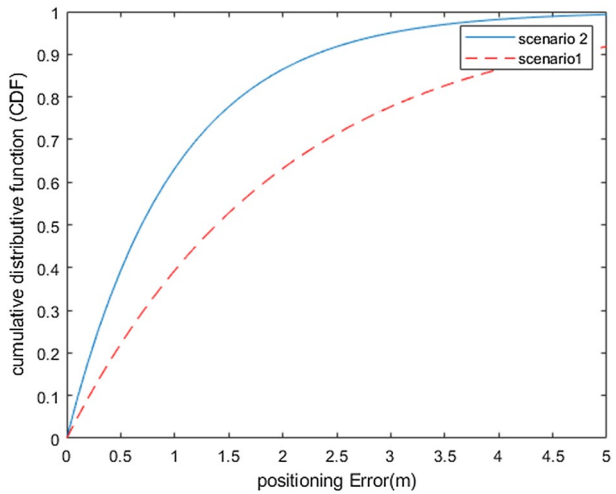


**Fig. 9** Cumulative distribution function of scenario 1 and scenario 2



matrix of process noise is given by  $\mathbf{Q}=\mathbf{I}\times 10^{-10}$ , here  $\mathbf{I}$  is the identity matrix. The comparison of EKF and UKF tracking algorithms is shown in Fig. 11. UKF still provides better estimation accuracy than EKF does. We can see that the tracking result is quite good with the estimated result from UKF.

The function of cumulative distribution of the tracking errors for all the algorithms are given in Fig. 12. It is noticed that UKF tracking algorithm is the best precise technique with an error around 2 m in 90% of situations, but for EKF a similar exactness is accomplished in 75% and only 60% in case of UWB.

#### 4.1 Density of the Reference Nodes

By expanding the number of the reference sensors may reduce the positioning errors. For four reference sensors, the position is similar to in Fig. 4. The position of 8

**Fig. 10** Performance comparison of UWB and EKF tracking algorithms with the actual ground truth trajectory

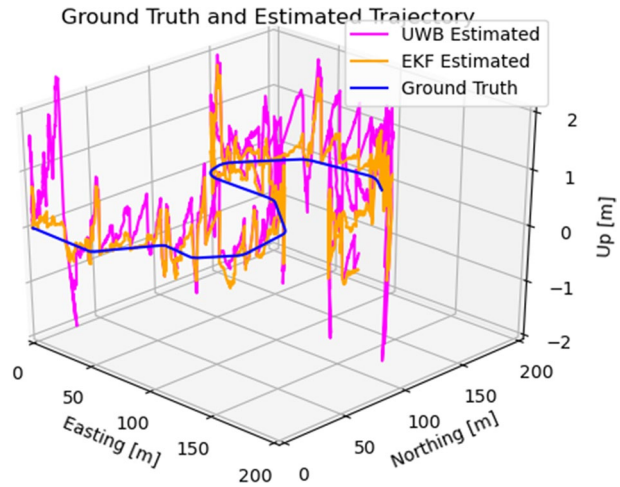
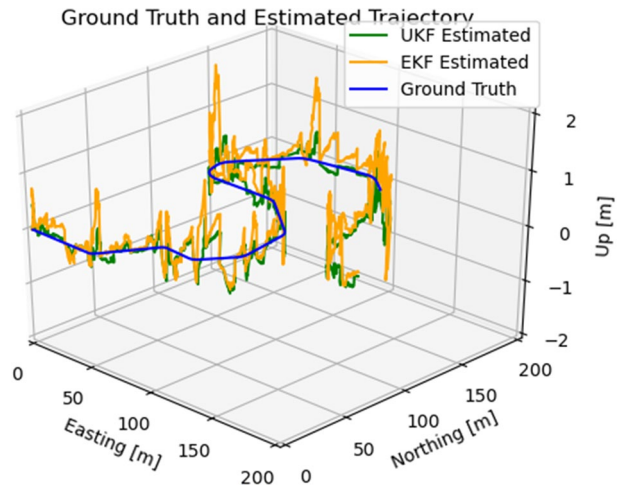


**Fig. 11** Performance comparison of UKF and EKF tracking algorithms with the actual ground truth trajectory



reference sensors is acquired from that of 4 reference sensors by embedding an extra sensor halfway between each two neighbouring reference sensors. The position of 12 reference sensors relates to that of 8 reference sensors with 4 extra sensors set at the focal point of the rectangular zone. At last, the position of 16 reference sensors is acquired by embedding 4 new sensors halfway between the 4 past sensors.

The mean square error (MSE) for different numbers of reference nodes is summarized in Table 1 for all algorithms. To sum up, we can say that expanding the quantity of reference sensors diminishes the positioning errors basically when utilizing techniques dependent on nonlinear Kalman filtering. However, no substantial improvement is achieved by expanding the quantity of reference nodes beyond some point. This must be evaded, since expanding this number increments mostly the complication.

**Fig. 12** Cumulative distribution function of UWB, EKF and UKF Algorithms

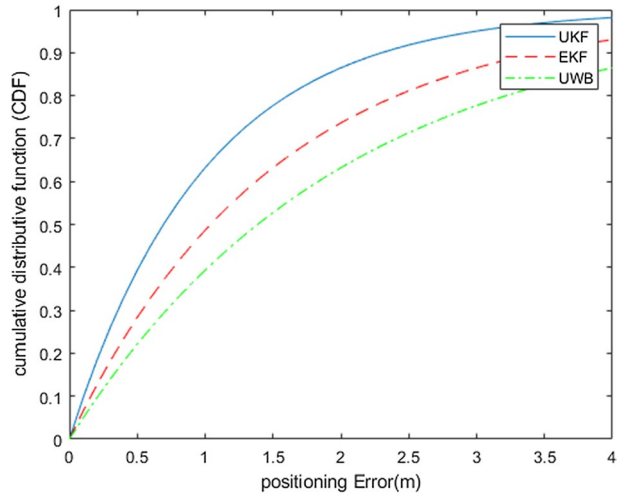


**Table 1** Impact of number of reference sensors on MSE

No. of reference sensors	4	8	12	16
UWB-IMU	2.93	2.87	2.74	2.65
UWB-EKF	2.09	1.75	1.54	1.43
UWB-UKF	1.65	1.43	1.05	0.94

## 5 Conclusion

In this paper, we have proposed an effective approach for indoor tracking and positioning systems in 3D. The positioning is calculated using Ultra Wideband with the TOA values received from all four reference nodes. The TOA values are obtained using Maximum energy Selection Search Back algorithm. And the position is calculated using an iterative method by using those TOA values. The positioning using Iterative method is compared with the linear least squares algorithm and showed that Iterative method gives better performance compared with linear least square algorithm. The positioning performance is compared in two scenarios, reference nodes placed at top corners of the building and other as cuboid shape configuration. The latter gives better results compared to previous configuration. The position of reference nodes has a significant effect on the exactness of localization.

The tracking is done by integrating UWB with IMU. And the performance can still be increased by using the nonlinear Extended and Unscented kalman filters. The state equations of the Kalman filters are obtained from IMU data and the observation equation from UWB measurements. EKF is compared with UKF and showed that later can improve the performance.

The outcomes got shows that the proposed UKF technique have been contrasted with the EKF and have shown significant gain in tracking of moving objects. The UKF displays excellent performance when contrasted with regular EKF since the series approximations in the EKF calculation can lead to poor representations of the nonlinear functions and probability distributions of interest.

In this paper the impact of the quantity of reference sensors on the position exactness has also been analysed. Undoubtedly, as expected, normally, the position exactness increments when the quantity of reference sensors increments, however just up to a specific value. Anyway the cost to pay for this is an expansion in the computational load.

**Funding** Not Applicable.

**Declaration**

**Conflict of interest** The author declare that they have no conflict of interest.

## References

- Oguntala, G., Abd-Alhameed, R., Jones, S., Noras, J., Patwary, M., & Rodriguez, J. (2018). Indoor location identification technologies for real-time IoT-based applications: An inclusive survey. *Computer Science Review*, 30, 55–79.
- Feng, D., Wang, C., He, C., Zhuang, Y., & Xia, X. G. (2020). Kalman filter based integration of IMU and UWB for high-accuracy indoor positioning and navigation. *IEEE Internet of Things Journal*, 7(4), 3133–3146.
- Gezici, S., & Poor, H. V. (2009). Position estimation via ultra-wide-band signals. *Proceedings of the IEEE*, 97(2), 386–403.
- Xu, Y., Shmaliy, Y. S., Li, Y., & Chen, X. (2017). UWB-based indoor human localization with time-delayed data using EFIR filtering. *IEEE Access*, 5, 16676–16683.
- Alari, A., Al-Salman, A., Alsaleh, M., Alnafessah, A., Al-Hadhrami, S., Al-Ammar, M. A., & Al-Khalifa, H. S. (2016). Ultra wideband indoor positioning technologies: Analysis and recent advances. *Sensors*, 16(5), 707–742.
- Bharadwaj, R., Alomainy, A., Parini, C. (2012). Localisation of body-worn sensors applying ultra wideband technology. In *Antennas and Propagation (APCAP), 2012 IEEE Asia-Pacific Conference on*, 106(107), 27–29.
- Sahinoglu, Z., Gezici, S., & Guvenc, I. (2008). *Ultra-wideband positioning systems: theoretical limits ranging algorithms and protocols*. Cambridge University Press.
- Gezici, S., Tian, Z., Giannakis, G. B., Kobayashi, H., Molisch, A. F., Poor, H. V., & Sahinoglu, Z. (2005). Localization via ultra-wideband radios: A look at positioning aspects for future sensor networks. *IEEE Signal Processing Magazine*, 22(4), 70–84.
- DWM1000 UWB Transceiver Module (2015) Product specification data sheet, Decawave Ltd.
- Jimenez Ruiz, A. R., & Seco Granja, F. (2017). Comparing ubisense, be- ´ spoon, and decawave UWB location systems: Indoor performance analysis. *IEEE Transactions on Instrumentation and Measurement*, 66(8), 2106–2117.
- Zhang, D., Xia F., Yang, Z., Yao, L., Zhao, W. (2010) Localization technologies for indoor human tracking. In *Proceedings of the IEEE international conference on future information technology*, Pusan, Korea.
- Bharadwaj, R., Parini, C., & Alomainy, A. (2014). Ultra wideband-based 3-D localization using compact base-station configurations. *Antennas and Wireless Propagation Letters IEEE*, 13, 221–224.
- Inam Ullah, Yu., Shen, X. S., Esposito, C., & Choi, C. (2020). A localization based on unscented kalman filter and particle filter localization algorithms. *IEEE Access*, 8, 2233–2246.
- Bregar, K., Novak, R., & Mohorci, M. (2019). Evaluation of range-based indoor tracking algorithms by merging simulation and measurements. *EURASIP Journal on Wireless Communications and Networking*. <https://doi.org/10.1186/s13638-019-1489-y>
- Kim, H. J., Xie, Y., Yang, H., Lee, C., & Song, T. L. (2019). An efficient indoor target tracking algorithm using TDOA measurements with applications to ultra-wideband systems. *IEEE Access*, 7, 91435–91445.
- Yao, L., Wu, Y. W. A., Yao, L., & Liao, Z. (2017) An integrated IMU and UWB sensor based indoor positioning system. In: *Proceeding IEEE International Conference on Indoor Positioning and Indoor Navigation (IPIN)*, pp. 1–8.
- Zhong, Y., Liu, T., Li, B., Yang, L., & Lou, L. (2018) Integration of UWB and IMU for precise and continuous indoor positioning. In: *Proceeding IEEE ubiquitous positioning, indoor navigation and location-based services (UPINLBS)*, pp. 1–5.
- Yoon, P. K., Zihajehzadeh, S., Kang, B., & Park, E. J. (2017). Robust biomechanical model-based 3-D indoor localization and tracking method using UWB and IMU. *IEEE Sensors Journal*, 17(4), 1084–1096.

19. Zihajezadeh, S., Yoon, P. K., Kang, B. S., & Park, E. J. (2015). UWB-aided inertial motion capture for lower body 3- D dynamic activity and trajectory tracking. *IEEE Transactions on Instrumentation and Measurement*, 64(12), 3577–3587.
20. Chang, L., Li, J., & Chen, S. (2015). Initial alignment by attitude estimation for strapdown inertial navigation systems. *IEEE Transactions on Instrumentation and Measurement*, 64(3), 784–994.
21. Bing, W., Yanyan, L., Qingquan, L., Yan, Z. (2018) A High precision dynamic indoor localization algorithm based on UWB Technology. In IEEE conference on Ubiquitous computing, Indoor navigation and location Based Services.

**Publisher's Note** Springer Nature remains neutral with regard to jurisdictional claims in published maps and institutional affiliations.



**B. Venkata Krishnaveni** received her B.Tech. degree in electronics and communication engineering (ECE) from Jawaharlal Nehru Technological University, Hyderabad, AP, India in 2003 and the M.Tech. degree in electronics and communication engineering from Pondicherry university in 2007. She is currently pursuing the Ph.D. degree in Wireless Communications at Jawaharlal Nehru Technological University, Anaparthapuramu, AP, India. Her research interests include Indoor Localization, Ultrawide band technology and wireless communications.



**K. Suresh Reddy** received the M.Tech (Communication Systems) degree from Gulbarga University in 1999 and Ph.D in the area of Signal Processing from Jawaharlal Nehru Technological University Hyderabad (JNTUH), Hyderabad, India, in 2012. Now he is working as Professor & Dean, Department of ECE, G. Pulla Reddy Engineering College, Kurnool, AP, India. He has 7 years of research experience and 19 years of teaching. His research interests are in the areas of Optical Networks and signal processing. He has published 12 papers in different International Journals and 5 papers in different conferences both in international and national level. At present he is supervising 8 PhD scholars. He carried out two Projects which are funded by AICTE.



**P. Ramana Reddy** received the M.E (Electronics) from SGGSC&T, Nanded, Maharashtra in 1994 and Ph.D in the area of Image Processing from Jawaharlal Nehru Technological University Ananthapuramu (JNTUA) in 2010. Presently he is working as Professor & Head, Department of ECE, JNTUA College of Engineering, Ananthapuramu, AP, India. He has 25 years of teaching & 17 years of research experience. His interests include signal processing and Image Processing. He has about 99 publications in various International/National Journals/Conferences. He is currently guiding 15 and guided 8 PhD students. He is fellow of IEI and IETE and life member of ISTE.

# Indoor Tracking by Adding IMU and UWB using Unscented Kalman Filter

B Venkata Krishnaveni, K. Suresh Reddy, and P. Ramana Reddy

## Abstract

In recent days Internet of Things (IoT) applications becoming prominent, like smart home, connected health, smart farming, smart retail and smart manufacturing, will lead to a challenging task in providing low cost, high precision localization and tracking in indoor environments. Positioning in indoor is yet an open issue mostly because of not receiving the signals of GPS in the context of indoor. Inertial Measurement Unit (IMU) can give an exact indoor tracking, however, they regularly experience the cumulated error as the speed and position are gotten by incorporating the increasing acceleration constantly as for time. At the same time Ultra Wideband (UWB) localization and tracking will be influenced by the real time indoor conditions. It is difficult to utilize an independent localization and tracking system to accomplish high precision in indoor conditions. In this paper, we come up with an incorporated positioning system in indoor by joining IMU and the UWB over the Unscented Kalman Filter (UKF) and the Extended Kalman Filter (EKF) to enhance the precision. All these algorithms are analyzed and assessed dependent on their exhibition.

**Key Words** Extended Kalman Filter, Indoor positioning, IoT, Ultra Wideband, IMU, Unscented Kalman Filter

## 1 Introduction

High-precision and low-cost localization and navigating systems for indoor portable devices have gotten basic in IoT applications, like smart home and smart manufacturing [1]. As of late, real-time location systems (RTLS) are being utilized for stock administration and security uphold in manufacturing plants and circulation focuses. It is vital in RTLS to appraise the position of moving articles, for example, forklifts and laborers along with the fixed bodies. To evaluate the position of movable items, an exceptionally fast and exact algorithm is needed.

The precise and strong indoor position is a major facilitator in forthcoming Internet applications. Inertial navigation is a technique utilizing the estimation from the IMU, primarily, gyroscopes and accelerometers for positioning and navigation. Utilizing the estimation given by the IMU, the Inertial Navigation System (INS) can enumerate the velocity, position and the direction of the system beginning from some known starting point. In any case, because of their drawn out floats, for example, accelerometer inclination and scale factor mistakes, from the calculated states of navigation (position, velocity, and attitude) will gain with time.

For indoor 3D human tracking, there are many technological hurdles to overcome because of the complexity of indoor conditions [2, 3]. The influence of obstacles like walls, equipment, furniture, the existence of people etc. leads to fading and multi path issues. There are individual technologies which are used in wireless network, for example, Bluetooth, Wi-Fi, UWB and ZigBee. The better appropriate innovation for large precision localization is UWB.

Ultra-Wideband is a radio innovation, which is essentially different in relation to the at present generally utilized conventional radio technologies. It transmits signals over various groups of frequencies (3.1 GHz to 10.6 GHz) all the while with hundreds MHz of transmission capacity (more prominent than 500 MHz). It is intended for Indoor Positioning Systems (IPSs) to conquer numerous difficulties, for example, signals because of extreme multi path reflect from furniture and wall, Non-Line-of-Sight (NLOS) signal because of blockages, and scattering of signal because of more prominent thickness of obstacles. With the known positions of reference nodes, by estimating the Time-of-Arrival (TOA) between the target node and each of the receivers, reference nodes, and their relating distances can be calculated. By using calculated distances, the location of the target can be estimated utilizing various methods of positioning [3-7]. Since 2010, localization devices based on UWB radio sensor, like Pozyx from KickStarter and DWM1000 from DecaWave [8], have gotten industrially accessible. At present, a few IPSs like the Ubisense System and Zebra System, utilizing UWB radio sensor have been conveyed [9-10].

---

B Venkata Krishnaveni is with the Electronics and Communication Engineering Department, Jawaharlal Nehru Technological University Anantapur, Ananthapuramu, Andhra Pradesh, 515002, India, (e-mail: Krishnavenibv@gmail.com).

Dr. K. Suresh Reddy is with the Electronics and Communication Engineering Department, G Pulla Reddy Engineering College (Autonomous), Kurnool, 518007, Andhra Pradesh, India (e-mail:sureshkatam@gmail.com).

Dr. P. Ramana Reddy is with the Electronics and Communication Engineering Department, Jawaharlal Nehru Technological University Anantapur, Ananthapuramu, Andhra Pradesh, 515002, India (e-mail:prjntu@gmail.com)

In spite of the fact that UWB has been recognized as perfect radio technology in indoor scenario for getting accurate data about the location, still there is a challenge for the IPS based on UWB technology to predict precise location data because of the multi path propagation of the direct LOS signal and propagation of the NLOS signal. To defeat the multi path impacts, a simple method is to eliminate the obstructions that may cause those inferences or to consider the open zone. This choice may not be conceivable in most indoor situations. IMU-based INSs are obtuse toward these interference but the errors resulted from the estimated position will increase over time. So these two technologies, IMU and UWB can be coupled for applications of IPS because these two technologies are corresponding to one another

In [11], the examination on three-dimensional UWB positioning utilizing distinctive conservative reference node configurations is conducted. Linear least squares with TOA values obtained using threshold based search back algorithm is used for positioning.

To defeat the issues with respect to positioning, the development of the structure of two algorithms named Extended Kalman Filter (EKF) and Unscented Kalman Filter (UKF) positioning methods are presented at [12]. But here the authors considered a two -dimensional system only. Demonstration of calculating the TOA values utilizing the two-way-ranging, positioning using the least squares (LS) and tracking with help of the EKF algorithm presented in [13].

In [14] an altered EKF sequential update, here, the Jacobian matrix and vector of measurement with the pseudo versions, for tracking of the target in indoor following applications to ultra-wideband systems utilizing Time Difference of Arrival (TDOA) estimation is introduced. We will get high exactness with TDOA on account of the enormous transmission capacity of UWB signals, however, its application is compelled by the corresponded measurement noise because of TDOA values. A multi-sensor combination design is presented in [15] for the IPS. At the point when UWB is accessible and reliable, the long-term drift error of IMU is aligned by UWB. Something else, the system will change from UWB to IMU promptly to obtain the status of positioning and navigation. In [16], a combined localizing solution of UWB and IMU is presented, which can give continuous and reliable position, particularly on account of NLOS situations. But, in [16], regarding the time synchronization issue, all the UWB modules are associated with a central regulator through the fibre line. This will build the complexity of the deployment and the expense of the system.

TOA algorithm is used in both [15] and [16] and have not taken the clock drift impact into account. Besides, despite the fact that noise of acceleration from IMU is considered in the measurements of acceleration, the impact of acceleration noise on the displacement and velocity because of incorporation is not evaluated in [15, 16].

In [17], a tracking and positioning algorithm coupling IMU, UWB and sensors specific to an area is proposed. It is indicated that the combination algorithm can acquire more precise three-dimensional velocity and information of height by utilizing the lower body biomechanical model. Note that large portion of the current indoor navigation and positioning systems are depended on human lower body MOCAP frameworks [18], which expands the expense and difficulty in deployment.

Hence, to accomplish less price and high precision of the indoor navigation and positioning system, this paper centers on the coupling of IMU and UWB dependent on Kalman Filter (KF) calculations. The information received by IMU is utilized for the equation of state, while the information received by UWB is utilized for the equation of observation in KF calculations. To improve further the accuracy of indoor positioning, the nonlinear kalman filter, namely, UKF algorithm is considered in this paper.

The main contributions of this paper can be summarized as follows:

Positioning with UWB using the Iterative method compared with linear least squares method using TOA values for two different configurations of reference node placement. An UKF fusion positioning algorithm introduced to decrease the computational complexity and to get better accuracy compared with EKF. From the results of simulation, we can conclude that the UKF fusion algorithm can obtain better accuracy of position compared to EKF fusion positioning algorithm in a three-dimensional area. The effect of the number of reference nodes or reference nodes density is also performed for all the algorithms.

In Section II, Indoor positioning System using IMU is explained first and then positioning using UWB, which uses TOA values as range measurements and Iterative Method for position estimation is explained. In Section III, the calculations dependent on coupling IMU and UWB positioning system is introduced in environment of 3D. In Section IV, simulation results are given and positioning performances of all algorithms are analyzed and explained. Conclusions are given in Section V.

## **2 Positining and Tracking System Using the coupling of IMU and UWB**

The proposed positioning and tracking system by coupling sensor based IMU and UWB localizing system in indoor environment of three dimension is given in Fig. 1. Here the three axis(x, y, and z) accelerometers, one UWB radio sensor (given as Target sensor) are placed on the body of a platform, and four UWB radio sensors (given as reference sensors) are placed inside the building with known locations.

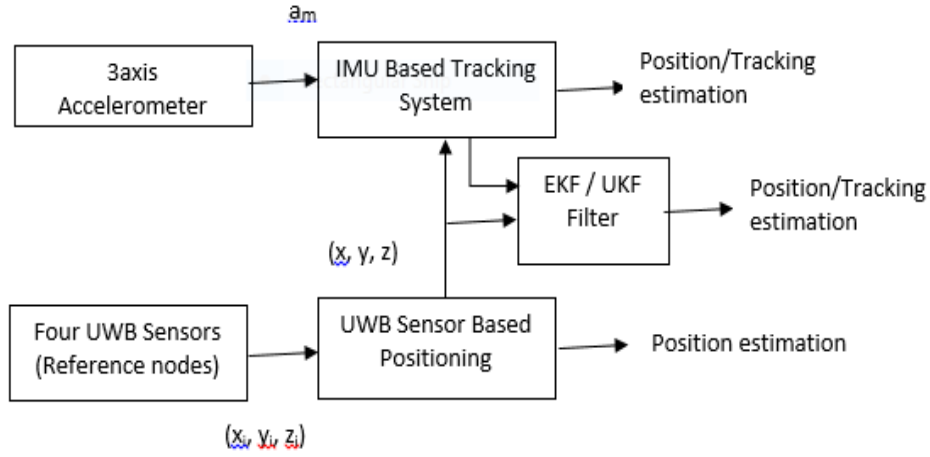


Fig. 1. Proposed sensor based indoor positioning and tracking system by coupling IMU and UWB

## 2.1 Positioning algorithm using IMU

To change the coordinates from one set to another, we need a rotation matrix that reveals to us precisely how one frame is rotated with respect to the other. Rotations are especially precarious mathematical objects and they can be the source of significant bugs if not managed cautiously and determinedly. There is a wide range of approaches to represent rotations [19].

The best method of representing a rotation is utilizing the euler angles. These angles represent an arbitrary rotation as the creation of three separate rotations about different principal axes. Euler angles are attractive in part because they are a parsimonious representation, requiring only three parameters instead of nine for a full rotation matrix, and it is easier to understand than another way of quaternion method and no need to calculate quaternion multiplication.

C1, C2, and C3 are the Euler angles about x, y, and z axis respectively, given as shown below.

$$C_3 = \begin{bmatrix} \cos\theta_3 & \sin\theta_3 & 0 \\ -\sin\theta_3 & \cos\theta_3 & 0 \\ 0 & 0 & 1 \end{bmatrix}$$

$$C_2 = \begin{bmatrix} \cos\theta_2 & 0 & -\sin\theta_2 \\ 0 & 1 & 0 \\ \sin\theta_2 & 0 & \cos\theta_2 \end{bmatrix}$$

$$C_1 = \begin{bmatrix} 1 & 0 & 0 \\ 0 & \cos\theta_1 & \sin\theta_1 \\ 0 & -\sin\theta_1 & \cos\theta_1 \end{bmatrix} \quad x$$

And

$$C = C_3 \times C_2 \times C_1 \quad (1)$$

By considering rotations with infinite, then the functions of trigonometry approximate as  $\sin(\theta) \approx \theta$  and  $\cos(\theta) \approx 1$ . Using these approximations, C can be written in terms of angular velocity as shown in (2).

$$C \approx \begin{bmatrix} 1 & 0 & 0 \\ 0 & 1 & -\theta_1 \\ 0 & \theta_1 & 1 \end{bmatrix} \begin{bmatrix} 1 & 0 & \theta_2 \\ 0 & 1 & 0 \\ -\theta_2 & 0 & 1 \end{bmatrix} \begin{bmatrix} 1 & -\theta_3 & 0 \\ \theta_3 & 1 & 0 \\ 0 & 0 & 1 \end{bmatrix}$$

$$\approx \begin{bmatrix} 1 & -\theta_3 & \theta_2 \\ \theta_3 & 1 & -\theta_1 \\ -\theta_2 & \theta_1 & 1 \end{bmatrix} \quad (2)$$

$\mathbf{a}$ , the accelerometers of the three axis are used to calculate the acceleration in system A as follows

$$\mathbf{a} = \begin{bmatrix} a_x & a_y & a_z \end{bmatrix}^T \quad (3)$$

Then, the acceleration in system B,  $\mathbf{a}^b$ , can be calculated using the rotation matrix as follows

$$\mathbf{a}^b = \begin{bmatrix} a_x^{b1} & a_y^{b1} & a_z^{b1} \end{bmatrix}^T = \mathbf{C} \times \mathbf{a} \quad (4)$$

If we consider the acceleration gravity  $g$ , then the acceleration in system B can be calculated by subtracting it from its value as follows

$$\mathbf{a}^b = \begin{bmatrix} a_x^b \\ a_y^b \\ a_z^b \end{bmatrix} = \begin{bmatrix} a_x^{b1} \\ a_y^{b1} \\ a_z^{b1} \end{bmatrix} - \begin{bmatrix} 0 \\ 0 \\ g \end{bmatrix} \quad (5)$$

If we consider the sampling interval is short, then constant force is subjected to the carrier with a linear motion of uniform acceleration. Let the position of the system B be  $\mathbf{x}^b$ , can be calculated as follows

$$\begin{bmatrix} x_x^b(t+1) \\ x_y^b(t+1) \\ x_z^b(t+1) \end{bmatrix} = \begin{bmatrix} x_x^b(t) \\ x_y^b(t) \\ x_z^b(t) \end{bmatrix} + \begin{bmatrix} v_x^b \\ v_y^b \\ v_z^b \end{bmatrix} (\Delta t) + \frac{1}{2} \begin{bmatrix} a_x^b \\ a_y^b \\ a_z^b \end{bmatrix} (\Delta t)^2 \quad (6)$$

Where  $x^b(t)$ ,  $v^b(t)$ , and  $a^b(t)$  be the position, velocity and the acceleration of the system at time  $t$ ,  $x^b(t+1)$  be the position of system B at time  $(t+1)$ ,  $(\Delta t)$  be the sampling interval.

## 2.2 Position processing algorithm using UWB

UWB positioning of an unknown target node can be made by using fixed known locations of reference nodes. For a 3D environment a minimum of four reference nodes will be enough for positioning. Positioning of the target node can be performed in two steps. First one is measuring the signal parameters either time difference of arrival (TDOA) or time of arrival (TOA) or direction of arrival (DOA) or received signal strength (RSS), of the transmitted signal from reference nodes utilized as range values for target positioning. Second step, using range values, the location of the target can be calculated. The most applicable one for the UWB system is TOA as this takes the advantage of a huge time resolution of UWB signals [20]

### 2.2.1 TOA Estimation Algorithms

Measuring the TOA values is difficult due to the high dispersive nature of UWB channels. Always the first arrival path need not be the strongest path. Hence, there is a need for precise ranging and less complicated techniques at achievable sampling rates. The Fig.2 shows the method for the calculation of TOA values. Here the TOA estimation is done utilizing the samples  $z[n]$ , which are taken after the square-law device.

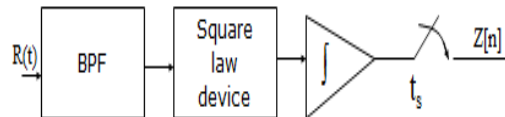


Fig. 2. Energy samples of the received signal

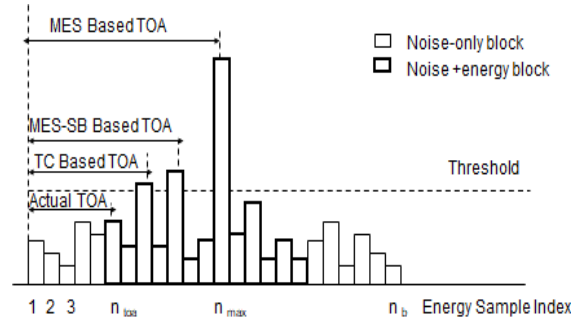


Fig. 3. TOA estimation algorithms using the samples of energy

The algorithms for TOA calculation using the samples of energy received after a square law device, summarized in Fig.3. Maximum Energy Selection, where the sample output with maximum energy is selected as the first path. But in indoors due to multi path it is not necessary that the maximum energy sample is the direct path between the target and reference node. Next one is Threshold Comparison, where the sample first exceeds the threshold can be calculated as TOA value. This method performance is poor at lower SNR's because there may be more threshold crossings due to the noise addition. The next suitable technique is Maximum energy Selection Search Back, where the window of search-back from a maximum energy selection sample given by  $w_{sb}$  assigned using the measurements of the channel. It performs best among the above mentioned techniques. The equation for calculating TOA value using Maximum energy Selection Search Back is given by

$$t_{\text{MES-SB}} = [\min \{ \check{Z}[n] > \xi \} - 0.5 + n_{\text{max}} - w_{\text{sb}} + 1] T_b \quad (7)$$

here

$$\check{Z}[n] = \{ z[n_{\text{max}} - w_{\text{sb}}] z[n_{\text{max}} - w_{\text{sb}} + 1] \dots z[n_{\text{max}}] \}$$

## 2.2.2 Position Estimation

Position of the target node can be calculated by using well known triangulation/ trilateration (2D) or multilateration for higher dimensions by two ways. One is nonlinear equations obtained directly from the nonlinear relationships between target and the range measurement like maximum likelihood (ML) and nonlinear least squares (NLS) algorithms. Another way is converting these equations into linear like, weighted linear least squares (WLLS) and linear least squares (LLS) algorithms. But in triangulation/ trilateration the three circles with radius as the measured distance between a reference sensor and the target sensor using TOA values may not converge to a single point there by the performance of the system decreases. If we consider three dimensions where we require four reference nodes, this convergence issue still extends and degrades the performance. So another method called Iterative method with Hessain function is used.

The function for optimization method is

$$f(\mathbf{x}) = \sum_{i=1}^N [ [(p - p_i)^2 + (q - q_i)^2 + (r - r_i)^2]^{1/2} - c(t_i - t_m)^2 ]^2 \quad (8)$$

Where,

$$\mathbf{x} = [p, q, r, t_o]^T \text{ be the position to calculate}$$

$t_i, t_m$  be the  $i^{\text{th}}$  reference sensor received time and target sensor transmitted time

To calculate the location of the target sensor the following iterative equation is used.

$$\mathbf{x}_{k+1} = \mathbf{x}_k - \delta \mathbf{B}_k \mathbf{s}_k \quad (9)$$

Where,

$\mathbf{x}_k$  be the location at the  $k^{\text{th}}$  iteration,

$\delta$  be the size of the increment,

$\mathbf{s}_k$  be the objective function

$$\mathbf{s}_k = \Delta f(p, q, r, t_o) = \left[ \frac{\partial f}{\partial p}, \frac{\partial f}{\partial q}, \frac{\partial f}{\partial r}, \frac{\partial f}{\partial t_o} \right]_{p=p_k}^T$$

$\mathbf{B}_k$  is the Hessain function increased by utilizing below equation

$$\mathbf{B}_{k+1} = \mathbf{B}_k + \frac{\mathbf{h}_k \mathbf{h}_k^T}{\mathbf{h}_k^T \mathbf{q}_k} - \frac{\mathbf{B}_k \mathbf{q}_k \mathbf{q}_k^T \mathbf{B}_k}{\mathbf{q}_k^T \mathbf{B}_k \mathbf{q}_k} \quad (10)$$

here,

$$\mathbf{h}_k = \mathbf{x}_{k+1} - \mathbf{x}_k$$

$$\mathbf{q}_k = \mathbf{s}_{k+1} - \mathbf{s}_k$$

The mean of known reference nodes is taken as the initial estimate and the Identity matrix (I) as the hessian grid beginning.

### 3. Algorithm based on IMU and UWB

To beat the individual deficiencies of the UWB and IMU, we execute an UKF that couple the two positioning systems so that the UWB sensor based result of position is used to change the IMU mistakes and the IMU sensor based result of position solution is used to distinguish and isolate the adjusted UWB sensor data to build the general precision of positioning performance. Here, we present the coupling algorithm using EKF first, then the coupling algorithm using UKF.

#### 3.1 EKF algorithm

Here we are considering a plane of three -dimensions target moving with uniform acceleration. The vector of state at time  $k$ , is given by

$$\mathbf{x}(k) = \left[ x_x(k) \ x_y(k) \ x_z(k) \ v_x(k) \ v_y(k) \ v_z(k) \ a_x(k) \ a_y(k) \ a_z(k) \right] \quad (11)$$

here,

$x(k)$  be the position,  $v(k)$  be the velocity, and  $a(k)$  be the acceleration

Let  $(\Delta t)$  be the sample interval and  $(\Delta t) w(k)$  is the process noise of acceleration . Then  $\frac{(\Delta t)^2}{2} w(k)$  represents the process noise of velocity and  $\frac{(\Delta t)^3}{6} w(k)$  represents the process noise of position, because of integrating acceleration two times. The velocity and acceleration values can be obtained from IMU.

The equation of state at time  $(k+1)$  with uniform acceleration motion is given in (12)

$$x_x(k+1) = x_x(k) + v_x(k) (\Delta t) + a_x(k) \frac{(\Delta t)^2}{2} + \frac{(\Delta t)^3}{6} w_x(k)$$

$$x_y(k+1) = x_y(k) + v_y(k) (\Delta t) + a_y(k) \frac{(\Delta t)^2}{2} + \frac{(\Delta t)^3}{6} w_y(k)$$

$$x_z(k+1) = x_z(k) + v_z(k) (\Delta t) + a_z(k) \frac{(\Delta t)^2}{2} + \frac{(\Delta t)^3}{6} w_z(k)$$

$$v_x(k+1) = v_x(k) + a_x(k) (\Delta t) + \frac{(\Delta t)^2}{2} w_x(k)$$

$$v_y(k+1) = v_y(k) + a_y(k) (\Delta t) + \frac{(\Delta t)^2}{2} w_y(k)$$

$$v_z(k+1) = v_z(k) + a_z(k) (\Delta t) + \frac{(\Delta t)^2}{2} w_z(k)$$

$$a_x(k+1) = a_x(k) + (\Delta t) w_x(k)$$

$$a_y(k+1) = a_y(k) + (\Delta t) w_y(k)$$

$$a_z(k+1) = a_z(k) + (\Delta t) w_z(k)$$

(12)

The matrix form of the state equation written as

$$\mathbf{x}(k+1) = \mathbf{F}\mathbf{x}(k) + \mathbf{G}\mathbf{w}(k)$$

(13)

Where  $\mathbf{F}$  represents the transition matrix of state,

$\mathbf{G}$  represents the driving matrix of noise.

The process noise vector with zero mean and covariance matrix  $\mathbf{Q}$  is given by

$$\mathbf{w}(k) = \left[ w_x(k) \ w_y(k) \ w_z(k) \right]^T$$

And

$$\mathbf{Q} = \text{diag} \left( \left[ \sigma_{ax}^2 \ \sigma_{ay}^2 \ \sigma_{az}^2 \right] \right)$$

$$F = \begin{bmatrix} 1 & 0 & 0 & (\Delta t) & 0 & 0 & \frac{(\Delta t)^2}{2} & 0 & 0 \\ 0 & 1 & 0 & 0 & (\Delta t) & 0 & 0 & \frac{(\Delta t)^2}{2} & 0 \\ 0 & 0 & 1 & 0 & 0 & (\Delta t) & 0 & 0 & \frac{(\Delta t)^2}{2} \\ 0 & 0 & 0 & 1 & 0 & 0 & (\Delta t) & 0 & 0 \\ 0 & 0 & 0 & 0 & 1 & 0 & 0 & (\Delta t) & 0 \\ 0 & 0 & 0 & 0 & 0 & 1 & 0 & 0 & (\Delta t) \\ 0 & 0 & 0 & 0 & 0 & 0 & 1 & 0 & 0 \\ 0 & 0 & 0 & 0 & 0 & 0 & 0 & 1 & 0 \\ 0 & 0 & 0 & 0 & 0 & 0 & 0 & 0 & 1 \end{bmatrix}$$

And

$$G = \begin{bmatrix} \frac{(\Delta t)^3}{6} & 0 & 0 \\ 0 & \frac{(\Delta t)^3}{6} & 0 \\ 0 & 0 & \frac{(\Delta t)^3}{6} \\ \frac{(\Delta t)^2}{2} & 0 & 0 \\ 0 & \frac{(\Delta t)^2}{2} & 0 \\ 0 & 0 & \frac{(\Delta t)^2}{2} \\ (\Delta t) & 0 & 0 \\ 0 & (\Delta t) & 0 \\ 0 & 0 & (\Delta t) \end{bmatrix}$$

Let the observation vector be  $Z(k)$ , including the correct distance from reference sensor to target sensor  $d_i(k)$  and the observation noise  $n_i(k)$

The equation of observation matrix including the range between the target sensor, four reference sensors and the angle between target sensor to four reference sensors is expressed as

$$z(k) = \begin{bmatrix} d_1(k) + n_1(k) \\ d_2(k) + n_2(k) \\ d_3(k) + n_3(k) \\ d_4(k) + n_4(k) \\ \phi_1(k) + n_5(k) \\ \phi_2(k) + n_6(k) \\ \phi_3(k) + n_7(k) \\ \phi_4(k) + n_8(k) \end{bmatrix} = H(k) x(k) + n(k)$$

(14)

Here at time  $k$ ,  $H(k)$  denotes the observation matrix

And  $n(k)$  represents the vector of noise having mean with zero and covariance of the matrix as

$$R = \text{diag}(\sigma_{d1}^2, \sigma_{d2}^2, \sigma_{d3}^2, \sigma_{d4}^2, \sigma_{\phi1}^2, \sigma_{\phi2}^2, \sigma_{\phi3}^2, \sigma_{\phi4}^2)$$

The equations of true distances are given as

$$\begin{bmatrix} d_1(k) \\ d_2(k) \\ d_3(k) \\ d_4(k) \end{bmatrix} = \begin{bmatrix} \sqrt{(x_x(k) - x_1)^2 + (x_y(k) - y_1)^2 + (x_z(k) - z_1)^2} \\ \sqrt{(x_x(k) - x_2)^2 + (x_y(k) - y_2)^2 + (x_z(k) - z_2)^2} \\ \sqrt{(x_x(k) - x_3)^2 + (x_y(k) - y_3)^2 + (x_z(k) - z_3)^2} \\ \sqrt{(x_x(k) - x_4)^2 + (x_y(k) - y_4)^2 + (x_z(k) - z_4)^2} \end{bmatrix} \quad (15)$$

And equations of true angle are given by

$$\phi_i(k) = \arccos\left(\frac{(\mathbf{x}(k) \cdot \mathbf{x}_i)}{|\mathbf{x}(k)| |\mathbf{x}_i|}\right) \quad \text{for } i=1, 2, 3, 4 \quad (16)$$

Where

$(\mathbf{x}(k) \cdot \mathbf{x}_i) = x_x x_{i1} + x_y y_{i1} + x_z z_{i1}$  be the dot product of two vectors namely the position of reference sensor and the position of target sensor for  $i=1$ .

$$\text{And } |\mathbf{x}(k)| = \sqrt{x_x^2 + x_y^2 + x_z^2}, \quad (17)$$

$$|\mathbf{x}_i| = \sqrt{x_i^2 + y_i^2 + z_i^2} \quad \text{for } i=1, 2, 3, 4 \quad (18)$$

The above nonlinear equations require linearization, so the EKF algorithm is used with Taylor expansion of first order.

$H(k)$ , the matrix of Jacobian is given as in (19).

Here in EKF we are calculating the matrix of Jacobian, which increases the algorithm's complexity of computation. If the assumption of linearization is not correct, then algorithm of EKF performance will diverge and degrade. Algorithm 1 gives the EKF algorithm process step by step.

$$H(k) = \begin{bmatrix} \frac{\partial d_1(k)}{\partial x_x(k)} & \frac{\partial d_1(k)}{\partial x_y(k)} & \frac{\partial d_1(k)}{\partial x_z(k)} \\ \frac{\partial d_2(k)}{\partial x_x(k)} & \frac{\partial d_2(k)}{\partial x_y(k)} & \frac{\partial d_2(k)}{\partial x_z(k)} \\ \frac{\partial d_3(k)}{\partial x_x(k)} & \frac{\partial d_3(k)}{\partial x_y(k)} & \frac{\partial d_3(k)}{\partial x_z(k)} \\ \frac{\partial d_4(k)}{\partial x_x(k)} & \frac{\partial d_4(k)}{\partial x_y(k)} & \frac{\partial d_4(k)}{\partial x_z(k)} \\ \frac{\partial \phi_1(k)}{\partial x_x(k)} & \frac{\partial \phi_1(k)}{\partial x_y(k)} & \frac{\partial \phi_1(k)}{\partial x_z(k)} \\ \frac{\partial \phi_2(k)}{\partial x_x(k)} & \frac{\partial \phi_2(k)}{\partial x_y(k)} & \frac{\partial \phi_2(k)}{\partial x_z(k)} \\ \frac{\partial \phi_3(k)}{\partial x_x(k)} & \frac{\partial \phi_3(k)}{\partial x_y(k)} & \frac{\partial \phi_3(k)}{\partial x_z(k)} \\ \frac{\partial \phi_4(k)}{\partial x_x(k)} & \frac{\partial \phi_4(k)}{\partial x_y(k)} & \frac{\partial \phi_4(k)}{\partial x_z(k)} \end{bmatrix} \quad (19)$$

Where,

$$\begin{aligned} \frac{\partial d_i(k)}{\partial x_x(k)} &= \frac{x_x(k) - x_i}{\sqrt{(x_x(k) - x_i)^2 + (x_y(k) - y_i)^2 + (x_z(k) - z_i)^2}} \\ \frac{\partial d_i(k)}{\partial x_y(k)} &= \frac{x_y(k) - y_i}{\sqrt{(x_x(k) - x_i)^2 + (x_y(k) - y_i)^2 + (x_z(k) - z_i)^2}} \\ \frac{\partial d_i(k)}{\partial x_z(k)} &= \frac{x_z(k) - z_i}{\sqrt{(x_x(k) - x_i)^2 + (x_y(k) - y_i)^2 + (x_z(k) - z_i)^2}} \end{aligned} \quad (20)$$

Initialization: Mean  $\mu(0) = E[x(0)]$   
Covariance  $P(0) = var(x(0))$

1: Prediction of state  
 $\bar{x}_k = F\hat{x}_{k-1} + Gw_{k-1}$

2: Prediction of state covariance  
 $\bar{P}_k = F_{k-1} P_{k-1} F_{k-1}^T + G_{k-1} Q_{k-1} G_{k-1}^T$

3: Gain calculation of Kalman filter  
 $K_k = \bar{P}_k H_k^T [H_k \bar{P}_k H_k^T + R_k]^{-1}$

4: State correction  
 $\hat{x}_k = \bar{x}_k + K_k (Z_k - H_k \bar{x}_k)$

5: State co-variance correction  
 $\hat{P}_k = (I - K_k H_k) \bar{P}_k$

---

### 3.2 Unscented Kalman Filter

For the estimation of parameter EKF is the standard technique, but EKF is having some drawbacks. In EKF, the non-linear equations of the system are converted into linear equations. In this situation, the accuracy of EKF can attain up to first order of Taylor's series and also, it needs to calculate the matrix of Jacobian. Because of the mentioned drawbacks and issues, UKF has been used to present better performance as compared to the EKF algorithm and especially for the non-linear systems. UKF is based on unscented transformation (UT), the approach used to estimate the statistics of the random variable. In UKF, some points are used to catch the actual covariance and mean of the random variables.

Dissimilar to EKF, UKF doesn't have to calculate matrix of Jacobian at each time and embraces UT to make the measurements save reliable for the random variables which undergo transformation of nonlinear. For the random variable with distribution as Gaussian, by choosing the sample points cautiously, UT can catch the covariance and mean precisely to the Taylor series third order. So it can successfully conquer the low precision restriction of the EKF algorithm. So the algorithm of UKF is more advantageous and exact when contrasted with the algorithm of EKF.

In the 3D plane expecting that the target sensor is moving with uniform acceleration, the vector of state contains acceleration, velocity and position and the vector of measurement containing distances and angles from reference sensors to target sensors is the equivalent to that in the algorithm EKF.

Here the  $2n+1$  sigma points can be calculated by using (21), these points are propagated through the nonlinearity and are used to calculate the covariance and mean of the variable after transformation.

$$\mathbf{X} = [m \quad \dots \quad m] + \sqrt{c} [0 \quad \sqrt{P} \quad -\sqrt{P}] \quad (21)$$

And calculate the weights using (22).

$$\begin{aligned} W_m^{(0)} &= \lambda / (n + \lambda) \\ W_c^{(0)} &= \lambda / (n + \lambda) + (1 - \alpha^2 + \beta) \\ W_m^{(i)} &= \lambda / 2(n + \lambda) \\ W_c^{(i)} &= \lambda / 2(n + \lambda) \end{aligned} \quad (22)$$

$i = 1, \dots, 2n$ .

here  $\lambda$  is a scaling parameter to decrease the total error of prediction which is given by

$$\lambda = \alpha^2 (n + k) - n$$

$\alpha, \beta$  and  $k$  are positive values

where  $W_m^{(i)}$  is the sigma points mean weight and  $W_c^{(i)}$  is the sigma points covariance weight,  $i$  in the above weights is the sample point index.

Generally,  $\alpha$  is normally taken as a small positive value to maintain the sigma points mean nearer to  $x$ ,  $\beta$  is a positive

coefficient to integrate the x prior distribution, and  $\kappa$  is taken as zero to make the matrix  $(n + \lambda) P$  as a semi-positive definite matrix. The algorithm begins considering the initial mean as  $m_0$  and co-variance as  $P_0$ .

The algorithm of Unscented Kalman Filter algorithm is given below

---

Algorithm 2 Unscented Kalman Filter Algorithm

---

**Initialization:**

$$m_0 = E[x_0]$$

$$P_0 = E[(x_0 - m_0)(x_0 - m_0)^T]$$

**Step 1:** Calculate the predicted mean of state  $m_k^-$  and covariance  $P_k^-$  from transformed sigma points

$$\mathbf{X}_{k-1} = [m_{k-1} \quad \dots \quad m_{k-1}] + \sqrt{c} [0 \quad \sqrt{P_{k-1}^-} \quad -\sqrt{P_{k-1}^-}]$$

$$\mathbf{X}_k = f_d(\mathbf{X}_{k-1}, k-1)$$

$$m_k^- = \sum_k \mathbf{w}_m \mathbf{X}_k$$

$$P_k^- = \sum_k \mathbf{W} [\mathbf{X}_k] [\mathbf{X}_k]^T + Q_{k-1}$$

Here vector  $\mathbf{w}_m$  and weighted matrix  $\mathbf{W}$  are given as

$$\mathbf{w}_m = [W_m^0 \quad \dots \quad W_m^{2n}]^T$$

$$\mathbf{W} = (I - [\mathbf{w}_m \quad \dots \quad \mathbf{w}_m]) \times \text{diag}[W_m^0 \quad \dots \quad W_m^{2n}]$$

$$\times (I - [\mathbf{w}_m \quad \dots \quad \mathbf{w}_m])^T$$

**Step 2:** Calculate the measurement predicted covariance  $S_k$  and mean  $\mu_k$ , the measurement and state cross covariance  $C_k$  as

$$\mathbf{X}_k^- = [m_k^- \quad \dots \quad m_k^-] + \sqrt{c} [0 \quad \sqrt{P_k^-} \quad -\sqrt{P_k^-}]$$

$$\mathbf{Y}_k^- = h_d(\mathbf{X}_k^-, k)$$

$$\mu_k = \mathbf{Y}_k^- \mathbf{w}_m$$

$$S_k = \mathbf{Y}_k^- \mathbf{W} [\mathbf{Y}_k^-]^T + R_k$$

$$C_k = \mathbf{X}_k^- \mathbf{W} [\mathbf{Y}_k^-]^T$$

**Step 3:** Calculate the gain of the filter  $K_k$  and mean  $m_k$  and co-variance  $P_k$  of the state

$$K_k = C_k S_k^{-1}$$

$$m_k = m_k^- + K_k (y_k - \mu_k)$$

$$P_k = P_k^- - K_k S_k K_k^T$$


---

#### 4. Results and Discussion

A number of Monte Carlo simulations were performed to estimate the performance of algorithms, in terms of precision for both the localization and tracking methods. We are considering two scenarios for placement of reference nodes. First one, at the top four corners of the building and second one Cuboid-Shape Configuration as shown below. For the given two scenarios the reference nodes are fixed accordingly and the unknown target position is randomly selected. The estimated position of the target using Iterative method (IM) is compared with the traditional linear least squares (LLS) method of UWB for two scenarios in Fig.4 and Fig.5

The estimated target position for each run result is obtained and averaged over 1000 runs are presented. The result shows that the Iterative method gives better accuracy compared to the linear least squares method.

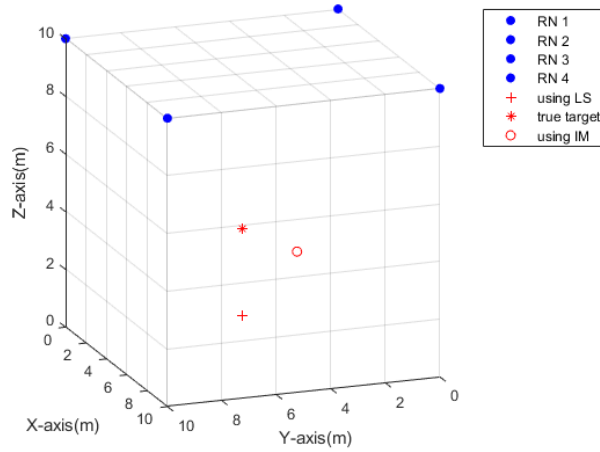


Fig. 4. Comparison of linear least squares and Iterative method for scenario 1

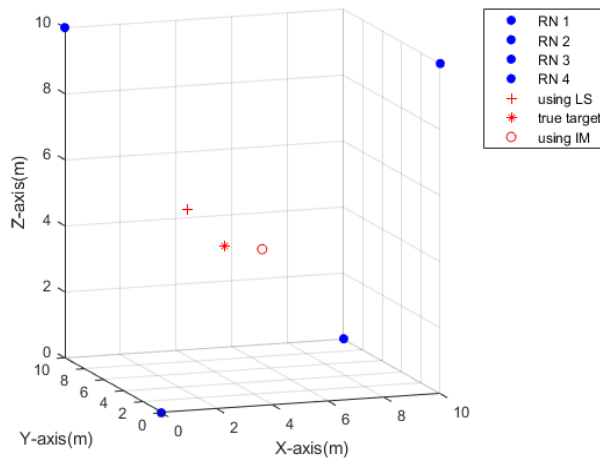


Fig. 5. Comparison of linear least squares and Iterative method for scenario 2

The variance of time of arrival error,  $\sigma_{TOA,i}^2$ , is assigned proportional to the distance between reference node  $i=1,2,3,4$  and the target node,  $d_i^2$  with  $SNR = d_i^2 / \sigma_{TOA,i}^2$ .

Here the mean square position error MSPE of the linear least squares (LLS) method and iterative method (IM) for SNR belongs to  $[-10, 60]$  dB are compared. The MSPE is given by

$MSPE = E\{(\hat{x} - x)^2 + (\hat{y} - y)^2 + (\hat{z} - z)^2\}$ . As expected, the iterative method is preferable to the LLS method and the MSPE is less for both scenarios as given in Fig.6 and Fig.7 for two scenarios respectively.

The comparison of two scenarios is given in Fig. 8. And among the scenarios, the second with Cuboid-Shape Configuration gives better performance compared to the first scenario with reference nodes at the top four corners of the building. The MSPE of iterative method, with reference nodes fixed as second scenario is smaller by around 1 dB at  $SNR \in [-10, 60]$  dB compared to the first scenario. For the second scenario, the reference nodes occupy four corners including top and bottom of the area of localization. Hence, almost the total area of localization is covered. In the case of the scenario1 reference sensors at top of the positioning area covered less area compared to previous one. So geometry of the reference nodes plays an important role in calculating positioning. The Cumulative distribution function of location errors for both scenarios are given in Fig.9. It can be observed that scenario 2 is the best precise technique with an error under 2 meters in 90% of situations, for scenario 1 a similar exactness is accomplished in just between 60 % and 70 % of situations

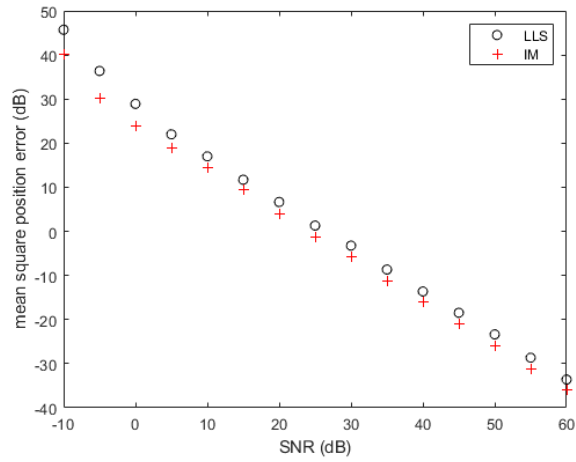


Fig. 6. Comparison of mean square position error for linear least squares and iterative method for scenario 1

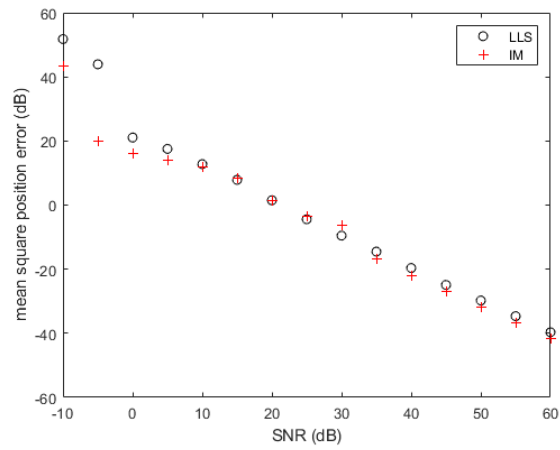


Fig. 7. Comparison of mean square position error for linear least squares and iterative method for scenario 2

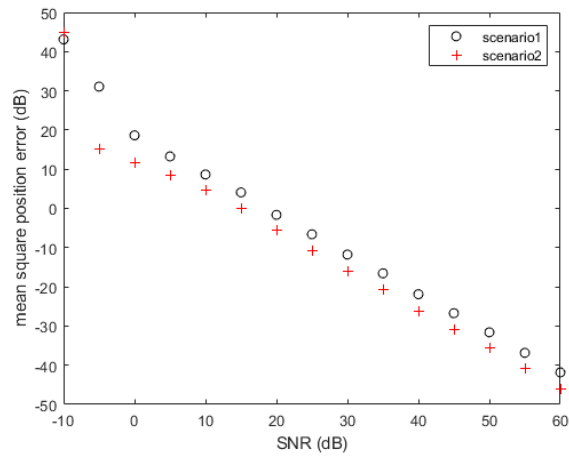


Fig. 8. Comparison of mean square position error scenario 1 and scenario 2

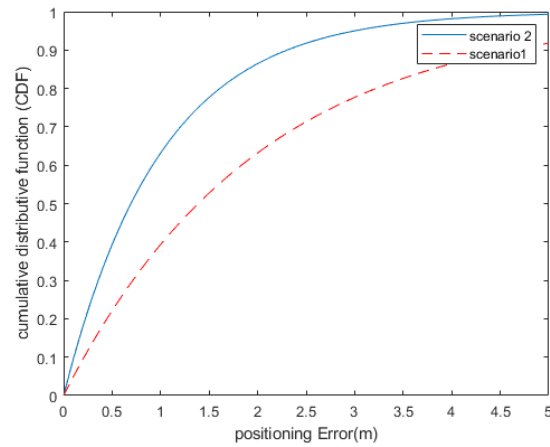


Fig. 9. Cumulative distribution function of scenario 1 and scenario 2

A simulation to evaluate the performance of indoor tracking with UWB positioning and IMU tracking is compared with EKF and is compared with the true (ground truth) trajectory in Fig 10. EKF gives better performance compared to UWB with IMU. In this simulation, for the first time the estimated state vector is taken as  $X_{est}$  is Zero matrix, in which  $X_{true} = X_{est}$ . The parameters of UKF are taken as  $\alpha = 0.001$ ,  $k = 0$ , and  $\beta = 2$ . The state vector size is  $n = \text{length}(X_{est})$ . Where the process noise vector is taken as Gaussian white sequences noise with zero mean and covariance  $R = I \sigma^2$ , where,  $\sigma = 0.01$ . The covariance matrix of process noise is given by  $Q = I \times 10^{-10}$ , here  $I$  is the identity matrix. The comparison of EKF and UKF tracking algorithms is shown in Fig 11. UKF still provides better estimation accuracy than EKF does. We can see that the tracking result is quite good with the estimated result from UKF.

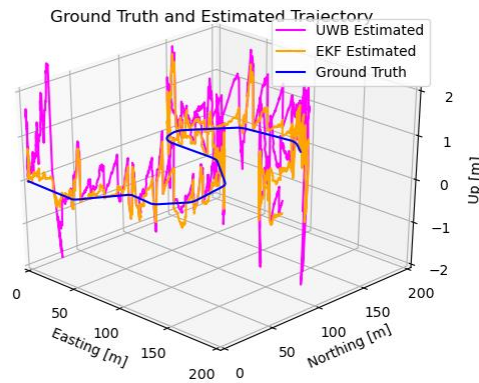


Fig. 10. Performance comparison of UWB and EKF tracking algorithms with the actual ground truth trajectory

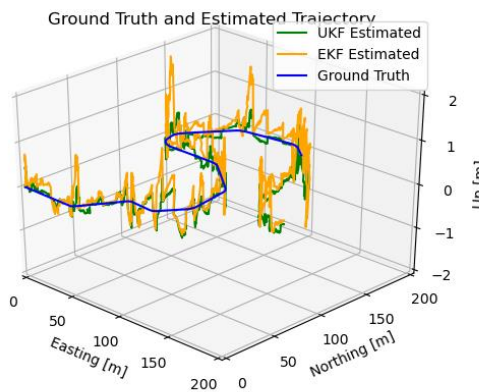


Fig. 11. Performance comparison of UKF and EKF tracking algorithms with the actual ground truth trajectory

The function of cumulative distribution of the tracking errors for all the algorithms are given in Fig.12. It is noticed that UKF tracking algorithm is the best precise technique with an error around 2 meters in 90% of situations, but for EKF a similar exactness is accomplished in 75 % and only 60 % in case of UWB.

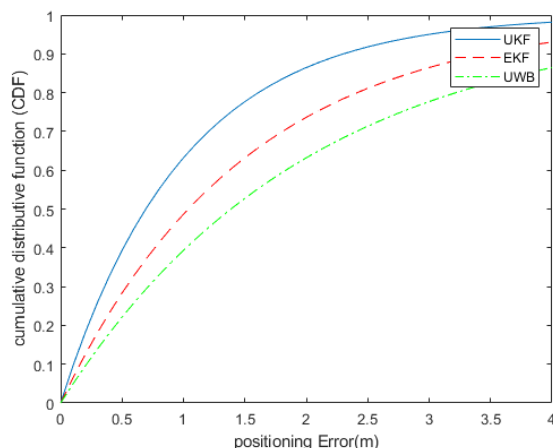


Fig. 12. Cumulative distribution function of UWB, EKF and UKF Algorithms

#### 4.1 Density of the Reference Nodes

By expanding the number of the reference sensors may reduce the positioning errors. For four reference sensors, the position is similar to in Fig 4. The position of 8 reference sensors is acquired from that of 4 reference sensors by embedding an extra sensor halfway between each two neighbouring reference sensors. The position of 12 reference sensors relates to that of 8 reference sensors with 4 extra sensors set at the focal point of the rectangular zone. At last, the position of 16 reference sensors is acquired by embedding 4 new sensors halfway between the 4 past sensors.

The mean square error (MSE) for different numbers of reference nodes is summarized in table1 for all algorithms. To sum up, we can say that expanding the quantity of reference sensors diminishes the positioning errors basically when utilizing techniques dependent on nonlinear Kalman filtering. However, no substantial improvement is achieved by expanding the quantity of reference nodes beyond some point. This must be evaded, since expanding this number increments mostly the complication.

**Table 1**  
Impact Of Number Of Reference Sensors On MSE

No.of Reference Sensors	4	8	12	16
UWB-IMU	2.93	2.87	2.74	2.65
UWB-EKF	2.09	1.75	1.54	1.43
UWB-UKF	1.65	1.43	1.05	0.94

#### 5. Conclusion

In this paper, we have proposed an effective approach for indoor tracking and positioning systems in 3D. The positioning is calculated using Ultra Wideband with the TOA values received from all four reference nodes. The TOA values are obtained using Maximum energy Selection Search Back algorithm. And the position is calculated using an iterative method by using those TOA values. The positioning using Iterative method is compared with the linear least squares algorithm and showed that Iterative method gives better performance compared with linear least square algorithm. The positioning performance is compared in two scenarios, reference nodes placed at top corners of the building and other as cuboid shape configuration. The latter gives better results compared to previous configuration. The position of reference nodes has a significant effect on the exactness of localization.

The tracking is done by integrating UWB with IMU. And the performance can still be increased by using the nonlinear Extended and Unscented kalman filters. The state equations of the Kalman filters are obtained from IMU data and the observation equation from UWB measurements. EKF is compared with UKF and showed that later can improve the performance.

The outcomes got shows that the proposed UKF technique have been contrasted with the EKF and have shown significant gain in tracking of moving objects. The UKF displays excellent performance when contrasted with regular EKF since the series approximations in the EKF calculation can lead to poor representations of the nonlinear functions and probability distributions of interest.

In this paper the impact of the quantity of reference sensors on the position exactness has also been analysed. Undoubtedly, as expected, normally, the position exactness increments when the quantity of reference sensors increments, however just up to a specific value. Anyway the cost to pay for this is an expansion in the computational load.

## Declarations

**Funding:** Not Applicable

**Conflicts of interest/Competing interests:** Not Applicable

**Availability of data and material:** Not Applicable

**Code Availability:** Not Applicable

## References

- [1] G. Oguntala G., R. Abd-Alhameed R., S. Jones S., J. Noras, M. Patwary, J. Rodriguez, "Indoor location identification technologies for real-time IoT-based applications: An inclusive survey", *Computer Science Review*, Vol. 30,2018, Pages 55-79.
- [2] Y. Xu, Y. S. Shmaliy, Y. Li, X. Chen, "UWB-based indoor human localization with time-delayed data using EFIR filtering", *IEEE Access*, vol. 5, pp. 16676-16683, 2017.
- [3] Gezici, S.; Poor, H.V.; , "Position Estimation via Ultra-Wide-Band Signals," *Proceedings of the IEEE* , vol.97, no.2, pp.386-403, Feb. 2009.
- [4] A. Alari, A. Al-Salman, M. Alsaleh, A. Alnafessah, S. Al-Hadhrami, M. A. Al-Ammar, and H. S. Al-Khalifa, "Ultra wideband indoor positioning technologies: Analysis and recent advances," *Sensors*, vol. 16, no. 5, pp. 707-742, 2016.
- [5] Bharadwaj, R.; Alomainy, A.; Parini, C., "Localisation of body-worn sensors applying Ultra Wideband technology," *Antennas and Propagation (APCAP), 2012 IEEE Asia-Pacific Conference on* , vol., no., pp.106,107, 27-29 Aug. 2012.
- [6] Z. Sahinoglu, S. Gezici, and I. Guvenc, *Ultra-Wideband Positioning Systems: Theoretical Limits, Ranging Algorithms, and Protocols*, Cambridge University Press, 2008
- [7] S. Gezici, Z. Tian, G. B. Giannakis, H. Kobayashi, A. F. Molisch, H. V. Poor, and Z. Sahinoglu, Localization via ultra-wideband radios: A look at positioning aspects for future sensor networks, *IEEE Signal Proc. Mag.*, vol. 22, no. 4, pp. 70-84, 2005.
- [8] "DWM1000 UWB Transceiver Module", *Product Specification Data Sheet*, Decawave Ltd., 2015.
- [9] A. R. Jimenez Ruiz and F. Seco Granja, "Comparing Ubisense, Be- Spoon, and DecaWave UWB location systems: indoor performance analysis," in *IEEE Transactions on Instrumentation and Measurement*, vol. 66, no. 8, pp. 2106-2117, Aug. 2017
- [10] D. Zhang, F. Xia, Z. Yang, L. Yao, W. Zhao, Localization technologies for indoor human tracking, in: *Proceedings of the IEEE International Conference on Future Information Technology (FutureTech'10)*, Pusan, Korea, May 2010.
- [11] Bharadwaj, R.; Parini, C.; Alomainy, A., "Ultra wideband-Based 3-D Localization Using Compact Base-Station Configurations," *Antennas and Wireless Propagation Letters, IEEE* , vol.13, no., pp.221,224, 2014
- [12] Inam Ullah , Yu Shen , Xin Su , Christian Esposito , and Chang Choi , "A Localization Based on Unscented Kalman Filter and Particle Filter Localization Algorithms", *IEEE Access*, Vol 8, 2020, pp.2233-2246
- [13] Klemen Bregar , Roman Novak and Mihael Mohorci , "Evaluation of range-based indoor tracking algorithms by merging simulation and measurements", *EURASIP Journal on Wireless Communications and Networking*, 2019, Articl no .173.
- [14] Hyung June Kim , Yifan Xie , Heekwon Yang , Chankil Lee , and Taek Lyul Song , "An Efficient Indoor Target Tracking Algorithm Using TDOA Measurements With Applications to Ultra-Wideband Systems" *IEEE Access*, Vol 7, 2019 ,pp.91435-91445.
- [15] L. Yao, Y.-W. A. Wu, L. Yao, and Z. Liao, "An integrated IMU and UWB sensor based indoor positioning system," *Proc. IEEE Int. Conf. on Indoor Positioning and Indoor Navigation (IPIN)*, pp. 1-8, Sep. 2017.
- [16] Y. Zhong, T. Liu, B. Li, L. Yang, and L. Lou, "Integration of UWB and IMU for precise and continuous indoor positioning," *Proc. IEEE Ubiquitous Positioning, Indoor Navigation and Location-Based Services (UPINLBS)*, pp. 1-5, Mar. 2018
- [17] P. K. Yoon, S. Zihajezadeh, B. Kang and E. J. Park, "Robust Biomechanical Model-Based 3-D Indoor Localization and Tracking Method Using UWB and IMU," in *IEEE Sensors Journal*, vol. 17, no. 4, pp. 1084-1096, 15 Feb.15, 2017.
- [18] S. Zihajezadeh, P. K. Yoon, B. S. Kang, and E. J. Park, "UWB-aided inertial motion capture for lower body 3- D dynamic activity and trajectory tracking," *IEEE Trans. Instrum. and Meas.*, vol. 64, no. 12, pp. 3577-3587, Dec. 2015.
- [19] L. Chang, J. Li, and S. Chen, "Initial alignment by attitude estimation for strapdown inertial navigation systems,"*IEEE Trans. Instrum. and Meas.*, vol. 64, no. 3, pp. 784- 994, Mar. 2015
- [20] Wang Bing, Liu Yanyan, Li Qingquan and Zhuang Yan,"A High Precision Dynamic Indoor Localization Algorithm Based on UWB Technology ", March 2018, *IEEE conference on Ubiquitous computing, Indoor navigation and location Based Services*.



# Liver Tumor Segmentation using Superpixel based Fast Fuzzy C Means Clustering

Munipraveena Rela<sup>1</sup>, Suryakari Nagaraja Rao<sup>2</sup>, Patil Ramana Reddy<sup>3</sup>

Department of Electronics and Communication Engineering<sup>1, 2, 3</sup>

Jawaharlal Nehru Technological University Anapapur, Ananthapuramu, Andhra Pradesh, India<sup>1</sup>

G. Pulla Reddy Engineering College (Autonomous), Kurnool, Andhra Pradesh, India<sup>2</sup>

JNTUA College of Engineering (Autonomous), Ananthapuramu, Andhra Pradesh, India<sup>3</sup>

**Abstract**—In computer aided diagnosis of liver tumor detection, tumor segmentation from the CT image is an important step. The majority of methods are not able to give an integrated structure for finding fast and effective tumor segmentation. Hence segmentation of tumor is most difficult task in diagnosing. In this paper, CT abdominal image is segmented using Superpixel-based fast Fuzzy C Means clustering algorithm to decrease the time needed for computation and eradicate the manual interface. In this algorithm, a superpixel image with perfect contour can be obtained using a Multiscale morphological gradient reconstruction operation. Superpixel is pre-segmentation algorithm and is employed to obtain segmentation accuracy. FCM with modified object is used to obtain the color segmentation. This method is examined on 20 CT images gathered from liveratlas database, results shows that this approach is fast and accurate compared to most of segmentation algorithms. Statistical parameters which include accuracy, precision, sensitivity, specificity, dice, rfn and rfp are calculated for segmented image. The results shows that this algorithm gives high accuracy of 99.58% and improved rfn value of 8.34% compared with methods discussed in the literature.

**Keywords**—CT scan image; image segmentation; fuzzy c mean clustering; liver mask; superpixel image

## I. INTRODUCTION

Liver cancer causes third most deaths in world-wide [1]. Computed tomography is commonly used modality for liver cancer diagnosis. The cancer is treated effectively providing it's detected in early stage. In order to diagnose liver tumors, such as hepatocellular carcinoma and metastatic carcinomas, computer aided diagnosis (CAD) is used. Importance of Segmentation algorithms are to separate cancerous portion which is essential for medical diagnosis of cancer [2]. Structure of liver changes with age, sex, body shape, hence the tumor detection is complicated using CAD system.

There are two sorts of segmentation algorithms that are supervised and unsupervised. Unsupervised does not depend on training data samples and labeling of data, these include GraphCut [3], watershed transform (WT) [4], fuzzy entropy [5], clustering [6], etc. Training data and labelling images are required for supervised segmentation, and these include neural networks [7-8]. In these methods, features are used for learning and to achieve segmentation.

In unsupervised segmentation, clustering is the common form of segmentation utilized for color and grayscale images

[9]. In this method, Segmentation depends on Fuzzy c mean clustering (FCM) with minimized objective function.

## II. RELATED WORK

Deepesh Edwin et al used fuzzy logic based thresholding and Shannon's entropy function for tumor segmentation [10]. Amita Das et al utilized adaptive thresholding and FCM for segmentation. The tumor is classified using Multi-Layer Perceptron (MLP) and C4.5 decision tree classifiers [11]. Ramin Ranjbarzadeh et al used the Kirsch filter for extracting organ edges, then calculated the concave and convex points, the mean shift is implemented to obtain uniform images, and eventually FCM is carried out to segment the liver [12].

Muthuswamy J suggested a method in which pre-processing is carried out using median filter and neutrosophic (NS) domain with FCM thresholding for segmentation, then liver contour is obtain using morphological operations, The classifier of support vector machines is used to categorize the tumor [13]. Munipraveena Rela et al used region growing algorithm for tumor segmentation. The tumor is categorized by the area and perimeter of the tumor as benign or malignant. [14].

Jing Zhao et al mentioned a technique to reduce image noise. Here, initially neutrosophic image is obtained, then FCM and particle swarm optimization is utilized to improve the global search [15]. Souhil Larbi Boulanouar et al proposed an algorithm based on the FCM and Modified Fuzzy Bat Algorithm (MFBA) to get better initial cluster centers [16]. Xiaofeng Zhang et al discussed a segmentation method using patch-weighted distance and FCM. Initially patch weighted distance is used to find the correlation between adjacent pixels, and then the influence of neighboring information in fuzzy algorithms is replaced with the pixel correlation, hence this method enhances segmentation[17].

FCM based segmentation algorithms discussed in the literature are sensitive to noise and requires more computation time. These methods require to select the cluster which has liver region, then liver portion is extracted using morphological operations.

Since Superpixel is used in computer vision to enrich the information extracted from an image and group pixels with similar visual properties. Also, a convenient image representation that is reason for computationally efficient. A superpixel picture can give better neighborhood spatial data

# Micro strip Antenna Design for Low Power Cognitive Radio Applications

T.Sarath Babu, S. Nagaraja Rao, T.V. Rama Krishna

**Abstract**— *Wireless Communication Antenna for cognitive radio applications is proposed in this paper by furnishing the design, simulation, and its radiation characteristics. This antenna is simulated under the numerical analysis of IE3D electromagnetic simulator. It shows -12dB return loss, gain of 6 dBi and maximum efficiency of above 60% at 2.40 GHz and 3.40 GHz. This antenna suits in the place of small area and produces radiation in S-band of microwave frequencies.*

**Keywords:** *Cognitive Radio, Wideband, Reconfigurable, Narrow band Antennas.*

## 1. INTRODUCTION

Microstrip antennas are low profile planar printed patch antennas. Depending on the design of the antenna, its performance varies in electrical manner. A sheet of conducting material is spread over a grounded dielectric substrate, known as microstrip patch. A low rate glass epoxy FR4 Substrate may be used for processing the patch. Usually thickness is selected as  $t \ll \lambda$  and patch dimension is less than  $\lambda/2$ ,  $\lambda$  is operating wavelength.

Cognitive radio (CR) is an upcoming technology in which a transceiver has the cognitive ability to detect spectral holes in the available spectrum and instantly move into unused channels. Cognitive Radio is needed for effective utilization of the bandwidth by identifying the spectral holes or vacant spaces in the wireless spectrum. CR components may be classified into hardware and software categories (Christos, 2016). Impedance synthesizer RF power sensor & Detector, analog to digital converter, antenna control unit are hardware parts in antenna tuning unit (ATU). Wideband frequency sensing, auto configuration, adaptive algorithms, and security issues come under software modules. CR technology uses two types of antennas namely Narrow band and wide band antennas.

To tune dynamically to a particular frequency within the frequency spectrum to perform data transfer, narrow band reconfigurable antenna is required. To monitor continuously the frequency spectrum for activity, wide band sensing antenna is required. The task of spectrum sensing may be accomplished using the wide band antenna and the task of communication may be accomplished using the narrow band

antenna.

The logic flow cycle of CR network mechanism includes Sensing the environment for spectral holes and tuning the reconfigurable antenna by adapting the transceiver parameters accordingly to access the vacant spectrum. The design of a microstrip patch for cognitive radio applications, with the simulations carried out and the results obtained by using IE3D tool are presented in this paper.

## 2. PROBLEM FORMULATION

The problem formulation is identified from the literature survey based on the previous research. It is furnished here. Microstrip antennas array with a reconfigurable methods are discussed by Sayed Missaoui et al (2014) presentations. Youssef Rhazi et al (2013) investigated the circular shaped patch antennas in K-band of microwave frequencies. The radiation beam characteristics of an antenna using Circular Patch were demonstrated by Ali El Alami et al (2013) using Cavity Model for RFID Applications. Noman Murtaza et al (2013) proposed a reconfigurable antenna for cognitive radio applications. Girish Kumar et al (2003) have given elaborately the concepts of narrow band, broad band microstrip antenna. A reconfigurable antenna for Cognitive Radio which can easily adapt to the existing conditions by changing its parameters was developed by Sonia Sharma (2017). The design of microstrip antenna for the cognitive radio is selected as a problem in this research.

## 3. DESIGN CASE STUDY

Frequency reconfigurable antennas may be preferred over multiband antennas as they improve the performance by enhancing the efficiency of current wireless systems,. Various switches with re-configurability which facilitate the direct incorporation onto antenna structures were studied and examined during the course of research.

Here annular ring of Circular shaped microstrip patch for the S-band of microwave is considered for the research. The edges are etched to form 64 sides of a polygon. After cut, it looks like circular shaped antenna. Substrate having dielectric constant of  $\epsilon_r = 4.4$ , loss tangent = 0.025 with thickness of  $t = 1.6$  mm is utilised. The location of the feed point (x,y) is such that it is placed to the right side of the centre of the patch. Radius of 28 mm with the ground plane dimension of 40x40 mm<sup>2</sup> was preferred for the antenna design. The proposed antenna design is shown in the Figure 1. Proposed antenna is

**Revised Version Manuscript Received on March 10, 2019.**

**T. Sarath Babu**, Research Scholar, KL Deemed to be University and Assistant Professor, Department of ECE, G.Pulla Reddy Engineering College, Kurnool, Andhra Pradesh, India. (E-mail: tsarath@rediffmail.com)

**Dr. S. Nagaraja Rao**, Professor Department of ECE, G.Pulla Reddy Engineering College, Kurnool, Andhra Pradesh, India. (E-mail: suryakari2k1@yahoo.com)

**Dr. T.V. Rama Krishna**, Professor, Department of ECE, KL Deemed to be University, Vaddeswaram, Guntur, Andhra Pradesh, India. (E-mail: tottempudi@kluniversity.in)



designed as two circular parts. A reconfigurable switch is inserted between these two parts. Three dimensional view is shown in Figure 2.

The case study design has been presented to prove that the proposed model is efficient. IE3D software simulator has been used to implement the proposed model.

**Table-I Antenna Specifications**

Sl. No	Description	Parameter
1	Antenna	Circular shaped annular ring
2	Substrate material	FR4 epoxy
3	Feed	Coaxial probe

This antenna is simulated by an electromagnetic simulator called IE3D. The distribution of current from the feed point of the patch is shown in Figure 2. Uniform current distribution was noticed with nearing 3dB power level. Radiated power of this antenna gives efficiencies of 70% and 60% for 2.40 GHz and 3.40 GHz respectively.

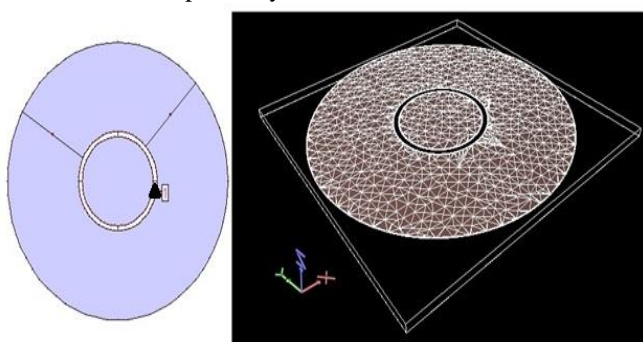


**Figure 1. Geometry and Three Dimensional View of the proposed microstrip patch antenna**

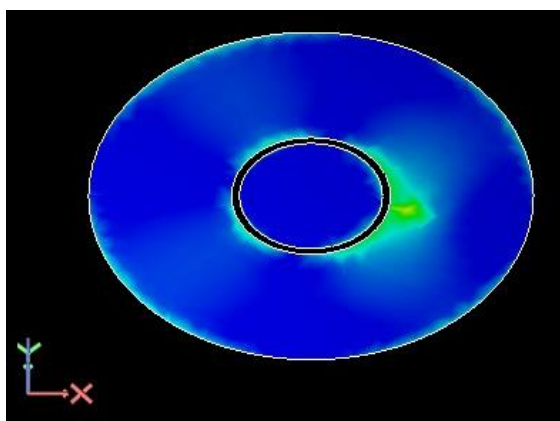


**Figure 2. The Current distribution view in the antenna patch**

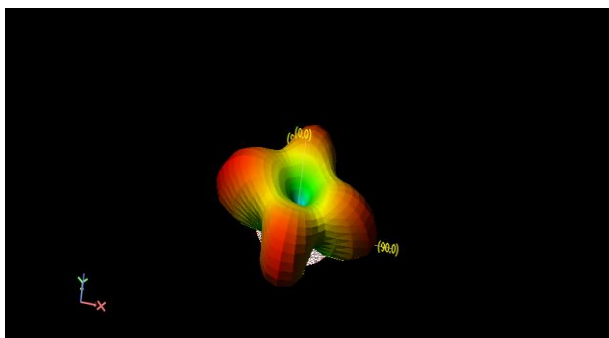


**Figure 3. The Three dimensional radiation pattern of antenna patch**

The current is spread in all over the patch and at the edges of the patch radiation takes place. When compared to circular patch, in the proposed design, area reduces and the sharp edges give rise to more bandwidth like fractal structure.

**4. RESULTS AND DISCUSSION**

Simulations were carried out for the proposed patch antenna design and the results were recorded. Scattering parameter (S-parameter), VSWR, impedance parameters, Gain, Directivity, Antenna Efficiency, Radiation Efficiency, radiation patterns for elevation and azimuthal angles are presented. The value of the S-parameter obtained shows that the antennas transmitted power is properly distributed.

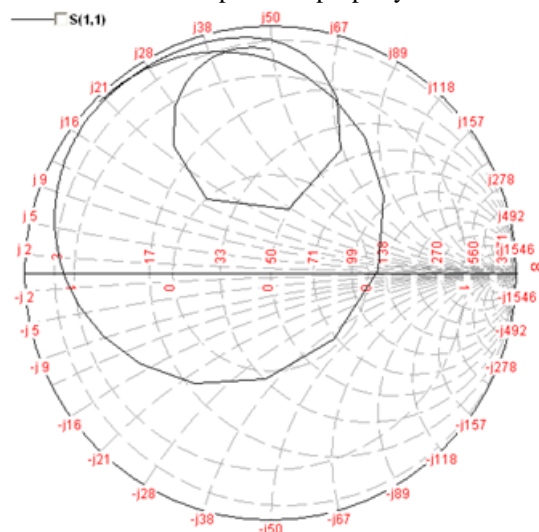


**Figure 4. Overview of the Smith Chart.**

Proper impedance matching can be noticed from the smith chart.

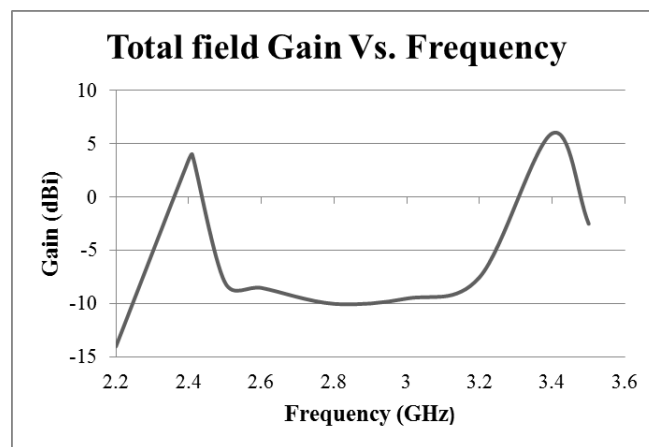


**Figure 6. Directivity versus frequency characteristics.**

The directivity graph is shown in Figure 6, exhibits the value of the directivity of the antenna takes place well for the frequencies.

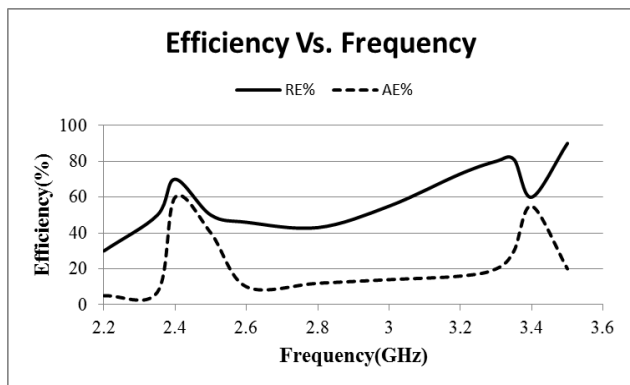


Figure 7. Efficiency versus frequency characteristics

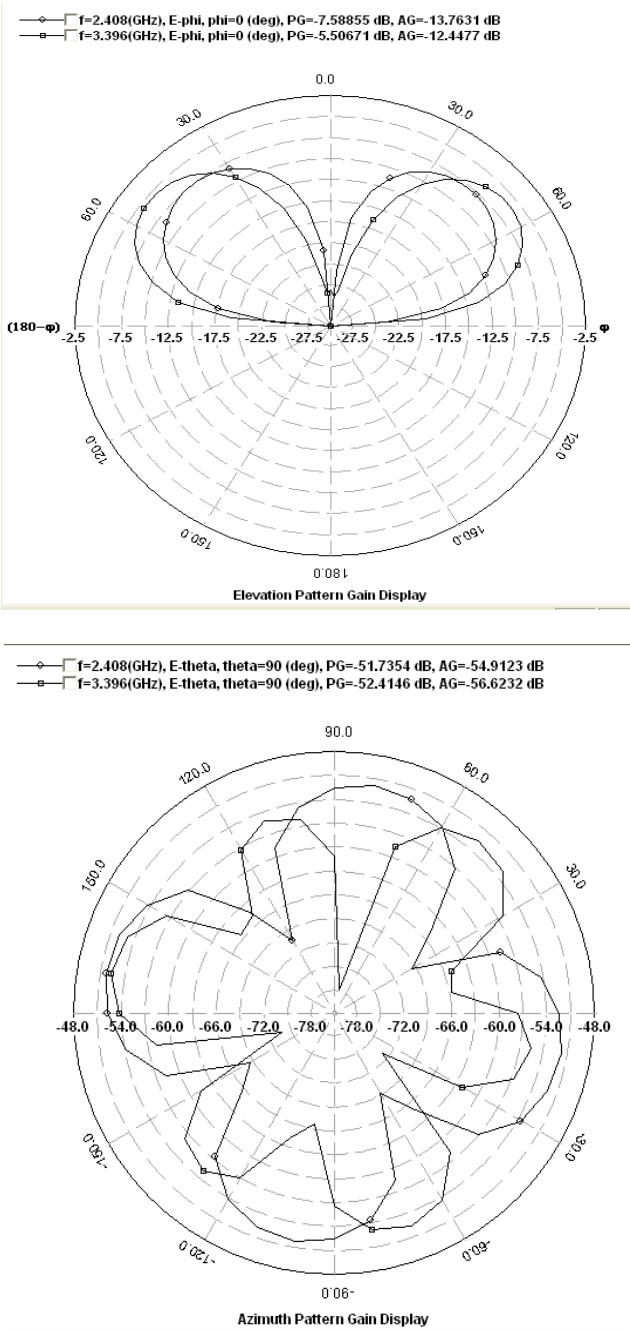


Figure 8. Radiation Pattern of Elevation and Azimuthal direction.

Table 2 Switch functions

Sl. No	Position	Selection frequency
1	ON	3.4 GHz
2	OFF	2.4 GHz
3	Without switch	2.4 GHz and 3.4 GHz

### 5. CONCLUSION

Microstrip patch antenna for S-band frequencies of cognitive radio applications was proposed. Low power energy was used in this antenna and their results were recorded. The antenna simulation and measured results show that this radiator exhibits reasonable efficiencies in low power.

### 6. ACKNOWLEDGMENTS

The Author is thankful to the management of G.Pulla Reddy Engineering College, Kurnool, Andhra Pradesh, India for giving us moral and technical support to conduct this research work.

### REFERENCES

1. Ali El Alami, Saad Dosse Bennani, Moulhime El Bekkali and Ali Benbassou, (2013), Optimization and High Gain of a Microstrip Patch Antenna Excited by Coaxial Probe for RFID Reader Applications at 2.4 GHz, European Journal of Scientific Research, Volume 104 No 3, June, 377-391.
2. Christos Christodoulou, Joseph Costantine, Youssef Tawk, (2016), Antenna Design for Cognitive Radio, Artech house, Boston.
3. Girish Kumar, K.P.Ray, (2003), Broadband Microstrip Antennas, Artech House.
4. IE3D 14.0, Zeland Software Inc., Fremont, CA.
5. Noman Murtaza, Rajesh K. Sharma, Reiner S. Thoma, and Matthias A. Hein, (2013), Directional Antennas For Cognitive Radio: Analysis and Design Recommendations, Progress in Electromagnetics Research, Vol. 140, 1-30.
6. SalaiThillaiThilagam.J, Dr.P.K. Jawahar, A.Sivakumar, (2012), Rectangular Microstrip Patch Antenna Characteristic Study for Wireless Communication Applications, International Journal on Communications Antenna & Propagation, Vol.2, No.1, pp.10-15.
7. SalaiThillaiThilagam.J, Dr.P.K.Jawahar, (2014), Planar Antenna Design with low power for Wireless Technology Applications, European Journal of Scientific Research, Vol. 127 No 1 December, pp.108-116.
8. Sayed. Missaoui, Sihem. Missaoui and Mohsen. Kaddour, (2014), Integration of a Compact Circularly Polarized Antenna Array with a Reconfigurable Symmetric Stub Phase Shifter using Liquid Crystals Substrates, European Journal of Scientific Research, Volume 120 No 2, March, 152-160.
9. Sonia Sharma, C.C. Tripathi,(2017), A versatile reconfigurable antenna for Cognitive Radio, IEEE Xplore.=
10. Youssef Rhazi, Seddik Bri, Rajaa Touahani and Ahmed Mamouni, (2013), A Novel Circular Shaped Microstrip Patch Antenna in the K-Band, European Journal of Scientific Research, Volume 116 No 2 Dec, 287-293.



# Non-Subsampled Contourlet Transform based Multimodal Medical Image Fusion and its Performance Evaluation

Shaik Afroz Begum, K.Suresh Reddy, M.N.Giri Prasad

**Abstract**— Integration of medical images from different sensors can create data that can't be obtained by observing the images separately. Here, in this framework, the fusion of the images is implemented using non-subsampled Contourlet transform (NSCT) and this tool offers some special features like multi-resolution, invariant shifting, and multi-directional band decomposition tool. First, the input images of medical field decomposed into complementary low frequency and frequency of high range sub-bands by NSCT is implemented. Then, by considering the significance of these complementary sub images, a new selection method is implemented in different ways. This scheme use local energy rule to select the low-frequency band and the weighted sum of modified Laplacian (WSML) rule to select high-frequency directional bands. In the final step, the merged image is recovered by inverse NSCT tool implementation on merged bands. This effective novel fusion scheme is compared with existing traditional image merging rules in the transform domain. The results can reveal the efficiency of the novel fusion structure through visual and quantitative measures.

**Keywords**— Nonsubsampled contourlet transform, Computed Tomography(CT) image, Magnetic resonance Imaging(MRI), Local energy, Modified Laplacian.

## 1. INTRODUCTION

Emergence in extensive number of medical instruments like: CT sensor, MRI sensor, X-ray, ECG, and so forth have been included in visual output of these sensors regarding analysis and clinical investigation [1-3]. In medical field, the doctor can detect diseases accurately by extracting and analyzing sufficient data from the medical sensors. The acquired images of various sensors contain complementary data, i.e., a sensor images lack the details of another imaging sensor. For instance, a CT image contains the details of bony structure, and MRI represents the soft tissue information. Hence, a doctor always prefers to do the simultaneous investigation of the output of multi-medical modalities. Through image integration (fusion) techniques, there is a possibility to merge multiple images and present significant information in an effective way [4-5]. Fused medical images present more and significant information to Neurologists, Oncologists, Cardiologists, and others. In current years, a series of fusion algorithms have been developed. The existing fusion algorithms are categorized into multi-modal, multi-focus, multi-view and multi-temporal techniques.

Revised Manuscript Received on March 10, 2019.

Shaik Afroz Begum, Research Scholar, ECE Department, JNTUA, Andhra Pradesh, India. (Email:afroz.phd16@gmail.com)

Dr.K. Suresh Reddy, Professor & Head, ECE Department, G Pulla Reddy Engineering College, Andhra Pradesh, (India. Email:sureshkatam@gmail.com)

Dr.M.N. Giri Prasad, Professor, ECE Department, JNTUA, Andhra Pradesh, India. (Email:giriprasadmn@jntua.ac.in)

Presently, the merging rules of images are preferred to implement by multi-scale decomposition (MSD) technique. The biomedical images are separated into high-frequency (HF) and low-frequency (LF) sub-bands, and these bands are merged via different fusion rules in transform domain. In the final step, implementing the inverse MSD of the merged coefficients to recover the image in spatial domain. The quality of any fused image relies on the selection of the domain and merging rules. The general procedure of merging in transform domain is as shown in Fig 1.

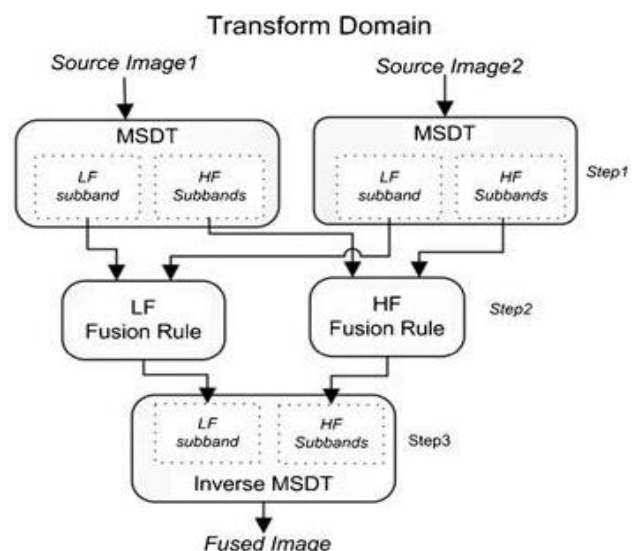


Fig.1.Transform domain Image fusion

The Contourlet transform (CT) is used to represent the images in real two-dimensional transform domain space [6]. Here, the Laplacian pyramid (LP) is decomposing the source medical images in to various bands [7], and after that the directional filters are applied to distinct the coefficients of sub-bands to understand the anisotropic properties. The decomposition of images into multi-scales and multi-direction sub-bands is possible with the CT tool. The pseudo-Gibbs phenomenon is observed at image singularities due to shift invariant property of CT. NSCT[8] has been proposed in 2006 and this is effectively applied to reduce image noise, enhancement of images, and integrating images etc. NSCT acquired the perfect qualities of CT as well as it offers the characteristics of shift-invariance, better directionality, and regularity. To include all important features in this fusion work, NSCT is selected to transform an image in to multiple bands.



The work presented in this framework is organized in the following sections: II section explains an image decomposition procedure in NSCT domain and III section illustrates fusion rules of medical images. The results of simulation work and its quantitative measures will be observed in Section IV. Lastly, the section V concludes the proposed work.

## II. NON-SUBSAMPLED CONTOURLET TRANSFORM

NSCT tool offers multi-directional feature, shift-invariant feature, and multi-resolution feature [8-11]. It is implemented by combining the non-subsampled directional filter bank (NSDFB) and non-subsampled pyramid structure (NSP). NSP offers the feature of multiscale and the multi-direction feature is provided by NSDFB. The important Shift-invariance feature of NSCT is achieved by avoiding downsampling and upsampling processes in NSDFB and NSP as well. The NSCT is implemented through the combination of the NSP and NSDFB as shown in below Fig.2a and Fig. 2b.

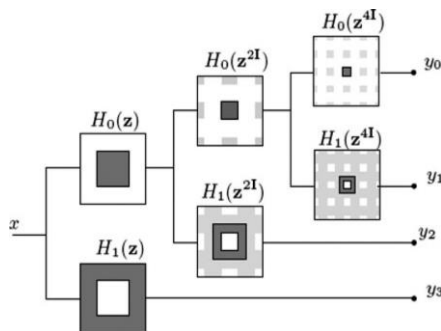


Fig.2a. Multi-stage decomposition using NSP.

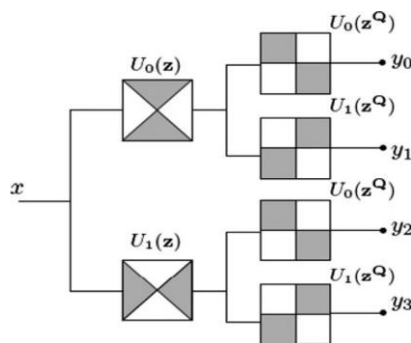


Fig.2b. Directional bands generation using multi-channel NSDFB.

### A. NSP

The NSP has a two-channel filter bank block without down samplers and upsamplers. Each level of NSP generates one low-pass sub-image (y0) and one bandpass sub-image (y1). The three-level decomposition using NSP is presented in Fig. 2a. The NSP filter banks of the following stages are executed via upsampling the previous stage filters. The above feature of NSCT eliminates the requirement of additional channel. The initial level LF and HF filters are signified as H0(Z) and H1(Z) respectively and next level LF and HF filters are given by H0(Z2) and H1(Z2), respectively.

### B. NSDFB

The bandpass images of NSP are entered NSDFB to obtain directional bands. The NSDFB consists of a two-channel fan filter bank as its basic structure which is presented in Fig. 2b. The analysis filters are given as Um(Z) (m =0,1) and synthesis filters are given as Vm(Z) (m =0,1).

## III. PROPOSED METHOD

The multi-modality images (MRI and CT) are considered and these images comprises of significant and complementary information. For precise detection and fast diagnosis, all these details must be extracted into a single highly informative image. In this fusion work, the NSCT has been applied to integrate the brain images. The initial step of the novel fusion algorithm is to change the considered bio-medical images into LF sub-band images and HF directional sub-band sets of different scales. These multi-scale image sets are then merged utilizing individual fusion rules [12-13].

### A.LF Sub-Band Fusion of last decomposition level

Low-frequency sub-bands of medicinal images are approximated forms of the original image. In this work, the NSCT decomposition levels have been confined to two, therefore the LF band has most of the image energy and last level of decomposition contains few high frequency details. Consequently, the low-frequency sub-band images are merged for preserving approximate information as well as details present in it. The fusion rule in this work applied to LF bands is the local energy of the coefficients in a 3×3 window. The activity of LF coefficient CAL(x,y) of the image A at position (x, y) obtained using the following expression.

$$e_A(x,y) = \sum_{x=-1}^{x=1} \sum_{y=-1}^{y=1} (C_A^L(x, y))^2 \tag{1}$$

Similarly, the image B local energy of the low-frequency coefficient CBL(x,y) at location (x, y) is:

$$e_B(x,y) = \sum_{x=-1}^{x=1} \sum_{y=-1}^{y=1} (C_B^L(x, y))^2 \tag{2}$$

The initial image fusion decision map (DL(x,y)) of merged coefficients(images) is obtained by selecting the sub-band coefficient with the maximum activity i.e. if (DL(x,y)) = 1 then the coefficient of image A is selected at (x, y) location and if (DL(x,y)) = 0 then image B coefficient is selected. Then, by using a majority filter, consistency verification is done in a 3×3 window to obtain final image fusion binary decision map (Df). Therefore, in each 3×3 region, the condition where most coefficients observed from image A and only the center coefficient is derived from image B, therefore for such cases, the center coefficient also have to be taken from the image A. Otherwise, the coefficient value will remain same. This verification process gets repeated at each coefficient of fused low-pass sub-band. The neighboring coefficients are considered in this process

to eliminate the noise problem and therefore ensure the presence of homogeneity feature in the fused image.

**B.HF directional Sub-Bands Fusion Rule**

HF (directional) sub-bands provide various features of the source image, which includes: contours, edges, boundaries and lines, etc. High frequency bands use the conventional fusion rules to select the coefficient that achieves maximum absolute value. This process is highly sensitive to noise pixels and there is a chance of losing some important information when selection is according to a single coefficient rather than the neighboring coefficients. The effective fusion rule for activity level measurement which preserves fine details of the image in all directions is considered and it integrates the HF coefficients without introducing noise. While dealing with our proposed work, the weighted sum of modified Laplacian (WSML) fusion scheme is employed on HF sub-band coefficients as a activity measure.

Modified Laplacian is applied to I(x,y) and is specified by expression (3).

$$ML_f = \frac{|2 * I(x, y) - I(x-1, y) - I(x+1, y)| + |2 * I(x, y) - I(x, y-1) - I(x, y+1)|}{4} \quad (3)$$

WSML of I(x,y) is given by the equation (4),

$$WSML_{f(x,y)} = \sum_{m=-1}^1 \sum_{n=-1}^1 (w(m+1, n+1)) * (ML_f(x+m, y+n)) \quad (4)$$

Here w is the matrix which contains weights for HF rule implementation. The city block distance measure is proposed for the calculation of weight matrix in our proposed work and it is given as,

$$w = \frac{1}{16} \begin{bmatrix} 1 & 2 & 1 \\ 2 & 4 & 2 \\ 1 & 2 & 1 \end{bmatrix}$$

On each HF(directional) coefficients CAij, and CBij of A and B images, WSML is calculated. Here, CAij is ith decomposition level, jth directional HF band coefficient of the image A and CBij is ith level, jth directional HF band coefficient of image B having their position as (x,y) with their activity measure.

WSML expression is computed at each HF(directional) sub-band coefficient CAij, and CBij of images at location (x,y) as their activity measure. Thus at the end, a final binary decision map (Df) is found by means of consistency verification which is considered in the low-frequency scheme.

Finally, the spatial domain fused image is recovered by the implementation of two-level inverse NSCT on merged coefficients.

**IV. EXPERIMENTAL RESULTS AND PERFORMANCE EVALUATIONS**

The investigations on an effective image fusion scheme have been made with two different data sets of brain images. Dataset-1 and dataset-2 contains CT and MRI (multi-modal images) images (shown in Fig. 3a, b and Fig. 4a, b) corresponding to various pathologies. This novel fusion scheme is compared with existing transform based image fusion techniques like (i)DWT [14-16], (ii)SWT [17] (iii)CT [6], and (iv)NSCT [8] image fusion methodologies using basic merging rule, i.e. by analyzing the absolute maximum value for HF directional bands and the averaging process is done for LF frequency sub-band. They include: (i) DWT\_av\_mx, (ii)SWT\_av\_mx (iii)CT\_av\_mx, and (iv) NSCT\_av\_mx. Simulation results are shown in Figs. 3 and 4.

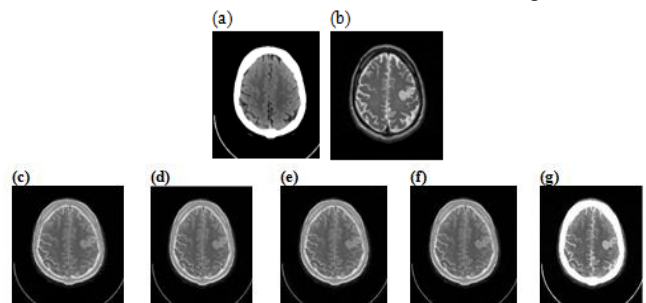


**Fig. 3 Comparison of various transform domain fusion methodologies with brain (Dataset-1)images. (a) CT Sensor output (b) MR Sensor output (c) DWT(av\_mx) (d) SWT(av\_mx) (e)CT(av\_mx) (f) NSCT(av\_mx) (g) Proposed method**

Visual analysis of the experimental results show that the proposed fusion rules retain the fused MRI as well as CT images with better contrast, showing clear hard and soft tissue information without any artifacts.

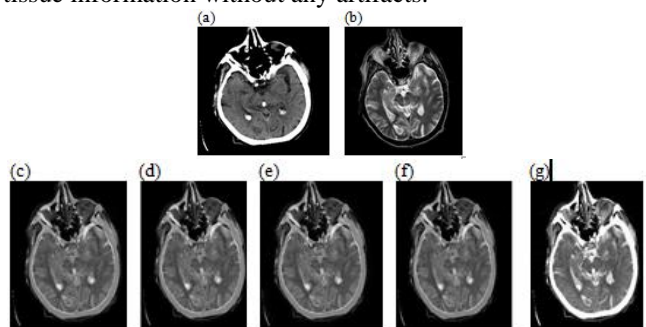


**Fig. 4 Comparison of various transform domain fusion techniques for brain (Dataset-2) images. (a)CT Sensor output (b)MRI Sensor output (c) DWT(av\_mx) (d) SWT(av\_mx) (e)CT(av\_mx) (f) NSCT(av\_mx) (g) Proposed method**

The performance of this work is evaluated with quality measurement metrics like (1) Mutual Information(MInf), (2) Information Entropy(En), (3) Spatial Frequency(SFr), (4) Ratio of spatial frequency error(RSFErr), (5) Correlation coefficient(CorC)

1. MI<sub>F</sub>: Mutual info represents the details that one sensor image comprises of other sensor image details. Assuming sensor images A and B, in addition to that an integrated image (F), the quantity of data that image(F) encompasses about A and B is considered as:

$$MI_{FA} = \sum_{F,A} P(F,A) \log \frac{P(F,A)}{P(F)P(A)} \quad (5)$$

$$MI_{FB} = \sum_{F,B} P_{FB}(F,B) \log \frac{P(F,B)}{P(F)P(B)} \quad (6)$$

Thus the Mutual information is computed as

$$MI_F = MI_{FA} + MI_{FB} \quad (7)$$

2. En: Information entropy computes the quantity of data existing in images. Higher entropy denotes the more data capacity. According to the Shannon data philosophy, the IE of a fused image is specified by the mathematical expression.

$$En = - \sum_{k=0}^{L-1} P_F(k) \log_2 P_F(k) \quad (8)$$

3. SFr: The Spatial Frequency measures the activity level of image(F) and it tells about amount of fine details.

$$SFr = \sqrt{R_F^2 + C_F^2} \quad (9)$$

Here, R<sub>F</sub> : The row frequency and  
C<sub>F</sub> : The column frequency.

An image with a large spatial frequency will have better fusion quality.

4. RSFE<sub>err</sub>: The Spatial frequency error reveals the differences amid the activity of fused image as well as the reference ideal fused image, which is expressed as follows:

$$RSFE_{err} = (SFr_F - SFr_R) / SFr_R \quad (10)$$

Here SFr<sub>F</sub> is said to be the fused image spatial frequency and SFr<sub>R</sub> is referred as the reference ideal image spatial frequency.

5. CorC: Correlation coefficient measures similarity of small objects present in the input and fused images. Higher the value of correlation, more the information preserved in the image(F). CorC between image IA and the fused image IF is expressed as:

CorC(IF,IA)=

$$\frac{\sum_{x=0}^{M-1} \sum_{y=0}^{N-1} (I_F(x,y) - \bar{I}_F)(I_A(x,y) - \bar{I}_A)}{\sqrt{\sum_{x=0}^{M-1} \sum_{y=0}^{N-1} (I_F(x,y) - \bar{I}_F)^2 \sum_{x=0}^{M-1} \sum_{y=0}^{N-1} (I_A(x,y) - \bar{I}_A)^2}} \quad (11)$$

Here, the quantity  $\bar{I}_F$  as well as  $\bar{I}_A$  are considered as the average values of the F and A images. Repeat the above expression to compute CorC(I<sub>F</sub>,I<sub>B</sub>).

Tables I and II show the quality measurement metrics of integrated fused images for two pairs of medical images. The best values are highlighted for each quality metric in Tables I and II. The advantages of effective NSCT scheme over other existing methods are shown in visual analysis results and furthermore they are reliable with the quality metrics. Henceforth, the novel merging rules in NSCT domain are appropriate for MRI-CT image merging.

**TABLE I Evaluation of quality metrics for Fused Medical Images(Dataset-1) (Shown In Fig. 3a, b)**

Fusion method	Metrics					
	IE	MI	SF	RSFE	CCI	CC2
DWT_ave rage_max	5.5471	3.0699	27.2902	-0.1401	0.8711	0.7248
SWT_ave rage_max	5.4616	3.2492	23.4849	-0.2710	0.8772	0.7303
CT_ave rage_max	6.2897	2.9314	28.4287	-0.1515	0.8714	0.7253
NSCT_ave rage_max	5.3717	3.4119	22.2680	-0.2953	0.8790	0.7315
<b>Proposed</b>	5.7532	<b>3.7998</b>	<b>36.9700</b>	<b>0.1608</b>	<b>0.9044</b>	0.6082

**TABLE II Evaluation of quality metrics for Fused Medical Images( Dataset-2) (Shown In Fig. 4a, b)**

Fusion method	Metrics					
	IE	MI	SF	RSFE	CCI	CC2
DWT_ave rage_max	5.3739	3.5774	22.6149	-0.1380	0.9278	0.8283
SWT_ave rage_max	5.2767	3.8620	19.8283	-0.2592	0.9308	0.8314
CT_ave rage_max	5.9242	3.2381	23.4822	-0.1479	0.9277	0.8285
NSCT_ave rage_max	5.2213	4.0523	18.1489	-0.2992	0.9319	0.8325
<b>Proposed</b>	5.7014	<b>4.5622</b>	<b>30.2424</b>	<b>0.1374</b>	<b>0.9595</b>	0.7146

## V. CONCLUSION

An effective Multi-modal image fusion in NSCT domain has been proposed to integrate biomedical images. In this fusion work, the datasets of CT and MRI images have been combined through two individual fusion schemes to preserve the more information present in multi-directional bands. The LF bands are integrated by considering local energy rule, whereas weighted sum-modified Laplacian is considered as the HF fusion rule. In our work, two data sets of brain images including CT and MRI images are integrated using traditional fusion techniques and the proposed image fusion. The visual and quantitative measures clearly explain that the proposed fusion framework can retain more details of images (CT and MRI) with enhancement of details and less distortion than conventional fusion methods.



## REFERENCES

1. B.S. Hoyle, "A schema for generic process tomography sensors," IEEE Sensors J., vol. 5, no. 2, pp. 117–124, Apr. 2005.
2. A.Alkan, S.A.Tuncer, and M.Gunay, "Comparative MR image Analysis for thyroid nodule detection and quantification," Measurement, vol.47, pp. 861-868, Jan. 2014.
3. Alex Pappachen James, Belur V. Dasarathy: "Medical image fusion: A survey of the state of the art", Information Fusion 19 (2014) 4–19, Volume 19, Sep 2014, pp 4-19, Elsevier.
4. Zaid Omer and Tania Stathaki, "Image fusion: An overview" in fifth International conference on Intelligent systems, Modelling and Simulation, IEEE 2014.
5. Gemma Piella,: Image Fusion for Enhanced Visualization:A Variational Approach International journal on Computer Vision, Volume 83, Issue 1,June 2009,pp 1-11
6. M.N.Do and M. Vetterli, "The contourlet transform: An efficient directional multiresolution image representation," IEEE transactions on Image processing, Volume 14, Issue 12, Dec 2005,pp. 2091-2106.
7. Burt, P.T., Anderson, E.H., 1983. The Laplacian pyramid as a compact image code. IEEE Trans. Comm. 31, 532–540.
8. Arthur L. da Cunha, Jianping Zhou, Member, IEEE, and Minh N. Do, Member, "The Nonsubsampled Contourlet Transform: Theory, Design, and Applications", IEEE Transactions On Image Processing, Vol. 15, No. 10, October 2006
9. Yang, L., Guo, B.L., Ni, W.: Multimodality medical image fusion based on multiscale geometric analysis of contourlet transform, Neurocomputing, Volume 72, Issues (1–3), Dec 2008, pp 203–211.
10. Vikrant Bhateja, Himanshi Patel, Abhinav Krishna, Akanksha Sahu, and Aimé Lay- Ekuakille: Multimodal Medical Image Sensor Fusion Framework Using Cascade of Wavelet and Contourlet Transform Domains,IEEE Sensors Journal, Volume 15, Issue. 12, Dec 2015,pp 6783-6790
11. Gaurav Bhatnagar, Q.M. Jonathan W, and Zheng Liu,: "Directive Contrast Based Multimodal Medical Image Fusion in NSCT Domain, IEEE Transactions on Multimedia, volume 15, Issue 5, Aug 2013,pp.1014-1024.
12. Richa Srivastava, Om Prakash, Ashish Khare,"Local energy-based multimodal medical image fusion in curvelet domain," IET Computer Vision, Volume 10, Issue 6, Sep 2016, pp 513-527.
13. P Ganasala and V Kumar, "CT and MR image fusion scheme in NSCT domain" in Journal of digital imaging 27 (3), 407-418, 2014, Springer.
14. Gonzalo Pajares and Jesus Manuel de la Cruz, " A wavelet-based Image Fusion Tutorial" in Pattern Recognition, Volume 37, Issue 9, Sep 2004, pp. 1855-1872, Elsevier.
15. Hui Li, B.S.Manjunath, and Sanjit K.Mitra, " Multi-sensor Image fusion using the wavelet transform" in Image Processing, 1994. Proceedings. ICIP-94., IEEE International Conference.
16. Vijayarajan R, Multan S, " Discrete wavelet transform based Principal component averaging fusion for medical images", AEU - International journal of electronics and Communications, Volume 69, Issue 6, June 2015, pp 896–902, Elsevier.
17. Mirajkar Pradnya P and Sachin D.Ruikar, "Image fusion based on Stationary wavelet transform" in International Journal of Advance research and studies,2013.
18. Zheng Y, Essock E A, Hansen BC, Haun AM, "A new metric based on extended spatial frequency and its application to DWT based fusion algorithms" in Information Fusion, Vol 8, pp 177-192,2007.
19. Qu G, Zhang D,Yan P, " Information measure for performance of image fusion", Electronic Letters,38,pp 313-315,2002.

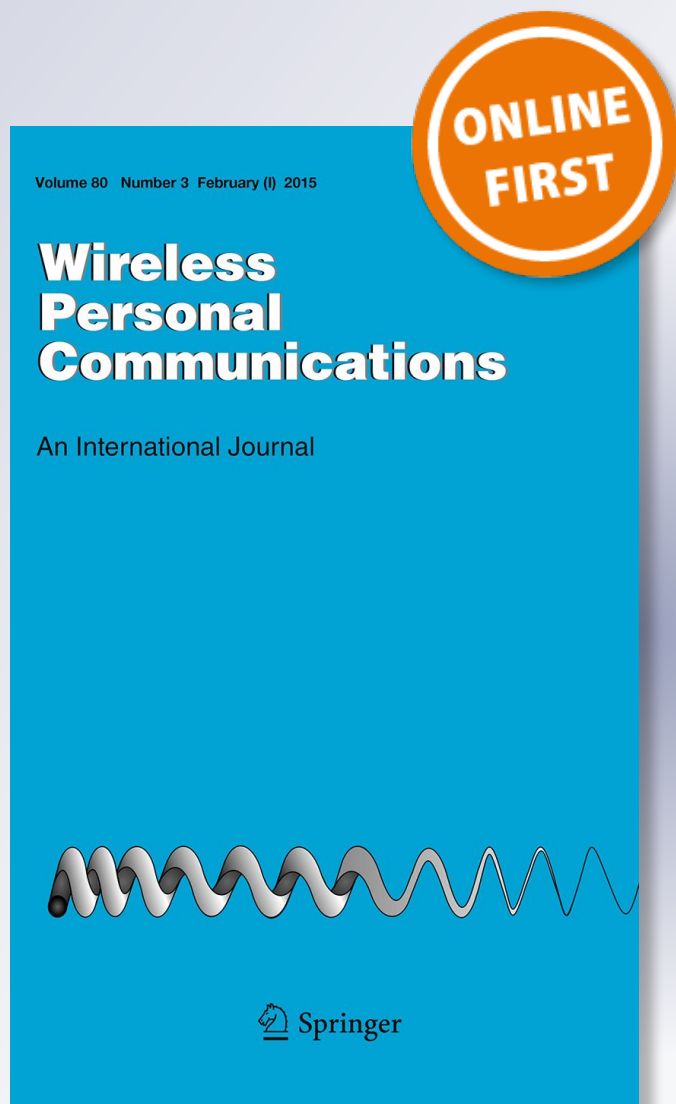
# *Optical Burst Routing by Balanced Wavelength Allocation Under Multi-objective Quality Metrics*

**Veparala Kishen Ajay Kumar, Katam Suresh Reddy & Mahendra Giri Prasad**

**Wireless Personal Communications**  
An International Journal

ISSN 0929-6212

Wireless Pers Commun  
DOI 10.1007/s11277-019-06326-w



**Your article is protected by copyright and all rights are held exclusively by Springer Science+Business Media, LLC, part of Springer Nature. This e-offprint is for personal use only and shall not be self-archived in electronic repositories. If you wish to self-archive your article, please use the accepted manuscript version for posting on your own website. You may further deposit the accepted manuscript version in any repository, provided it is only made publicly available 12 months after official publication or later and provided acknowledgement is given to the original source of publication and a link is inserted to the published article on Springer's website. The link must be accompanied by the following text: "The final publication is available at [link.springer.com](http://link.springer.com)".**



# Optical Burst Routing by Balanced Wavelength Allocation Under Multi-objective Quality Metrics

Veparala Kishen Ajay Kumar<sup>1</sup> · Katam Suresh Reddy<sup>1</sup> · Mahendra Giri Prasad<sup>2</sup>

© Springer Science+Business Media, LLC, part of Springer Nature 2019

## Abstract

The optical burst switching is promising optical network technique that intends to transmit data in the form of bursts with the ability of dynamic switching between sub-wave lengths. One among the crucial issues of the OBS networks is burst loss due to suboptimal and often impediment burst scheduling and wavelength allocation strategies. Hence, the major contributions of the contemporary research in regard to OBS networks entails to portray the optimal burst routing strategies. The contribution of this manuscript is balanced wavelength allocation using differential evolution method in short referred as BWADE, which selects an optimum multi-hop route that intends to uses multi-objective QoS aspects as a fitness scale for differential evolution algorithm. The experimental study concluding that the proposed BWADE outperforming the other contemporary routing approaches through simulation outcomes.

**Keywords** BWADE · OBS network · WDM-OBS transmission system · JAVOBS · GA algorithm · DE approach

## 1 Introduction

The Internet Protocol based transmissions (IP traffic) are stabilized at balanced level in recent past. This is since, the network paradigm called “optical burst switching” (OBS) [1], which became crucial and reliable to transmit IP based traffic. The activities of control plane from data-plane are segregated by OBS to exploit their different benefits in the optical and electronic areas. At each node route, the “burst header packets (BHPs)”

---

✉ Veparala Kishen Ajay Kumar  
vkishenajaykumar@gmail.com

Katam Suresh Reddy  
sureshkatam@gmail.com

Mahendra Giri Prasad  
mahendragiri1960@gmail.com

<sup>1</sup> Department of Electronics and Communication Engineering, G. Pulla Reddy Engineering College (Autonomous), JNTUA, Kurnool, India

<sup>2</sup> Department of Electronics and Communication Engineering, JNT University Anantapur, Anantapuram, India

or the control messages are electronically processed, whereas the data bursts were optically transmitted from end–end [2]. And in brief, the method OBS maintains balance among “optical packet switching” and “optical circuit switching”.

In optical burst switching, any “data burst transmission” is always headed by BHP for reserving the resources of wavelength along the route for forthcoming burst. The source node does not wait for any acknowledgment that an end-to-end connection is established. However, it waits for an offset time given to initiate transmission of the bursts [3]. The default tenure of this offset time is the sum of the header packet processing time at each of the node involved in transmission.

The default transmission method of the OBS doesn't allow the buffering of the transmitting burst. Hence, the burst drop is often observed, which is the default constraint of the loss networks category [4]. This is since, the buffering based burst transmission downgrades the quality of service in OBS that compared to the IP networks [5]. Generally, for the OBS network, the QoS provisioning experiences the contentions of wavelength when 2 or more of the data burst strive to attain the similar output port and at the same time utilizing the similar wavelength. For the OBS network, the lower “burst loss probability” is assured by reducing the level of contentions of wavelength among data bursts.

In the occurrence of the multi-class traffic, 2 types of “QoS differentiation schemes” are stated namely, “absolute QoS differentiation [6]” and “relative QoS differentiation [7]”. In crucial implementations, the “absolute QoS provisioning” is obtained by allocating the resources of wavelength approximately in the network links [8]. And for “provisioning absolute QoS”, the “wavelength allocation scheme” is an attainable solution because presently, the fiber links function by utilizing the “Dense Wavelength Division Multiplexing (DWDM) technology [9]”. Now, the DWDM assists multiplexing from 160 to 320 wavelengths into one fiber.

In this work, the general issue of escalating the quality of service in burst routing through optimal allocation and scheduling of the wavelengths in “OBS Network” is addressed. The scheduling issue is addressed in this contribution as multi-objective QoS factor. The proposal of this manuscript denotes as “Balanced Wavelength Allocation using differential evolution (BWADE)” that optimizes the burst routing. In regard to this, the proposal BWADE endeavors to pair the set of bursts expected at an event of time and the set of wavelengths available.

## 1.1 OBS Architecture

The standard “Optical Switching schemes” are of 3 types and are (1) packet switching (OPS), (2) burst switching (OBS) and (3) circuit switching (OCS). From the current literature it is reported that among 3 strategies, OBS is the best as it is planned in esteem to overwhelm the constraints noticed in other 2 switching schemes. The OBS method is developed such that it recalls the advantages of OPS and OCS and eliminates the confines of these 2 switching strategies. The OBS accumulates the packets which are to be transferred to the similar target in the form of burst; therefore, optimal utilization of resources through “low transmission control overhead” is obvious. And in the networks of OBS (a) ratio of the control channels (CC) which are involved in the conversion of O–E–O are few and typically 1 CC per the fiber [10], (b) the process of burst switching is purely optical (O–O) and (c) multiplexing and data sliding occurs simultaneously. The default format of optical burst switching is portrayed in the Fig. 1.

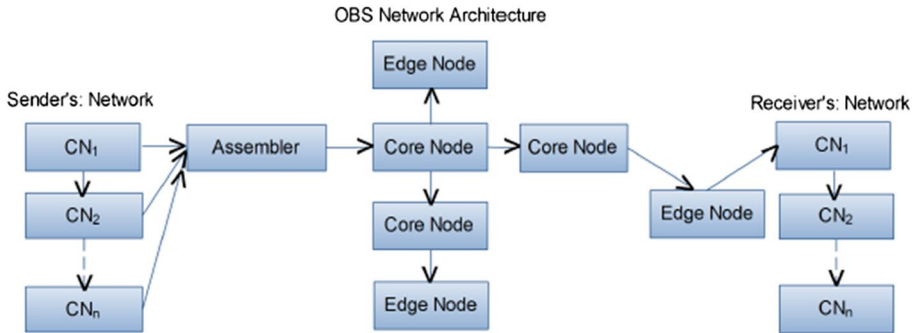


Fig. 1 Default flow of the OBS architecture

## 1.2 OBS Routing

In the OBS networks, the routing models have 2 stages i.e., route selection and route calculation [11]. These 2 stages can either be dynamic or static. And in the instance of “static route calculation”, 1 or more of the routes are computed before the time. Unlike, in the “dynamic route calculation”, the routes are periodically calculated to lessen the network overhead like amount of the burst losses or link load.

After the computation of routes, 1 route is chosen for transferring burst traffic. And in the “static route selection”, traffic is partitioned among the computed routes. The “dynamic route selection” deliberates the information of network state for selecting the route which optimizes the specified cost function. Generally, dynamic routing tries to alter the decisions of routing for reflecting the variations in the topology and network state.

The paper is organized as follows. In Sect. 2 we present an overview of the routing approaches. In Sect. 3 we describe the quality metrics of the proposed model and in Sect. 4 validations of the results are discussed. In Sect. 5 main conclusions are presented.

## 2 Related Research

This section explores the contemporary research contributions related to burst routing through wavelength allocation in optical burst switching networks.

In literature [12] different scheduling algorithms differ in their complexity and performance in terms of burst loss. Scheduling algorithms can be classified as two types: with void filling [13] and without void filling or horizon [2]. Horizon algorithms are First fit unscheduled channel (FFUC) [14], Latest available unscheduled channel (LAUC) [15], and that of void filling algorithms are first fit unscheduled with void filling (FFUC-VF) [16]. Latest available unscheduled channel with void filling (LAUC-VF) [17] and Minimum End Void (Min-EV) [18]. Both LAUC and FFUC have same complexity, but LAUC is superior to FFUC in utilizing network resources. Though LAUC-VF, FFUC-VF have higher network resource utilization, they are more complex compared to that of FFUC and LAUC.

The other method of optimizing the routing in OBS by evade the contention by wavelength conversion [19] that defuse the ratio of burst drop. The deflection routing [20] is the other method of optimizing the burst routing with minimal contention. This method

evades the contention by delivering the contended bursts to other ports than the port intended to receive the respective burst. The performance of this approach often found to be limited, which is due to the violation in order of the burst delivery, and evincing the need of retransmission of the bursts.

The performance of WDM systems is affected due to the non-linear effects in fiber, which lead to interference and signal degradation. Different non-linear impacts that occur in fiber are discussed in [21] out of which four-wave mixing (FWM) have adverse effects. In [22], to solve the critical static routing by wavelength allocation problem in WDM systems, the authors addressed new integer-linear programming methods with optimal RWA policies.

In [23], an investigation is conveyed in optical fiber transmission system to reduce non-linear impairments. The impediments of non-linear distortions in optical networks are overcome in [24] by utilizing multichannel digital back-propagation (MC-DBP) technique. In MC-DBP technique, there are noteworthy difficulties in terms of complexity and the sensitivity of DBP performance to linear channel impairments.

An analysis of the routing by wavelength allocation task of the WDM, and time division multiplexing (TDM) transmission system for handling the non-TDM driven RWA allocation task limitations was stated in the works [25, 26]. But these studies have the limitation of the shortest-route implementation in the routing code due to non-dynamic path identification program.

Routing by wavelength allocation approach for TDM transmission system [27] improves the rates of path usage rates, especially when the corresponding burst routing seeks partial bandwidth among the available. This method multiplexes the wavelength for various sessions through allocating a piece of time-slots to each session. On contrary to the study [25], the research work used pre-fixed routing and alternative-routing programs to determine the path. And to allocate wavelength and time-slots, first-fit path allocation coding was incorporated. Because of adding the three algorithms, incorporating and implementing process had become simple and easy. Even though, this study also had limitations such as limited scalability, real-time implementation due to prior identification of the routes before data incoming. The work [28] had same shortcomings as it was also studied with same basics of [27].

A centralized control infrastructure along with time-slot allocation approach for time-slot OBS transmission system was explained in the study [29]. The scholars made an attempt of reducing burst competition for wavelength and also achieving highest path usage rates and succeeded in achieving highest resource usage; confronted significant limitations such as huge buffering lags at the same node and scalability challenges. Moreover, there is no possibility of extending the method to use in practical systems such as OBS transmission.

A distributed and variable routing by wavelength allocation coding depending on the dynamic-programming method was recommended by the study [30]. The scholars tried to obtain minimum blocking chances. This model also had challenges such as static path determination and more long lags chances, and the study didn't assess these.

An integrating single-way, dual-way signaling and combined coding approaches for time-slot OBS [31] were used in the study [32]. The study [33] recommended a new non-static routing by wavelength allocation coding based on the principle of highest-contiguous. Though the experiment findings showed declination of probability blocking together with optimal resource usage, the method confronted the problems of large overheads as the model demands accurate wavelength usage data as well as time-slot assignment.

Optical time-slot switching (OTS) model to set time-slot sized as the primary switching granularity was studied and tested in this study [34]. And here the switching function was done on the time-domain instead of the wavelength-domain. The work was pioneered on highlighting routing by wavelength allocation problems in WDM-OBS transmission system.

An ANT optimization route allocation coding to deal with the issues of allocating the path and wavelength in OBS was contributed in work [35]. It was restricted to work in non-slot environments and no possibility of application extension that suits time-slot scenario.

Thus, the most of the contemporary methods of Burst routing through wavelength scheduling were intended to either correlate the wavelength and time-slot, shortest path or first-fit.

In order to this argument, Barpanda et al. [36], and Gravett et al. [37] devised optimal burst routing through wavelength allocation using evolutionary computation techniques called “differential evolution”, and “ANT Colony Optimization” in respective order. The technique bi-objective DE [36] is using quality of service objectives congestion and hop count as fitness factors of the Differential Evolution technique. This bi-objective DE approach concludes the route optimality that limited to present congestion state and hop count. The route that considered as optimal can experience congestion during the burst transmissions. The later contribution is Ant Colony Optimization based technique that referred as “flexible spectrum ant colony (FSAC) [37] algorithm that intends to optimize the route in regard to number of hops involved in the route. However, the limited hop count is least significant to define the route optimality towards the quality of service, which is critical constraint of these contemporary models [36, 37].

Henceforth, this manuscript portrayed an evolutionary technique that built upon the differential evolution (DE) approach. The multiple objectives of the quality of service in routing through the balanced wavelength allocation were considered as the critical objective of the proposal.

### 3 Methods and Materials

The proposed model is adequate to allocate appropriate wavelength to achieve optimal burst routing with minimal burst drop and maximal wavelength utilization. The proposed model should also be aimed to achieve linearity in process time. Unlike the existing contemporary models that are considering the one or two quality metrics to assess the routing fitness, the proposal is assessing the route fitness under multiple Quality Metrics, which described in following section (Sect. 3.1). In order to this, differential evolution Technique is adapted that relies on the fitness function which estimates the route fitness under multiple quality metrics prescribed and recommended by this proposed model. The notations used in the description mathematical model of the proposal are listed in Table 1.

#### 3.1 Multi Objectives of the Route Quality

The routing quality is measuring metrics utilized for depicting the possibility of the node to get an optimal end to end burst transmission is explained below, which are estimating regarding the wavelength available at each node involving in the given route.

**Table 1** Notations used in mathematical model of the BWADE

Formula	Description	Used
$tor$	Transmission overlay ratio	Equation (1)
$ot_n(w_i)$	Ratio of overlaid transmissions of the scheduled wavelength $w_i$ of node $n$	Equation (1)
$tt_n(w_i)$	Total transmissions of the scheduled wavelength $w_i$ of node $n$	Equations (1)–(3)
$(efr)$	Egress failure rate	Equation (2)
$db_n(w_i)$	Ratio of the dropped bursts of wavelength $w_i$ of node $n$	Equation (2)
$(wir)$	Wavelength interference rate	Equation (3)
$(wdrr)$	Wavelength data rate residual	Equation (4)
$awdr_n(w_i)$	Actual wavelength data rate of the wavelength $w_i$ of node $n$	Equation (4)
$rwdr_n(w_i)$	Required wavelength data rate of the wavelength $w_i$ of node $n$	Equation (4)
$drrt$	Data rate residual threshold	Equation (4)
$(wesr)$	Wavelength existence span residual	Equation (5)
$awes_n(w_i)$	Available wavelength $w_i$ existence span	Equation (5)
$rwes_n(w_i)$	Required wavelength existence span	Equation (5)
$r$	Route	Equation (6)
$\langle tor \rangle$	Average transmission overlay ratio	Equation (6)
$tor_{rmsd}$	Root mean square distance of the transmission overlay ratio	Equation (7)
$\langle efr \rangle$	Average egress failure rate	Equation (9)
$efr_{rmsd}$	Root mean square distance of the egress failure rate	Equation (10)
$\langle wir \rangle$	Average wavelength inference Rate	Equation (12)
$wir_{msd}$	Root mean square distance of the wavelength inference rate	Equation (13)
$\langle wdrr \rangle$	Average wavelength data rate residual	Equation (15)
$wdrr_{rmsd}$	Root mean square distance of the wavelength data rate residual	Equation (16)
$\langle wesr \rangle$	Average wavelength existence span residual	Equation (18)
$wesr_{rmsd}$	Root mean square distance of the wavelength existence span residual	Equation (19)
$\langle f \rangle$	All metrics average	Equation (21)
$mc$	The total number of metrics considered	Equation (21)
$f_e$	All metrics root means square error	Equation (22)

### 3.1.1 Transmission Overlay Ratio ( $tor$ )

The scope of overlapped transmission of the bursts leads to escalating the burst drop ratio [38]. Hence the transmission overlay ratio that observed at a given node under scheduled wavelength defines the possibility of burst dropping at the corresponding scheduled wavelength.

The metric shows overlaid transmissions ratio against to total transmissions carried in new time capsule given through the same node under scheduled wavelength. The metric is measured with

$$tor_n(w_i) = \frac{ot_n(w_i)}{tt_n(w_i)} \tag{1}$$

In the (Eq. 1),  $tor_n(w_i)$  indicates Transmission overlay ratio. The ratio of overlaid transmissions  $ot_n(w_i)$  of the scheduled wavelength  $w_i$  and total transmissions  $tt_n(w_i)$  of the scheduled wavelength  $w_i$  of the node  $n$  represents Transmission overlay ratio.

### 3.1.2 Egress Failure Rate (*efr*)

The node responsible to send the scheduled bursts often denotes as the egress node and the delay in response to send the target bursts at an egress node under scheduled wavelength causes burst drop at ingress nodes (the node that scheduled to receive the bursts) [39]. The burst drops due to response delay at an egress node under scheduled wavelength is termed as Egress Failure Rate. The metric shows the ratio of bursts dropped in recent time capsule given, which is against the bursts sent over scheduled wavelength  $w_i$  of the node  $n$  which is calculated with

$$efr_n(w_i) = \frac{db_n(w_i)}{tt_n(w_i)} \quad (2)$$

In the Eq. (2),  $efr_n(w_i)$  represents the ratio of the dropped bursts  $db_n(w_i)$  against the total transmissions  $tt_n(w_i)$  in recent time capsule of the corresponding wavelength  $w_i$  of the node  $n$ .

### 3.1.3 Wavelength Interference Rate (*wir*)

The interference of the two or more wavelengths scheduled to different bursts transmitted by divergent egress nodes escalates the scope of burst drops at corresponding ingress nodes [40]. As there is need of adequate wavelength to do transmission with fewer interference, the optimal wavelength has to be scheduled for getting an interference-free burst transmission. This metric interference rate shows the ratio of the number of bursts affected by interference against the total number of bursts transmitted in new time capsule through the corresponding node at a scheduled wavelength.

$$wir_n(w_i) = \frac{|bi_n(w_i)|}{|tt_n(w_i)|} \quad (3)$$

The schedule of the transmission controller gets data packets from various users; buffers with respect to their latency of incoming data time and assembles these collection of buffered data packets as bursts. To get optimal wavelength for transmitting the data to the destination, the access point schedules the bursts. The main aim of this work is to schedule an optimum wavelength to get the highest transmission quality.

### 3.1.4 Wavelength Data Rate Residual (*wdr*)

This metric is principle QoS factor, which is since the adequate data rate is needed to do transmission with a little guarantee. The wavelength data rate should be higher than the corresponding burst load data rate required and lower than required data rate sum and given residual data rate threshold [41]. To select optimal wavelength, schedule the data rate should be either lesser than the expected or greater than required data rate sum and residual data rate threshold. If the wavelength data rate ranges between the values of required data rate and some of the total required data rate and threshold residual data rate then the respective wavelength is optimal. The formula to measure the compatibility of data rate is mentioned in (Eq. 4):

$$wdr_n(w_i) = 1 - \frac{1}{(awdr_n(w_i) - rwd_r(w_i))} \quad (4)$$

The Eq. (4),  $wdr_r_n(w_i)$  represents the data rate residual of the wavelength  $w_i$ , and the notation  $awdr_n(w_i)$  indicates actual wavelength data rate of the wavelength  $w_i$  of node  $n$ , and the  $rwdr_n(w_i)$  represents the required wavelength data rate of the wavelength  $w_i$  of node  $n$ .

In this calculation,  $wdr_r_n(w_i)$  must be lower than the specified data rate residual threshold  $dr_r_t$  that is since,  $wdr_r_n(w_i) > dr_r_t$  represents oversized wavelength  $w_i$  is for existing scheduling data-rate requirement. This can be earmarked for scheduling with high data-rate requirement in the future.

### 3.1.5 Wavelength Existence Span Residual ( $wes_r$ )

The fitness of respective wavelength gets decided only on the availability of greater Existence Span of the wavelength than the residual lifespan of specified burst [42]. The existence Span should be higher than the burst residual lifespan. The exact variance of the wavelength existence span and burst residual lifespan should be less than the existence spans residual threshold ( $es_r_t$ ). If the wavelength satisfies the above conditions, the wavelength is optimal. In case if the total variance between the wavelength existence span residual is higher than the  $es_r_t$ , then scheduling is not feasible. In such case, the respective wavelength will be kept on reserve for the future load that satisfies the condition, i.e., higher wavelength existence span. It is measured with

$$wes_r_n(w_i) = 1 - \frac{1}{(awes_n(w_i) - rwes_n(w_i))} \tag{5}$$

In the (Eq. 5),  $wes_r_n(w_i)$  represents the existence span of wavelength  $w_i$ , and  $awes_n(w_i)$  denotes the available wavelength  $w_i$  existence Span, and  $rwes_n(w_i)$  represents the required wavelength existence span for transmitting the target burst.

In case of  $0 < wes_r_n(w_i) \leq es_r_t$  then the wavelength  $w_i$  is considers as optimal, if not, scheduling is not feasible.

The route to be scheduled to bursts should be a quality specific towards burst transmission. The work presents the route selection through balanced wavelength allocation and optimal transmission rate scheduled to the specified burst. The transmission quality factors presented here are explained below:

- A route can be rated by considering the defined QoS factors, however, may fail to perform with the same quality for various multiple factors of QoS.
- A route can obtain diversified rating for different QoS factors. For instance, a route outperforms with available bandwidth; performs moderately with regard desertion rate; does worst with a Transmission overlay ratio.
- The QoS factors' significance may differ with contextual scheduling.

### 3.1.6 Route Level Assessment of the Multi-Objective Quality Metric

The values obtained for aforesaid metrics in regard to each node involving the target route are indicating the state of the corresponding node. Further these metric values are in use to obtain the metric values at route level, the assessment process is as follows:

For each aforesaid metrics,

- Find the average of the values obtained for corresponding metric at all of the nodes involved in the route,

- Find the root mean square distance of the values obtained for that metric.

If greater value of the metric is most fit, then find the absolute difference of the average metric value and root mean square distance of that values, or if the least values of the metric is more fit, then find the sum of the average metric value and root mean square distance of that values, which is further subtracts from 1, then the resultant value refers as the route level value of that metric.

For a given route  $r$

I. *Route level fitness of the transmission overlay ratio*

$$\langle tor \rangle = \frac{\sum_{i=1}^{|r|} tor(n_i)}{|r|} \tag{6}$$

//Average transmission overlay ratio  $\langle tor \rangle$  observed for all the nodes in target route  $r$

$$tor_{rmsd} = \frac{\sum_{i=1}^{|r|} \sqrt{(\langle tor \rangle - tor(n_i))^2}}{|r|} \tag{7}$$

//Root mean square distance of the transmission overlay ratio  $tor_{rmsd}$  observed for all the nodes in target route  $r$

$$tor_r = 1 - (\langle tor \rangle + tor_{rmsd}) \tag{8}$$

//route level fitness of the transmission overlay ratio  $tor_r$  of the given route  $r$

II. *Route level fitness of the egress failure rate*

$$\langle efr \rangle = \frac{\sum_{i=1}^{|r|} efr(n_i)}{|r|} \tag{9}$$

//Average egress failure rate  $\langle efr \rangle$  observed for all the nodes in target route  $r$

$$efr_{rmsd} = \frac{\sum_{i=1}^{|r|} \sqrt{(\langle efr \rangle - efr(n_i))^2}}{|r|} \tag{10}$$

//Root Mean Square Distance of the egress failure rate  $efr_{rmsd}$  observed for all the nodes in target route  $r$

$$efr_r = 1 - (\langle efr \rangle + efr_{rmsd}) \tag{11}$$

//route level fitness of the Egress Failure Ratio  $efr_r$  of the given route  $r$

III. *Route level fitness of the wavelength inference rate*

$$\langle wir \rangle = \frac{\sum_{i=1}^{|r|} wir(n_i)}{|r|} \tag{12}$$

//Average wavelength inference rate  $\langle wir \rangle$  observed for all the nodes in target route  $r$

$$wir_{msd} = \frac{\sum_{i=1}^{|r|} \sqrt{(\langle wir \rangle - wir(n_i))^2}}{|r|} \tag{13}$$

//Root mean square distance of the wavelength inference rate  $wir_{msd}$  observed for all the nodes in target route  $r$

$$wir_r = 1 - (\langle wir \rangle + wir_{msd}) \quad (14)$$

//route level fitness of the wavelength inference rate  $wir$  of the given route  $r$

IV. *Route level fitness of the wavelength data rate residual*

$$\langle wdr \rangle = \frac{\sum_{i=1}^{|r|} wdr(n_i)}{|r|} \quad (15)$$

//Average wavelength data rate residual  $\langle wdr \rangle$  observed for all the nodes in target route  $r$

$$wdr_{msd} = \frac{\sum_{i=1}^{|r|} \sqrt{(\langle wdr \rangle - wdr(n_i))^2}}{|r|} \quad (16)$$

//Root mean square distance of the wavelength data rate residual  $wdr_{msd}$  observed for all the nodes in target route  $r$

$$wdr_r = 1 - (\langle wdr \rangle + wdr_{msd}) \quad (17)$$

//Route level fitness of the wavelength data rate residual  $wdr$  of the given route  $r$

V. *Route level fitness of the wavelength existence span residual*

$$\langle wes \rangle = \frac{\sum_{i=1}^{|r|} wes(n_i)}{|r|} \quad (18)$$

//Average wavelength existence span residual  $\langle wes \rangle$  observed for all the nodes in target route  $r$

$$wes_{msd} = \frac{\sum_{i=1}^{|r|} \sqrt{(\langle wes \rangle - wes(n_i))^2}}{|r|} \quad (19)$$

//Root mean square distance of the wavelength existence span residual  $wes_{msd}$  observed for all the nodes in target route  $r$

$$wes_r = 1 - (\langle wes \rangle + wes_{msd}) \quad (20)$$

//Route level fitness of the wavelength existence span residual  $wes_r$  of the given route  $r$ .

As per the effect of QoS factors of presented wavelengths study, it is understood that the selection of the route depending upon the performance with a single factor of QoS factor is not ideal always. The route doesn't have the standard performance with respect to the prioritized QoS factors as it varies from one prioritized QoS factors to other. Hence the devised scale transmission optimality rate identifies the optimum route with balanced wavelength. In addition, the transmission optimality rate is used as fitness scale of the differential evolution (DE) to select and schedule the optimal route.

All of these QoS metrics are considered to test the optimum route to perform selection and scheduling process that is described here. The metrics have a mix of expected high and low values.

### 3.2 Differential Evolution Process

The functioning of this algorithm is almost same as the functioning of GA algorithm [43]. The essential difference between the two models is that in GA,  $t$  value varies with respect to operating with new genotypes. Both the parent and child chromosomes are assessed with respect to their fit to the proposed model, and if the later ones are observed to have high fit value, it remains, and the other group is disregarded. The vice versa also remains true in the context. The fittest child substitutes the related parent.

The differentiated fitness processes and multiple cross-over approaches incorporated in DE algorithm marks the disparity between various DE strategies available in existing studies [44–47]. One of the new DE approaches that are efficient in this context has been put forward in the contemporary study [48].

#### 3.2.1 Fitness Scale

The average of the values obtained for all the metrics considered will be assessed initially, which is as follows,

For a given route  $r$

$$\langle f \rangle \geq \frac{(tor_r + efr_r + wir_r + wdrr_r + wesr_r)}{mc} \tag{21}$$

//All metrics average is  $\langle f \rangle$  and the notation  $mc$  indicates the total number of metrics considered, which is 5 in our contribution.

$$f_e = \frac{\left( \begin{aligned} &\sqrt{(\langle f \rangle - tor_r)^2} + \sqrt{(\langle f \rangle - efr_r)^2} \\ &+ \sqrt{(\langle f \rangle - wir_r)^2} + \sqrt{(\langle f \rangle - wdrr_r)^2} \\ &+ \sqrt{(\langle f \rangle - wesr_r)^2} \end{aligned} \right)}{mc} \tag{22}$$

//All metrics root means square error is  $f_e$ .

$$f(r) = \langle f \rangle - f_e \tag{23}$$

//the difference of average  $\langle f \rangle$  and root mean square error  $f_e$  is the fitness

$$f(r) = \langle f \rangle - f_e \tag{24}$$

//The difference of average  $\langle f \rangle$  and root mean square error  $f_e$  is the fitness.

### 3.2.2 Differential Evolution

Step 1. DE-MAIN ( $PR$ ) Begin //  $PR$  be the all possible routes between source and destination.

Let  $tPR$  be the clone of all possible routes  $PR$  depicted.

Let  $\overline{PR} \leftarrow \emptyset$  be the empty set used to store the routes formed by Differential evolution.

Identify cross over points (common node sequence with fitness higher than the specified threshold in both the routes) that is not begin at first node in both input routes as follows.

Step 2.  $\forall_{i=1}^{v_{CL}} \{r_i \exists r_i \in tPR\}$  Begin//for each route  $r_i$

Step 3.  $\forall_{j=1}^{v_{PM}} \{r_j \exists r_j \in tPR \wedge i \neq j\}$  Begin// for each route  $r_j$ , which is not the other route  $r_i$

Step 4. *for each*  $\{\{pr\}_m \exists \{pr\}_m \in r_i \wedge m = 1 \text{ to } |r_i|\}$  Begin//node sequence  $\{pr\}_m$  with optimal fitness in route  $r_i$

Step 5. *for each*  $\{\{pr\}_n \exists \{pr\}_n \in r_j \wedge n = 1 \text{ to } |r_j|\}$  Begin//node sequence  $\{pr\}_n$  with optimal fitness in route  $r_j$

Step 6. If begin // if node sequence  $\{pr\}_n$  of route  $r_i$  is identical to node sequence  $\{pr\}_n$  of route  $r_j$  ( $\{pr\}_m \equiv \{pr\}_n \wedge m \neq 1$ )

Step 7. The node sequence that be present before the crossover point  $\{pr\}_m$  in  $r_i$  and the node sequence that is present after the crossover point  $\{pr\}_n$  in  $r_j$  are allied with crossover point  $\{pr\}_m$  that leads to new route  $r_m$  such that the route  $r_m$  which wasn't present in  $\overline{PR}$

$$\begin{aligned} r_m &\leftarrow \overline{r_i} \\ r_m &\leftarrow \overline{r_j} \end{aligned}$$

Step 8. The node sequence that exists before the crossover point  $\{pr\}_m$  in  $r_j$  and the node sequence that exists after the crossover point  $\{pr\}_n$  in cluster  $r_i$  are connected with crossover point  $\{pr\}_m$  that forms new route  $r_n$  such that the route  $r_n$  does not exist in  $\overline{PR}$

$$\begin{aligned} r_n &\leftarrow \overline{r_j} \\ r_n &\leftarrow \overline{r_i} \end{aligned}$$

Step 9. Estimate the fitness of the  $r_i, r_j, r_m, r_n$

Step 10. If  $((f(r_m) > f(r_i)) \& \& (f(r_m) > f(r_j)))$

// if fitness of the route  $r_m$  is qualified then add  $r_m$  to  $\overline{PR}$

Step 11.  $\overline{PR} \leftarrow r_m$

Step 12. If  $((f(r_n) > f(r_i)) \& \& (f(r_n) > f(r_j)))$

// if fitness of the route  $r_n$  is qualified then add

$$r_n \text{ to } \overline{PR}$$

Step 13.  $\overline{PR} \leftarrow r_n$

- Step 14. End of Step 6
- Step 15. End of Step 5
- Step 16. End of Step 4
- Step 17. End of Step 3
- Step 18. End of Step 2
- Step 19.  $PR \leftarrow PR \cup \overline{PR}$  Route set  $PR$  is defined again by discarding routes that are close to one another, of few, by means of the succeeding steps
- Step 20.  $\forall_{i=1}^{|PR|} \{r_i \exists r_i \in PR\}$  Begin
- Step 21.  $\forall_{j=1}^{|PR|} \{r_j \exists r_j \in PR \wedge i \neq j\}$  Begin
- Step 22. If  $(r_i \triangleq r_j)$  then Begin //  $r_i$  and  $r_j$  nearly same based on the most similar number of nodes in both routes
- Step 23.  $PR \leftarrow PR \cup \setminus r_i$  delete  $r_i$  from  $PR$
- Step 24. End of Step 22
- Step 25. End of Step 21
- Step 26. End of Step 20
- Step 27. If  $(PR \neq tPR)$  then DE-Main ( $PR$ )
- Step 28. End Function DE-Main //End of Step 1

Hence each stable and optimal route is signified, and then under contextual requirements selects the route from  $PR$

### 3.3 Choosing Route with Optimum Quality of Service

On the end of the process of differential evolution algorithm, the identified routes are sorted in the decreasing order of fitness in the sequence. Later the best suitable route of the entire  $PR$  will be chosen.

## 4 Simulation Setup and Observations

Here, in this section, the simulation analysis outcomes of the proposal BEWADE are mentioned. The parameters used for simulating the model are (see Table 2), NSF topology with 38 clients that affected by using JAVOBS [49], which is a java-based OBS network simulator. The primary benefit of the simulation is that its cost is much lesser than genuine experimentation and it gives results extremely near to the reality compared to mathematical modeling.

**Table 2** Traffic assumptions considered for experimental study

Network topology	NSF
Nodes	38
Connectivity	Uni directed transmission
Burst transmission channels count	41
Control packet transmission channels used	1 per each connection
Data packet average size	64 bytes
Data packets used to frame the burst	Average of 1000 packets
Simulation time	900 s
Reservation protocol	Horizon
Data generation	Poisson distribution
Scheduling algorithms	BWADE, bi-objective DE
Reservation protocol	JIT+

#### 4.1 Traffic Assumptions

The experimental study carried on simulations of optical burst switching, where the input traffic is generated under NSF network architecture as Poisson distribution. The Burst routing by wavelength allocation is carried through the proposed model BWADE, and the contemporary models bi-objective DE [36], Flexible Spectrum Ant Colony (FSAC) [37] algorithm and Shortest path [26] under variable traffic routing factors. The JIT+ [50] is the resource reservation protocol with partial wavelength conversion and feed forward FDL buffers.

The 64 bytes is the average volume of a data message that taken, and the data packets of an average 1000 are taken in to account to build each burst. It is confirmed that these packets have possess to assemble bursts of having variable sizes, which transmits under variable transmission time, and to assemble bursts with stable size, which transmits under stable transmission time. The simulation mean duration is set to 900 s. The testing is done to detail the performance advantage of the proposal BWADE that compared to the contemporary approaches bi-objective differential evolution (DE) Approach [36] and shortest path (SP) [26].

The following are assessment parameters to evaluate the BWADE performance:

1. Burst loss under
  - variable burst load and stable transmission time
  - stable burst load and variable transmission time
2. Wavelength utilization under
  - variable burst load and stable transmission time
  - stable burst load and variable transmission time

#### 4.2 Results and Discussion

The outcomes of the experiment clearly demonstrate that the proposal BWADE has marked higher performance against the benchmark scheduling approaches, bi-objective

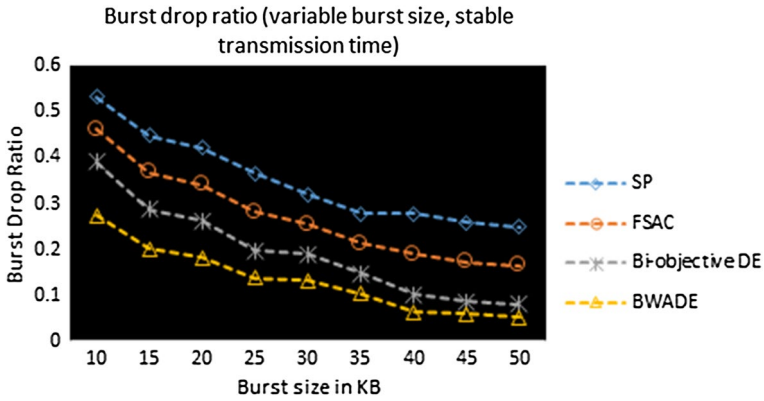


Fig. 2 The burst drop ratio under variable burst size and stable transmission time

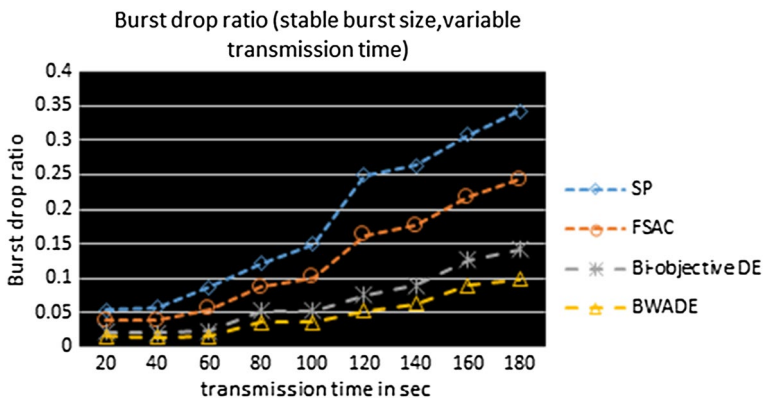


Fig. 3 Burst drop ratio under stable burst size and variable transmission time

DE, and SP which are chosen for comparison. The ratio of bursts dropped when the variable size bursts transmitted under stable transmission time is depicted in Fig. 2. The average ratio of burst drop observed for BWADE is 12% lesser than the average burst drop ratio observed for FSAC, 7% and 4% lesser than the average burst drop ratio observed for SP and bi-objective DE in respective order.

In regard to the transmission of stable burst load under variable transmission time, the burst loss observed from FSAC, bi-objective DE, and SP are scaled as high that compared to the proposed model BWADE. The burst loss ratio evinced from SP is above 18% high that compared to the burst loss observed for the proposal BWADE. The burst loss ratio observed for FSAC and bi-objective DE are also critical as they evinced 5% and 8% additional loss hat compared to the BWADE in respective order (see Fig. 3).

The Fig. 4 portrayed the ratio of wavelength utilization observed from BWADE, SP, and bi-objective DE under stable burst load and variable transmission time. According

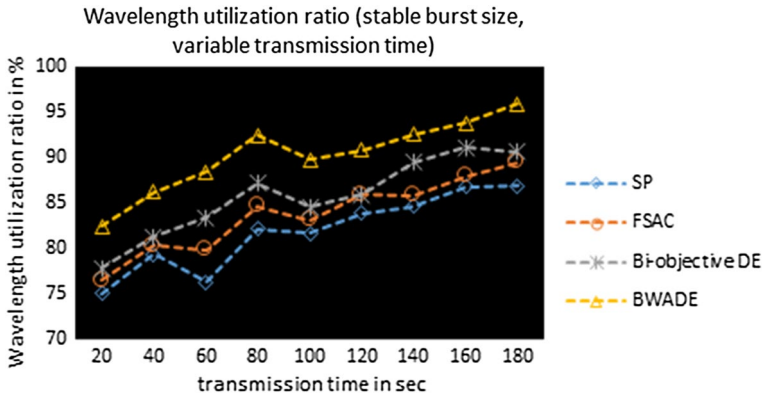


Fig. 4 The wavelength utilization ratio under stable burst size and variable transmission time

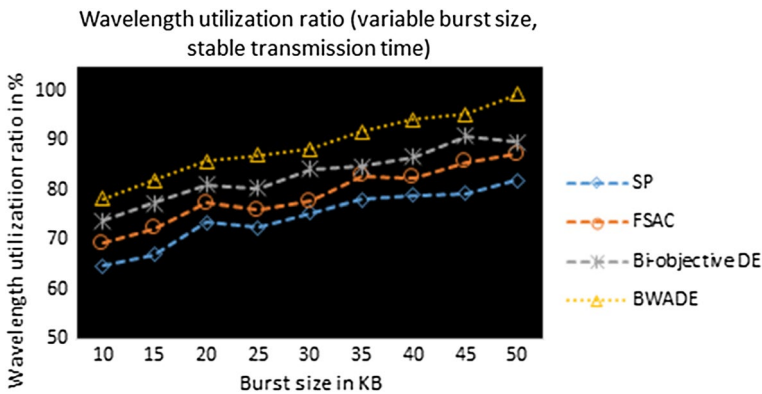


Fig. 5 The wavelength utilization ratio under variable burst size and stable transmission time

to these statistics, the proposed model the wavelength utilization by BWADE is 9% more than the contemporary method SP, 7%, and 5% more than the other contemporary models FSAC, and bi-objective DE in respective order.

The Fig. 5 portrays the wavelength utilization ratio of the BWADE and other contemporary models SP, FSAC, and bi-objective DE under stable transmission time and variable burst size. The average of the wavelength utilization ratio observed from BWADE is significant, which is 12% greater than the average wavelength utilization ratio observed for SP, whereas 8% and 4% excess that compared to FSAC and bi-objective DE in respective order.

According to the observations portrayed in Figs. 6 and 7, the BWADE, SP, FSAC and bi-objective DE has taken almost same time for executing the routing decision for the fewer number of initial routes. However, the BWADE is performing better than the other contemporary models SP, FSAC, and bi-objective DE, if the transmission time increases (Fig. 6) or if burst size increase (Fig. 7).

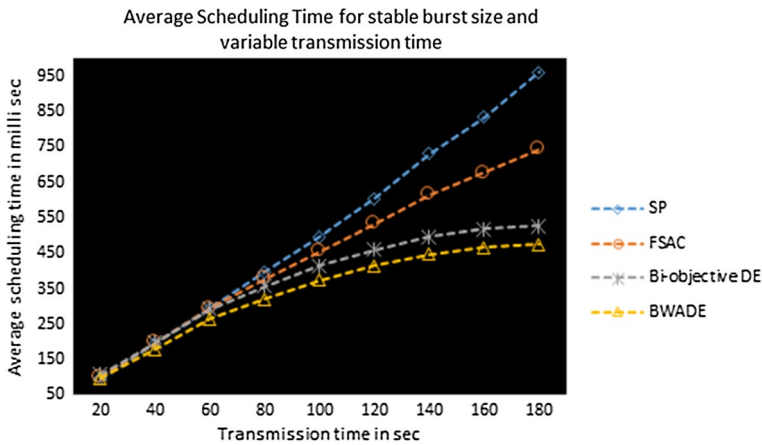


Fig. 6 The average scheduling time in milliseconds under stable burst size and variable transmission time

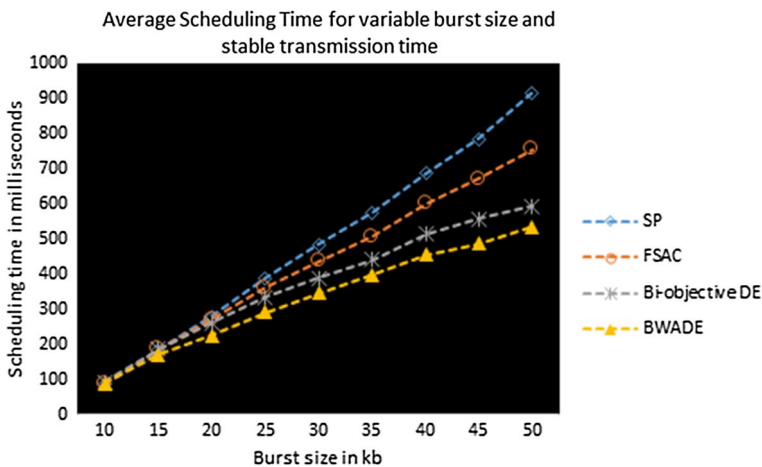


Fig. 7 The average scheduling time in milliseconds under variable burst size and stable transmission time

The average of the time taken for wavelength allocation process under stable burst size and variable transmission time observed from BWADE is 46%, 29%, and 12% lesser than the contemporary models SP, FSAC, and bi-objective DE in respective order. The context of experiments under variable burst size and stable transmission time (Fig. 7) evincing that the average scheduling time observed for BWADE is 51%, 31%, and 11% lesser than the average scheduling time observed for contemporary models SP, FSAC, and bi-objective DE in respective order.

Due to the nature of the Differential Evolution Algorithm, both the proposed model BWADE and bi-objective DE evincing the time complexity as NP-Complete. However, the time complexity of the method FSAC that uses ant colony optimization is NP-Hard. Due to the ability of assessing fitness under multiple objectives, the proposal BWADE limits the number of evolutions that compared to bi-objective DE. Hence the time complexity is significantly less than the contemporary models.

## 5 Conclusion

An approach of multi-objective QoS aware balanced wavelength allocation-based route discovery for OBS networks is proposed here in this manuscript. The depicted model built on differential evolution approach uses the multiple QoS factors (defined in this manuscript) as fitness scale. The experimental study was carried through NSF protocol-based simulations built by Java OBS. Through simulation we found that performance is increased smoothly thus preventing end to end delay from becoming too large. In buffer less OBS networks, the proposed BWADE algorithm performed better than the existing models bi-objective DE and SP in terms of cost and time parameters. The simulation results evince the performance advantage of the proposal over other contemporary models bi-objective DE [36], FSAC [37], and SP [26] under assessment metrics called burst loss ratio, wavelength utilization ratio, and time taken to establish the route. Also, the results have shown that timer-based assembly is desirable as it not only controls the edge buffering delay but also reduce the burst loss ratio. The future research can incorporate the proposal with other burst scheduling strategies to achieve optimal competence of burst transmissions in OBS networks.

## References

1. Chen, Y., Qiao, C., & Yu, X. (2004). Optical burst switching (OBS): A new area in optical networking research. *IEEE Network*, 18(3), 16–23.
2. Xiong, Y., Vandenhoute, M., & Cankaya, H. C. (2000). Control architecture in optical burst-switched WDM networks. *IEEE Journal on Selected Areas in Communications*, 18(10), 1838–1851.
3. Barpanda, R. S., Turuk, A. K., & Sahoo, B. (2018). QoS aware routing and wavelength allocation in optical burst switching networks using differential evolution optimization. *Digital Communications and Networks*, 4(1), 3–12.
4. Rosberg, Z., Le Vu, H., Zukerman, M., & White, J. (2003). Performance analyses of optical burst-switching networks. *IEEE Journal on Selected Areas in Communications*, 21(7), 1187–1197.
5. Belbekkouche, A., Hafid, A., Gendreau, M., & Tagmouti, M. (2011). Path-based QoS provisioning for optical burst switching networks. *Journal of Lightwave Technology*, 29(13), 2048–2063.
6. Zhang, Q., Vokkarane, V. M., Jue, J. P., & Chen, B. (2004). Absolute QoS differentiation in optical burst-switched networks. *IEEE Journal on Selected Areas in Communications*, 22(9), 1781–1795.
7. Chen, Y., Hamdi, M., & Tsang, D. H. (2001). Proportional QoS over OBS networks. In *Global telecommunications conference, 2001. GLOBECOM'01. IEEE* (Vol. 3, pp. 1510–1514). IEEE.
8. Ramaswami, R., Sivarajan, K., & Sasaki, G. (2009). *Optical networks: A practical perspective*. Burlington: Morgan Kaufmann.
9. Brackett, C. A. (1990). Dense wavelength division multiplexing networks: Principles and applications. *IEEE Journal on Selected Areas in Communications*, 8(6), 948–964.
10. Qiao, C., & Yoo, M. (1999). Optical burst switching (OBS)—A new paradigm for an Optical Internet<sup>1</sup>. *Journal of high speed networks*, 8(1), 69–84.
11. Thodime, G. R., Vokkarane, V. M., & Jue, J. P. (2003, December). Dynamic congestion-based load balanced routing in optical burst-switched networks. In *Global telecommunications conference, 2003. GLOBECOM'03. IEEE* (Vol. 5, pp. 2628–2632). IEEE.
12. Dolzer, K., Gauger, C., Späth, J., & Stefan, B. (2001). Evaluation of reservation mechanisms for optical burst switching. *AEU-International Journal of Electronics and Communications*, 55(1), 18–26.
13. Ljolje, M., Inkret, R., & Mikac, B. (2005, January). A comparative analysis of data scheduling algorithms in optical burst switching networks. In *2005 conference on optical network design and modeling*.
14. Yoo, M., Qiao, C., & Dixit, S. (2000). QoS performance of optical burst switching in IP-over-WDM networks. *IEEE Journal on Selected Areas in Communications*, 18(10), 2062–2071.

15. Yang, M., Zheng, S. Q., & Verchere, D. (2001). A QoS supporting scheduling algorithm for optical burst switching DWDM networks. In *Global telecommunications conference, 2001. GLOBECOM'01. IEEE* (Vol. 1, pp. 86–91). IEEE.
16. J Xu, J., Qiao, C., Li, J., & Xu, G. (2003, March). Efficient channel scheduling algorithms in optical burst switched networks. In *INFOCOM 2003. Twenty-second annual joint conference of the IEEE computer and communications societies. IEEE Societies* (Vol. 3, pp. 2268–2278). IEEE.
17. Vokkarane, V. M., Zhang, Q., Jue, J. P., & Chen, B. (2002, November). Generalized burst assembly and scheduling techniques for QoS support in optical burst-switched networks. In *Global telecommunications conference, 2002. GLOBECOM'02. IEEE* (Vol. 3, pp. 2747–2751). IEEE.
18. Ping, D. U. (2007). *QoS control and performance improvement methods for optical burst switching networks*. PhD Dissertation, department of informatics, School of multidisciplinary sciences, The graduate university for advanced studies (SOKENDAI).
19. Danielsen, S. L., Mikkelsen, B., Joergensen, C., Durhuus, T., & Stubkjaer, K. E. (1997). WDM packet switch architectures and analysis of the influence of tunable wavelength converters on the performance. *Journal of Lightwave Technology*, 15(2), 219–227.
20. Forghieri, F., Bononi, A., & Prucnal, P. R. (1995). Analysis and comparison of hot-potato and single-buffer deflection routing in very high bit rate optical mesh networks. *IEEE Transactions on Communications*, 43(1), 88–98.
21. Ozdaglar, A. E., & Bertsekas, D. P. (2003). Routing and wavelength assignment in optical networks. *IEEE/ACM Transactions On Networking (ton)*, 11(2), 259–272.
22. Chraplyvy, A. R. (1990). Limitations on lightwave communications imposed by optical-fiber nonlinearities. *Journal of Lightwave Technology*, 8(10), 1548–1557.
23. Liga, G., Xu, T., Alvarado, A., Killey, R. I., & Bayvel, P. (2014). On the performance of multi-channel digital backpropagation in high-capacity long-haul optical transmission. *Optics Express*, 22(24), 30053–30062.
24. Maher, R., Xu, T., Galdino, L., Sato, M., Alvarado, A., Shi, K., et al. (2015). Spectrally shaped DP-16QAM super-channel transmission with multi-channel digital back-propagation. *Scientific Reports*, 5, 8214.
25. Wen, B., & Sivalingam, K. M. (2002). Routing, wavelength and time-slot assignment in time division multiplexed wavelength-routed optical WDM networks. In *INFOCOM 2002. Twenty-first annual joint conference of the IEEE computer and communications societies. Proceedings. IEEE* (Vol. 3, pp. 1442–1450). IEEE.
26. Wen, B., Shenai, R., & Sivalingam, K. (2005). Routing, wavelength and time-slot-assignment algorithms for wavelength-routed optical WDM/TDM networks. *Journal of Lightwave Technology*, 23(9), 2598.
27. Rajalakshmi, P., & Jhunjunwala, A. (2006, September). Routing wavelength and timeslot reassignment algorithms for TDM based optical WDM networks-multi rate traffic demands. In *14th IEEE international conference on networks, 2006. ICON'06* (Vol. 2, pp. 1–6). IEEE.
28. Rajalakshmi, P., & Jhunjunwala, A. (2007). Routing wavelength and time-slot reassignment algorithms for TDM based optical WDM networks. *Computer Communications*, 30(18), 3491–3497.
29. Um, T. W., Choi, J. K., Choi, S. G., & Ryu, W. (2006, July). Centralized resource allocation for time-slotted OBS networks. In *International conference on networking and services, 2006. ICNS'06* (p. 40). IEEE.
30. Yang, W., & Hall, T. J. (2006, May). Distributed dynamic routing, wavelength and timeslot assignment for bandwidth on demand in agile all-optical networks. In *Canadian conference on electrical and computer engineering, 2006. CCECE'06* (pp. 136–139). IEEE.
31. Zhang, Z., Liu, L., & Yang, Y. (2007). Slotted optical burst switching (SOBS) networks. *Computer Communications*, 30(18), 3471–3479.
32. Noguchi, H., & Kamakura, K. (2008, December). Effect of one-way mode of hybrid reservation on slotted optical burst switching networks. In *International symposium on information theory and its applications, 2008. ISITA 2008* (pp. 1–6). IEEE.
33. Jia, L., Fang-yuan, J., & Xiao-xiao, X. (2010, May). A dynamic routing, wavelength and timeslot assignment algorithm for WDM-TDM optical networks. In *2010 2nd international conference on future computer and communication (ICFCC)* (Vol. 1, pp. V1–533). IEEE.
34. Shan, G., Zhu, G., & Liu, D. (2011). Study on the problem of routing, wavelength, and time-slot assignment towards optical time-slot switching technology. *Photonic Network Communications*, 22(2), 162–171.
35. Donato, E., Joaquim, C. J., Antnio, V., & Ahmed, P. (2012). A proposal of dynamic RWA using ant colony in optical burst switched networks. In *The proceedings of the eleventh international conference on networks (ICN 2012)* (pp. 246–252).

36. Barpanda, R. S., Turuk, A. K., & Sahoo, B. (2017). QoS aware routing and wavelength allocation in optical burst switching networks using differential evolution optimization. *Digital Communications and Networks*, 4, 3–12.
37. Gravett, A. S., du Plessis, M. C., & Gibbon, T. B. (2017). A distributed ant-based algorithm for routing and wavelength assignment in an optical burst switching flexible spectrum network with transmission impairments. *Photonic Network Communications*, 34(3), 375–395.
38. Shuo, L. (2014). *Analysis and synthesis of optical burst switched networks*.
39. Battestilli, T., & Perros, H. (2003). An introduction to optical burst switching. *IEEE Communications Magazine*, 41(8), S10–S15.
40. Teng, J., & Rouskas, G. N. (2005). Wavelength selection in OBS networks using traffic engineering and priority-based concepts. *IEEE Journal on Selected Areas in Communications*, 23(8), 1658–1669.
41. Cao, X., Li, J., Chen, Y., & Qiao, C. (2002, November). Assembling TCP/IP packets in optical burst switched networks. In *Global telecommunications conference, 2002. GLOBECOM'02. IEEE* (Vol. 3, pp. 2808–2812). IEEE.
42. Rocha, J. F., Cartaxo, A. T., Silva, H. J., Pinto, J. L., Teixeira, A. L., Gameiro, A. S., et al. (2005). Optical communications research at institute of telecommunications. *Fiber and Integrated Optics*, 24(3–4), 411–428.
43. Mitchell, M., Forrest, S., & Holland, J. H. (1992, December). The royal road for genetic algorithms: Fitness landscapes and GA performance. In *Proceedings of the first European conference on artificial life* (pp. 245–254).
44. Brest, J., & Maučec, M. S. (2008). Population size reduction for the differential evolution algorithm. *Applied Intelligence*, 29(3), 228–247.
45. Qin, A. K., Huang, V. L., & Suganthan, P. N. (2009). Differential evolution algorithm with strategy adaptation for global numerical optimization. *IEEE Transactions on Evolutionary Computation*, 13(2), 398–417.
46. Mininno, E., Neri, F., Cupertino, F., & Naso, D. (2011). Compact differential evolution. *IEEE Transactions on Evolutionary Computation*, 15(1), 32–54.
47. Islam, S. M., Das, S., Ghosh, S., Roy, S., & Suganthan, P. N. (2012). An adaptive differential evolution algorithm with novel mutation and crossover strategies for global numerical optimization. *IEEE Transactions on Systems, Man, and Cybernetics, Part B (Cybernetics)*, 42(2), 482–500.
48. Das, S., & Suganthan, P. N. (2011). Differential evolution: A survey of the state-of-the-art. *IEEE Transactions on Evolutionary Computation*, 15(1), 4–31.
49. Quoc, N. H., Nhat, V. V. M., & Son, N. H. (2014). Group scheduling for multi-channel in OBS networks. *REV Journal on Electronics and Communications*, 3(3–4), 134–137.
50. Teng, J., & Rouskas, G. N. (2005). A detailed analysis and performance comparison of wavelength reservation schemes for optical burst switched networks. *Photonic Network Communications*, 9(3), 311–335.

**Publisher's Note** Springer Nature remains neutral with regard to jurisdictional claims in published maps and institutional affiliations.



**Veparala Kishen Ajay Kumar** was born in Proddatur, India, in 1980. He received the B.Tech. degree in Electronics and Communications Engineering from the University of Sri Krishnadevaraya, Anantapuram, India, in 2001, and the M.Tech. degree in Digital Systems and Computer Electronics from Jawaharlal Nehru Technological University (JNTU), Hyderabad, India, in 2007. During the years 2007–2015, he worked as an assistant professor and associate professor, and in 2015, he joined as a full-time research scholar in G. Pulla Reddy engineering college (Autonomous), which is affiliated to JNTU, Anantapuram, India. His current research interests include optical networks, communication networks. He is a Life Member of the Indian Society for Technical Education (ISTE). He has published three peer reviewed research articles in the area of optical networks.



**Dr. Katam Suresh Reddy** received the B.Tech. degree in Electronics and Communication engineering (ECE) from the University of Sri Krishnadevaraya, Anantapuram in 1996, M.Tech in Communication Systems from Gulbarga University in 1999 and Ph.D in the area of Signal Processing from Jawaharlal Nehru Technological University Hyderabad (JNTUH), Hyderabad, India, in 2012. Presently he is working as Professor & Head in Electronics and Communication Engineering in the Department of ECE, G. Pulla Reddy Engineering College, Kurnool. He has 19 years of teaching & 7 years of research experience. His interests include signal processing and Optical Networks. He has about 12 publications in various International Journals, 5 papers in various international/national conferences. He is currently guiding 5 PhD students. He successfully executed two AICTE funded Projects.



**Dr. Mahendra Giri Prasad** received the B.Tech. degree in Electronics and Communication Engineering from Jawaharlal Nehru Technological University (JNTU) College of Engineering, Anantapur in 1982, M.Tech in Electronic Instrumentation and Communication Systems from SV University College of Engineering in 1994 and Ph.D in the area of Bio-medical Signal processing from JNTU Hyderabad, India in 2003. He had 32 years of teaching and 16 years of research experience. Presently he is working as a professor in the department of Electronics and Communication Engineering and Director of Admissions at JNTUA, Ananthapuramu, India. His research interests include Bio-medical Signal Processing & Bio Informatics, Signal and Image Processing, Digital System Design, Microprocessors and Microcontrollers and Biomedical Instrumentation. He published 104 papers in various International Journals and 38 papers in international/national conferences.

## Optimized segmentation and classification for liver tumor segmentation and classification using opposition-based spotted hyena optimization

Munipraveena Rela ✉, Suryakari Nagaraja Rao, Patil Ramana Reddy

First published: 04 December 2020

<https://doi.org/10.1002/ima.22519>

### Abstract

In today's world, liver cancers are one of the mainly popular cancers occurring in the human body. The greater part of liver carcinomas is more prone to alcohol-related hepatitis and cirrhosis conditions. Moreover, there is another form of cancer namely, metastatic liver cancer, where the tumor is initiated from other organs and extends to the liver. Early and premature diagnosis of liver cancer is necessary as it tends to improvise life expectancy. Nowadays, discriminating the liver and tumor parts from medical images with the aid of completely automated computer-aided software is a more challenging task, since the liver disease can vary from person to person. This article attempts to implement the novel liver tumor segmentation and classification model using the optimization driven segmentation and classification model. The developed model carries out the task in five steps (a) Pre-processing, (b) liver segmentation, (c) tumor segmentation, (d) feature extraction, and (e) classification. At first, the gathered CT images are subjected to pre-processing with three steps that follow contrast enhancement by histogram equalization and noise filtering by the median filter. Next to the pre-processing of the image, the liver is segmented from the CT abdominal image using adaptive thresholding pursued by level set segmentation. Further, a modified algorithm termed as Fuzzy Centroid-based Region Growing Algorithm with tolerance optimization is developed and used for the tumor segmentation. From the segmented tumor image, three sets of features like gray-level co-occurrence matrix (GLCM), shape features, and local binary pattern (LBP) is utilized for the classifier training. In the classification side, two deep learning algorithms are used: recurrent neural network (RNN), and convolutional neural network (CNN). The tumor segmented image is given as input to the CNN, and the extracted features are given as input to the RNN. As an improvement, an optimized hybrid classifier is adopted for the hidden neuron optimization. Moreover, an improved meta-heuristic algorithm called opposition-based spotted hyena optimization (O-SHO) is introduced to perform the optimized segmentation and classification. The experimental results show that the overall accuracy attained by the proposed model is efficient, less sensitive to noise, and performs superior on a diverse set of CT images.

[Download PDF](#)

About Wiley Online Library

# QoS Guaranteed metrics for Dynamic Scheduling through Void filling and Burst Segmenting in OBS Networks

Kishen Ajay Kumar, Katam Suresh Reddy, Mahendra Giriprasad

**Abstract**— Optical burst switching (OBS) is an optical networking technology which consolidates the advantages of optical packet switching and optical circuit switching, while at the same time keeping away their limitations. Since OBS utilizes one-way reservation scheme, hence, due to contention bursts might be dropped at the intermediate nodes before they reach the destination. Hence, the burst dropping ratio is the critical performance estimation in OBS networks. The majority of the scheduling models in contemporary literature aimed to attain scheduling optimality are based on optimal utilization of their idle time. Not very many contributions endeavored to choose channels through any of the quality metric, and remarkably less contributions offer on wavelength allocation to lessen the burst drop ratio. In this regard, this manuscript endeavored to attain optimal wavelength allocation under divergent metrics that denoted as QoS metrics for dynamic scheduling through Void Filling and Burst Segmenting (QDS-VF). The proposed model is compared to the other contemporary model depicted in recent literature and found that burst loss ratio is lower in the proposed scheme.

**Index Terms**—Optical Burst Switching, OBS Networks, Burst drop ratio, Void filling, Burst Scheduling.

## 1. INTRODUCTION

At present times, media transmissions still experience huge quantity of traffic. With a view to manage traffic growth, telecom operators swung to optical fiber as a transmission clairvoyant having an immense capacity with provision of bandwidth. With the explosive and fast development of the internet, wavelength division multiplexing (WDM) in optical network has made conceivable throughput backbone network. Optical burst switching [1] is a step towards the extreme objectives of optical packet switching (OPS) in next era and it is proposed to gain an awesome balance between wavelength routing and OPS in WDM optical networks.

Circuit-switching model is the most prominent optical-switching models currently being implemented in commercial networks. The circuit-switching model sets up a light path from the switch to switch for a longer duration. The network is also termed as WR-network and accommodates light-paths through the fibers. Further, these paths vary based on their respective projected wavelengths. However, the traditional WR model is relatively less effective in times of huge traffic and its performance varies

over time. This is due to the fact that a wavelength routed (WR) light-path is a bandwidth assured tunnel, resulting in insufficient or unused bandwidth due to inefficient information transmission.

OBS is based on a one-way reservation protocol where the packets are assembled into a burst that follows a corresponding control packet (CP) without waiting for an acknowledgement. In OBS networks, a burst has two segments: payload and control [2]. Payload is the actual data transmitted and the CP carries the header information. Since OBS uses one-way reservation scheme, bursts may be dropped at intermediate nodes due to contention and there is no guarantee that bursts sent will reach its destination.

The functional diagram of OBS network shown in figure 1 has two types of nodes: edge nodes and core nodes. Edge routers can be an egress router (egress node) or an ingress router (ingress node). At the ingress node, data from access network destined to the same egress node is accumulated into large data bursts at the ingress node.

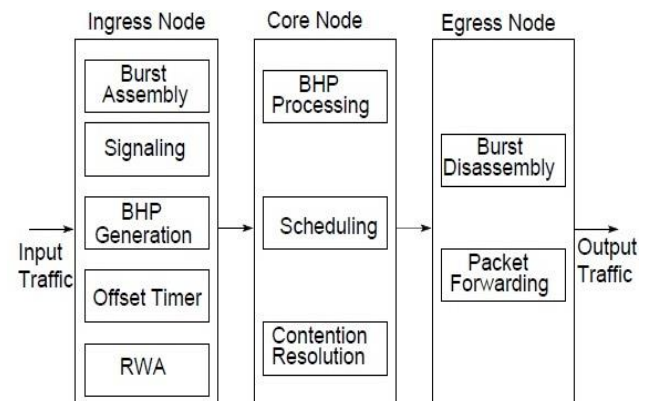


Fig 1: Functional diagram of an OBS Network

The model considers a burst switching entity comprising of a cluster of data-packets transmitted between nodes. This burst dropping in the OBS environment can evoke from numerous issues including unavailability of data channels, path congestion and data contention. Accordingly these issues can prompt to lower network utilization and also affects network throughput. Primarily, in OBS networks, the bursts are lost on account of the failure of resources reservation, which implies that there is a large number of reservation attempts than the number of available resources.

Revised Manuscript Received on March 10, 2019 .

Kishen Ajay Kumar, Research Scholar, Gprec, Jntua, Kurnool , AP, India (E-Mail:vkishenajaykumar@gmail.com)

Katam Suresh Reddy, Katam Suresh Reddy AP, India (E-Mail:sureshkatam@gmail.com)

Mahendra Giriprasad, Professor, Department of ECE, Jntua, AP, India (mahendragiri1960@gmail.com)



The contemporary literature presents several studies focusing on burst based models and associated switching framework. Further, data contention also remains one of the interesting study areas in the OBS context [3]. In addition to managing fairness challenges, the environment can challenge the ability of multiplexing along with switching.

### 2. RELATED RESEARCH

The research in [4] put forward a bi-state Markov Chain approach to manage burst dropping in JET context. It utilized the FF-VF filling context as a path sequencing program. The study in [5] built a loss chance estimation tool in view of various FDLs buffering granularities. Researchers in [6] and [7] developed the estimation tool through retransmission and deflection models. The study in [8], an advanced variant of JET signaling is suggested and the authors named it as VFO. The VFO time sequences the burst considering its initial arrival time. Further, a different variant of JET signaling, termed as S-JET is suggested in [9], which reduces the processing duration for JET when registration occurs at the last of the list. The authors in [10] designed an asymptotical scenario for the null burst drop possibility with respect to various projected wavelengths. This assists in recognizing areas having small burst drop chances.

The study in [11] developed a probabilistic method for determining the burst loss possibility in the context of channel usage convertor sharing is implemented. The method regards the burst onset as the Markovian-arrival procedure to manage diverse traffic distributions. The volume of the burst is apparent to be swiftly distributed. The study in [12] developed an optimal burst sequencing code. The code depends on invariable time burst rescheduling method. The method primarily deletes the deviations in offset durations. Accordingly, the duration based priority mechanisms are not supported. Data contention and loss possibilities are researched in the context of multiple routing codes [13]. In [14], the study built a lowered load fixed-point method to assess the chances of data loss. The method functions for both JIT and JET concepts associated with data segmentation along with path-based priorities. The concept suggests that data segmentation results in the least loss possibility while the path-based priority concept also resulted in increased loss reduction, but the outcome was not significant.

Another important area of focus has been achieving fairness in OBS networks with Pre-emption being mostly used [15]. The study in [16] put forward LHP mechanism for handling unfairness issues in the environment. According to the study, if the cumulative count of hops is more than the preset threshold, it can preempt another burst at the final hop. However, due to the preemption being executed only at the final hop, the method is ineffective to function in OBS environment. As an alternative to this solution, the authors in [17] presented an in-between hop preemption concept. This concept is based on two predetermined threshold levels. Further, in [18], a fair FPP model is suggested. It is built on the basis of first offset duration, mean burst volume, successful hops and leftover hops. In the context of data contention, pre-emption is executed through FPP method to trade off both network

fairness level and throughput value. Experimental study of the model depicted superior performance of the FPP model as compared the approaches put forward in [15] and [16].

The authors in [19] suggested FCSA sequencing program for attaining tradeoff among fairness and blocking efficiency. The algorithm integrates a dynamic priority with every burst. The related priority determines the key attributes of any burst. Further, in the context of data contention, the suggested approach utilizes these priorities to select a desirable burst and ignore another burst. In [20], the researchers included the possibility that a subcarrier being engaged in the path capacity.

The study in [21] utilized sequencing mechanisms to incorporate a huge volume of users for super speed paths. The program attempted to enhance short-term fairness and distributes the available bandwidth on the weighted fair basis. In [22], DPCC mechanism is put forward, which balances the rate and reliability through proper distribution of traffic and resources. Further, the method also alters the message transmission speeds and reliability. For altering these parameters, it relies on traffic congestion, pricing and feedback data. Because the model relies on feedback data, it faces the challenge of obtaining this information. Accordingly, certain bursts face high loss rates, in particular, when restricting their input flows. This can result in biased network usage. In [23], route based on ant scenario, wavelength, and time-slot distribution program is suggested to lower the burst drop ratio and achieve an overall high efficiency.

Within the Just-Enough-Time (JET) scheme, there is a probability of a burst being blocked by any other burst that is scheduled to reach later because the offset time differs as per the path length. This phenomenon is known as retro-blocking [24] in step with which the bursts with large offset time are successful in reserving the wavelength earlier than the burst control packet (BCP) of a burst with smaller offset time arriving. This idea outcome within the decline in throughput at the side of resource usage. Further it is able to also result in big unfairness. Though the essential advantage of JET is in lowering end-to-end transmission delay, however, it results in higher burst loss [25], [26], [27].

The previously mentioned research works fundamentally endeavored to decrease the burst loss possibilities, thereby enhancing the overall network throughput. This manuscript endeavors to advance another model that enables the effective utilization of void depicted in channels that already scheduled.

### 3. QOS METRICS FOR DYNAMIC SCHEDULING THROUGH VOID FILLING AND BURST SEGMENTING

The proposed burst scheduling method for OBS networks that referred as “QoS metrics for dynamic scheduling through Void Filling and Burst Segmenting (QDS-VF)” is depended on Void filling, which indicates the unused

capacity of a channel is adapted as an essential process in the proposed solution.

Let the time taken to process the control frame  $fc_i$  be  $s(lf_i)$  and the time taken by the  $lf_i$  to reach the scheduler from the assembler be  $\tau(lf_i)$  and  $\tau(b_i)$  be the assessed time to transmit burst  $b_i$  from assembler to scheduler. The total expected transmission time  $tett(b_i)$  will be measured as shown in equation 1.

$$tett(b_i) = s(lf_i) + \tau(lf_i) + \tau(b_i) \quad (1)$$

Scheduling a burst must be of transmission quality in particular but often the scheduled wavelength is not optimal under all quality metrics considered. The quality metrics adapted to evaluate the wavelength optimality ratio are investigated following:

*Wavelength arbitration rate (war):*

This metric shows the ratio of elapsed schedules of the wavelength to the number of times that wavelength scheduled which can be measured as follows:

$$war(w_i) = \frac{ls(w_i)}{ts(w_i)} \quad (2)$$

The notation  $war(w_i)$  in equation 2 denotes wavelength arbitration rate,  $ls(w_i)$  is the elapsed schedules of wavelength  $w_i$  against total schedules  $ts(w_i)$ .

*B. Desertation rate (der):*

This metric indicates observed unsuccessful transmissions to the total number of times, the corresponding wavelength scheduled which can be measured as follows:

$$der(w_i) = \frac{ds(w_i)}{ts(w_i)} \quad (3)$$

The notation  $ds(w_i)$  in the equation denotes the number of deserted transmissions with respect to the total schedules  $ts(w_i)$ .

*C. Transmission realization rate (trr):*

This metric is the ratio of transmission realizations to the total number of times that wavelength was scheduled, which can be measured as follows:

$$trr(w_i) = \frac{ts(w_i) - ds(w_i)}{ts(w_i)} \quad (4)$$

The notation  $trr(w_i)$  in equation 4 denotes transmission realization rate of wavelength  $w_i$  which is the difference between total schedules  $ts(w_i)$  and the deserted schedules  $ds(w_i)$ .

*D. Inference rate (irr):*

The wavelength in given range that is distinct at given threshold from the other wavelengths that scheduled in parallel measuring of wavelength compatibility is as follows:

$$irr(w_i) = \sqrt{(w(i) - nw(i))^2} \quad (5)$$

The notation  $nw(i)$  denotes the nearest wavelength in nanometers.

*E. Wavelength data rate (wdr):*

This metric is the important Qos factor and the data compatibility can be measured as follows

$$wdr(w_i) = adr(w_i) - cdr(w_i) \quad (6)$$

Here the notation  $adr(w_i)$  denote the data rate available at  $w_i$  and  $cdr(w_i)$  is the data rate required for the corresponding burst.

*F. Wavelength existence span (wes):*

Except the existence span of the wavelength is extra than the residual life span of corresponding burst, the respective wavelength isn't always match to schedule. This can be measured as follows:

$$wes(w_i) = sea(w_i) - lsr(w_i) \quad (7)$$

The notation  $sea(w_i)$  denotes the existing span of the wavelength  $w_i$ , and the notation  $lsr(w_i)$  indicates the residual life span of burst  $b$  to transmit target burst.

#### 4. ASSESSMENT OF OPTIMAL RATIO OF WAVELENGTHS

Let  $war, der, trr, irr, wdr$ , and  $wes$  as a set of QoS metrics  $N = \{[war(w_i), der(w_i), trr(w_i), wdr(w_i), wes(w_i)] \forall i = 1 \dots x\}$  of available projected wavelengths  $W = \{w_1, w_2, \dots, w_x\}$  under scheduler  $s_k$ .

The scope of each wavelength for Qos factors  $wdr(w_i)$ ,  $wes(w_i)$  are assessed as follows. Initial process normalizes the bandwidth compatibility and existence span as follows:

- step 1.  $\forall_{i=1}^x \{w_i \exists w_i \in W\}$  Begin
- step 2.  $diff \leftarrow rdrt - wdr(w_i)$  // the set  $diff$  contains the difference between residual data rate  $wdr(w_i)$  of each wavelength  $w_i$  against residual bandwidth threshold  $rdrt$
- step 3.  $diff_{abs} \leftarrow abs(diff\{w_i\})$  // the set  $diff_{abs}$  contains absolute values of entries in  $diff$
- step 4. End
- step 5.  $\forall_{i=1}^x \{w_i \exists w_i \in W\}$  Begin
- step 6. wavelength data rate normalized such that wavelength with optimal in regard to data rate is between 0 and 1.
- step 7. End
- step 8.  $\forall_{i=1}^x \{w_i \exists w_i \in W\}$  Begin
- step 9.  $diff \leftarrow est - wes(w_i)$
- step 10.  $diff_{abs} \leftarrow abs(diff[w_i])$
- step 11. End
- step 12.  $\forall_{i=1}^x \{w_i \exists w_i \in W\}$  Begin
- step 13.  $wes(w_i) = 1 - \frac{1}{(diff\{w_i\} + \max(diff_{abs}) + 1)}$
- step 14. End
- step 15.  $\forall_{i=1}^x \{w_i \exists w_i \in W\}$  Begin



step 16  $ps(w_i) = 1 - (wdr(w_i) \times wes(w_i))$   
 step 17 End

For each of the projected wavelength, further the model delineates the wavelength optimality rate ( $wor$ ) as follows.

$$\forall_{i=1}^x \{w_i \exists w_i \in W\} \text{ Begin // for each projected wavelength}$$

$$\mu(w_i) = \frac{\{W_{ps}\{w_i\} + W_{war}\{w_i\} + W_{der}\{w_i\} + W_{trr}\{w_i\} + W_{irr}\{w_i\}\}}{|Q|} \quad (8)$$

The equation 8 assess the mean of the indices for multiple metrics of wavelength  $w_i$

$$d(w_i) = \sqrt{\frac{1}{|Q|} \{(\mu(w_i) - W_{ps}\{w_i\})^2 + (\mu(w_i) - W_{war}\{w_i\})^2 + (\mu(w_i) - W_{der}\{w_i\})^2 + (\mu(w_i) - W_{trr}\{w_i\})^2 + (\mu(w_i) - W_{irr}\{w_i\})^2\}} \quad (9)$$

The notation  $\mu(w_i)$  indicates corresponding wavelength  $w_i$  those obtained for different Qos metrics.

$$wor(w_i) = \frac{1}{d(w_i)}$$

The optimal entries of the set  $W_{ps}$  are chosen, which the projected wavelengths are having primary score greater than the given threshold. Further these wavelengths are sorted in descending order of their wavelength in regard to schedule the corresponding burst. Here in QDS-VF, it first endeavors to follow the optimum wavelength under the effect of divergent Qos metrics.

**5. EXPERIMENTAL SETUP AND EMPIRICAL ANALYSIS & RESULTS**

The simulation study and the results from the phase are cited in this chapter. The NSF-network structure is assessed by interconnecting 38 senders by means of one-way communication path, enabling two-way order by using JAVOBS [28]. Every burst size is fixed as a group of 1,024 data-packets with every data-packet consisting of 64 bytes size. The simulations have been conducted over the suggested approach QDS-VF along with similar approach sharing similar concept, but having divergent approach called POCS-VF [29].

Topology	NSF
Data Sources	25
Transmission channels	19
Dedicated channels for control packets transmission	9
Burst Sizes range	32KB to 1024KB
Range of bandwidth allocated per channel	2 mb/s
Error scope of the thresholds used	$\pm 0.25$
Up time of the network	900,000 $\mu s$
Range of time frames	10 $\mu s$ to 50 $\mu s$

**Table 1: Statistics of the simulation environment**

The parameters used to assess the performance are; a. burst loss ratio (BLR) against divergent burst load and fixed size of time frame; b. burst loss ratio against divergent sizes of time frames and fixed burst load; c. channel utilization ratio against divergent burst loads and fixed size of the time frame; d. channel utilization ratio (CUR) against divergent sizes of the time frames and fixed burst load; e. and average scheduling duration.

**A. Performance assessment:**

The outcomes accomplished from the simulation study delineates that the proposed model called QDS-VF is outperformed compared to benchmark model called POCS-VF that compared under different metrics as stated above. The BLR against varied bursts as shown in the figure 2 states that QDS-VF is 7% less than the burst loss that observed for POCS-VF.

The BLR against divergent time frames with fixed sizes of burst as shown in the figure 3 states that QDS-VF is 6% less than burst loss that observed for POCS-VF.

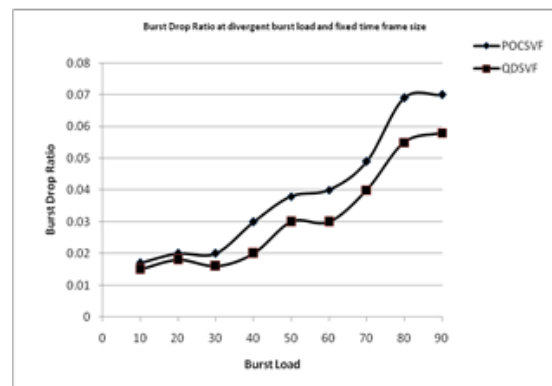


**Fig 2: Burst Drop ratio against divergent burst load and fixed timeframe of size of 35 μs**

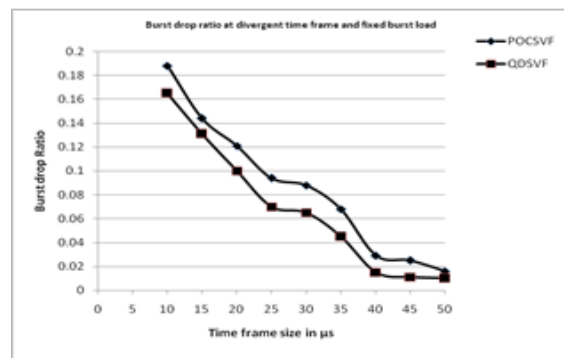


**Fig 3: Depiction of Burst Drop Ratio against Divergent size of timeframes and fixed burst size of 35480 bytes**

The CUR against divergent burst loads and fixed size of the time frame as depicted in figure 4 is average of 3% more in QDS-VF than POCSVF.

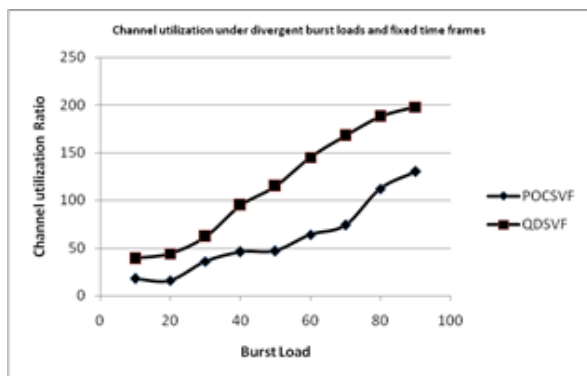


Fig 4: Depiction of Channel utilization ratio under divergent burst load and fixed timeframe of size 35  $\mu$ s

The scheduling time against divergent burst loads and fixed size of the time frame and varied time frame sizes with fixed burst load as depicted in figure 5 is average of 9% less in QDS-VF than POCSVF.

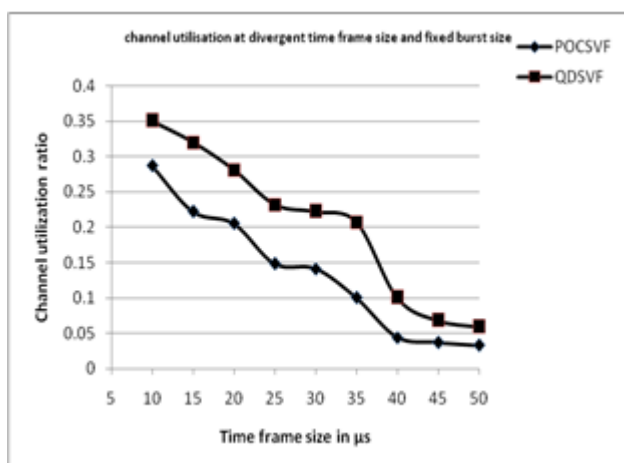


Fig 5: Depiction of Channel Utilization under divergent sizes of timeframes and fixed burst load of 35680 bytes.

Further in figures 6 and 7, the mean time to schedule the burst is nearly same, but the time taken by QDS-VF is lower than POCSVF.

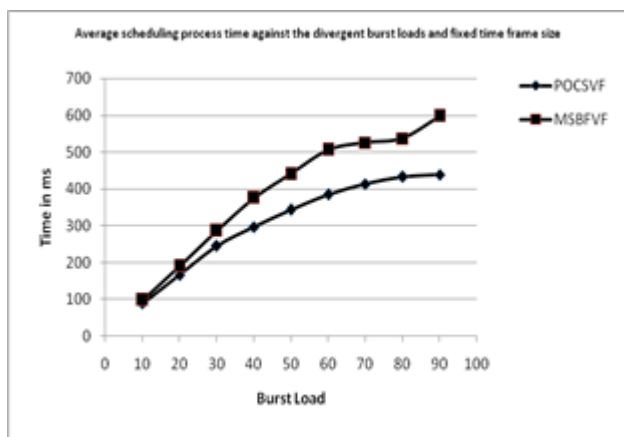


Fig 6: Depiction of Average time to schedule bursts: divergent burst loads with fixed timeframe of size 35  $\mu$ s

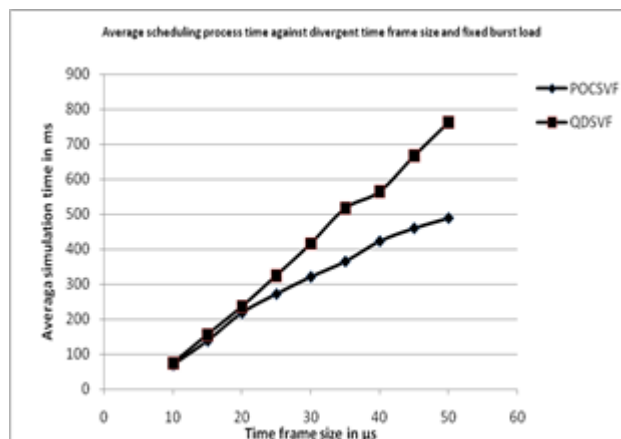


Fig 7: Depiction of Average time to schedule bursts divergent sizes of timeframes and fixed burst load of 35680 bytes

## 6. CONCLUSION

This manuscript is a novel burst scheduling model which is termed as “QoS metrics for dynamic scheduling through Void Filling and Burst Segmenting (QDS-VF)”. The core competence of the manuscript has tried to raise the channel utilization with extreme throughput under divergent burst sizes in addition to volatile time frames. It is clearly evinced from the simulation results that the proposed model is simplifying the process of scheduling with minimal burst drop ratio.. While the proposed model considers only limited channels which are often not true, future work can incorporate batch scheduling through multiple nodes.

## REFERENCES

1. C. Qiao and M. Yoo. Optical Burst Switching (OBS) - A New Paradigm for an Optical Internet. *Journal of High Speed Networks (JHSN)*, 8(1):69 - 84, 1999.
2. Y. Chen, C. Qiao, and X. Yu. Optical Burst Switching: A New Area in Optical Networking Research. *IEEE Network Magazine*, 18(3):16 -23, 2004.
3. Lamba, Rohit, and Amit Kumar Garg. "Survey on contention resolution techniques for optical burst switching networks." *International Journal of Engineering Research and Applications* 2.1: 956-961, 2012.
4. Kaheel, Ayman Malek, Hussein Alnuweiri, and Fayez Gebali. "A new analytical model for computing blocking probability in optical burst switching networks." *IEEE Journal on Selected Areas in Communications* 24.12 (2006).
5. Zhu, Xiaoming, and Joseph M. Kahn. "Queueing models of optical delay lines in synchronous and asynchronous optical packet-switching networks." *Optical Engineering* 42.6: 1741-1748, 2003.
6. Zhang, Qiong, et al. "TCP over optical burst-switched networks with controlled burst retransmission." *Photonic Network Communications* 22.3 (2011): pp. 299-312, 2011

7. Hsu, Ching-Fang, Te-Lung Liu, and Nen-Fu Huang. "Performance analysis of deflection routing in optical burst-switched networks." INFOCOM 2002. Twenty-First Annual Joint Conference of the IEEE Computer and Communications Societies. Proceedings. IEEE. Vol. 1. IEEE, 2002.
8. Li, Jikai, et al. "Maximizing throughput for optical burst switching networks." *IEEE/ACM Transactions on networking* 15.5 (2007): pp. 1163-1176, 2007
9. Sansò, Brunilde, Felisa Vázquez-Abad, and Eloim Gutiérrez-Cabrera. "S-JET: efficient reservation scheduling algorithm for optical burst switches." *Journal of Optical Networking* 4.8 (2005): 476-498.
10. Andrew, L., et al. "The asymptotics of optimal OBS wavelength assignment." *ACM Sigmetrics: Performance Evaluation Review* 31 (2003): 14-16.
11. Akar, Nail, EzhanKarasan, and Kaan Dogan. "Wavelength converter sharing in asynchronous optical packet/burst switching: an exact blocking analysis for markovian arrivals." *IEEE Journal on Selected Areas in Communications* 24.12 2006.
12. Chen, Yuhua, Jonathan S. Turner, and Pu-Fan Mo. "Optimal burst scheduling in optical burst switched networks." *Journal of Lightwave Technology* 25.8 (2007): pp. 1883-1894, 2007.
13. Yuan, Penghui, and Anshi Xu. "Two lower bounds on the burst loss probability in optical burst switching networks." *Photonic Network Communications* 20.2 (2010): 113-119.
14. Tintor, Vladica, PetarMatavulj, and Jovan Radunović. "Analysis of blocking probability in optical burst switched networks." *Photonic Network Communications* 15.3: pp. 227-236, 2008.
15. Loi, Chi-hong, Wanjiun Liao, and De-nian Yang. "Service Differentiation in Optical Burst Switched Networks." In *Proceedings of GLOBECOM*, 2002.
16. Ueda, Masayuki, Takuji Tachibana, and Shoji Kasahara. "Last-hop preemptive scheme based on the number of hops for optical burst switching networks.", 2005.
17. Ueda, Masayuki, Takuji Tachibana, and Shoji Kasahara. "Intermediate-hop preemption to improve fairness in optical burst switching networks." *IEICE transactions on communications* 91.3 (2008): pp. 710-721, 2008.
18. Gao, Xingbo, Mostafa A. Bassiouni, and Guifang Li. "Addressing conversion cascading constraint in OBS networks through proactive routing." *Photonic Network Communications* 18.1 (2009): pp. 90-104, 2009.
19. Hsu, Ching-Fang, and Li-Cheng Yang. "On the fairness improvement of channel scheduling in optical burst-switched networks." *Photonic Network Communications* 15.1 (2008): pp. 51-66, 2008.
20. Guo, Songtao, Yunqiang Zhang, and Yuanyuan Yang. "Distributed power and rate allocation with fairness for cognitive radios in wireless ad hoc networks." *Global Telecommunications Conference (GLOBECOM 2011)*, 2011 IEEE, 2011.
21. Chrysos, Nikolaos, et al. "Tandem queue weighted fair smooth scheduling." *Design Automation for Embedded Systems* 18.3-4 (2014): pp. 183-197,2014.
22. Zhang, Tairan, et al. "A Dual Price-Based Congestion Control Mechanism for Optical Burst Switching Networks." *Journal of Lightwave Technology* 32.14 (2014): pp. 2492-2501, 2014.
23. Coulibaly, Yahaya, et al. "QoS- aware ant- based route, wavelength and timeslot assignment algorithm for optical burst switched networks." *Transactions on Emerging Telecommunications Technologies* 26.11 (2015): 1265-1277.
24. T. Venkatesh and C. S. R. Murthy, *An analytical approach to optical burst switched networks*. USA: Springer, 2010
25. I. Baldine, G. N. Rouskas, H. G. Perros, D. Stevenson, "JumpStart: a Just-In-Time Signaling Architecture for WDM Burst-Switched Networks," *IEEE Communications Magazine*, vol. 40, no. 2, pp. 82-89, 2002.
26. I. Baldine, A. Bragg, G. Evans, M. Pratt, M. Singhai, D. Stevenson, R. Uppalli, "JumpStart Deployments in Ultra-High-Performance Optical Networking Testbeds," *IEEE Communications Magazine*, vol. 43, no. 11, pp. S18-S25, November 2005.
27. K. Dolzer, C. Gauger, "On Burst Assembly in Optical Burst Switching Networks - A Performance Evaluation of Just-Enough-Time," *Proceedings of the 17th International Teletraffic Congress, (ITC 2001)*, pp. 149-160, 2001.
28. O. Pedrola, S. Rumley, M. Klinkowski, D. Careglio, C. Gaumier and J. Solé-Pareta: Flexible simulators for OBS network architectures, in *Proc. ICTON 2008*, Athens, Greece, June 2008
29. Kishen Ajay Kumar, K. Suresh Reddy, M.N. Giri Prasad. "POCS-VF: Proximate Optimum Channel Selection through Void Filling and Burst Segmenting for Burst Scheduling In OBS Networks". *Journal of Theoretical & Applied Information Technology*, vol 96, no.4, pp.8-10, 2017.



## Statistical Analysis of a New Optimally Controlled Adaptive Algorithm for Acoustic Echo Cancellation

\*Shaik Sazia Athar<sup>1</sup>, Dr. P. Abdul Khayum<sup>2</sup>

<sup>1</sup>PG student, Electronics & Communication Engineering, G. Pulla Reddy Engineering College (Autonomous), Kurnool, India.

<sup>2</sup>Professor, Electronics & Communication Engineering, G. Pulla Reddy Engineering College (Autonomous), Kurnool, A.P, India.

**Abstract:** One of the major issues involved in today's Telecommunication technology is Acoustic echo during the conversations or full duplex configuration in Hands free communication systems. Acoustic echo cancellation is one of the most formidable system identification problems and several appealing solutions have been developed in past years. Predominantly used adaptive filter is NLMS algorithm, which has to confront the compromise between rapid convergence and low misalignment to meet these contrary requirements, choosing the best possible step-size is the matter of interest. In this paper, a new efficient NLMS based algorithm similar to the state variable model has been presented. The algorithm depends on the minimization of the misalignment by an interesting optimization criterion follows an iterative procedure for the evaluation of individual control factors. Simulations performed for acoustic echo cancellation evident for good behavior and effectiveness of the approach.

**Keywords:** Control factor, Misalignment, NLMS, Optimally controlled, Convergence

Date of Submission: 15-07-2017

Date of acceptance: 29-07-2017

### I. Introduction

The acoustic echo cancellation problem arises when acoustic coupling between a loudspeaker and a microphone occurs in applications like hands-free telephone and teleconferencing. Due to this coupling the far-end talker's signal being fed back to the far-end taker creating annoying echoes and instability in the system [7]-[9]. The key to reducing the undesirable echoes electrically is to generate a replica of the microphone signal and subtract it from the actual microphone signal as illustrated in Fig. 1. As a result, the adaptive echo canceller has the task of not only estimating the echo path, but also keeping track of changes in it. Adaptive filters are widely used in many system identification scenarios. In this frame of reference, the primitive idea is to update each coefficient of the filter independently of the others, by adjusting the adaptation step size in proportion to the magnitude of the estimated filter coefficient [10], [14]. In this way, among all the coefficients, the adaptation gain is "proportionately" redistributed. Emphasizing the large ones in order to boost up their convergence and, apparently, to increase the overall convergence rate.

In this paper, we propose an optimally controlled NLMS based adaptive filter for system identification. First, we consider a more general framework, assuming that the unknown system is modeled by a time-varying system following a first-order Markov model. In this way, we deal with a state variable model, similar to Kalman filtering [4], [10].

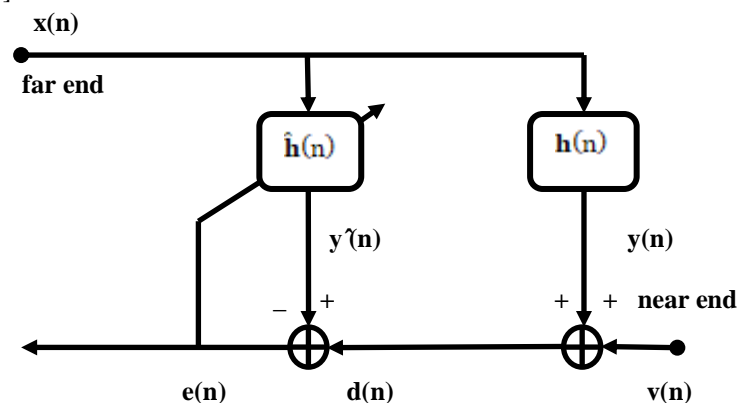


Fig. 1 Acoustic echo cancellation configuration

Here we follow an interesting optimization criterion based on the minimization of the system misalignment, which is a reasonable approach for system identification problems, e.g., see [12], and the references therein. The individual control factors results in a more rigorous way, depending on the coefficients' misalignment (instead on the coefficients' magnitude, as in the case of the classical proportionate-type algorithms). Simulations performed in the context of acoustic echo cancellation (AEC) indicate that the proposed algorithm could be an attractive choice for system identification problems.

## II. NLMS Based Optimal Algorithm

Let us consider a system identification problem, where adaptive filter is used to model an unknown system, both driven by the same zero-mean input signal  $x(n)$ . In this context, the output (microphone or desired) signal at the discrete-time index  $n$  is

$$d(n) = \mathbf{h}^T(n)x(n) + v(n), \tag{1}$$

Where  $\mathbf{h}(n) = [h_0(n) \ h_1(n) \ h_2(n) \ \dots \ h_{L-1}(n)]^T$  is the impulse response(of length  $L$ ) of the system (from the loudspeaker to the microphone) that we need to identify, and  $v(n)$  is the system noise, usually considered as a zero-mean white Gaussian noise signal. The variance of this additive noise is  $\sigma_v^2$ ,  $\mathbf{x}(n) = [x(n) \ x(n-1) \ x(n-2) \ \dots \ x(n-L+1)]^T$  is a vector containing the  $L$  most recent time samples of the zero-mean input (loudspeaker) signal  $x(n)$ , superscript  $T$  denotes transpose of a vector or a matrix.

Let us assume that  $h(n)$  follows a simplified first-order Markov model

$$h(n) = h(n-1) + w(n) \tag{2}$$

where  $w(n)$  is a zero-mean white Gaussian noise signal vector, which is uncorrelated with  $h(n-1)$ . The correlation matrix of  $w(n)$  is assumed to be  $\mathbf{R}_w = \sigma_w^2 \mathbf{I}_L$ , where  $\mathbf{I}_L$  is the  $L \times L$  identity matrix of  $w(n)$  and the variance,  $\sigma_w^2$  it captures the uncertainties in  $h(n)$ . This model can be valid in many system identification problems, like in acoustic echo cancellation [4], [6]. The objective is to estimate or identify  $\mathbf{h}(n)$  with an adaptive filter, defined by  $\mathbf{h}(n) = [\hat{h}_0(n) \ \hat{h}_1(n) \ \hat{h}_2(n) \ \dots \ \hat{h}_{L-1}(n)]^T$  a state variable model, similar to kalman filtering.

### 2.1 NLMS algorithm:

The NLMS algorithm is defined by the update

$$\begin{aligned} \hat{h}(n) &= \hat{h}(n-1) + \mu x(n)e(n) \\ \mu &= \frac{\alpha}{\mathbf{x}^T(n)\mathbf{x}(n) + \delta} \end{aligned} \tag{3}$$

where  $\mu$  is the step size parameter

$$e(n) = d(n) - \hat{h}^T(n-1)x(n) \tag{5}$$

is the error signal of the adaptive filter.

### 2.2 JO- NLMS algorithm:

The JO- NLMS algorithm is defined as follows

Let us define posterior misalignment as  $q(n) = h(n) - \hat{h}(n)$ , the update results in

$$q(n) = q(n-1) + w(n) - \mu x(n)e(n) \tag{6}$$

$$e(n) = \mathbf{x}^T(n)q(n-1) + \mathbf{x}^T(n)w(n) + v(n) \tag{7}$$

$$\mu(n) = \frac{1}{(L+2)\sigma_x^2 + \xi}$$

where  $\xi = L\sigma_v^2/[m(n-1) + L\sigma_w^2]$ . So, the filter update is

$$\hat{h}(n) = \hat{h}(n-1) + \mu x(n)e(n) \tag{9}$$

The step-size from (10) is introduced in (9) to update the parameter  $m(n)$

$$m(n) = [1 - \mu(n)\sigma_x^2][m(n-1) + L\sigma_w^2] \tag{10}$$

Summarizing the resulting JO-NLMS based algorithm defined by relations (8), (9) and (10), using the initialization  $\hat{h}(n) = 0$  and  $m(0) = \varepsilon$ , (where  $\varepsilon$  is a positive constant). This algorithm is very similar to the simplified kalman model [4], [10].

## III. Proposed Algorithm: Optimally Controlled NLMS

We extend JO NLMS algorithm to an optimized NLMS with individual control factors. The update equation is [8]:

$$\begin{aligned} \hat{h}(n) &= \hat{h}(n-1) + \mu \mathbf{A}(n-1)x(n)e(n) \\ \mu &\text{ is the step-size } \mu = \frac{\alpha}{\mathbf{x}^T(n)\mathbf{x}(n) + \delta} \end{aligned} \tag{11}$$

where  $\mathbf{A}(n)$  is a diagonal matrix ( $L \times L$ ) containing the control factors at time index  $n$ , the filter update (11) can also be written in terms of posterior misalignment as

$$q(n) = q(n - 1) + w(n) - \mu \mathbf{A}(n - 1)x(n)e(n) \quad (12)$$

### 3.1 Analysis of convergence and misalignment:

Taking  $\ell_2$  norm in (12) on both then mathematical expectations on both sides removing correlated products

$$E[\|q(n)\|_2^2] = E[\|q(n - 1)\|_2^2 + L\sigma_w^2 - 2\mu E[x^T(n)\mathbf{A}(n - 1)q(n - 1)e(n)] - 2\mu E[x^T(n)\mathbf{A}(n - 1)w(n)e(n)] + \mu^2 E[e^2(n)x^T(n)\mathbf{A}^2(n - 1)x(n)]] \quad (13)$$

Finally after some recommended computations

$$m(n) = m(n - 1) + L\sigma_w^2 - 2\mu\{\mathbf{R}_q(n - 1) + \sigma_w^2 I_L\}\mathbf{A}(n - 1) + \mu^2 \sigma_x^2 \text{tr}[\mathbf{A}^2(n - 1)]\{\sigma_v^2 + \sigma_x^2[m(n - 1) + L\sigma_w^2]\} \quad (14)$$

Imposing  $\partial m(n)/\partial \mu(n) = 0$  to (14), (Considering the step size is time dependent), optimal step size is obtained by

$$\mu(n) = \frac{\text{tr}\{\mathbf{R}_q(n-1) + \sigma_w^2 I_L\}\mathbf{A}(n-1)}{\text{tr}[\mathbf{A}^2(n-1)]\{\sigma_v^2 + \sigma_x^2[m(n-1) + L\sigma_w^2]\}} \quad (15)$$

The update of  $m(n)$  becomes

$$m(n) = m(n - 1) + L\sigma_w^2 - \frac{-\sigma_x^2 \{\text{tr}\{\mathbf{R}_q(n-1) + \sigma_w^2 I_L\}\mathbf{A}(n-1)\}^2}{\text{tr}[\mathbf{A}^2(n-1)]\{\sigma_v^2 + \sigma_x^2[m(n-1) + L\sigma_w^2]\}} \quad (16)$$

After several computations and simplifications, the optimal step size results in

$$\mu(n) = \frac{1}{c\{\sigma_v^2 + \sigma_x^2[m(n-1) + L\sigma_w^2]\}} \quad (17)$$

The update of the parameter becomes

$$m(n) = m(n - 1) + L\sigma_w^2 - c\mu(n)\sigma_x^2 \|\gamma(n - 1)\|_2^2 \quad (18)$$

Finally the filter update is obtained as

$$\hat{h}(n) = \hat{h}(n - 1) + c\mu(n)\gamma(n - 1)x(n)e(n) \quad (19)$$

where element wise product between  $\gamma(n-1)$  and  $x(n)$ .

$$c = \frac{L}{m(n-1) + L\sigma_w^2} \quad (20)$$

The vector contains the diagonal elements of the matrix

$$\gamma(n) = \gamma(n - 1) + \sigma_w^2 \mathbf{1}_{L \times 1} + c\mu(n)\sigma_x^2\{\sigma_v^2 + \sigma_x^2[m(n - 1) + L\sigma_w^2] - 2c\mu(n)\} \times \gamma(n - 1) * \gamma(n - 1) \quad (21)$$

Where  $\mathbf{1}_{L \times 1}$  denotes a column vector with all its  $L$  elements equal to one. Summarizing the result, the optimally controlled NLMS (OC-NLMS) algorithm with individual control factors is defined by relations (17)-(20) and (21).

$$\hat{\sigma}_w^2(n) = \frac{1}{L} \|\hat{h}(n) - \hat{h}(n - 1)\|_2^2$$

The interesting parameter in proposed algorithm is  $m(n)$  this can be used to evaluate the overall performance of the algorithm. A well known performance measure is echo to return loss enhancement (ERLE), as it requires priori knowledge of the impulse response or the echo signal. Here we propose to monitor the parameter  $M(n) = \|\hat{h}(n)\|_2^2/m(n)$ , which has similar significance with ERLE.

## IV. Simulation Environment

Simulations are performed for the acoustic echo cancellation using MATLAB [4], [6]. In this context, an adaptive filter is used to estimate the impulse response. The length of the impulse used in the experiments  $L=10$ , the same length is set for the adaptive filter. The input signal,  $x(n)$ , is a white Gaussian noise, the output of the echo is corrupted by an independent white Gaussian noise  $v(n)$ , the SNR is 20dB. Here it is assumed that  $\sigma_v^2$  is known, in practice it can be estimated [5]. An echo path change scenario is simulated, by shifting or inverting the impulse response, in the middle of the simulation.

### 4.1 Simulation results:

Interpreting the results, fig. 2, depicts the performance measure is mean square error (in dB), as noticed in the figure Mean square error is better for proposed OC-NLMS algorithm compared to JO-NLMS algorithm.

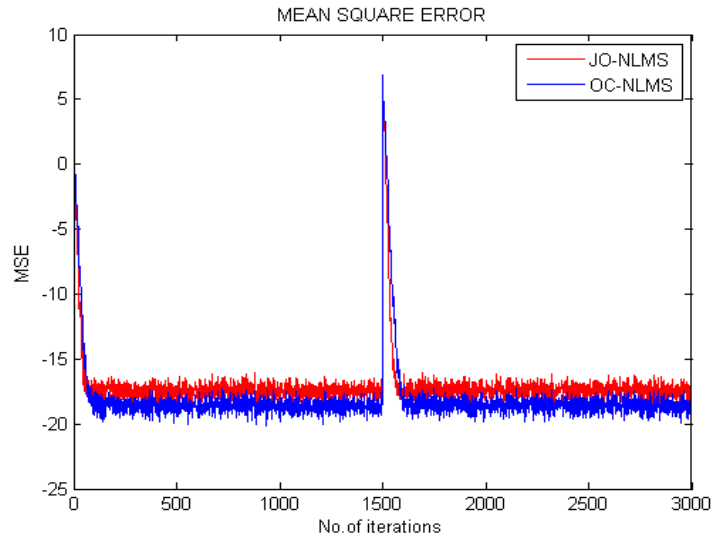


Fig. 2. Mean square error (dB) of JO-NLMS and OC-NLMS

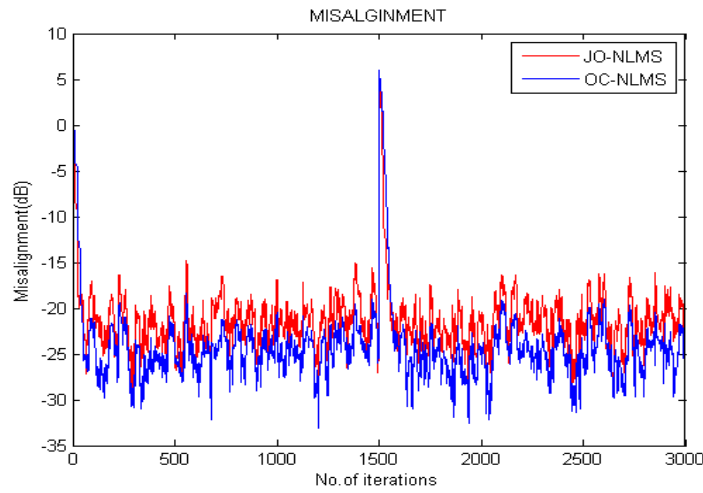


Fig.3. Evaluation of Misalignment of JO-NLMS and OC-NLMS algorithm

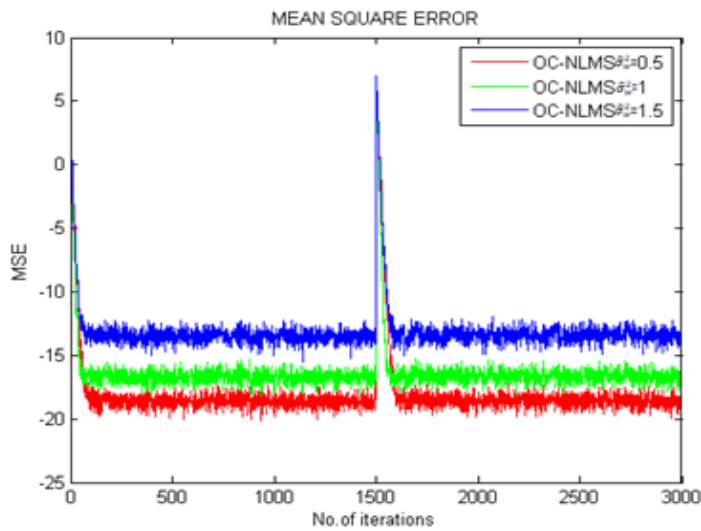


Fig.4. Performance of OC-NLMS algorithm as  $\sigma_w^2$  varies MSE changes

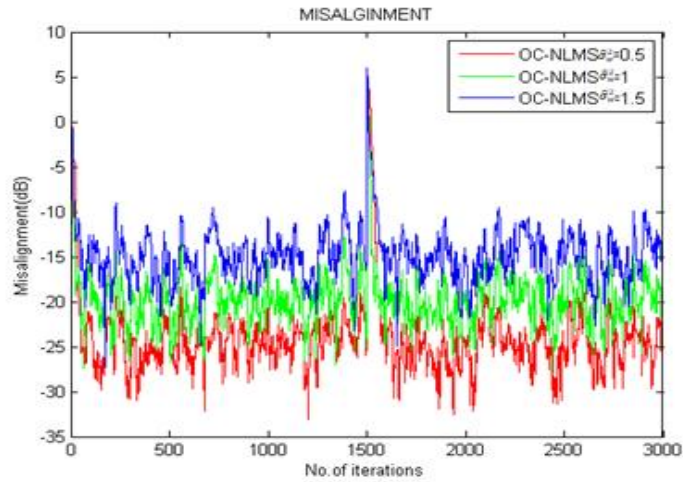


Fig.5. Performance of OC-NLMS algorithm as  $\sigma_w^2$  varies Misalignment changes

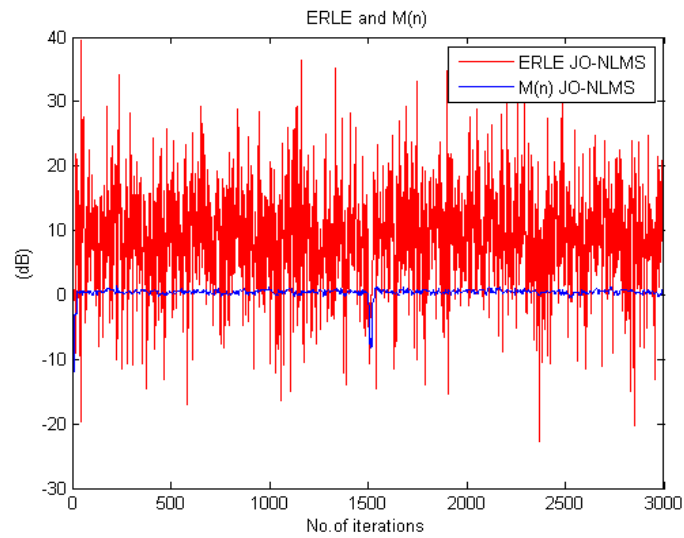


Fig. 6. Evaluation of the parameter M(n) and ERLE of JO-NLMS

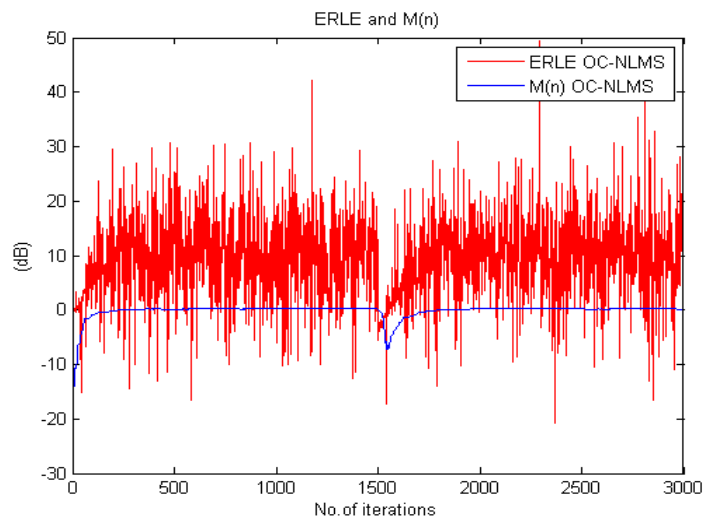


Fig. 7. Evaluation of the parameter M(n) and ERLE of OC-NLMS

The other essential performance measure is normalized misalignment (in dB) defined as  $20\log_{10}\|\hat{h}(n) - \hat{h}(n)\|_2 / \|\hat{h}(n)\|_2$ . As we can notice from this figure, the algorithm has better convergence rate, while achieving lower misalignment level as depicted in fig. 3. The variance  $\sigma_w^2$  captures the uncertainties in echo path,  $\sigma_w^2$  is varied for analysing the performance of the system. The observations describe that as the uncertainties in echo path increases the convergence of the algorithm is increasing, but the misalignment increases. The proposed algorithm traces the uncertainties in the echo path and works well for the large uncertainties in terms of convergence, as illustrated in figures (4) and (5). The parameter  $M(n) = \|\hat{h}(n)\|_2^2 / m(n)$  proposed to monitor the performance, which has similar significance with ERLE [4] in both the algorithms as depicted in the figures (6), (7).

Comparison of JO-NLMS and OC-NLMS algorithms in terms of Steady state error, ERLE and percentage of misalignment is illustrated in the table

**TABLE FOR COMPARISON**

Measure of performance	JO-NLMS	OC-NLMS
Steady state error(dB)	-17.366	-19.7320
ERLE(dB)	38.250	49.4520

### V. Conclusion

In this paper, we presented a qualitative optimized NLMS based algorithm which has a great potential in the context of sparse system identification. The optimization criterion employed is a minimization of the system misalignment, which is a natural approach the proposed algorithm OC-NLMS ensures better convergence, good traceable expression and controllable low misalignment compared to JO-NLMS which indicates qualitative performance of the system. Consequently, it is characterized as resisting the uncertainties in the echo path. Simulations justify performance and effectiveness of the approach, reducing the computational complexity in estimations of the parameters will be the next work in the future.

### References

- [1] H.-C. Shin, A. H. Sayed, and W.-J. Song, "Variable step-size NLMS and affine projection algorithms," *IEEE Signal Processing Lett.*, vol. 11, pp. 132–135, Feb. 2004.
- [2] H. Rey, L. Rey Vega, S. Tressens, and J. Benesty, "Variable explicit regularization in affine projection algorithm: robustness issues and optimal choice," *IEEE Trans. Signal Processing*, vol. 55, pp. 2096–2108, May 2007.
- [3] G. Enzner, H. Buchner, A. Favrot, and F. Kuech, "Acoustic echo control," in *Academic Press Library in Signal Processing*, vol. 4, ch. 30, pp. 807–877, Academic Press 2014
- [4] S. Ciochin'a, C. Paleologu, and J. Benesty, "An optimized NLMS algorithm for system identification," *Signal Processing*, vol. 118, pp. 115–121, Jan. 2016
- [5] C. Paleologu, S. Ciochin'a, and J. Benesty, "Variable step-size NLMS algorithm for under-modeling acoustic echo cancellation," *IEEE Signal Processing Lett.*, vol. 15, pp. 5–8, 2008.
- [6] R. E. Kalman, "A new approach to linear filtering and prediction problems," *J. Basic Engineering*, vol. 82, pp. 35–45, Mar. 1960
- [7] A. H. Sayed, *Adaptive Filters*. (New York, NY: Wiley, 2008).
- [8] P. S. R. Diniz, *Adaptive Filtering: Algorithms and Practical Implementation*. Fourth Edition, (New York, NY: Springer-Verlag, 2013).
- [9] J. Benesty, T. Gaensler, D. R. Morgan, M. M. Sondhi, and S. L. Gay, *Advances in Network and Acoustic Echo Cancellation*. Berlin, Germany: Springer-Verlag, 2001
- [10] S. Ciochin'a, C. Paleologu, J. Benesty, and S. L. Grant, "An optimized proportionate adaptive algorithm for sparse system identification," in *Proc. IEEE Asilomar*, 2015, 5 pages
- [11] G. Enzner, "Bayesian inference model for applications of time-varying acoustic system identification," in *Proc. EUSIPCO*, 2010, pp. 2126–2130
- [12] P. A. C. Lopes and J. B. Gerald, "New normalized LMS algorithms based on the Kalman filter," in *Proc. IEEE ISCAS*, 2007, pp. 117–120.
- [13] M. A. Iqbal and S. L. Grant, "Novel variable step size NLMS algorithms for echo cancellation," in *Proc. IEEE ICASSP*, 2008, pp. 241–244
- [14] J. Benesty and S. L. Gay, "An improved PNLS algorithm," in *Proc. IEEE ICASSP*, 2002, pp. II-1881–II-1884.

IOSR Journal of Electronics and Communication Engineering (IOSR-JECE) is UGC approved Journal with SI. No. 5016, Journal no. 49082.

Shaik Sazia Athar. "Statistical Analysis of a New Optimally Controlled Adaptive Algorithm for Acoustic Echo Cancellation." *IOSR Journal of Electronics and Communication Engineering (IOSR-JECE)* 12.4 (2017): 01-06

## Time of Arrival Estimation of Ultra Wideband Indoor Wireless System

B. Venkata Krishnaveni<sup>1</sup>, K. Suresh Reddy<sup>2</sup>, P. Ramana Reddy<sup>3</sup>

<sup>1</sup> *Research scholar, Electronics and Communication Engineering, JNTUA, Anantapuram, AP, India*

<sup>2</sup> *Head of the Department, Electronics and Communication Engineering, G. .Pulla Reddy Engineering College, Kurnool, AP, India*

<sup>3</sup> *Head of the Department, Electronics and Communication Engineering, JNTUA, Anantapuram, AP, India*

### **Abstract**

*The time of arrival (TOA) estimation is a very challenging task due to the high diffusive behaviour of channels in ultra wideband technology, here the first arriving signal is not consequently the efficient path. The Nyquist rate sampling of UWB is difficult due to high bandwidth of UWB signal. So accurate ranging methods at lower sampling rates is needed to be designed. In this paper we are estimating TOA values using samples of the observed signal from reference nodes after calculation of energy. Performance of different time of arrival estimation algorithms are analysed using simulations for channel models of IEEE 802.15.4a standard.*

### **1 Introduction:**

The developments in the technology of wireless communication and the explosion of wireless sensor networks and mobile communication, the global positioning and navigation technology is maturing. In the environment of outside building, the Global Positioning System (GPS) is a widely used positioning method, which can attain nearly 10m accuracy without additional apparatus. Due to the complex propagation behaviour of indoor environment, more obstructions occurred in the propagating medium of wireless signals. This gains the complexity in calculating specific position in indoor environment [1]. Now a days, area based services are turning into an indispensable piece of individuals' lives and employments because of the enormous uses of indoor positioning in safety at public areas, commerce and military. Along these lines, how to give steady, ongoing and precise position data has become a hot purpose of present research.

Present positioning methods in indoor environments are different, including Bluetooth, Wi-Fi fingerprint, RFID, Laser, and UWB technology [2], [3]. Among these methods, UWB technology has an expansive application aspect of wireless communications in the region of short range positioning and tracking due to its properties of large transmission speed, strong penetrating power, low consumption of power, simple structure, and good anti multipath performance [4]. UWB is more appropriate for exact positioning in indoor situations related to other methods [5], [6]. As of late, there have been many distributed research on the subject of indoor positioning dependent on UWB technology. A large portion of these looks into focused on improving the positioning exactness by setting up the channel model or wiping out the error in range of UWB [7], [8]. With dissecting the UWB signal quality in multipath situations, it is realized that the ranging exactness and performance of UWB change broadly under various propagation modes and paths [9]. Real-time and exact positioning can be accomplished when Time of Arrival (TOA) technique is used in UWB [10].

In this paper we are interested in performance investigation of time of arrival estimation algorithms. We first discuss system model in section II. In section III explains the TOA estimation methods followed by results, discussion and conclusion in sections IV and V respectively.

## II. Model of the System

So as to characterize a ranging issue, we expect that the transmitter and the recipient are synchronized with one another. By taking an impulse radio (IR) UWB signal, the received signal in a multipath domain can be modeled using equation (1). [11].

$$r(t) = \sum_{l=1}^L \alpha_l s(t - \tau_l) + n(t). \quad (1)$$

The waveform  $s(t)$  indicates the authoritative single-path signal.  $\alpha_l$  and  $\tau_l$  are the channel attenuation coefficient and delay of the  $l^{\text{th}}$  multipath channel, respectively,  $L$  is the number of multipath channels. Here  $\tau_l = \tau_{\text{TOA}}$  is the TOA to be evaluated. We assume that  $n(t)$  is a complex zero mean additive white Gaussian noise (AWGN) and  $r(t)$  is a complex signal.

We characterize  $z[n]$  ( $n=1,2,\dots,N$ ) as the absolute values of the samples, The sampling can be done either for the received signal or is sampled the output of the energy detection. Here the total number of the samples is  $N$ .

## III. TOA Estimation

Due to the high dispersive behaviour of ultra-wideband (UWB) channels, it is difficult to measure time of arrival (TOA) values. Here the first arrival path may not be the strongest path. The sampling of UWB signal at Nyquist rate is difficult because of the high bandwidth of it. Hence there is a need for precise ranging and less complicated techniques at achievable sampling rates. The Fig.1 shows the suggested method for the calculation of TOA values. Here the TOA estimation is done using the samples  $z[n]$ , which are taken after the square-law device.

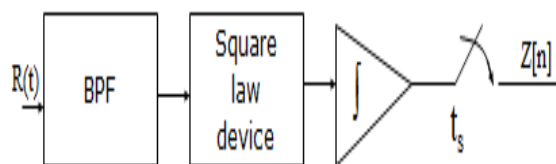


**Fig1. Energy samples of the received signal**

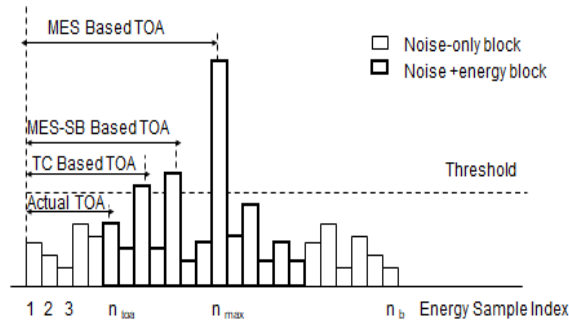


**Fig 2. TOA estimation algorithms using the samples of energy**

### TOA Estimation algorithms

There are three algorithms for TOA estimation using the energy samples received after square law device, summarized in Fig.2.

#### a) Maximum Energy Selection (MES)

By selecting the sample output with maximum energy as the first path is the easy way of estimating TOA value. According to this method the TOA value can be estimated using the below equation

$$t_{MES} = [\arg(\max\{z[n]\}) - 0.5] T_b$$

$$= (n_{max} - 0.5) T_b \quad (2)$$

The midpoint of the block is taken as the TOA estimated value in the equation (2). In many situations the first arriving energy block may not be the strongest energy block and the MES therefore produce errors even in a high signal to noise ratio (SNR). Its performance also decreases with  $N_b$ , since it may take only noise block as the maximum energy block.

#### b) Threshold Comparison (TC)

In this method an applicable threshold is selected and the samples are compared with this threshold, and the sample index which first crosses the threshold can be considered as the value of TOA to estimate, which is shown in equation (3).

$$t_{TC} = [\min\{n|z[n] > \xi\} - 0.5] T_b \quad (3)$$

Here  $\xi$  is a threshold value, which must be assigned using the statistics of the received signal. Normally this method performs poorly at low SNR area because the crossing of the threshold is more frequent in many situations due to the addition of noise.

#### c) MES Search Back (MES-SB)

So as to enhance the the threshold comparison method at low SNRs, the energy samples preceding to the maximum energy value has to searched. The window of search-back using the number of samples is given by  $w_{sb}$ , which is assigned using the measurements of the channel. This method alone produces good

results among all the mentioned methods above. The TOA value calculated using a backward search and threshold is mentioned in equation (4).

$$t_{\text{MES-SB}} = [\min\{\check{Z}[n] > \xi\} - 0.5 + n_{\text{max}} - w_{\text{sb}} - 1] T_b \quad (4)$$

here

$$\check{Z}[n] = \{z[n_{\text{max}} - w_{\text{sb}}] z[n_{\text{max}} - w_{\text{sb}} + 1] \dots z[n_{\text{max}}]\}$$

#### IV. Results and Discuss

TOA estimation is done for IEEE 802.15.4a model channel 1 of UWB system. Here the time to travel from access point to mobile unit is taken as TOA value. The optimum threshold is set to 0.5 for channel model 1 and corresponding  $w_{\text{sb}}$  set to 50 ns. To examine the performance of these algorithms Mean Absolute Error (MAE) is calculated at various Eb/No values. Among them, by using the window of search back MES-SB produces good results. The TC algorithm gives poor performance near lower Eb/No values because the noise levels cross the threshold value frequently. But at higher Eb/No values threshold comparison performs well.

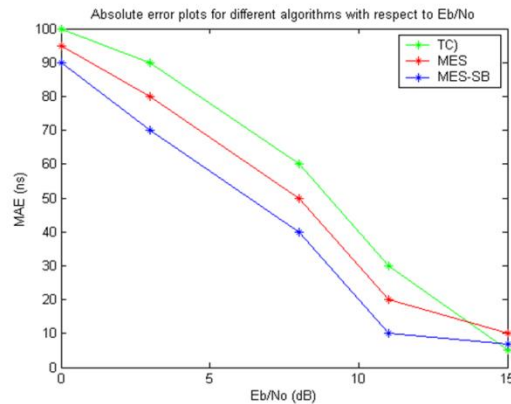


**Fig 3. Absolute error plots for different algorithms with respect to Eb/No(dB)**

#### V. Conclusion

The algorithms for TOA estimation of Ultra Wideband system at low sampling rate using the energy detection are evaluated via simulations for channel model 1. Simulation results among the three given algorithms, maximum energy selection supported with a search-back window gives better performance compared with other algorithms. But the threshold comparison algorithm gives better performance at a higher rate values.

## References

1. Y. Sun, W. Meng, C. Li, N. Zhao, K. Zhao, and N. Zhang, "Human localization using multi-source heterogeneous data in indoor environments," *IEEE Access*, vol. 5, pp. 812–822, Jan. 2017.
2. B. Venkata Krishnaveni, K. Suresh Reddy, P. Ramana Reddy, "Wireless Indoor Positioning Techniques Based on Ultra Wideband (UWB) Technology, *International Journal of Recent Technology and Engineering (IJRTE)* ISSN: 2277-3878, Volume-7, Issue-5C, February 2019
3. H. Liu, H. Darabi, P. Banerjee, and J. Liu, "Survey of wireless indoor positioning techniques and systems," *IEEE Trans. Syst., Man, Cybern. C: Applications and Reviews*, vol. 37, no. 6, pp. 1067–1080, Nov. 2007.
4. S. Gezici et al., "Localization via Ultra-Wideband Radios," *IEEE Signal Processing Magazine*, vol. 22, no. 4, pp. 70-84, July 2005.
5. Z. Sahinoglu, S. Gezici, and I. Guvenc, "Ultra-wideband Positioning Systems: Theoretical Limits, Ranging Algorithms, and Protocols," New York: Cambridge University Press, 2008.
6. L. Yang and G. B. Giannakis, "Ultra-wideband communications: An idea whose time has come," *IEEE Signal Process. Mag.*, vol. 21, no. 6, pp. 26–54, Nov. 2004
7. D. Dardari, A. Conti, U. Ferner, A. Giorgetti, and M. Z. Win, "Ranging with ultrawide bandwidth signals in multipath environments," *Proc. IEEE Special Issue on UWB Technology and Emerging Applications*, vol. 97, no. 2, Feb. 2009.
8. Li X, Cao F. "Location based TOA algorithm for UWB wireless body area networks", *IEEE 12th International Conference on. IEEE*, 2014: 507-511
9. A. F. Molisch, K. Balakrishnan, C. C. Chong, et al., *IEEE 802.15.4a channel model – final report*. Sep., 2004. [Online]. Available: <http://www.ieee802.org/15/pub/TG4a.htm>
10. A.A.D'Amico, U. Mengali, and L. Taponecco, "TOA estimation with the IEEE 802.15.4a standard," *IEEE Trans. Wireless Commun.*, vol. 9, no. 7, pp. 2238–2247, Jul. 2010.
11. I. Guvenc, C. C. Chong, and F. Watanabe, "Joint TOA Estimation and Localization Technique for UWB Sensor Network Applications," *Proc. IEEE Veh. Technol. Conf.*, Dublin, Ireland, pp. 1574-1578, April 2007

# UWB Antenna Design with Required Band Suppression Characteristics For Cognitive Radio Applications

<sup>1</sup>T.Sarath Babu, <sup>2</sup>Dr.S. Nagaraja Rao, <sup>3</sup>Dr.T.V. Rama Krishna

<sup>1</sup>Research Scholar, Department of ECE, KL Deemed to be University, Vaddeswaram, Guntur, Andhra Pradesh, India. (E-mail: tsarath@rediffmail.com)

<sup>2</sup>Professor and HOD, Dept. of ECE, G.Pulla Reddy Engineering College, Kurnool, Andhra Pradesh, India. (E-mail: suryakari2k1@yahoo.com)

<sup>3</sup>Professor, Department of ECE, KL Deemed to be University, Vaddeswaram, Guntur, Andhra Pradesh, India. (E-mail: tottempudi@kluniversity.in)

## Article Info

Volume 83

Page Number: 6248 - 6255

Publication Issue:

May-June 2020

Article History

Article Received: 19 November 2019

Revised: 27 January 2020

Accepted: 24 February 2020

Publication: 18 May 2020

## Abstract:

This paper presents the design of ultra wideband monopole antenna that can resonate over a range of frequencies from 2GHz to 10GHz which is appropriate for cognitive radio applications. The antenna is equipped with Split Ring Resonators which can notch two narrow band frequencies 4.47GHz to 4.82GHz, 6.94GHz to 7.77GHz and wide band greater than 8.41GHz. The design is simulated and the results are obtained using HFSS electromagnetic simulation software.

**Keywords:** wideband monopole, split ring resonator, wideband, cognitive radio.

## 1. Introduction

Cognitive radio is an emerging field which addresses the problem of shortage of available spectrum through dynamic spectrum allocation. In the cognitive radio environment, a group of secondary users coexist along with licensed primary users. The unlicensed users (SUs) can access the spectrum allocated to licensed users (PUs) when the licensed users are not accessing the spectrum. The licensed spectrum which is not being accessed by the primary users is called a spectral hole. These vacant spaces need to be identified to allocate them to the secondary users. This task requires the wideband antenna to continuously scan the spectrum over frequency band to detect the presence of a primary user. To access the spectral holes dynamically, narrow band antennas may be used. The microstrip antenna design for narrow band cognitive radio applications was presented in [1]. In the presence of

a licensed primary user, the spectrum cannot be allocated to a secondary user. Hence the narrow band frequencies where the licensed primary user is identified need to be notched to prevent the allocation to the secondary users.

In addressing the above two issues, ultra wideband antennas with frequency notching characteristic play a prominent role. This was clearly demonstrated in the research work contributed by Jawad Y. Siddiqui et al [2]. Notching of dual frequency bands and wide band was demonstrated using a circular monopole antenna equipped with two pairs of split ring resonators. Antenna response in three different configurations using SRRs, CRRs and parallel strips for obtaining notched, narrowband and UWB responses was also demonstrated in [3]. Different approaches for notching triple bands using an UWB antenna were presented in [4-5]. Several designs of

the extensively used monopole planar antenna are covered in [6-10]. The use of electromagnetic band gap structure for notching two frequency bands using an UWB was presented in [11]. The microstrip antenna design calculations for circular shaped radiating are covered in [12]. The paper is organized into two sections. The first section presents UWB antenna design which can resonate over 2GHz to 10GHz with out incorporating split ring resonators. The second one presents UWB antenna design with the incorporation of split ring resonators to notch the frequency bands.

**2. a)The Proposed Antenna Design and Geometry without Split Ring Resonators**

The ultra-wideband monopole antenna is designed for the frequencies 1GHz to 10GHz. The proposed consists of a circular patch in the top layer of radius 11.7 mm with feed line of width of 5 mm and length 22.7 mm. The space between the ground plane and the feed line is chosen as 0.5mm. The height of the circular radiating area above the ground plane is 1.58 mm. The ground plane’s length and width to the right and left of feed line are 22 mm and 22.7 mm respectively. FR4 substrate of 1.575mm thick,  $\epsilon_r=4.4$  and  $\tan \delta=0.02$  is used. The structural specifications and the proposed design parameters are shown in the Fig.1 & Table.1 respectively.

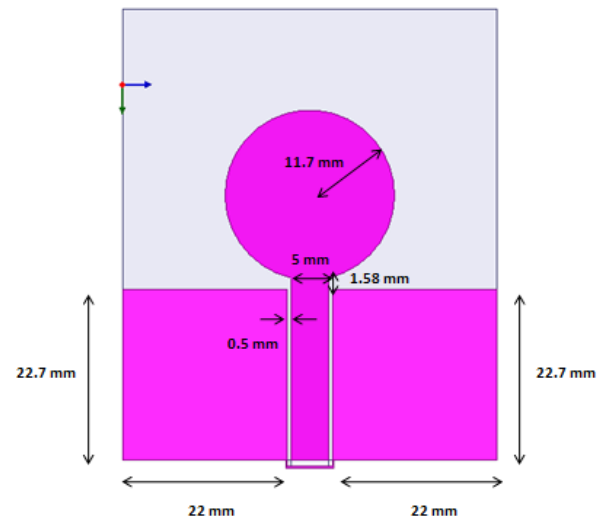


Fig.1 Structural and Design Specifications for the antenna proposed

Table 1. Design Specifications

Dimension	Size (mm)
Radius of the circular patch	11.3
Length of the transmission Line	22.7
Width of the Transmission Line	5
Thickness of the micro-strip substrate	1.575
Gap between feed line and ground plane on either side	0.5

**2. b) The Proposed Antenna Design and Geometry with Split Ring Resonators**

The wideband monopole antenna proposed is equipped with two single split ring resonators of rectangular shape and two square shape split ring resonators with concentric rings in the bottom layer on an FR4 substrate of thickness 1.575mm. The proposed antenna when equipped with Split Ring Resonators is presented below Fig.2.

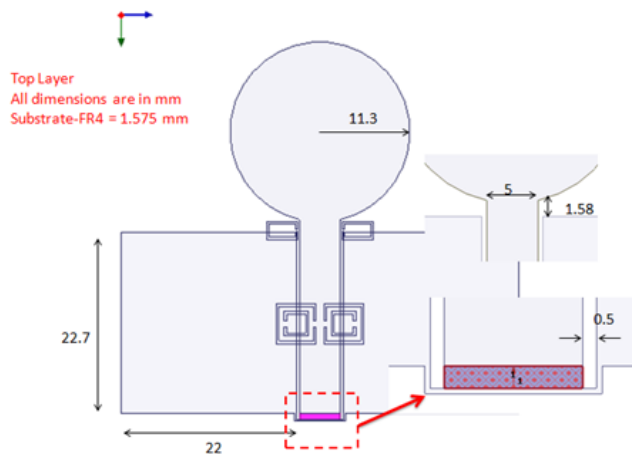


Fig.2a Proposed Antenna Design with SRRs

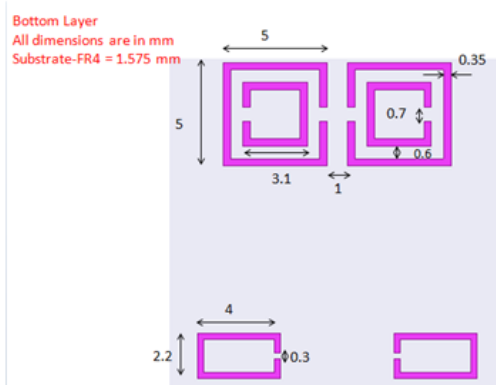


Fig.2b SRR Specifications

Fig.2 Structural and Design Specifications for the antenna proposed with SRRs

### 3. Results and Interpretation:-

Simulation results for the proposed design with out SRRs are presented in the figures 3a through 3d.

The  $S_{11}$  parameter characteristics is obtained for the ultra wide band. The resonant bands are achieved for less than -10dB for the frequencies between 2GHz to 10GHz as shown in Fig.3a. The maximum and minimum resonant frequencies are obtained at 2.3GHz and 9.3GHz respectively.

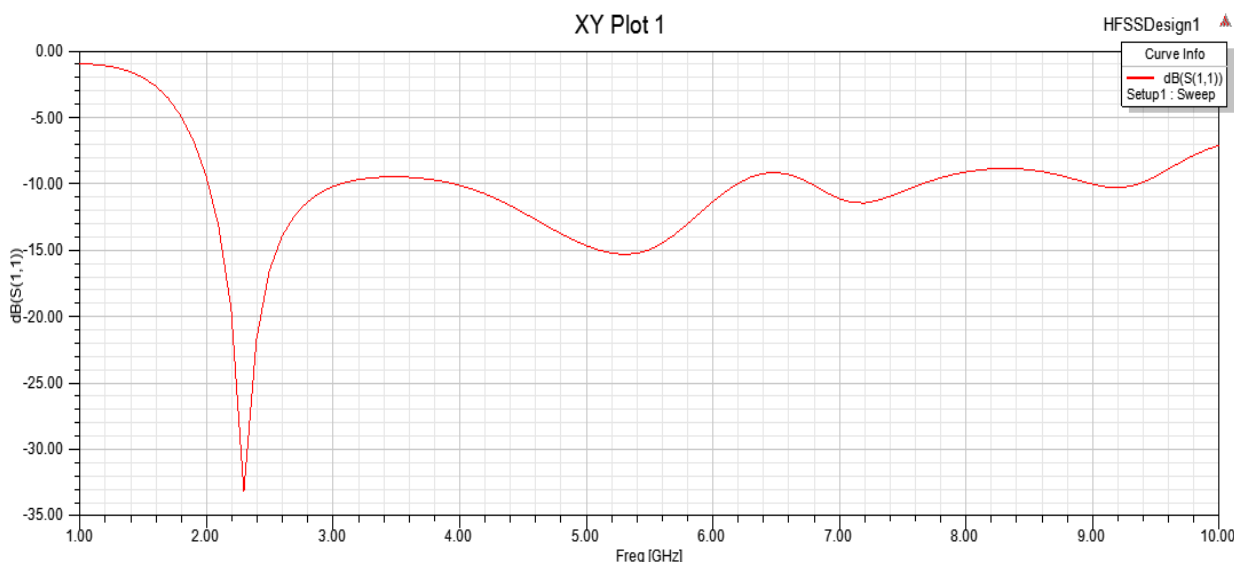


Fig.3a: Frequency v/s  $S_{11}$  parameter of the proposed design

Simulation results for Frequency v/s VSWR are satisfactory with the value of  $VSWR < 2$  for the frequencies between 2GHz to 10GHz as shown in Fig3b.



bands is shown in Figs 3e through 3i.

wide band greater than 8.41GHz is achieved as shown in the VSWR characteristics curve in Fig.3e.

The notching of narrow band frequencies viz. 4.47GHz to 4.82GHz, 6.94GHz to 7.77GHz and

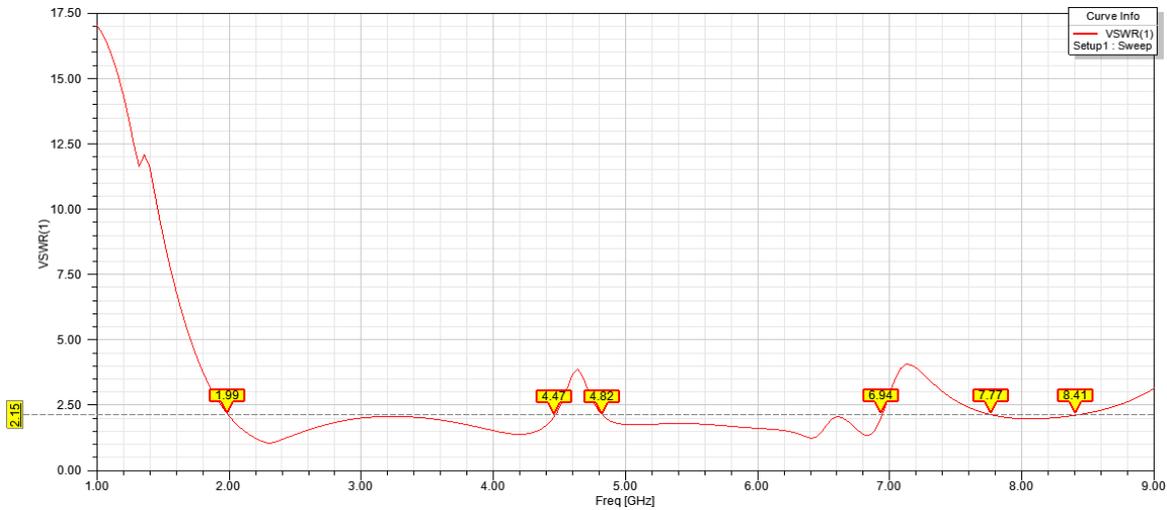


Fig.3e: Frequency v/s VSWR of proposed design with SRR

Results in Fig.3f show that except for the notch band frequencies shown in the Fig.3e, the value of

$S_{11}$  is less than -10dB.

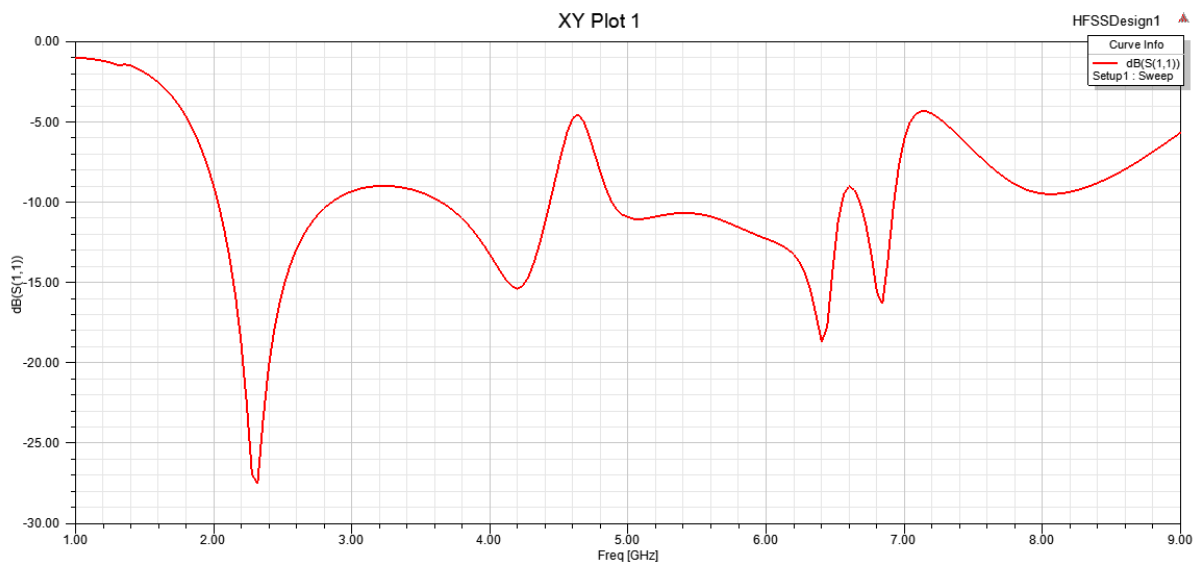


Fig.3f: Frequency v/s  $S_{11}$  of proposed design with SRR

Results of impedance for proposed UWB design  $50\Omega$  except for the notch band frequencies resonating between 2GHz to 10GHz are close to mentioned above as shown in the Fig.3g.

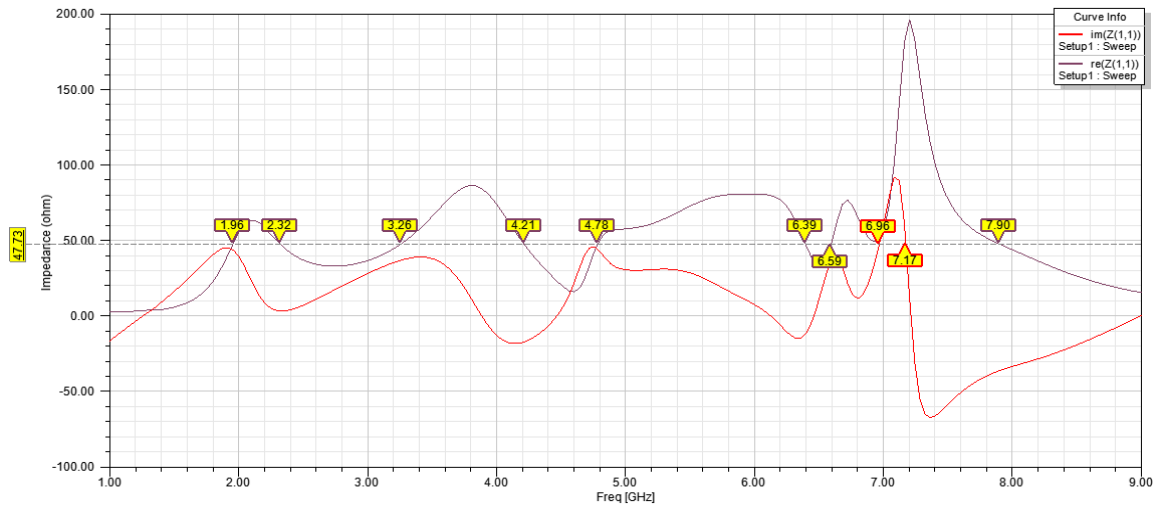


Fig.3g: Frequency v/s impedance of proposed design with SRR

The simulations of radiation patterns obtained for xy plane and yz plane shown in Figs. 3h and 3i are satisfactory.

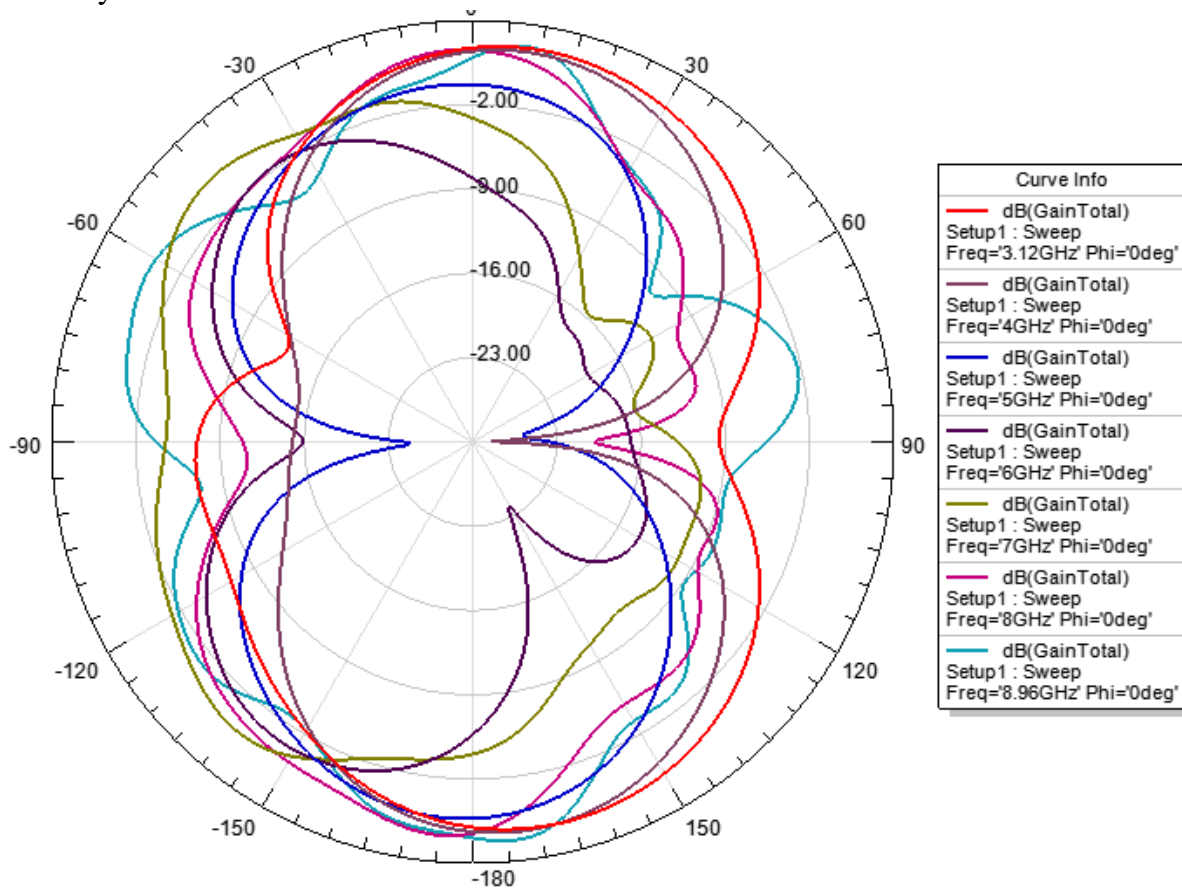


Fig.3h: Radiation Pattern for xy plane

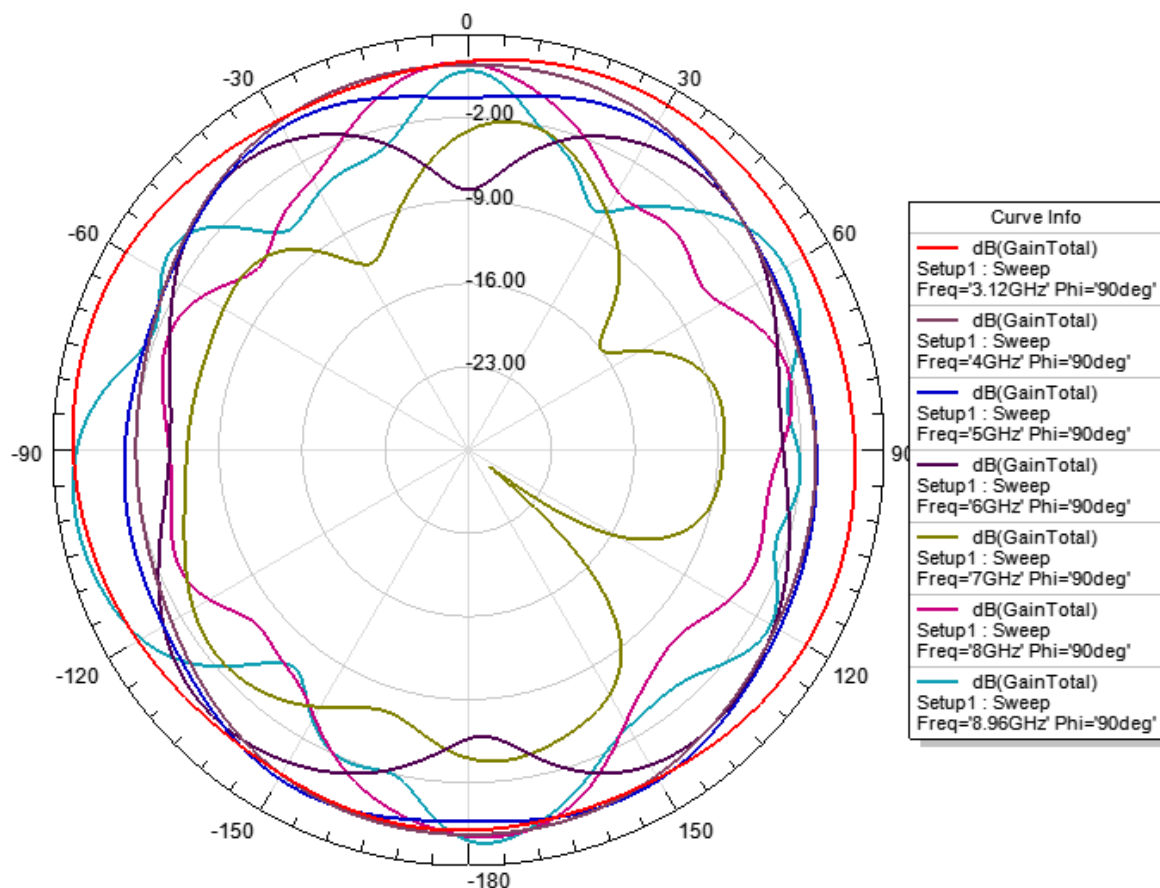


Fig.3i: Radiation Pattern for yz plane

**Conclusion:-**

The UWB antenna design with a circular patch which can resonate over 2GHz to 10GHz for cognitive radio applications was obtained. The notching of narrow frequency bands between 4.47GHz to 4.82GHz, 6.94GHz to 7.77GHz and wide band greater than 8.41GHz was achieved by equipping the proposed design with two rectangular shaped single split ring resonators and two square shape split ring resonators with concentric rings in the bottom layer. Simulation results of the proposed antenna before and after insertion of SRRs are within the acceptable limits for ensuring reasonably better performance of the proposed antenna design.

**REFERENCES**

1. T. Sarath Babu et.al, “Microstrip antenna design

for low power cognitive radio applications”, International Journal of Recent Technology and Engineering (IJRTE) ISSN: 2277-3878, Volume-7, Issue-6S, March 2019.

2. Jawad Y. Siddiqui et.al, “Compact Dual-SRR-Loaded UWB Monopole Antenna With Dual Frequency and Wideband Notch Characteristics”, IEEE Antennas and Wireless Propagation Letters, Vol.14,2015.

3. Jawad Y. Siddiqui et.al, “A Novel Ultrawideband (UWB) Printed Antenna With a Dual Complementary Characteristic”, IEEE Antennas and Wireless Propagation Letters, Vol.14,2015.

4. Ch.RamaKrishna et.al, “Compact Self Complementary UWB Antenna with Triple Band Notch Characteristics for Wireless Communications”, International Journal of Recent Technology and Engineering (IJRTE) ISSN: 2277-3878, Volume-8 Issue-3, September 2019.

5. Anju A Chandran et.al, Triple Frequency Notch in UWB Antenna with Single Ring SRR loading, 6th International Conference On Advances In Computing & Communications, ICACC 2016, 6-8 September 2016, Cochin, India, 1877-0509 © 2016 Published by Elsevier B.V.
6. Sudhanshu Belwal , Ahmad Rafiquee , Vibhor Bangwal “Modified UWB Antenna for Cognitive Radio Applications”, SSRG International Journal of Industrial Engineering ( SSRG – IJIE ) – Volume 5 Issue 3 – Sep to Dec 2018.
7. Santasri Koley, Dipen Bepari & Debjani Mitra ,“Band-Reconfigurable Monopole Antenna for Cognitive Radio Applications” IETE Journal of Research, ISSN: 0377-2063, Volume 61-2015, Issue 4, Pages 411-416.
8. Deeplaxmi V. Niture\*, Santosh S. Jadhav, and S. P. Mahajan, “Recon UWB Antenna for Cognitive Radio”, Progress In Electromagnetics Research C, Vol. 79, 79–88, 2017.
9. D.T.Nguyen, D.H.Lee, and H.C.Park, “Verycompactprintedtriple band-notchedUWBantennawithquarter-wavelengthslots,”IEEEAntennasWirelessPropag. Lett.,vol.11,pp.411–414,2012.
10. S. Soltani, M. Azarmanesh, P. lotfi and G. Dadashzadeh , “Two novel very small monopole antennas having frequency band notch function using DGS for UWB application” International Journal of Electronics and communications, vol. 65, Issue 11, November 2011, Pages 984.
11. H. Liu and Z. Xu, “Design of UWB monopole antenna with dual notched bands using one modified electromagnetic-bandgap structure,” Sci. World J., vol. 2013, pp. 1–9, 2013, ID 917975.
12. J. Salai Thillai Thilagam et.al “Simulation of circular patch antenna with probe feed and micro strip line feed, International Journal of Wireless Communication, Vol.4, No.10, PP 574-579, 2012.